Oxygen and CO Adsorption on Supported Pd Nanoparticles and Pd(111)

D I S S E R T A T I O N

zur Erlangung des akademischen Grades

doctor rerum naturalium
(Dr. rer. nat.)
im Fach Chemie

eingereicht an der
Mathematisch-Naturwissenschaftlichen Fakultät I
der Humboldt-Universität zu Berlin

von
Dipl.-Chem. Matthias Peter

Präsident der der Humboldt-Universität zu Berlin:
Prof. Dr. Jan-Hendrik Olbertz

Dekan der Mathematisch-Naturwissenschaftlichen Fakultät I:
Prof. Stefan Hecht PhD

Gutachter:
1. Prof. Dr. Hans-Joachim Freund
2. Prof. Dr. Joachim Sauer

eingereicht am: 29.10.2013
Tag der mündlichen Prüfung: 18.12.2013

Inhaltsverzeichnis

1 Introduction

Heterogeneous catalytic processes can be widely found in our everyday lives, including pollution control [1, 2], the conversion of chemical feedstocks into chemically pure raw materials [1, 3–6] and the processing of oils for manufacturing of food products [7, 8].
Current important issues in catalysis research are how to improve the yields and the selectivities of heterogeneous catalysts. Furthermore, it is of interest to extend their usage for example in asymmetric synthesis. A common strategy to achieve these goals is by testing empirically how changes in experimental conditions and in composition and structure of catalysts influence the catalytic performance. However, due to the large number of parameters, this approach is expensive and time consuming. This calls for a more fundamental understanding of catalytic processes, to enable a rational design of heterogeneous catalysts.
To resolve the microscopic structure of catalysts, to identify active sites and to gain detailed information about the mechanism, the energetics and kinetics of catalytic processes are important steps towards this goal. The high structural and chemical complexity of industrial catalysts hampers a detailed atomistic understanding of surface processes. Their chemical composition is generally non uniform and they exhibit a large number of geometrically different surface sites, which complicates the identification of catalytically active centers [9]. Furthermore, industrial catalysts are generally non planar and often poorly conductive, which limits the use of modern spectroscopic and microscopic techniques.
For these reasons, early studies have been performed on single crystals, on which the study of catalytic processes is more straightforward using current surface science methods. Based on these investigations, an atomistic level understanding on the activity of a large number of structurally and chemically different surfaces could be gained [10–15]. Despite the ongoing importance of such studies, these systems, in many cases, only poorly resemble the nanodispersed, catalytically active component of technical catalysts. Therefore, many crucial features, inherent to industrial powder catalysts, such as the influence of the support, the presence of different facets, size effects and many more cannot be understood by studying catalytic processes on single crystals.
In order to address these issues, an increasing number of investigations are performed on nanostructured supported model systems, which exhibit many features of industrial catalysts, but where a high degree of control of the chemical composition and the structure can be achieved. These model systems can be oxide single crystals [16] or well ordered thin oxide films, grown on metal substrates [17–21]. Thin oxide films are particularly advantageous for surface science studies: they can be grown planar with a uniform composition/structure on a metal substrate and exhibit an increased conductivity compared to oxide single crystals. Thus standard surface science techniques can be applied to provide valuable information on the structural, electronic and catalytic properties of these systems. In order to achieve a close structural similarity to supported technical catalysts, a metal may be deposited on the oxide either by physical vapor deposition [19, 22] or by the deposition of clusters, formed in the gas phase [23, 24].

The structural confinement of the active metal on the nanoscale introduces several additional features in comparison to extended single crystals. The various steps of a reaction may preferentially occur on different adsorption sites of the nanoparticles, which are linked to each other by adsorbate diffusion. Secondly, the electron density on these adsorption sites may differ from that on geometrically identical sites of extended crystals, due to the small size of the nanoparticles. The influence of the support includes the trapping and diffusion of adsorbates on oxides, which might lead to the transfer of adsorbates from the support to the active centers or vice versa [25–28]. Additionally, the geometric and electronic structure of the nanoparticles can be affected by their interaction with the support [20, 29, 30].

The size of nanoparticles may crucially affect their reactivity. The adsorption properties of adsorbates on Pd nanoparticles, which are larger than a few tens of a nm are usually considered to be very similar compared to single crystal facets. [20, 31–35]. With decreasing particle size, however, the chemical and structural/electronic properties often change [20, 31, 35, 36]. For nanoparticles which are smaller than a few nm, these properties become significantly different with respect to the bulk metal [33, 37–39]. As support effects might affect the properties of smaller nanoparticles more strongly, care has to be taken to separate support and particle size effects.

Although there is disagreement in the literature about the change in the reactivity of nanoparticles, which are a few nm in size, much is known about the changes in the particle properties in this size range. Mostly, a decreasing particle size results in a decrease in the lattice constant [40–42]. Furthermore, the apparent binding energy of the various metal bands shift to higher values with respect to the bulk metal [21, 43–45] and the vibrational features of CO change as well [31, 46]. However, it is not straightforward to associate changes in the lattice constant/electronic states of the nanoparticles and the vibrational features of adsorbates with changes in the catalytic activity, which is of central interest for practical applications.

In the present study, Pd nanoparticles of different sizes were prepared on a Fe_3O_4 oxide film, which has been grown on a Pt(111) substrate by physical vapor deposition. Due to previous characterization with STM and reactivity measurements, many structural features of these model systems are known, such as the abundance of different Pd facets, the particle shape, the orientation on Fe_3O_4 and the reactivity e.g. in the CO oxidation reaction [46–48].

The activity of a catalyst for a specific surface reaction is determined by the reaction rate, which is a convolution of the reaction constant and the adsorbate coverages of the various surface species. The adsorbate coverage is controlled by the bond strength of the surface species to the substrate, adsorbate-adsorbate interactions and entropical effects, thus the adsorption energy has a significant influence on this quantity. The activation energy of unimolecular surface reactions has often been successfully correlated to the binding strength of the corresponding reactant, which therefore strongly influences the reaction constant. Hence, the surface coverage of the reactants and the reaction constants, both of which control the surface reaction rate might be strongly affected by the binding energies of the reactants.

Despite of the importance of this parameter, often no consistent literature data on adsorbate binding energies on supported nanoparticles are available. For example, different authors have reported a higher [20, 49, 50], a lower [30, 34, 50, 51] or a similar [29, 31, 52, 53] CO binding energy on small Pd nanoparticles in comparison to Pd(111).

One reason for the lack in consistency can be attributed to disadvantages of the commonly used desorption based methods to probe binding energies [54–57]. These methods can only be used

to study fully reversible processes, but most chemically relevant processes are not reversible. For example, most hydrocarbons decompose on Pt(111) before desorption [58]. Secondly, to deduce the binding energy of a surface species with desorption based methods, kinetic models of the desorption process have to be applied, which often involve assumptions on the preexponential factor and the activation barrier for adsorption.
In addition to that, it is usually difficult to accurately control and determine the adsorbate coverage on a small scale with conventional experimental setups and find a correlation between the adsorbate coverage and the binding energy. Therefore, it is highly desirable to apply an experimental method that allows for a direct determination of the energetics of surface processes with good control over the coverage.
This can be achieved by single crystal adsorption calorimetry [59, 60]. This method relies on the detection of a temperature rise, that is caused by the adsorption of gas phase molecules on a surface. The energetics of the surface process can be directly probed with this method and no kinetic modeling of the desorption process is necessary. In addition to that, the combination with molecular beam methods allows for a better control of the adsorbate coverage, compared to desorption based methods. The combination of Single Crystal Adsorption Calorimetry (SCAC) with molecular beam methods was first established by King and coworkers [61]. A rise in the surface temperature, caused by a heat release during adsorption was detected by measuring an increase in the blackbody radiation. However, due to the strong decrease of blackbody radiation with decreasing temperature, this method cannot be applied at T<300 K. Campbell et al. further developed this approach and used a thin, pyroelectric foil to detect temperature changes caused by adsorption processes. With this setup, it was possible to detect adsorption energies at lower temperatures, additionally, a significant improvement in the sensitivity could be achieved [62].
A central part of this work concerns the investigation of the elementary adsorption and reaction steps, involved in the CO oxidation reaction on Pd(111) and supported Pd particles. The CO oxidation reaction is one of the best studied reactions in surface science [11, 63, 64, 64, 65, 65, 66, 66, 67, 67–70], which may be partially due to its relatively simple reaction mechanism and the high reaction probability but also due to its importance for its application in autocatalytic converters [71]. On Pd surfaces, the reaction proceeds with a Langmuir-Hinshelwood-(LH) mechanism, in which molecularly adsorbed CO reacts with dissociatively adsorbed oxygen. CO inhibits the dissociative adsorption of oxygen, which is why the reaction rate drops at high CO partial pressures, whereas adsorbed oxygen does not limit the adsorption of CO molecules. The groups of Matolin and Henry, among others, found, that the nature of the support and the particle size influence the reaction probability [20, 26, 27, 29, 30, 36, 50, 68, 72–77]. Libuda et al. investigated the steady state CO oxidation kinetics on Pd/Fe_3O_4 as a function of the CO partial pressure [78–81]. Furthermore, they studied communication effects and investigated, to what extent the formation of an oxide species affected the reactivity [46, 48, 82–87].
As the dissociative adsorption of oxygen is a crucial step of this reaction, comprehensive investigations have been performed on the formation and structure of the various adsorbate overlayers, formed by oxygen on Pd. Moreover, a lot of information on the desorption energetics is available from TPD studies on Pd(111) [88–92], Pd(100) [93–96] and on Pd(110) [97, 98]. A few experimental results on the desorption from supported Pd nanoparticles have been published [45, 99, 100], but due to the experimental limitations of desorption based techniques, the accuracy of the corresponding results might be limited. During annealing of the Pd catalysts to

the oxygen desorption temperature (800 K - 900 K), subsurface O diffusion [88, 101, 102], surface oxide formation and for the case of desorption from nanoparticles, particle restructuring [45, 103–105] may take place. The desorption energy equals the oxygen binding energy plus the activation energy for desorption. To deduce the oxygen binding energy from desorption based studies, the latter quantity has to be neglected which might add additional inaccuracies.
For these reasons, the influence of the particle size dependence on the oxygen adsorption energy is still unclear and no clear information on how particle size effects are influenced by the adsorbate coverage, currently exist.
To study the energetics of the CO oxidation reaction, CO and oxygen have to be adsorbed simultaneously on the surface. By this means, the CO-O interaction can be investigated. Early investigations of the CO-O interaction on Pd have focused on the structural changes that occur during CO adsorption on oxygen covered Pd(111) [14, 69, 70, 106–109] and Pd(100) [94]. However, structural studies on mixed CO-O adsorbate overlayers on Pd nanoparticles have not been reported. Furthermore, as desorption based methods cannot be used to study the desorption energetics of CO in the presence of oxygen, no information on the CO-O interaction on Pd has been obtained in experimental studies so far.
Asymmetric heterogeneous synthesis is an important topic due to its numerous advantages in an industrial application [110, 111]. As low miller index surfaces are achiral, one method to impose chirality on such surfaces is by the adsorption of chiral molecules, so called chiral modifiers. This strategy has been found to be successful e.g. in the hydrogenation of β-ketoesters with tartaric acid modified nickel catalysts [112, 113] and the hydrogenation of α-ketoesters using platinum catalysts, modified by cinchona alkaloids [114–121]. The mechanism for chiral promotion is still under debate and the subject of numerous investigations. One reason for the lack of understanding in the reaction mechanism is the difficulty of probing surface interactions between reagents and chiral modifiers [122].
A central aspect of this work is the accurate measurements of adsorption/reaction energies on complex, nanostructured surfaces. This is achieved by combining the SCAC setup, developed by Campbell et al. [62] with the preparation/characterization of model systems [123]. Additionally, insights on the dynamics and kinetics of surface processes are gained from sticking/reactivity measurements.
This thesis is structured in the following way. In the second chapter, an introduction of the basic concepts that are relevant for understanding the thermodynamics and kinetics of fundamental surface processes will be given. In chapter 3 and 4, the surface science tools, which are used in this work are introduced and their implementation in the current setup is described. The procedure for filtering and analyzing of the experimental data, the development of which has been an important part of the present work, is explained in Chapter 5. Details on the preparation and the structure of the model catalysts are given in chapter 6. This chapter also comprises the structural data of the model catalysts, that were determined in previous studies [46–48].
The information on CO and oxygen interaction with the Fe_3O_4 support, which has been collected in this work, is provided in chapter 7. This chapter includes quantitative information on the capture zone effect for CO and O_2, which has been obtained by modeling the initial sticking coefficient of CO and O_2. The SCAC results for oxygen adsorption on Pd(111) and on Fe_3O_4 supported Pd nanoparticles of four different sizes are described in chapter 8. The influence of the coverage and particle size effects on the adsorption energy and the sticking probability will

be discussed. The oxygen uptake on Pd/Fe_3O_4 directly after preparation and after O_2 exposure, CO exposure at elevated temperatures and annealing are compared in chapter 9. Complementary measurements of the CO sticking probabilities on oxygen covered Pd/Fe_3O_4 and CO_2-evolution upon CO exposure of these systems will be discussed. Evidence on the formation of a subsurface oxygen species after oxygen exposure of the freshly prepared Pd/Fe_3O_4 systems at 300 K will be given, the oxygen content in the nanoparticles and the formation energy of this species are shown.
To obtain coverage dependent information on the CO-O interaction on Pd(111) and Pd nanoparticles, the SCAC results during CO adsorption on bare and on oxygen covered Pd at $\approx$ 110 K are compared and discussed in chapter 10. First, the sticking and SCAC data of CO adsorption are discussed and compared with the available literature data. With this information, the CO-O adsorbate interaction as a function of the coverage are discussed.
Chapter 11 contains the SCAC data on the CO_2 evolution reaction on Pd(111) and on Pd nanoparticles of two different sizes. The differences in the initial CO_2 evolution on oxygen covered Pd for these three systems is compared with the thermodynamic data on the CO_2 oxidation reaction, obtained from the SCAC results which are discussed in previous chapters.
In chapter 12, the SCAC results on the adsorption of Propylene oxide (PropO) on 1-(1-naphthyl)ethylamine (NEA) chirally modified Pt(111) surfaces are shown. The surface chirality was imposed by adsorption of the enantiopure NEA compound. To calibrate the NEA coverage as a function of the exposure, CO titration experiments have been carried out, which are subject of the first section of this chapter. The comparison of the coverage dependence of the adsorption energy for the two PropO enantiomers on S-NEA modified Pt(111) will be the subject of the second section of this chapter. In the final chapter, a summary of the obtained results and insights are given.

2 Theoretical background

The fate of molecules impinging on a surface may be of several kind: they may elastically or inelastically scatter from the surface or physisorb/chemisorb on the surface. Adsorbed species often lead to reconstructions of surfaces and small reactive atoms such as H, C, N and O can penetrate the surface and form subsurface and bulk species, depending on pressure and temperature. At the highest chemical potentials of the gas phase species, stoichiometric compositions between adsorbates and solids are often formed.
These phenomena can be treated macroscopically with chemical thermodynamics or microscopically by considering the fundamental interactions between solids and molecules. After a short thermodynamic description of gas-surface interactions, physisorption, chemisorption adsorbate-adsorbate interactions will be considered. Subsequently, an overview of the dynamical processes on surfaces is given before surface reactivity in general and more specifically the case of CO oxidation on Pd will be discussed.

2.1 Thermodynamics on surfaces

In early surface science studies, relationships between important thermodynamic quantities and macroscopic observables such as pressure, temperature and volume, which are straightforward to measure, have been established. Accordingly, these quantities can be obtained with relatively basic experimental equipment. In the following, it will be introduced how these macroscopic observables are related to quantities as the adsorption energy and the isosteric heat of adsorption.
A nonvolatile species (adsorbent) is considered to be in equilibrium with a volatile species (adsorbate), which is in equilibrium with the gas phase [124]. The Gibbs free energy for this system can be written as follows:

$$dG = -SdT + VdP + \mu_S dn_S + \mu_A dn_A \tag{2.1}$$

Here dG is the change in the free energy of the condensed phase, S and T are the entropy and the temperature and dT and dP infinitesimal changes in the temperature and pressure. μ_S and dn_S are the chemical potential and the infinitesimal changes in the amount of the nonvolatile species and μ_A and dn_A the chemical potential and the infinitesimal changes in the amount of the volatile species.
A change in the free energy of the condensed phase can be caused either by changes in the temperature/pressure or by the number of moles of the nonvolatile and the volatile component.
For an inert adsorbent, the thermodynamic properties of the solid and the adsorbate can be separated. The Clausius-Clapeyron equation for a gas phase species (subscript g) in equilibrium

with the adsorbate species at constant coverage (Θ) can be written as follows:

$$\left(\frac{\partial ln(P)}{\partial T}\right)_{\Theta} = \frac{H_g - H_A}{RT^2} = \frac{-\Delta H_{ads}}{RT^2} \tag{2.2}$$

, where H_g and H_A are the molar enthalpy of the gas phase and the adsorbed species and ΔH_{ads} is the isosteric enthalpy of adsorption, R is the ideal gas constant. The term isosteric refers to the constant coverage condition. According to Equ. 2.2, the isosteric adsorption heat can be calculated after detecting two pressure/temperature pairs that produce the same coverage [12, 125]. Note, that this equation can only be applied for reversible processes and in the limiting case of adsorption on an inert substrate.
The relation between the isosteric adsorption energy and the energy of adsorption is given by the following equation:

$$\Delta E_{ads} = \Delta H_{ads} - \Delta(pV) \tag{2.3}$$

where ΔE_{ads} is the energy of adsorption. The term $-\Delta(pV)$ arises due to the change in the gas volume above the surface during adsorption. For an ideal gas which adsorbs on a surface, $\Delta(pV)$=-RT if the quantities are normalized to 1 mole. The energy of adsorption, E_{ads} can be directly obtained from calorimetric measurements, more common however is the determination of the desorption energy with desorption based methods, which differs however from the adsorption energy by the activation energy of adsorption.

$$E_{des} = E_{ads} + E_{act} \tag{2.4}$$

, E_{des} is the activation energy for desorption and E_{act} is the activation barrier for adsorption. The thermodynamic driving force for the adsorption of a gas phase on a surface is the change in the free energy, which, besides from the adsorption enthalpy also depends on the adsorption entropy. The adsorption entropy can be deduced from the Clausius-Clapeyron equation if the surface coverage is known and the thermodynamic properties of adsorbate and substrate can be treated separately.

2.2 Gas-surface interactions

The magnitude of the adsorption energy/adsorption enthalpy, which is of central importance in the present work, can be understood on a microscopic level by considering the interactions between substrate and adsorbate. These lead to the differentiation between physisorption and chemisorption.
In the case of physisorption, the overlap between the adsorbate and the surface orbitals are generally weak. Chemisorption interactions on the other hand are associated with a strong overlap between adsorbate and surface orbitals.

2.2.1 Dispersion forces and Physisorption

The weakest forces between molecules and surfaces are the London forces, also called Van-der-Waals forces. The origin of these forces are charge fluctuations in the electron density of one species by which the other species forms an induced dipole.
The interaction between induced dipoles can often be described well by a Lennard-Jones 6-12 potential,

$$E_{VdW} = C_{Lond} \cdot \frac{0.5 \cdot (r_e)^6}{R_{A-B}^{12}} - \frac{1}{R_{A-B}^{6}} \tag{2.5}$$

where E_{VdW} is the VdW-interaction, r_e is the equilibrium distance between the atoms A and B with the distance R_{A-B} and C_{Lond} is a constant, which depends on the ionization potentials and the polarizabilities of A and B.
To estimate the potential for the interaction of an adsorbent with an extended solid $E_{VdW-solid}$, one has to sum E_{VdW} over all the atoms in the solid.

$$E_{VdW-solid} = \rho_S \pi C_{Lond} \left(\frac{0.2(r_e)^6}{z_{A-S}^9} - \frac{1}{z_{A-S}^3} \right) \tag{2.6}$$

z_{A-S} is the distance between the atomic species and the surface and ρ_S is the atom density of the surface. Comparing equations 2.5 and 2.6, it becomes evident, that the potential for the VdW interaction for a physisorbed species significantly differs from that between two single atoms. Additional contributions have to be taken into account when considering the interaction with a polar substrate [126].
On metals, where the conducting electrons are delocalized, the assumption of a pairwise interaction is not applicable. In case of a completely conducting metal, there cannot be any electric field parallel to the metal surface, as the induced charge of a dipole is compensated by the charge density of the metal. This situation is equivalent to assuming an image charge in the metal as schematically illustrated in Figure 2.1. By calculating the interaction between an electron state with its image charge with a repulsive force analogue to above, Lennard-Jones obtained an expression for the VdW interaction between a physisorbed species and a metal,

$$E_{VdW-metal} = \frac{C_{LJ}^{rep}}{z_{A-S}^9} - \frac{C_{LJ}^{attr}}{z_{A-S}^3} \tag{2.7}$$

where $E_{VdW\text{-}metal}$ is the VdW-interaction between a physisorbed species on a metal and C_{LJ}^{rep} are constants. Note the same form of Equ. 2.7 and Equ. 2.6.
Today, quantum chemical calculations are increasingly used to understand chemical problems. For an introduction to the methods, used for such calculations, I refer to the references [127, 128]. Within these calculations, empirical or semiempirical estimations of the VdW-interaction are necessary for the case that DFT calculations are performed when using common functionals. Examples for such corrections are the Grimme approach [129, 130] and the Tkatchenko-Scheffler approach [131].

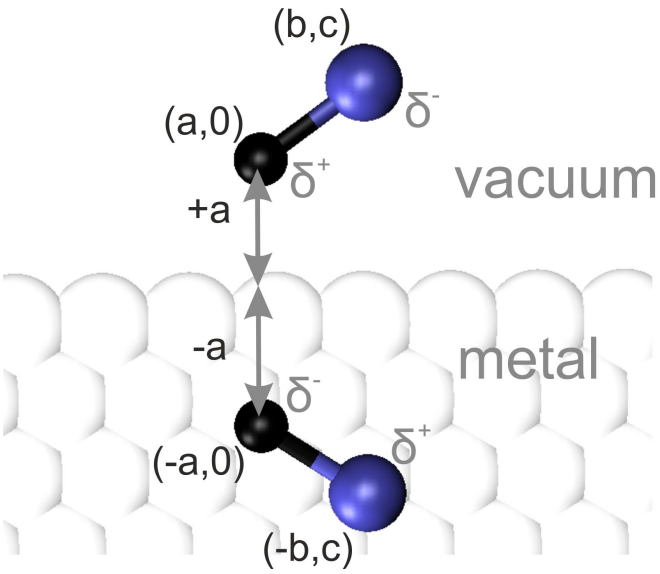

Abbildung 2.1: Schematic drawing of a dipolar particle with the corresponding image charge in a polarizable medium

2.2.2 Chemical bonding

In contrast to the interaction between non overlapping orbitals between surface and adsorbate, which give rise to the dispersion forces, chemical bonds may be formed by overlapping orbitals. For small molecules, the bond energy between dispersively bound species is often more than 10 times lower in magnitude as that of chemically bound species. In addition to that, the equilibrium distance is often larger for dispersively bound molecules. This is shown in Fig. 2.2, where the potential energy is shown qualitatively as a function of the bond distance for the case of chemical (Lennard-Jones potential) and dispersively bound species. The latter can be described by a Morse potential:

$$E_{chem} = -D_E \left(2e^{(-(r-r_0)/a)} - e^{(-2(r-r_0)/a)} \right) \tag{2.8}$$

E_{chem} is the potential energy, D_E is the equilibrium bond energy, r_0 the equilibrium distance and a is an adjustable parameter. Empirical potentials like the Morse potential can be used to simulate the time evolution of large systems, D_E, r_0 and a are obtained from experimental results or theoretical calculations.

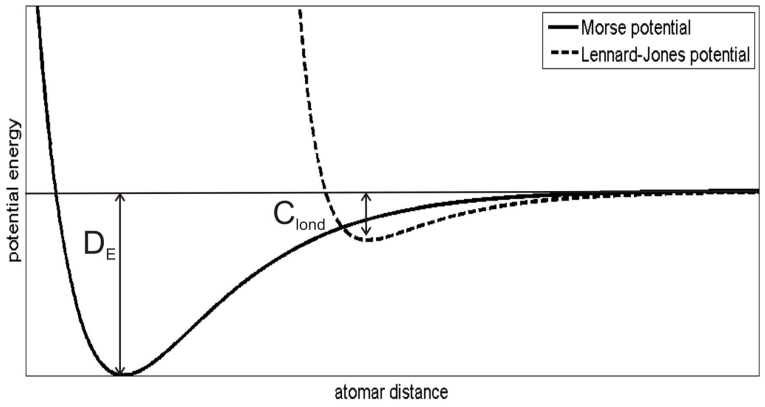

Abbildung 2.2: Comparison of the dependence of the bond energy on the interatomic distances between two atoms for a Lennard-Jones and a Morse potential

2.2.3 Chemisorption on surfaces

As the focus of the present work is to a large extend the binding strength of gas phase molecules on surfaces of different structures, chemisorption in general and the adsorbate bond energy are discussed in the following.
It has been observed experimentally, that the binding energy of adsorbates strongly varies with the chemical nature of the adsorbate and the support [132, 133]. Different approximations to describe the interaction between the surface and adsorbate electronic states exist. The most simple ones consider the energy and symmetry of the highest occupied and lowest unoccupied electronic levels of the adsorbate and the valence band of the substrate.
The substrate electron bands are schematically represented together with the electronic levels in Figure 2.3. E_F is the fermi energy of the substrate, ε_A is the highest occupied orbital of the substrate and ε_A^* the energy of the lowest unoccupied orbital. Perturbation-theory modeling has

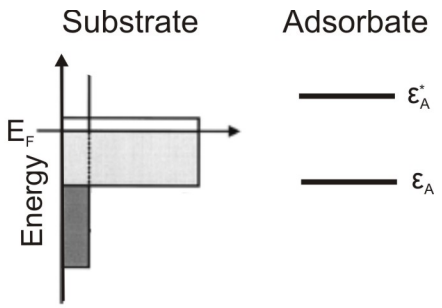

Abbildung 2.3: Schematic representation of a rather delocalized (s-, sp- band) and a rather localized band (d-band) in a solid and a bonding and antibonding electronic level in a molecule.

been used to estimate the interaction between an adsorbate and an electron band: according to this model, E_{ads} is inversely proportional to $E_F - \varepsilon_A$ and the number of holes in the valence band. For an electron acceptor, $E_{ads} \propto (\varepsilon_A^* - E_F)^{-1}$ [134, 135]. In spite of the simplicity of this model, the experimentally observed trend that E_{ads} of atomic radicals such as H, O and N typically decrease from left to right along a series of the periodic table and down a column [136] can be qualitatively understood by this model.
Similar models have been developed on the basis of the Tight-binding approach in which also the interaction of a single adsorbate orbital with a band of metal orbitals was considered [137–140]. Such models have been very useful to qualitatively understand metal-adsorbate interactions and to interpret Photoelectron spectra. To explain coverage effects and changes of the binding energy on different adsorption sites, observed in experimental studies, different models have been developed. Shustorovich adapted the BOC model to treat chemisorption on different adsorption sites and adsorbate-adsorbate interactions [136]. Within this model, just next nearest neighbor interactions are taken into account. The bond order x is defined to be $x = e^{-(r-r_0)/a}$ and the bond energy is calculated according to Equ. 2.8:

$$E_{chem} = -D_E \left(2x - x^2\right) \tag{2.9}$$

For a single atom adsorbing on a multifold adsorption site, the sum of the bond orders between the adsorbate atoms and the next nearest metal atoms is assumed to be 1 for all configurations. By Comparing E_{chem} for adsorption on several adsorption sites, one obtains within the assumptions of this model, that the E_{chem} for an atom is lowest on the most highly coordinated site, whereas for diatomic molecules E_{chem} it is often lowest on lower coordinated sites. This rule of thumb is often fulfilled for adsorption on transition metal surfaces [136].

2.2.4 Adsorbate-adsorbate interactions

The adsorption energy is generally coverage dependent due to adsorbate-adsorbate interactions. These are firstly direct interactions, which would be also present without the substrate and secondly indirect interactions, which mostly occur through coupling of the electronic states between adsorbate and the substrate [141–145].
Figure 2.4 shows the differential heat of adsorption of CO, which is approximately equal to the binding energy as a function of the CO coverage. This data has been measured by King et al. at 300 K. As can be seen in Fig. 2.4, the CO binding energy only decays very gradually at low coverages and decreases prominently at high coverages.
This decrease in the CO binding energy at high coverages is caused by CO-CO interactions.
Shustorovich used the BOC-model to explain the reduction of the adsorbate binding energy due to adsorbate-adsorbate interactions [136]. The coordination number m of an adsorbate is the number of surface atoms to which it is bound to. According to the BOC-model, the binding energy should be constant until a coverage of 1/m as there are enough surface atoms to which each adsorbate can bind separately at Θ<1/m. At higher coverages, surface atoms are bound to more than one adsorbate, which lowers the bond order of the adsorbate-surface bond and in turn the adsorption energy. Shustorovich used these considerations to approximate the coverage dependence of the adsorption heat, which is shown in Fig. 2.5 for adsorption on a hcp(001) and a

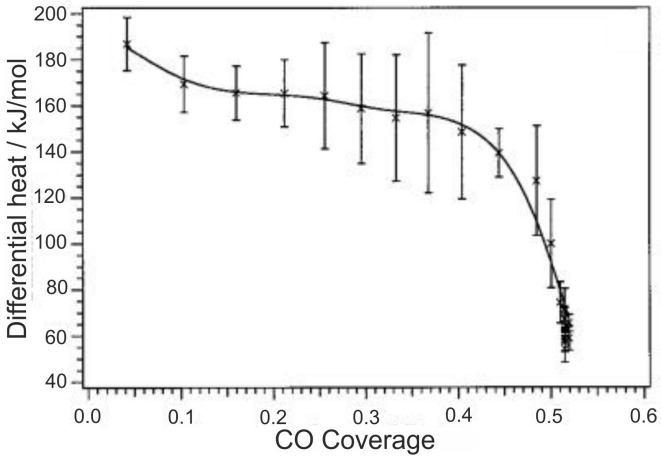

Abbildung 2.4: Heat of adsorption for CO on Pt(111) as a function of the coverage, measured at 300 K with SCAC [132].

fcc(111) surface. The adsorption heat in Fig. 2.5 is normalized to the adsorption heat in the zero coverage limit.
The continuous line and the two dashed lines show the relative adsorption heats for the adsorption on hollow, bridge and on top site. The coverage dependence of the adsorption energy qualitatively agrees with the trend, observed in Fig. 2.4. It can be seen in Fig. 2.5 that according to the BOC model, the decoration of the bridge or on top site is energetically more favorable at higher coverages. This agrees with experimental findings, in which phase transformations, connected with a change of the adsorption site are observed at high adsorbate coverages [146].
In addition to indirect adsorbate-adsorbate interactions, direct interactions (Dipole-Dipole interaction, VdW interaction, hydrogen bonding...) are present, which may either increase or decrease the adsorbate binding energy.

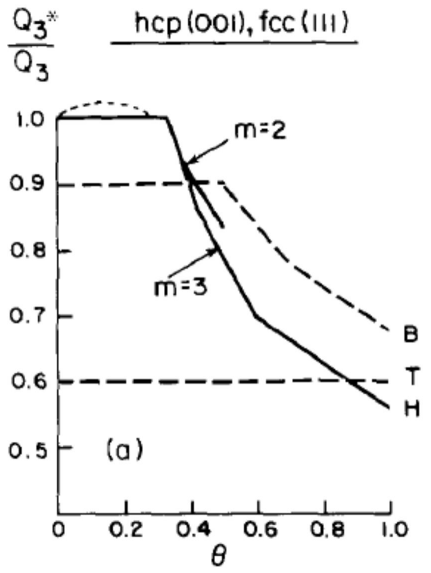

Abbildung 2.5: Coverage dependence of the adsorption energy relative to the initial adsorption energy according to the BOC model from [136]. The solid line shows the dependence of the adsorption heat on the hollow site and the two dashed lines show the relative dependence of the adsorption heat on bridge and on top position.

2.3 Dynamics on surfaces

The reactivity of gas phase molecules with surfaces is influenced by the thermodynamics of the various elementary reaction steps, but also to a large extent by the dynamical processes on surfaces. Experimental results on the coverage dependent sticking coefficient, which can be obtained with the current setup, can give valuable information on surface dynamical processes.
Molecules, which impinge on a surface may scatter elastically or inelastically from the surface or being trapped into a physisorbed or chemisorbed state. Molecules, which are trapped in a physisorbed state may either desorb after a residence time of typically a few milliseconds [147, 148] or may chemisorb but chemisorption may also occur directly without trapping into a physisorbed state. Exact quantum-mechanical formulae for these processes are available but an accurate treatment of this problem is very demanding. For a detailed description of methods to treat this problem, I refer to [149]. In this section, just a short introduction on the dynamical processes on surfaces will be given.

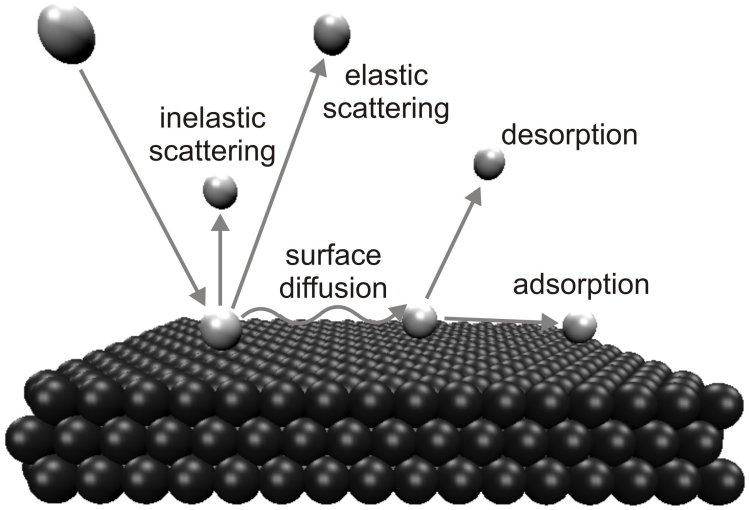

Abbildung 2.6: Schematical representation of the dynamical processes prior to adsorption

2.3.1 Trapping

If a molecule impinges on a surface, several initial processes are possible which are schematically shown in Fig. 2.6. In close proximity to the surface, the molecule experiences the VdW potential, which has been discussed in section 2.2.1. A molecule will be physisorbed, if it loses sufficient energy due to an inelastic collision with the surface so that it does not have enough energy to escape the energy well, otherwise it is inelastically scattered. Weinberg and Merril used Baule's hard sphere model to to determine the fraction of energy that will be transferred to the surface during a collision. According to this model, the molecule is trapped if it has a kinetic energy which is lower than a critical energy E_{crit}. For the case that the molecular energy is higher than E_{krit}, it is not trapped [150]:

$$E_{crit} = \frac{4m_g/m_s}{(1-m_g/m_s)^2}(w - E_s) \tag{2.10}$$

In Equ. 2.10, m_g and m_s are the masses of the molecule and surface atoms, w the depth of the VdW potential and E_S the energy of the surface atom. Integrating the Maxwell-Boltzmann distribution from $E = 0$ to $E = E_{crit}$, the trapping probability can be calculated. Equation 2.10 shows that more energy is transferred to the surface during the collision if the metal atoms and the molecule have similar masses. The impinging molecule cannot be physisorbed on the surface, if the energy of the surface atoms is equal or larger than the depth of the potential well. Energy dissipation of the excess energy may occur through phonon excitation and electron-hole pairing [151, 152].

2.3.2 Diffusion

The mobility of a surface species is related to the adsorbate binding strength and may additionally influence its reactivity. Species that are physisorbed or chemisorbed on the surface may diffuse along the two dimensions of the surface.
One can treat diffusion as the repeated crossing of the activation barrier between the lowest energy sites. Starting from Ficks law [153], which relates the diffusion flux of a one dimensional lattice gas to the concentration gradient, one can obtain the diffusion coefficient:

$$D = \nu_{diff} a^2 e^{-E_{diff}/kT} \tag{2.11}$$

D is the diffucion coefficient, ν_{diff} is the diffusion prefactor, E_{diff} is the activation barrier for diffusion and a the jump distance between the lowest energy sites. The mean square displacement $<r^2>$ during the time t is connected to the diffusion constant by:

$$Dt = < r^2 > \tag{2.12}$$

But trapped molecules do not diffuse an infinite time on a surface in this state, they either desorb or chemisorb on the surface. It is interesting to consider the mean square displacement for a molecule before desorption from the surface. This quantity can be determined by inserting the expression for the mean lifetime before desorption into Equ. 2.12.

$$\sqrt{< r^2 >} = \left(\frac{\nu_{diff}}{\nu_{des}} \right)^{1/2} a e^{\left(E_{des} - E_{diff}/2k_bT\right)} \tag{2.13}$$

ν_{des} is the exponential prefactor for desorption. The assumption that $E_{diff} \approx 0.12 - 0.33 \cdot E_{des}$ [154, 155] has been found to agree with many experimental results. According to Equ. 2.13, the mean square displacement strongly decreases with increasing temperature and increases approximately exponentially with the desorption energy.

2.3.3 Sticking

Molecules, which stick on a surface are permanently adsorbed either in a physisorbed or a chemisorbed state. The fraction of the impinging gas phase molecules, which stick on a surface is the sticking coefficient S, which is in general a function of the coverage Θ. The measurement of the sticking coefficient can be used to determine the adsorbate coverage and give information of the dynamics of the adsorption process.
Langmuir modeled the variation of the sticking probability with the adsorbate coverage by assuming that molecules, which impinge on an occupied adsorption site will scatter, whereas molecules, which impinge on an empty site will adsorb with the probability S(0).

$$S(\Theta) = S(0) \left(1 - \frac{\Theta}{\Theta_{sat}} \right)^n \tag{2.14}$$

Θ_{sat} is the saturation coverage and n is the order of the adsorption process.
Experimental data only rarely show a Langmuir-type adsorption behavior over the complete

coverage range. One reason for this finding is, that often molecules, which impinge on occupied adsorption sites are trapped into a precursor state and diffuse to unoccupied site, where they may adsorb [156]. This process is termed precursor mediated sticking. One of the models, which include precursor mediated sticking has been proposed by Kisliuk, who considered trapping onto an occupied and onto an empty surface site prior to adsorption.

$$S(\Theta) = S(0)\left(1 + \frac{K}{1-\Theta}\right)^{-1} \tag{2.15}$$

K, which can have values between 0 and ∞, is a measure for the mobility of the precursor. K is low for mobile precursors, immobile precursors have high K values. The influence of K on the sticking probability is shown in Figure 2.7 where $S(\Theta)$ is plotted for different values of K. $S(\Theta)$ is high until intermediate coverages, if the precursor is mobile whereas for an immobile precursor, the sticking probability decreases linearly with the coverage.

This model neglects firstly influences of adsorbate-adsorbate interactions on the sticking coef-

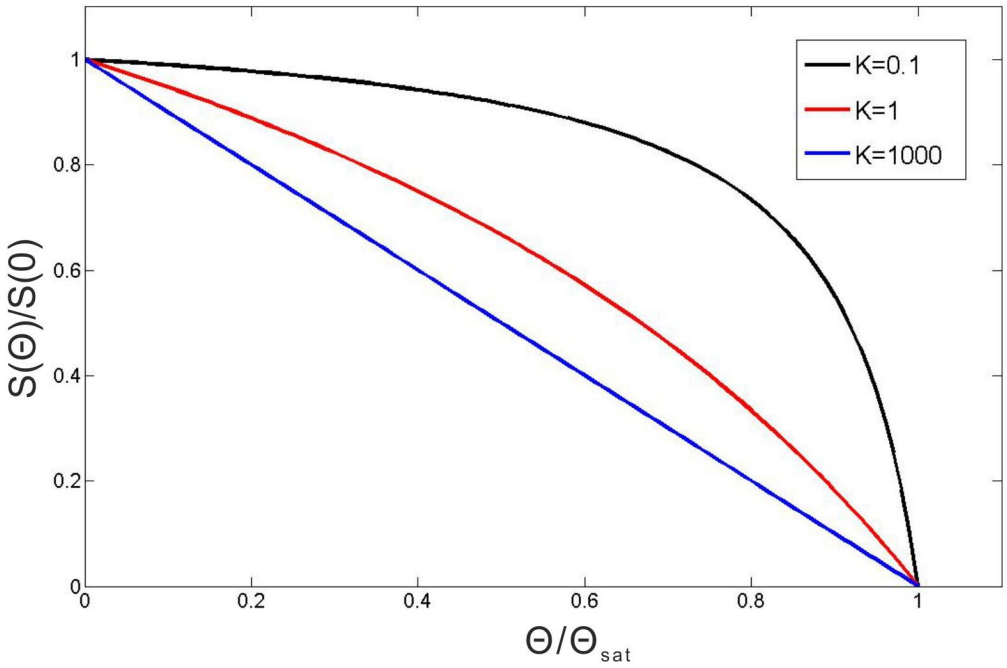

Abbildung 2.7: Influence of K in the Kisliuk expression on the coverage dependent sticking probability. Thehe coverage dependent sticking probability for a second order process in case of an immobile precursor is shown in blue

ficient. Secondly, changes in the electronic structure of the substrate with increasing adsorbate coverage may influence the sticking coefficient, which is not considered in this model either. As adsorbates often form different phases with different trapping and sticking probabilities in different coverage ranges, experimental plots of $S(\Theta)$ are often quite different from the ones, which are shown in Figure 2.7.

2.4 Heterogenous surface reactions

The study of surface reactions is a major area of heterogeneous catalysis research and also this work is aimed to contribute to the understanding of certain aspects of a surface reaction (the CO oxidation reaction). In the following section, I will introduce general aspects of bimolecular surface reactions and discuss CO oxidation on Pd in particular, as this reaction has been studied in the present work.

2.4.1 Reaction mechanisms

For a bimolecular reaction, the most important reaction mechanisms are the Langmuir-Hinshelwood (LH) and the Eley-Rideal (ER) mechanism, both are schematically shown in Figure 2.8 in a three step representation. In the Langmuir-Hinshelwood mechanism, both molecules adsorb on the surface, the two surface species react and the product desorbs from the surface. In an Eley-Rideal mechanism, only one species adsorbs on the surface and the other one reacts with it from the gas phase before the product desorbs.

In the following, I consider the surface reaction for the two species A and B: The surface

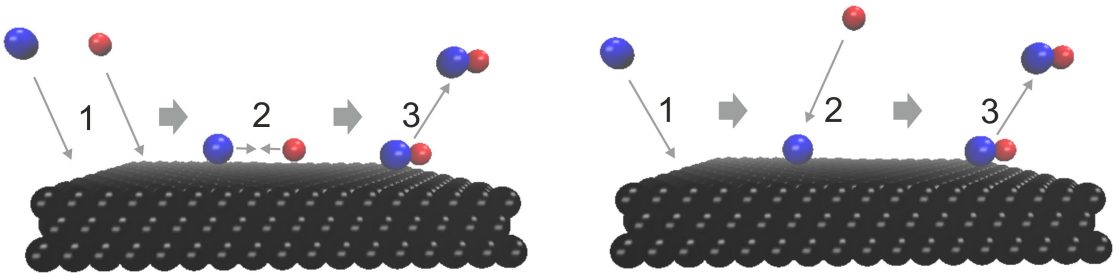

Abbildung 2.8: Reaction steps in a Langmuir-Hinshelwood (left) and an Eley-Rideal (right) mechanism

concentrations are denoted $[A]_{ads}$ and $[B]_{ads}$ and the pressures P_A and P_B. For an Eley-Rideal mechanism, the steady state reaction rate for non interacting molecules A and B on the surface is as follows:

$$R_{AB} = k_{AB}[A]_{ads}P_B \tag{2.16}$$

R_{AB} is the reaction rate, $[A]_{ads}$ is the surface concentration of the species A, P_B is the pressure of the species B and k_{AB} is the reaction constant. The backward reaction is neglected in this case and it is assumed that the product desorbs fast.

Generally, A and B are able to adsorb on the surface and the two species compete for free surface sites. Accordingly, the surface concentration $[A]_{ads}$ is influenced by P_A and P_B and the reaction rate sensitively depends on the pressures of both reactants. For the case, that $[A]_{ads} \gg [B]_{ads}$, $R_{AB} \propto P_B$. If, on the other hand, $[B]_{ads} \gg [A]_{ads}$, $R_{AB} \propto P_A$.

In a Langmuir-Hinshelwood mechanism, where both species are adsorbed on the surface, the steady state rate is given as follows:

$$R_{AB} = k_{AB}A_{ads}B_{ads} \tag{2.17}$$

The rate has a maximum, if the surface concentration of the two species is equal (assumed that A and B occupy the same number of sites on the surface). If A is the dominant species on the surface, the coverage of A is ≈ 1 and R_{AB} is proportional to $P_B \cdot P_A$. In this particular case, the reaction rate approximately depends on the relative pressures of the two species, not on the total pressure.

2.4.2 CO oxidation on Pd

As the CO oxidation reaction is one of the most widely studied reactions and of a major importance for many applications, (see for example [157] and references therein) some aspects of this reactions mainly on Pd will be discussed here in detail.
The mechanism of this reaction on transition metal surfaces was under debate for a long time. Early measurements on Pt wires showed, that $R_{CO2} \propto P_{O2}/P_{CO}$ under certain conditions, which was ascribed to the inhibition of oxygen adsorption by CO. As there was none such inhibition effect for CO adsorption, it was suggested that the reaction rate proceeded through an Eley-Rideal mechanism. Subsequent coadsorption experiments showed, that the situation is more complex because CO tends to form densely packed adlayers which inhibit dissociative oxygen adsorption. Oxygen on the other hand forms open structures, which do not noticeably affect the uptake of CO [158]. Thus time resolved measurements were needed to identify the reaction mechanism: O covered Pt(111) [159] and Pd(111) [66] surfaces were subject to modulated molecular beam measurements. An average surface lifetime for CO of 0.5 ms on Pt(111) definitely ruled out an ER-type mechanism (the residence time increases to >3 ms for high CO coverages since CO molecules diffusing on the surface need longer to find adsorbed oxygen molecules).
The activation energy of the CO oxidation reaction on Pd(111) sensitively depends on the coverage of oxygen and CO: it was reported to be around 105 kJ/mol for small CO and oxygen coverages [65, 66], $\sim$67 kJ/mol for $\Theta_{CO} < 0.25$ on an oxygen covered surface [65, 66, 68] and 41 kJ/mol at higher CO coverages [70].
As distinct adsorbate structures may generally exhibit different adsorbate binding energies and activation energies for reaction, it is instructive, to consider changes in the adsorbate overlayer with increasing adsorbate coverage. (In fact, not only the coverage but often the history of the system influences the adsorbate structure [96, 160])
On bare Pd(111), CO forms a p$(\sqrt{3}x\sqrt{3})R30^\circ$ structure with a coverage of 1/3 [146, 161, 162]. Upon further CO exposure, a c(2x4) overlayer is formed with a saturation coverage of 0.5 [163–165]. Oxygen, on the other hand dissociatively adsorbs on Pd(111) and eventually forms a p(2x2) structure, corresponding to the saturation coverage of 0.25 [89, 90, 166]. Upon CO adsorption on the p(2x2)O structure, oxygen forms a $p(\sqrt{3}x\sqrt{3})O$ phase [14, 69, 106, 107]. Further CO adsorption at 200 K>T>130 K [69, 70] causes a transformation of the $p(\sqrt{3}x\sqrt{3})O$ structure into a $(2x1)$ phase, which contains a mixture of alternating CO and O rows. [14, 69, 106–108].
The activation energy for CO_2 evolution is highest in the low coverage regime of both adsorbates, where they do not form ordered structures. In this case, $R_{CO2} = 0$ at 300 K. CO_2 is evolved upon completion of the $p(\sqrt{3}x\sqrt{3})O$-phase. Below 200 K, however, no reaction can be observed in this phase. The mixed (2x1) adsorbate structure was found to react at temperatures as low as 136 K [69, 70, 108]. Thus the activation energy for CO_2 evolution decreases for the more dense adsorbate structures.

On supported Pd nanoparticles, new features due to support effects, particle size effects and communication effects arise. Figure 2.9 shows the dependence of the CO oxidation rate on the CO flux fraction (x_{CO}). The CO flux fraction is the partial CO flux, divided by the total flux of molecules. The reaction rate was measured on a Pd/Al_2O_3 model catalyst with a particle size of $\sim$6 nm [82]. The reaction rate at a constant temperature was found to depend approximately linearly on the partial flux of CO for the lowest x_{CO}. This behavior is expected from a Langmuir-Hinshelwood kinetics. Combining these measurements with IRAS, it was shown that the CO coverage is low in this region and CO adsorbs on the 3-fold hollow sites [78, 79]. The increase in the CO coverage was found highest in proximity to the maximum in the CO_2 production rate. According to the assignment of the IRAS features, made by the authors, the decrease in CO_2 evolution for the highest CO coverages coincides with the occupation of additional adsorption sites. The high CO coverage regime is often termed the CO poisoning regime, because adsorbed CO prevents oxygen molecules to dissociatively adsorb, which in turn yields to the reduction in the CO_2 production rate in Fig. 2.9. The maximum in the reaction rate shifts to larger CO partial fluxes at higher temperature as CO desorption, which is the rate determining step in the CO poisoning regime, is faster at higher temperatures. It can be also observed that the CO_2 production rate is generally higher at higher temperatures which is caused by an increase in the rate constant. In an atomistic picture, more adsorbate molecules can overcome the activation barrier for reaction at higher temperatures, which leads to the increase in the reaction rate.

Analogue experiments have been performed on Pd single crystal facets, where a a similar trend

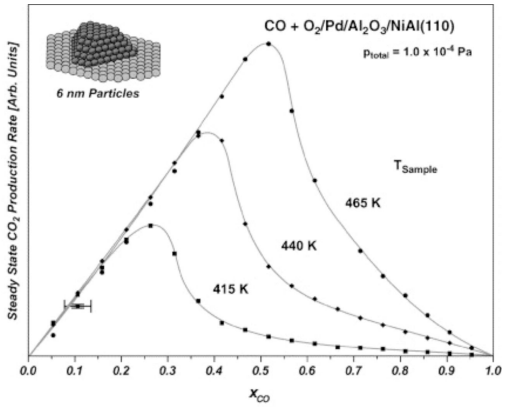

Abbildung 2.9: The steady state CO_2 evolution kinetics on a Pd/Al_2O_3 model catalyst as a function of the partial flux of CO [82], defined as the ratio of the CO flux and the total flux

was found [31, 67]. Qualitative differences between the steady state reaction rate on supported nanoparticles and single crystals were observed: for example, the kinetic transition between the increase of the reaction rate and the decrease with increasing CO flux fraction was found to be more gradual on supported nanoparticles.

The dependence of the CO_2 production rate on the temperature is shown in Figure 2.10, extracted from the work from Ertl. and Rau, measured on Pd(110) already in 1969 [12]. At the highest temperatures, no CO is present on the surface, the LEED results are equivalent to the ones on

pristine Pd(110). With decreasing temperature, CO increasingly decorates surface sites, which is accompanied by a rise in the CO_2 production rate. At the lowest temperatures, CO desorption limits the reaction rate (CO poisoning regime) and the LEED pattern is that of a fully CO covered surface.
It should be noted, that the CO_2 production rate is a product of the rate constant and the surface concentration of CO and oxygen. As the rate constant strongly depends on the temperature, changes in the CO_2 production rate with the temperature, shown in Fig. 2.10, do not only occur due to the changes in the surface concentrations of oxygen and CO. The temperature dependence of the CO_2 production rate is a convolution of the temperature dependent surface concentrations of oxygen and CO and the the dependence of the reaction rate constant on T.
At higher oxygen chemical potentials, the increasing formation of subsurface oxygen species

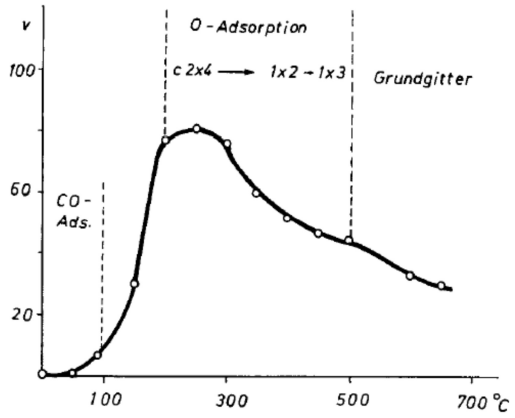

Abbildung 2.10: Temperature dependence of the CO_2 reaction rate on a Pd(110) surface from [12]

and oxides is taking place. It has been clearly shown on the single crystal surfaces Pd(110) and Pd(100) that the reactivity towards CO oxidation decreases with an increase in the oxygen concentration in the surface oxide phases at constant temperatures [93, 160].
Experiments in the steady state regime [167] and transient experiments on supported nanoparticles also showed a reduced reactivity of systems, which contain an oxide phase [48, 83, 84, 87]. The steady state reactivity in the CO oxidation reaction follows the order: chemisorbed oxygen > surface oxide > bulk oxide [50, 168–170]. It has been suggested, that the smaller reaction rate on systems where an oxide phase is present is caused by a drastically reduced sticking coefficient of CO. As the precursor mediated CO sticking probability increases with decreasing temperatures, transient experiments showed a more than three times higher CO oxidation rate of an oxide phase which was formed on Pd(110) at 357 K compared to 548 K [160].

3 Experimental techniques

In this chapter, a short background on the experimental methods which have been used in this work will be given. First, molecular beam methods, which form the basis of microcalorimetric measurements will be introduced. An overview on existing SCAC techniques will follow, before sticking coefficient measurements and the low-energy electron diffraction (LEED) technique are introduced.

3.1 Molecular Beams

A molecular beam is a volume of gas which is spacially well defined, directed, and where no collision occurs between the gas molecules [171, 172].
The application of molecular beams provides a unique way of performing quantitative experiments on the kinetics and dynamics of surface reactions. The well defined spatial distribution of molecular beams and the single collision condition open a variety of experimental possibilities. Due to the possibility to precisely measure the reactant flux, the measurement of absolute reaction probabilities as a function of the adsorbate coverage is possible. A fast modulation of the reactant flux allows to obtain unique information on the reaction system during the transient phase. As many reactant properties like the kinetic energy or occupation of rotational and vibrational states of the incident gas molecules can be controlled, reactivity studies with respect to changes in these parameters are possible. There are two types of molecular beams, effusive and suporsonic beams, which differ in the expansion conditions. This results in a different energy distributions of the gas phase molecules within these two types of molecular beams. As only effusive beams are used in the present study, supersonic sources are not considered in the following.
Figure 3.1 schematically shows the principle of a molecular beam for the study of surface processes. In stage 1, the pressure is comparably high, typically in the range 10^{-3} mbar - 1 mbar. From this stage, expansion occurs into the vacuum. In stage 2, a collinear beam is produced by selecting molecules with a certain direction while molecules with other directions are pumped away, which happens usually in several pumping stages. This is achieved by directing the beam through several apertures and a glass capillary array (GCA). The latter consists of multiple long channels with a small diameter. In addition to extracting molecules from only a small solid angle of the reactant flux, the GCA allows a collimation of the flux usually over several orders of magnitude. The molecules enter the UHV system with a very well defined spacial distribution. In order to minimize the divergence of the beam flux before impingement of the beam on the sample, the distance between sample and surface has to be sufficiently small. A variable temporal beam distribution can be achieved by shutters or choppers.

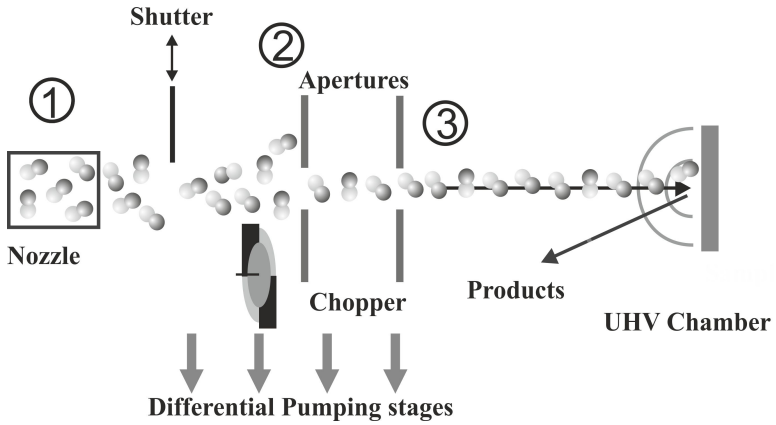

Abbildung 3.1: Schematic representation of a molecular beam experiment for the study of gas surface interactions, the setup is divided into three stages

The Knudsen number Kn

$$Kn = \frac{\lambda}{d} \tag{3.1}$$

is a measure of the dynamic properties of the molecular beam, where λ is the mean free path and d is the length of the opening through which the expansion takes place. The Knudsen number for effusive beams is much higher than one. Under these conditions, the reactant gas retains its equilibrium dynamic properties and thus it maintains a Maxwell-Boltzmann velocity distribution.

For thermodynamic studies, it has to be considered that a molecular flux through a surface per time interval has a different mean kinetic energy than a volume of gas. This has the effect, that the molecular flux impinging on the catalyst and the one being reflected also have a mean higher kinetic energy [173]:

$$< E >_{mean}^{flux} - < E >_{mean}^{volume} = \frac{1}{2} k_B T \tag{3.2}$$

$< E >_{mean}^{flux}$ is the mean kinetic energy of a flux of molecules and $< E >_{mean}^{volume}$ is the mean kinetic energy of a volume of molecules.

3.2 Single Crystal Adsorption Calorimetry

Calorimetric measurements were common in the early days of surface science, where a transient temperature change, caused by surface processes, was detected with resistance thermometers [174]. Alternatively, energetic changes on a sample, which is subject to a temperature ramp, could be measured by detecting the temperature difference between a sample and a reference [175]. Wedler adapted resistance calorimetry for the use in UHV to probe gas adsorption on polycrystalline transition metal films [176]. These methods could only be applied to polycrystalline films or powder catalysts, which are non uniform in structure. On such systems, it is therefore only possible to obtain vague information on the adsorption processes at the nanoscale and no

structural dependence of the adsorption energies could be investigated. These disadvantages can be circumvented by working with well defined single crystals, where the energetics of surface processes were often studied with temperature programmed desorption methods or alternatively by a Clausius-Clapeyron analysis of adsorption isotherms [177]. Such measurements can only provide the desorption energy of molecules which can be fully reversibly desorbed.
The first approach of calorimetry on single crystals was implemented by Kyser and Masel [59, 60] in 1986. King and coworkers established SCAC as a surface science technique [61]. The adsorption heats of many species has been measured on single crystal surfaces with this approach [132]. In 1998, Campbell and coworkers introduced a setup with a different heat detection compared to the one used by King [62]. The general principle of the microcalorimeters, used by King et al., Campbell et al. and our group will be described in the following.

3.2.1 Measurement principle

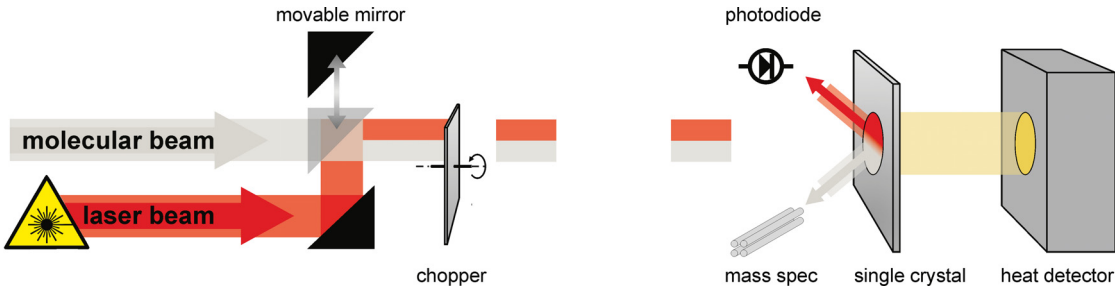

Abbildung 3.2: Representation of the measurement principle used in microcalorimetric measurements

Figure 3.2 schematically represents the main elements of the SCAC, which consists of a molecular beam, which is situated in front of an ultrathin single crystal. The continuous molecular beam is chopped into pulses of molecules that impinge onto the sample surface. Heat evolution during adsorption or reaction will result in a temperature rise on the crystal. This temperature rise can be measured by a suitable detector. To calibrate the detector signal, a laser beam is coupled into the molecular beam source as described in [178] and guided through the beam. The laser beam is chopped equivalently to the molecular beam and impinges on the sample surface. Knowing the reflectivity of the sample and measuring the power of the laser with a photodiode, the amount of energy absorbed by the sample can be calculated based on the detector signal. Subsequently, the evolved heat during the surface processes can be deduced. To obtain the heat evolution as a function of the number of reacting or adsorbing molecules on the surface, a King-Wells sticking coefficient measurement, as described in section 3.3, is performed.

3.2.2 Heat detection

The microcalorimeters which are used by King et al. and Campbell et al. differ in the method of heat detection. Kings group uses an infrared detector, on which the emitted light is focused via a parabolic cone. Black body radiation, which is emitted from the sample increases during

a temperature rise [61], is detected by the infrared detector. The sample thickness was chosen as 0.2 μm to minimize its heat capacity ($\sim$1 μJ/K) and thereby to maximize the sensitivity of the detector. In combination with a sticking probability measurement, the coverage dependent adsorption heats of a large number of molecules have been obtained [132].
Campbell and coworkers implemented a pyroelectric sensor for the detection of the heat release during surface processes. Pyroelectric materials are a subclass of piezoelectric materials, in which a temperature change results in a change of the net polarization vector in the crystal, which can be measured as a voltage. The group of Campbell et al. used a $9\mu m$ thick -polyvinylidene fluoride (PVDF) ribbon to establish the electric contacts, the ribbon was coated on both sides with a metal (NiAl or Au). Ribbon and detector housing are mechanically driven so that a spring force contact can be established during the measurement. The adsorption energies of metal atoms [74, 179–182] on oxide surfaces and organic molecules on metals have been investigated [58, 183, 184] with this setup.
Due to the different detection methods, these microcalorimeters operate at different temperatures: The detector, used by King et al., only allows measuremets at T>300 K, as the blackbody radiation is too low at lower temperatures ($\Delta P \propto \Delta T^3$). The pyroelectric ribbon, used by Campbells group, degrades at T>350 K, thus measurements can only be performed at T<350 K. Due to the higher sensitivity of this detection method, thicker single crystals between 1 μm up to 75 μm can be used. In the present setup, heat detection is achieved via a pyroelectric ribbon.

3.3 Sticking measurements

As described earlier, measurements of the sticking coefficient give valuable information on the dynamics of the adsorption process and the number of adsorbed/reacting molecules can be obtained in case the molecular flux is known. Detection of the background pressure is possible by mass spectrometry, which will be explained in more detail after discussing the general principle of sticking measurements.

3.3.1 Measurement principle

An early method which is still applied today for determining sticking coefficients is to measure the increase in the surface coverage with flash desorption methods [185] as a function of the deposition time. The experimental error of this method, however, has been reported as $\sim$50 % [186]. A more accurate procedure for the determination of sticking coefficients has been introduced by Bell and Gomer, in which the reflected flux of molecules is sampled with a Field emission tip [187]. In 1972, King and Wells introduced a method which is comparably simple for determining the sticking coefficient and coverage accurately [188].
The principle of a King-Wells sticking type measurement is shown in Figure 3.3. Initially, a gold flag is situated in front of the sample, on which the molecular beam is directed to. As the sticking coefficient of many molecules at room temperature is zero on gold, the impinging molecules are usually reflected from the gold flag. This causes a transient pressure rise in the chamber, which is detected with a QMS. The QMS signal during this molecular beam experiment is indicated in the inset of Figure 3.3.

Subsequently, the gold flag is removed and the molecular beam is directed onto the sample surface. This results in the adsorption of molecules from the molecular beam on the surface, which gives rise to a smaller pressure increase compared to the measurement on the gold flag. As the surface is being covered by adsorbates with increasing exposure, less molecules are being adsorbed and the pressure rise in the chamber increases with time.

As the gold flag is in a slightly different position than the sample, the scattering geometry is

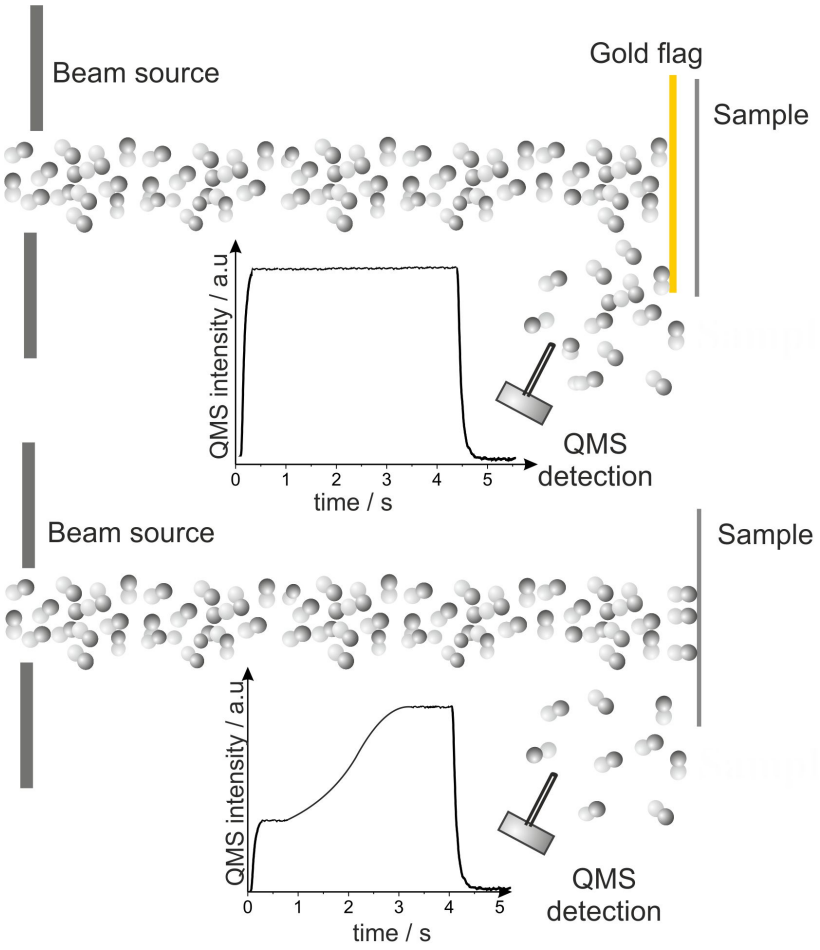

Abbildung 3.3: Representation of the measurement principle, used for measuring the King-Wells sticking coefficient.

changed when removing the gold flag. This influences the QMS signal. To take this into account, an additional experiment with a gold sample is performed. By comparing the QMS signal during impingement of the beam on the sample with the signal during impingement of the beam on the gold flag, the sticking coefficient can be obtained with additionally taking into account this change in the scattering geometry. For details to the evaluation procedure, I refer to section 5.2. In the present setup, pulses of molecules impinge on the sample which is necessary for the energy measurements. The measurement and detection principle in this special case of a King-Wells

sticking type measurement is described above. For the case that desorption of a surface species occurs in the time scale of the pulse, the situation arises in which molecules adsorb during the pulse and desorb in between the pulses. This has to be taken into account when calculating the sticking coefficient and the coverage.

3.3.2 Quadrupole mass spectrometry

In this work, a quadrupole mass spectrometer has been used for the sticking probability measurements and to detect gas phase products that are evolved during the molecular beam measurements.
In the first stage of the mass spectrometer, gas is ionized. This is usually achieved by electron impact. Electrons, which are emitted from a cathode, are accelerated onto the initially neutral molecules with energies in the range 10 eV - 100 eV. A fraction of this energy is thereby transfered to some of the impinging molecules, which may thereby form ions. These ions are often unstable and form fragments, which is very common for large organic molecules [189].
In the second stage, the ionized fragments are selected according to the mass: charge ratios

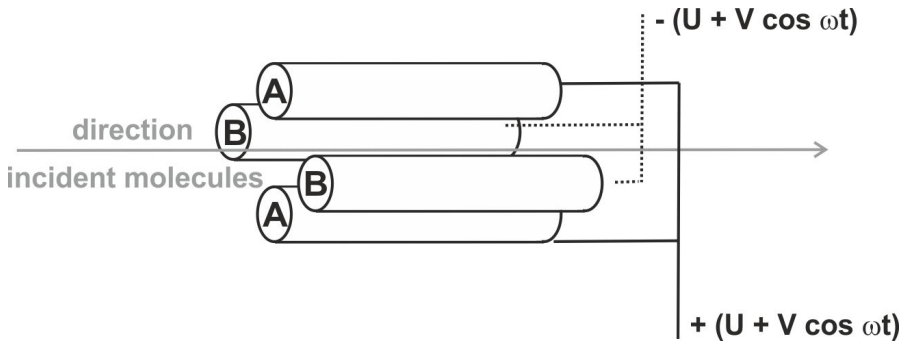

Abbildung 3.4: Schematic representation of the quadropole mass filter

(m/z). This is achieved by four electrodes which are arranged parallel to each other, as represented in Fig. 3.4. The voltage on the electrodes consists of a direct current component and of an alternating current component. The direct current is the same on opposing electrodes, while neighboring electrodes are on opposite potentials. The ions, which travel on a trajectory as shown in Fig. 3.4 are deflected by the electric field, produced by the electrodes, unless they have a specific m/z ratio. This ratio is determined by the direct-current potential and the amplitude and frequency of the alternating current component.
After passing the mass filter, the selected molecules are directed onto a detector. The use of channeltron electron multipliers are very common for detecting ions. Such a detector is used in our setup. However, they can be only used in low pressure regions ($p<10^{-6}$ mbar). CEM detectors consist of a small tube on which a potential of $\sim$1-3 kV is applied. The impact of the positively charged ions leads to the emission of electrons, which are accelerated towards the anode. On their way, the electrons create an avalanche of secondary electrons, which leads to amplification factors of up to 10^{8}.

3.4 LEED

LEED is one of the first and most commonly used methods for investigating the structure of periodic systems such as surfaces [190]. Similarly to X-ray scattering techniques, LEED is based on the constructive interference of an incident (**k**) and an outgoing wavevector (**k'**) so that

$$\mathbf{k}^2 = \mathbf{k'}^2 \tag{3.3}$$

The incident and outgoing electrons are typically in the energy range 20-1000 ev and thus have typically a mean free path between 5 and 20 Å. Thus LEED is a surface sensitive technique (note that LEED has a high surface sensitivity as both the incident and outgoing electron have a low mean free path). The components of the wavevector parallel and perpendicular to the surface can be separated and only the component parallel to the surface is conserved. $\mathbf{k'}_{\parallel}$ in equation 3.3 can be written as

$$\mathbf{k'}_{\parallel} + = \mathbf{k}^2_{\parallel} + \mathbf{g}_{hk} \tag{3.4}$$

where $\mathbf{g}_{hk}$ is a combination of the reciprocal lattice vectors. Thus, from a pattern on the LEED screen, the periodicity of the surface or adsorbate structure can be directly obtained.
To deduce information on the actual location of the atoms within the unit mesh, the diffracted beam intensities have to be compared to results from a quantitative scattering theory. For further information on this subject, I refer to the references [190, 191].
A schematic representation of a LEED apparatus is shown in Figure 3.5. The electrons are

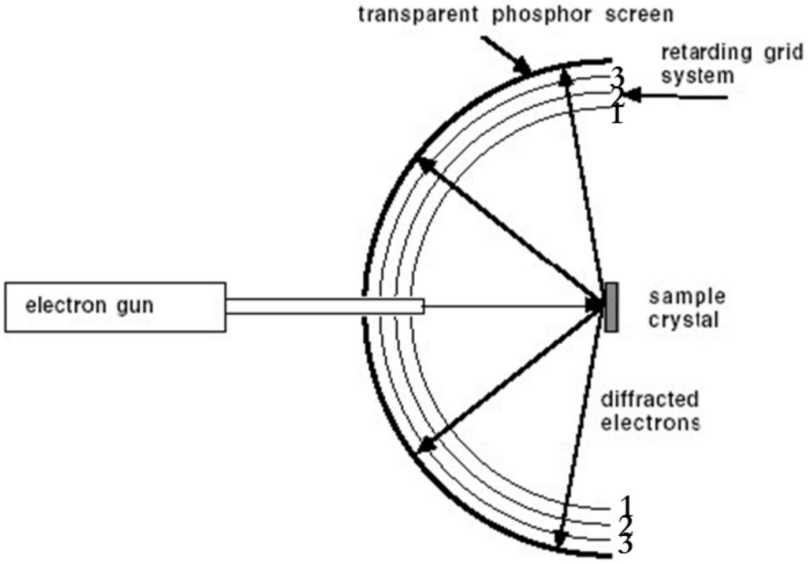

Abbildung 3.5: Schematics representation of the essential parts for a LEED experiment

emmitted from the electron gun and the scattered electrons leave the sample in the direction of the LEED screen. To ensure that only the electrons with the energy of the source reach the screen, a negative potential is applied on the inner grids G2 and G3. The screen is biased at a

positive voltage (5-6 keV) to accelerate the transmitted electrons to a high kinetic energy so that light emission is caused on the coated fluorescent glass screen.

4 Experimental Setup

In this chapter, explicit information on the experimental setup, that was used for this work will be given. This subject can be separated into two parts, one concerning the setup for the SCAC experiment with calibration and the other the setup for the preparation of the model catalysts.
The SCAC experiment, which is used in this work is based on the pyroelectric heat detection technique of Campbell et al. [62]. To allow for the study of supported model catalysts, facilities for the preparation of such have been integrated into the UHV-apparatus.
Figure 4.1 shows an overview of the apparatus, applied for the present studies. Preparations of

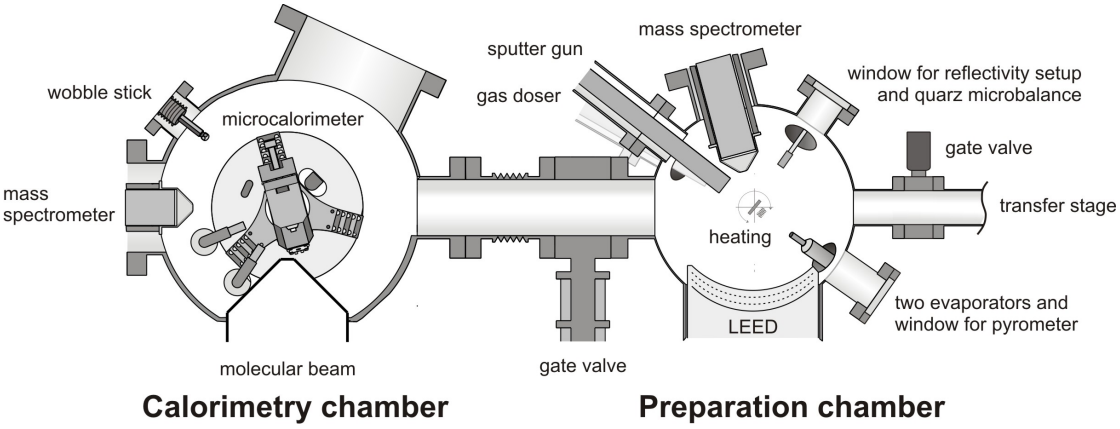

Abbildung 4.1: Schematic overview of the experimental setup, consisting of two separate chambers (from [123]). The chamber on the right hand side is used for preparing the model catalysts and the adsorption/reaction chamber is used for performing the SCAC experiments with the according calibration

the model catalysts are performed in the preparation chamber, while the the adsorption/reaction chamber is used for the SCAC experiments. Both chambers are independently pumped and separated by a gate valve. A translational rod is used to transfer the sample between both chambers. The transfer stage, indicated on the right part of Figure 4.1, is separated from the preparation chamber by a gate valve and pumped by a 50 L/s turbo molecular pump (Pfeiffer, TMH/U 071). On top of the Mo sample holders, a T-piece is added, which allows for an easy transfer between the transfer rod and the sample holders in the adsorption and in the preparation chamber by using wobble sticks.

4.1 Preparation chamber

The preparation chamber is continuously pumped by a 500 L/s turbo molecular pump (TMP) (Pfeiffer, TMU 521 P), the typical base pressure in this chamber is $1-2\cdot10^{-10}$ mbar. During sample preparation, the mounted crystal remains in a rotatable xyz-manipulator (VAb GmbH), which is equipped with a filament for electron bombardment and K-Type thermocouple connectors for temperature measurements. Figure 4.1 shows the equipment, situated around the central part of the preparation chamber: two metal evaporators (Omicron, EFM 3), a sputter gun (Omicron, ISE-10), a quartz crystal microbalance (Sigma Instruments) for calibrating the flux of the evaporating metals, a combined LEED/Auger electron spectrometer (AES) unit (SPECS, ErLEED) and a quadrupole mass spectrometer (Hiden, Halo 201). A gas doser is fixed on a translational stage with a 10 μm opening to the gas supply. Either thick (1 mm) samples or thin (1 μm) samples are mounted on the Mo sample holders with a central whole, which is 8 mm in diameter.
Besides AES and LEED, which can be used on both samples, TPD studies can be performed on the 1 mm thick single crystal. Therefore, the K-type thermocouple connectors are point-welded to the crystal, which can be heated by radiation from the filament or electron bombardment. The temperature ramp is controlled by an external Labview program, while the desorbing gas is detected with a QMS. Details on the standard setup of AES/LEED and TPD experiments are described elsewhere [190, 191]. To allow for low temperature measurements, a reservoir inside the manipulator can be filled with liquid nitrogen. In this assembly, it is possible to maintain the crystal temperatures in the range 100 K- 1200 K. The temperature of the 1 μm thin single crystal is monitored by a pyrometer (Sensotherm, MP25), as mounting of a contact probe would destroy the crystal. As the pyrometer is only calibrated for a fixed emissivity, which is different from the emissivity of Pt, calibration to the output voltage of the pyrometer by a K-type thermocouple on a 1 *mm* thick Pt(111) crystal has been performed.

4.1.1 Setup for the reflectivity measurement

A reliable knowledge of the sample reflectivity is crucial for the energy calibration with a laser during the microcalorimetric measurement. The reflectivity measurement is performed with a Helium-Neon laser (Lasos, 632.8 nm, 2 mW, cw) in a setup shown schematically in Figure 4.2. Laser, polarizer, beam splitter and the two photodiodes are mounted on a platform and can be attached to the UHV system, so that the laser points through the borosilicate window to the center of the chamber. To monitor the intensity of the incident laser beam, a fraction of the laser light is deflected by a prism to a photodiode before passing through the window. The fraction of the laser light, which is not deflected by the beam splitter impinges on the sample at an angle of $\sim5^\circ$ to the surface normal. The reflected laser light passes through the window again, its intensity is measured by a second photodiode (Silicon Sensor, PS100-2). The reflectivity is obtained by the following equation:

$$I_{Reflection}/I_{Laser} = C \cdot refl \tag{4.1}$$

$I_{Reflection}$ is the intensity of the reflected laser light and I_{Laser} is the intensity of the incident laser light. C is a factor, which is dependent on the experimental setup and $refl$ is the reflectivity. In order to obtain C, calibration with five dielectric mirrors (LayerTec) of known reflectivities

(41.4pm0.4 %, 59.7±0.9 %, 76.7±1.1 %, 86.2±0.2 % and 96.6±0.1 %) is carried out. Since the beam splitter is polarisation dependent and the polarisation of the initial laser beam changes with time, the usage of a linear polarizer, which is indicated in Figure 4.2, is necessary.

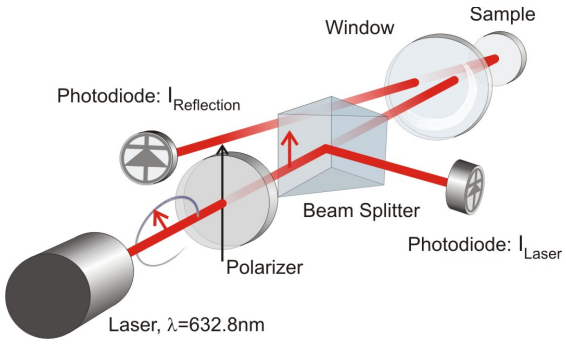

Abbildung 4.2: Setup for the reflectivity measurement, Laser, polarizer, beam splitter and the photodiodes are attached on the outside of the UHV system (from [123]).

4.2 Adsorption/Reaction chamber

4.2.1 chamber geometry

In the adsorption/reaction chamber, pumped by a 500 l/s TMP (Pfeiffer, TMU 521 P), simultaneous energy and sticking probability measurements can be performed. The typical base pressure is $\sim 2 \cdot 10^{-10}$ mbar. The general setup of the chamber is shown in Figure 4.3: An effusive molecular beam source with an integrated chopper (1) is used for gas deposition. Three types of detectors can be positioned in front of the molecular beam by a rotatable platform (2): the central part of the microcalorimeter (3) for pyroelectric heat detection, a photodiode (4) and a beam monitor (5). Further essential parts of the adsorption/reaction chamber are a mass spectrometer (6) and two gas dosers (7). To attenuate the vibrational noise in the microcalorimeter signal, the detector head and the sample holder mounting are placed on a vibrational damping stack (8). The Cu platform and the microcalorimeter can be cooled with liquid nitrogen. A programmable temperature control (Eurotherm 3508) allows to adjust the temperature of the platform in the range 110 K - 300 K with ∼1 K precision. To establish a contact between microcalorimeter and sample, an Allen wrench wobble stick (9) is used.
After establishing the pyroelectric contact to the sample, the sample is rotated in front of the molecular beam. Subsequently, the gold flag (not shown) for the King-Wells sticking measurement, which is described in detail in section 3.3, is positioned between the sample and the molecular beam. In order to obtain the sticking probabilities, the background pressure is monitored with a QMS (Hiden, HAL 301/3F PIC).

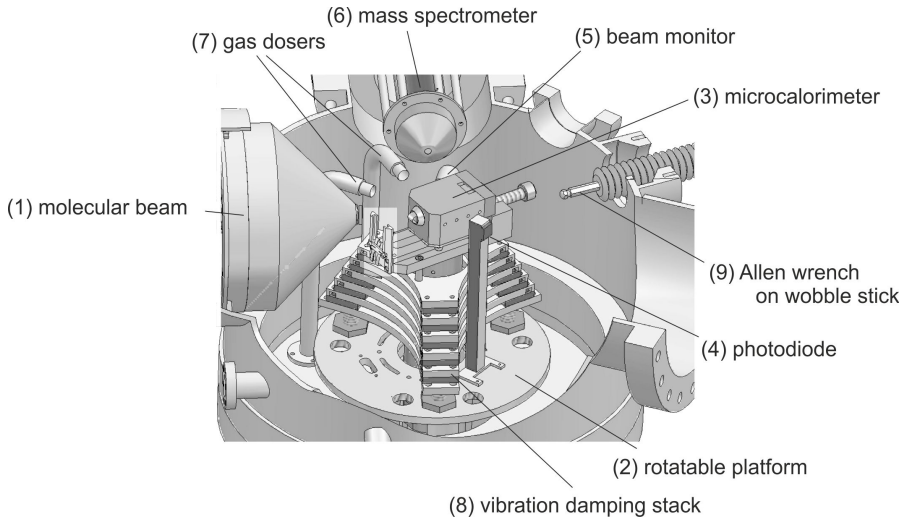

Abbildung 4.3: Overview of the adsorption/reaction chamber (from [123]). The labeled components are: (1) molecular beam source, (2) rotatable platform, (3) microcalorimeter (4) photodiode, (5) beam monitor, (6) QMS, (7) two gas dosers (8) vibration damping stack, (9) Allen wrench mounted on a wobble stick

4.2.2 Microcalorimeter

A schematic representation of the microcalorimeter, adapted from the original setup of Campbell et al. [62] and further developed, is given in Fig. 4.4.
Heat detection is achieved via the β-PVDF ribbon (1) (6 μm thick from Piezotech), which is polarized perpendicular to its faces and coated with Au for the conduction of the measured charge. The ribbon is cut into a 6.3 x 35 mm piece and etched according to the procedure used by Campbell et al. [192]. It is mounted into the detector housing (2) in such a way, that the ribbon forms a protruding 90° arch and is electrically connected to the amplifier circuit. Prior to each measurement, the detector housing with ribbon is mechanically driven on the Cu platform (3) with a translational screw (4) towards the sample holder mounting (5). An Allen wrench wobble stick ((9) in Fig. 4.3) is used to drive the detector housing on two sapphire plates (6).
A good reproducibility of the contact between sample and pyroelectric ribbon is established by the cone on the calorimeter head (7) with the corresponding counterpart on the sample holder (8). During the gentle mechanical contact to the sample holder, the flexible ribbon flattens and covers about 6 x 6 mm^2 of the crystal, which allows for heat transfer between sample and ribbon.
The adsorption/reaction processes produce a temperature change in the pyroelectric detector, which results in a transient face-to-face voltage. After amplification by a factor of 100, a measurable signal in the order of 10 V is recorded. The charge is conducted to a high impedance amplifier circuit, which is described in detail in [193]. Reduction of electromagnetic noise is achieved by applying a guarding potential to the coaxial cables. A band pass filter is used to additionally reduce noise in the signal.
To minimize the electric noise due to temperature fluctuations during the measurement on the

detector head, the sample holder is connected to a large 2 kg Cu thermal reservoir, which can be cooled with liquid nitrogen or precooled gases. The good thermal contact between sample holder and detector head leads to a fast temperature equilibration within a few minutes. A lower equilibration time increases the accuracy due to reduction of surface contamination, resulting from gas adsorption. To attenuate the vibrational noise in the detector signal, the Cu platform (3) in Figure 4.4, carrying the microcalorimeter is situated on a vibration damping stack, which consists of six stainless steel plates, separated by Viton plates of 5 mm thickness. Four support columns (9) have been used to connect the Cu platform to the upmost plate of the stack. As the Viton material becomes stiff at cryogenic temperatures, the contact between the thermal reservoir and the damping stack is established by four thin-walled stainless steel tubes with a low thermal conductance to avoid stiffening of the viton rings.

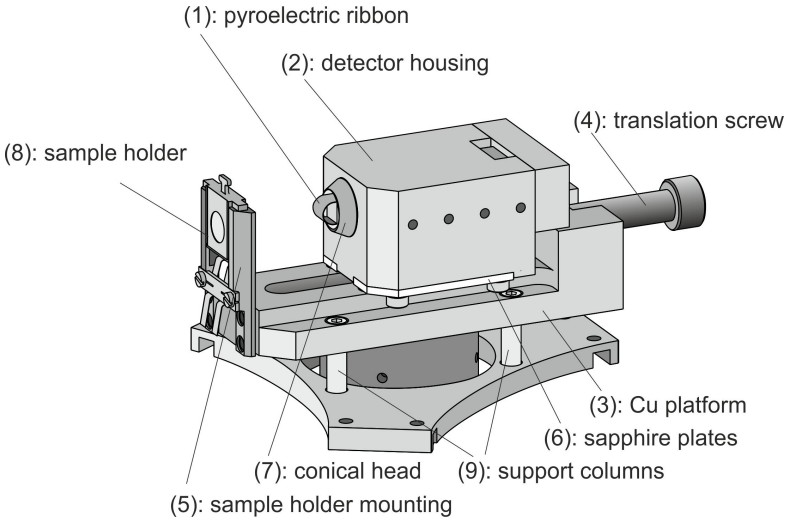

Abbildung 4.4: Essential parts of the microcalorimeter (from [123]): (1) pyroelectric ribbon, (2) detector housing, (3) Cu platform carrying the detector housing and the sample holder mounting, (4) translation screw, (5) sample holder mounting, (6) sapphire plates (7) conical head of the detector housing, (8) sample holder, (9) support columns

4.2.3 Energy calibration system

Due to changes in each mechanical/thermal contact between sample and pyroelectric ribbon, the detector voltage has to be calibrated directly after each microcalorimetric measurement. This is established by using light pulses from a He-Ne laser (Linos, 632.8 nm, 2 mW, continuous wave) according to the procedure described by Stuckless et al.. Figure 4.5 schematically represents the laser calibration system. The laser light is spread and collimated by a lens system and directed to one of six filters, mounted in an externally controlled wheel. By using six filters with the transmissions 1, 0.285, 0.104, 0.079, 0.068, 0.053, calibration with six different light intensities can be achieved.The laser beam passes through a window into the molecular beam source, where

it is deflected by a prism onto the sample. The chopper cuts the laser beam in an identical way as the molecular beam. Because it is essential for the accuracy of the SCAC experiment, that laser and molecular beam are aligned, their position with respect to each other is frequently checked. The detector response during impingement of molecular pulses can be directly compared to the signal due to heating by laser pulses. Because of a temporal drift in the laser power and variations in the prism position, the laser power is measured in each experiment by a photodiode (Silicon Sensor PS95-4), which has been externally characterized by a reference photodiode (Thorlabs, FDS1010, (4) in Figure 4.3). The sensitivity of the photodiode was determined to be 350.3 $\pm$ 0.49 mA/W, the wavelength of the laser is 632.8 nm. Details about the evaluation of microcalorimetric measurements will be given in section 5.

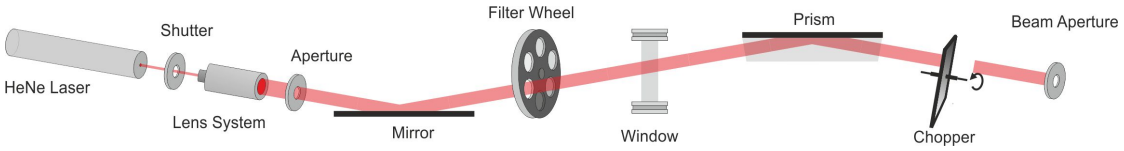

Abbildung 4.5: Schematic representation of the laser calibration system (from [123]). Laser, lens system and filter wheel are outside the UHV system.

4.2.4 Molecular beam

The molecular beam source was designed to provide a well defined, homogeneous gas flux and to allow a fast and variable chopping of the molecular beam. In addition to that, the possibility for directing the laser beam into the molecular beam path is provided.

Figure 4.6 shows a cross section of the molecular beam source. A glass capillary array (1)

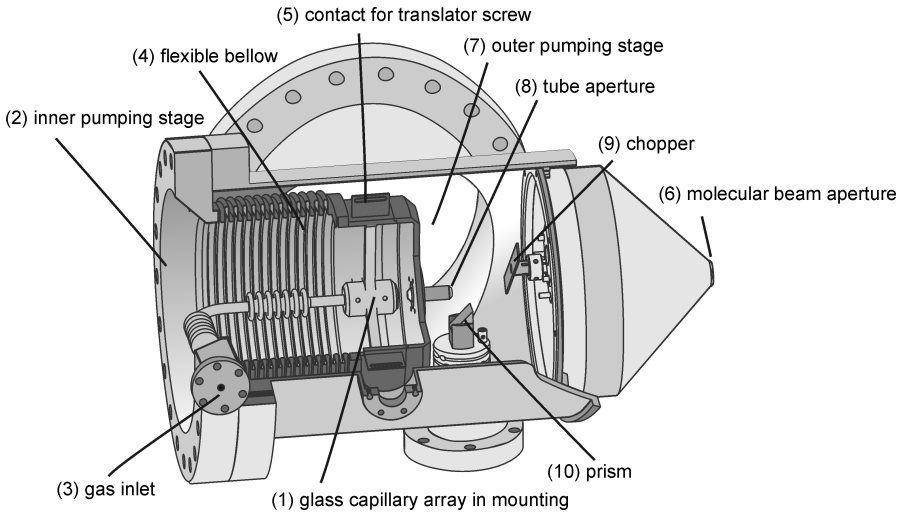

Abbildung 4.6: Profile of the molecular beam source (from [123]).

(Galileo, 50 μm channel diameter, 1 mm thickness) was used to collimate the molecular beam.

It is mounted in an inner pumping stage (2), which is pumped by a 500 l/s TMP (Pfeiffer, TMU 521 P) and connected to a gas inlet system (3). By using a flexible bellow (4) for mounting the inner pumping stage, the position of the glas capillary array can be adjusted with two translator-screws (5). To achieve a high pumping speed and a small distance to the beam aperture (6), the outer pumping stage (7) has been designed to be a part of the adsorption/reaction chamber. The gas exits this pumping stage through a nozzle aperture (8) (4 mm) to the outer pumping stage, which is pumped by a separate TMP. A remotely controlled chopper (9) is used to generate the pulses, which can be as short as 150 ms. For the energy calibration of the SCAC experiment, a prism (10), mounted on a translational stage can be coupled into the beam path.
The sample position is chosen as close as possible to the outer beam aperture (6), through which the molecular beam enters the UHV chamber to minimize the divergence of the gas flux, before the beam impinges on the sample.
As the detected heat linearly depends on the molecular beam flux and the area of the beam, an accurate determination of the spatial distribution and molecular flux of the gas is essential for performing accurate SCAC measurements. Therefore, a beam monitor, based on a high accuracy ion gage (Granville-Phillips, 370 Stabil-Ion), was mounted on the rotational platform ((5) in Figure 4.4), to measure the pressure in front of the molecular beam. To detect the molecular flux in the center of the molecular beam, the beam monitor is situated at a distance of 7 mm to the beam aperture. The pressure can be converted into a beam flux by the following relation derived from kinetic gas theory, for further details see e.g. reference [10]:

$$Flux = \frac{P}{\sqrt{2\pi M k_B T}} \tag{4.2}$$

The flux is given in molecules per time interval and area, P is the pressure, M the molar mass, k_B the Boltzmann constant and T is the temperature. To measure the flux, Argon has been used, for the adsorption of other gases, the flux was recalculated according to equation 4.2. A tunable beam flux was achieved by varying the backing pressure.
Figure 4.8a (a) shows the molecular beam flux as a function of the backing pressure. In the pressure range $1\cdot 10^{-3}$ mbar to $\sim 2\cdot 10^{-1}$ mbar, the molecular flux increases linearly with increasing backing pressure. At higher backing pressures, the flux levels of at an intensity of $\sim$1.5 10↑ molecules cm^{-2} s. The lowest flux that can be achieved with the beam source is $\sim 5 \cdot 10^{12}$ molecules cm^{-2} s^{-1}.
Figure 4.8b (b) shows a 3D representation of the beam profile at a source pressure of $3.75 \cdot 10^{-3}$ mbar. This measurement was performed by positioning the beam monitor in front of the molecular beam and adjusting the vertical and horizontal position. Variations in the beam intensity on the central plateau are less than 3 %. The beam diameter has been recently measured to be 4.2 mm.

Abbildung 4.7: Performance of the molecular beam source (from [123]): (a) molecular flux as a function of backing pressure, (b) beam profile

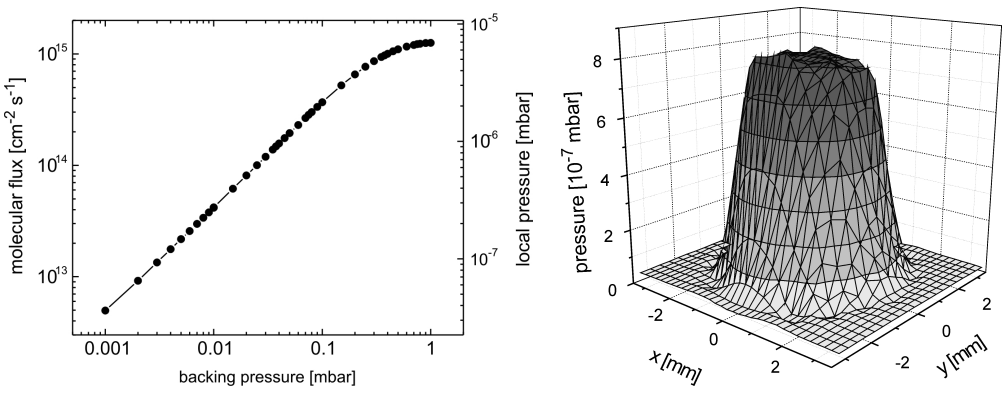

(a) (b)

4.2.5 Simulation of the beam profile

A two dimensional cross section of the beam intensity as a function of x or y shows, that the molecular flux decays within one millimeter from the maximum value to the background value. If this was the actual profile of the beam, it would significantly affect the sticking coefficients, as $\sim$50 % of the beam area would be within the region of this decay. It can be speculated though, that this behavior can be mainly attributed to the fact, that the beam monitor aperture has a diameter of 1 millimeter (measured with an optical microscope). To validate this hypothesis, the beam profile resulting from a perfectly rectangular beam profile has been simulated.
The scheme in Figure 4.9a (a) illustrates, that the measured beam profile is proportional to the cross section between molecular beam and beam monitor aperture. Therefore, an algorithm that calculates this cross section for different positions of the beam monitor is able to take into account the effect of the finite beam aperture size. Figure 4.9b (b) shows the data points, obtained by a measurement of the beam profile with the beam monitor normalized two dimensional beam profile (red circles). Furthermore, Fig. 4.9b (b) shows the simulated beam profile in case the intensity drops within 1 μm from the maximum to the background value (violet line) and a simulated beam profile, that originates from a beam profile with half the intensity within 0.5 mm radius (green line).
It is obvious from Fig. 4.9b (b), that the agreement between the profile, where the intensity drops within 1 μm from the maximum to the minimum value and the measured beam profile is almost perfect, whereas the agreement is significantly worse for the other profile.
Accordingly, this simulation shows, that the beam profile decays from the maximum value within a fraction of a millimeter. The resulting error for the sticking measurements is insignificant

Abbildung 4.8: Simulation of the measured beam profile: (a) drawing of the overlapping cross section of the beam monitor aperture and the molecular beam. (b) the normalized beam profile compared to the simulated beam profiles: the violet line shows the simulated beam shape for a profile, where the intensity decays within 1 μm from the maximum to the minimum value. The green line shows the simulated beam profile for a beam with half of the maximum flux within 0.5 mm

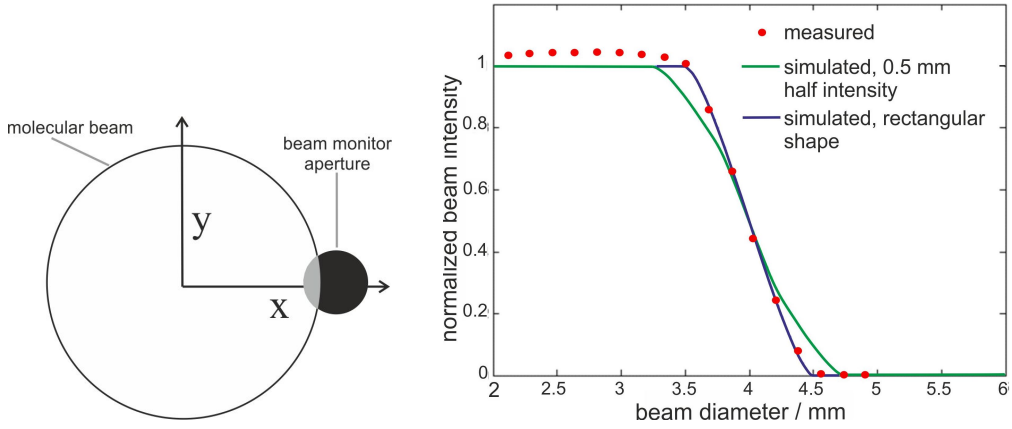

4.3 Statistical and systematic errors

The error in the measured adsorption heat plays a central role in how useful the obtained results are for further evaluations and for comparisons with results from theoretical calculations. It is customary to divide errors into two categories, the accuracy of a measurement relates to systematic errors and the precision to statistical errors. As statistical errors depend on the number of performed measurement, they can be significantly reduced by performing more experimental runs. Table 4.3 lists different experimental errors separated by error sources in the energy measurement and in the determination of the number of adsorbed molecules.
The major error source in the energy measurement arises from the determination of the laser energy, which is adsorbed by the sample per pulse and includes the photodiode sensitivity, the pulse length and the sample reflectivity. The systematic error in the reflectivity has the largest contribution to the total error. The precision on supported nanoparticles is worse than on single crystal surfaces, as additional errors in the thickness of the oxide film linearly influence the reflectivity.
A reduction of the precision and accuracy in the determination of the sticking probability arises due to errors in the determination of the beam intensity, the molecular beam stability, the beam profile area and the sticking probability. The error in the sticking coefficient has been discussed by King and Wells in [188] and depends on the pressure gage (in this case the QMS) and the position of the zero sticking reference. To test the experimental setup, the statistical error of the sticking coefficient measurement has been tested for the case of CO adsorption on Pd(111) for six independent measurements. The precision depends on the magnitude of the sticking coeffi-

cient: it amounts to $\sim$1 % if the sticking coefficient is high (>0.7) and is $\sim$30 % for low values of the sticking coefficient (<0.3). Thus for high coverages, the statistical error in the sticking coefficient has by far the largest contribution to the overall error.
For the case of a high sticking coefficient, the overall accuracy of the adsorption energy measurement is in the range 7-9 % for gas adsorption on a model oxide-supported catalyst for gases that do not stick on the chamber walls.

Adsorption heat		
photodiode sensitivity	Accuracy: 0.1%	Error of the mean, 62000 measurements
	Precision: <0.1%	Accuracy determined by calibration lab
Laser power stability	Precision: <0.08%	Standard deviation, 120000 measurements
Reflectivity	Accuracy: <1.3 %	Determined by using mirrors with known reflectivity
Reflectivity (single crystal surfaces)	Precision: <0.07%	Determined from 20 measurements on Pt(111)
Reflectivity (Pt(111)/Fe_3O_4 thickness $\sim$50 Å)	Precision: $\leq$1.3%	Maximum error in three different preparations
Pulse length	Accuracy: $\leq$0.4 %	Standart deviation over 50 pulses
Sticking probability		
Molecular beam intensity	Accuracy: 4%	Standard deviation from 46 measurements
	Precision: <1.1%	Accuracy as stated by the manufacturer
Molecular beam stability	Precision <0.2 %	Upper limit, set by the detection limit of the beam monitor;
Beam profile area	Accuracy: <5 %	The error in beam diameter is $\leq$0.1 mm
Sticking probability	Accuracy 2-6%	[188] Dependent on the gas and total magnitude of the sticking probability
When $\geq$0.7	Precision: 1 %	Standard deviation for six measurements of CO adsorption on Pt(111),
When $\leq$0.3	Precision: 30 %	Standard deviation for six measurements of CO adsorption on Pt(111),

5 Evaluation of SCAC experiments

Information from a microcalorimetric measurement includes several data sets from the SCAC detector and data from the QMS. In addition to that, data from the photodiode when measuring the energy of the laser beam is acquired. How this in situ obtained information is combined with ex situ determined observables to obtain the adsorption energy and the sticking coefficient as a function of the surface coverage, will be the subject of this chapter. First, the evaluation of the SCAC detector signal and the data from the microcalorimeter detector calibration will be explained. Subsequently, the evaluation of the QMS data for the determination of the sticking coefficient, the surface coverage and the calculation of the adsorption heat/adsorption energy per unit of molecules will be discussed. In the end, it will be introduced how the desorption rate constant and the desorption prefactor can be evaluated in cases where this is possible.

5.1 Determination of the adsorption heat

For the evaluation of the data from the microcalorimeter detector, a medianfilter has been used, which replaces each data point with the median of 4 circumjacent data points. In addition to that, a low pass filter removes frequencies which are significantly higher than 3.5 Hz. Figure 5.1 shows a comparison between the original and the filtered signal, obviously the filtering procedure only leads to insignificant changes the signal shape. The dotted line represents the detector signal caused by a laser pulse with the transmission 1 scaled to $\approx$20 % of the original signal. The signal shape, in detail discussed in [193], is influenced by the the heat transfer between sample and the sample holder, the pyroelectric ribbon and in addition by the electronics for filtering and amplification of the signal.
As shown in Figure 5.1, the signal shape for an adsorption experiment is exactly the same when pulsing with a molecular beam and with a Laser. This is true for adsorption processes, in which the surface reaction occurs on a timescale which is short in comparison to the time constant of the detection system. In such cases, any observable that is proportional to the signal intensity as the background substracted peak height or the initial slope [58, 58, 62] of the detector signal can be used for the evaluation, as long as the same procedure is used to evaluate the detector signal during the molecular beam experiment and during the laser calibration procedure. Figure 5.2 shows the evaluated detector signal in V on the left axis versus the pulse number, evaluated with two different procedures for an SCAC measurement of Propylene oxide on a partially covered Pd surface. As the peak height of the detector signal is proportional to the evolved heat on the surface, it can be used to calculate the adsorotion heat: the peak height of the microcalorimetry signal versus the pulse number is represented by black square scatters in Fig. 5.2.
The influence of the low frequency noise in the detector signal on the relative error can be minimized by fitting each pulse to a reference pulse, which is obtained by averaging over several

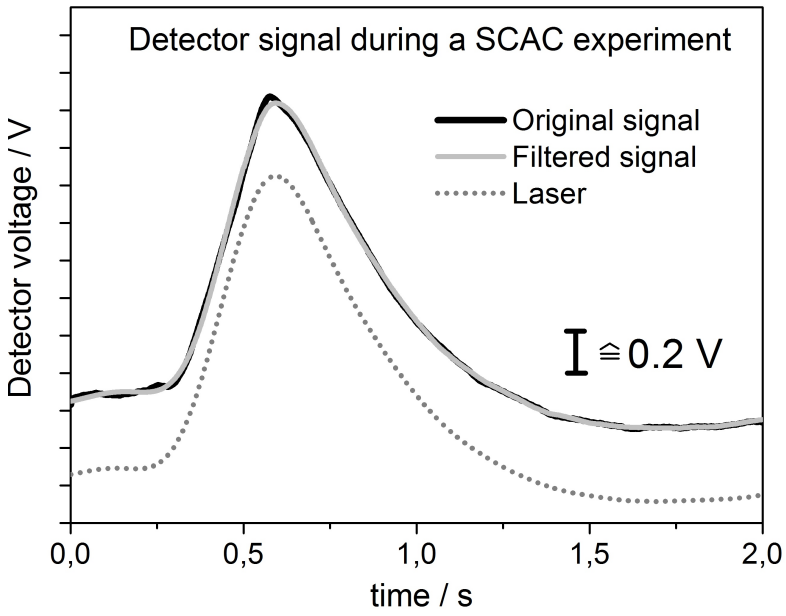

Abbildung 5.1: The original SCAC detector signal for a typical experiment (black) is shown with the filtered signal (grey). As a comparison, the detector signal during pulsing with the laser beam is shown as a dotted line

laser pulses. The relative scaling factor of this reference pulse, multiplied by the pulse height of the Laser pulse (in V) is shown by the gray circular scatters (shifted relative to the original result by -0.2 V) in Figure 5.2. The standard deviation is reduced by ≈30 % when using this method. In the scope of this work, the adsorption energy is evaluated by determining the peak height of the detector signal.

The detector voltage is proportional to the heat release on the sample [123]. Accordingly, the evaluation of the evolved heat requires the determination of the contact sensitivity of the pyroelectric detector in V/J, which is the proportionality factor between the detector voltage (in V) and the heat release (in J). Therefore, laser pulses of identical length than the molecular beam pulses impinge on the sample to produce a detector voltage. The laser power and the reflectivity of the sample are then used to determine the amount of absorbed energy by the sample per pulse. With this information, the contact sensitivity of the detector can be determined.

For each microcalorimetry measurement, the incident laser power is determined in situ with a calibrated photodiode. This is necessary due to the laser drift and slight variances in the prism position for each measurement. Figure 5.4a (a) shows a typical photodiode response during an incident laser pulse. The on and off time of the Laser was chosen to be 5 seconds to obtain sufficient statistics. The amplitude of 290 mV corresponds to a laser power P_{Laser} of 13.6 μW.

The contact sensitivity of the pyroelectric detector is calibrated for each new contact between ribbon and sample in order to take into account changes in the heat transfer. The incident laser power on the sample is varied by the use of filters with the transmissions 1, 0.285, 0.104, 0.079, 0.068, 0.053. To obtain the absorbed energy during a laser pulse on the sample, the reflectivity,

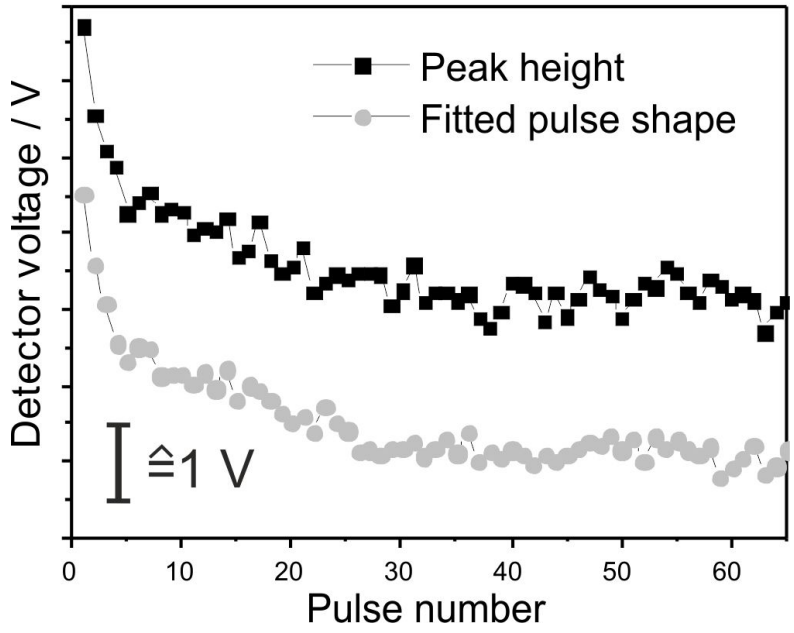

Abbildung 5.2: Evaluated detector signal obtained via two different evaluation procedures (for details, see text). The gray circular scatters are shifted by -0.2 V with respect to the original signal

which is measured with the procedure described in subsection 4.1.1 has been used. For supported catalysts, it is essential, that the thickness of the oxide layer amounts to ≈50 Å, as the reflectivity decreases approximately linearly with the oxide thickness. The heat release during Laser pulses $q_{cal,L}$ on the sample is calculated as

$$q_{cal,L} = P_{Laser} \cdot T \cdot t \cdot (1 - \alpha) \tag{5.1}$$

, where T is the transmission coefficient of the filter, t is the pulse time and α is the reflectivity. A plot of $q_{cal,L}$, corresponding to a pulse time of 266 ms as a function of the detector voltage of a typical measurement is given in 5.4b (b). Usually, the calibration is performed with 10 laser pulses for each filter. The standard deviation in that example is ≈2.7 nJ. As the evolved heat increases linearly with the detector voltage, the heat release for the pulsed molecular beam experiment can be calculated by multiplying the detector signal in V with the sensitivity factor, which is 0.09 $\mu J/V$ in the this case.

Abbildung 5.3: In situ calibration of the SCAC detector signal: (a) Voltage of the photodiode detector during impingement of the laser beam and (b) correlation between the heat release on the sample and the detector voltage

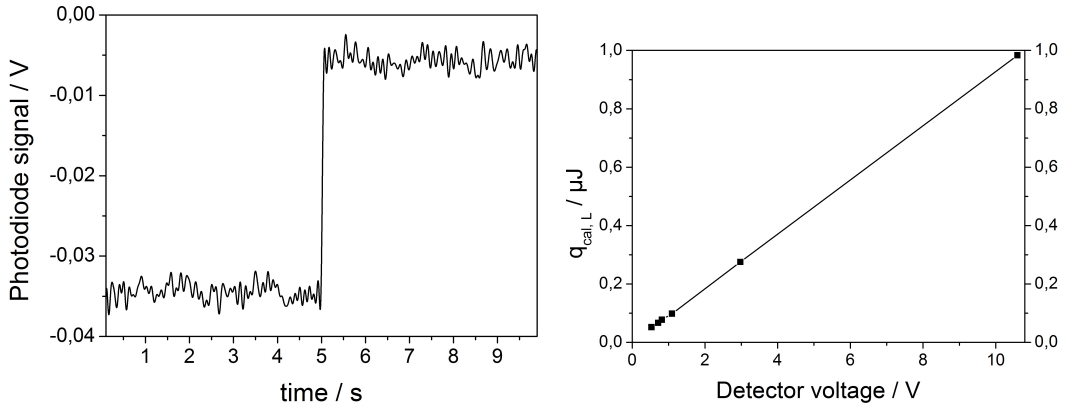

(a) (b)

5.2 Sticking coefficient

In general, the sticking coefficient strongly depends on the coverage, therefore, an exact measurement of the fraction of adsorbed molecules versus the pulse number is necessary to evaluate the heat release per unit of molecules and the coverage.
For many large organic molecules on cold surfaces, however, the sticking coefficient is one and independent of the coverage. In this case, the number of adsorbed molecules can be determined without performing a sticking coefficient measurement, if the molecular flux has been determined. To calculate the coverage, the number of adsorbed molecules in a filled monolayer has to be known. If this number is not known or adsorption in multilayer occurs, I will refer to the number of adsorbed molecules or number of adsorbed atoms instead of the coverage.
In cases, where the sticking coefficient is non unity and coverage dependent, the King-Wells sticking coefficient is evaluated as discussed in section 3.3. Therefore, the QMS signal taken for this evaluation is filtered with a median filter, which replaces each data point with the median of 5 circumjacent data points and a frequency filter, that removes frequencies which are higher than 4 Hz. This significantly reduces the noise and facilitates the evaluation of the signal. Figure 5.4 shows the original signal (gray) along with the filtered QMS signal (black). Not only the noise is removed by using the data processing procedure, but also the signal shape is influenced. Therefore, several tests with different data sets were performed to confirm, that the accuracy is not influenced by the filtering procedure.
A small amount of gas exits the molecular beam in case the chopper is closed but the gas inlet to the molecular beam is open. Although the flux on the sample is only 1-2 % compared to the flux in case of an open chopper, a noticable rise in the background pressure can be detected in this case. This background is substracted from the QMS signal before the analysis.
Fig. 5.5 shows a schematic representation of QMS signals, which are processed to determine the King-Wells sticking coefficients. In principle, the sticking coefficient can be obtained by

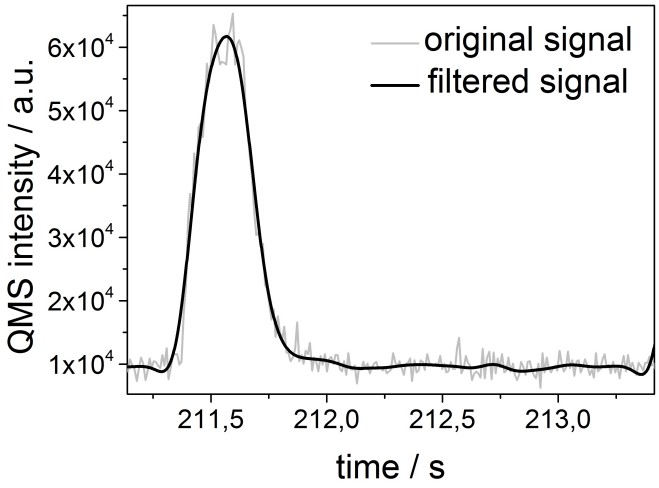

Abbildung 5.4: QMS signal during pulsing on a Pd(111) crystal surface with a chopper opeing time of 266 ms compared with the filtered signal used for the evaluation

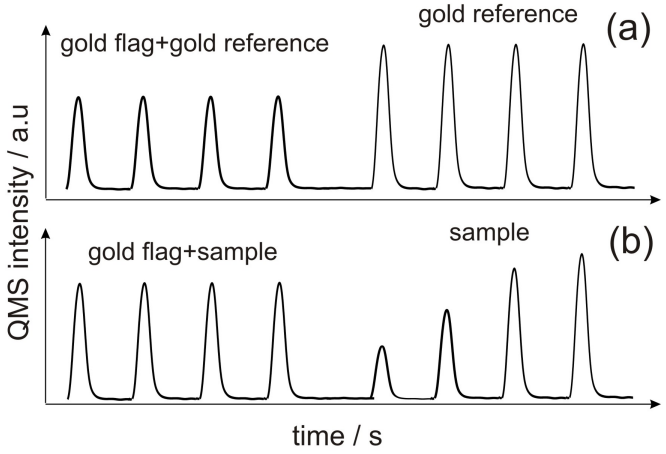

Abbildung 5.5: Schematic representation of the QMS signal during a pulsed molecular beam experiment on the gold flag/gold reference (a) and on the gold flag/reference (b)

calculating the difference QMS signals from sample and gold flag. However, the slightly different position of sample and gold flag lead to different scattering conditions for the two cases. Therefore, a systematic error would be introduced when using this procedure. To take this into account, a separate measurement with a gold reference is performed [194]. The sticking probability S versus the pulse number i can be calculated as follows:

$$S_i = \frac{\int_{i \cdot t_0}^{i \cdot t_0 + t_{end}} (I_{goldfl} - I_{sample})}{F_{corr} \int_0^{t_{end}} I_{goldfl}} \tag{5.2}$$

I_{goldfl} is the average intensity of all pulses on the gold flag and I_{sample} is the signal intensity on the sample. The correction factor F_{corr} includes the above mentioned correction due to the different scattering geometries during measurement with the gold flag and with the gold reference. t_0 is the time between two pulses (typically 2000 ms), t_{end} is the time until which the integration is performed. Accordingly, the sticking coefficient can be calculated versus the pulse number with Equ. 5.2 after integration over the QMS signals from sample, gold flag and gold reference.
For the choice of t_{end}, two cases have to be considered. If the pulse shape from the sample and the gold flag are identical, as depicted in Figure 5.7a (a), t_{end} can be chosen arbitrarily as long as $t_0 \geq t_{end} > 0$.
Figure 5.7b (b) shows a case, where the QMS signal shapes from sample and gold reference are

Abbildung 5.6: Comparison of the QMS signal shape during a pulsed molecular beam experiment on the sample and on the gold reference: (a) O_2 adsorption on Pd(111) at 300 K (b) CO adsorption on 1.5 Å Pd/Fe_3O_4 at 110 K

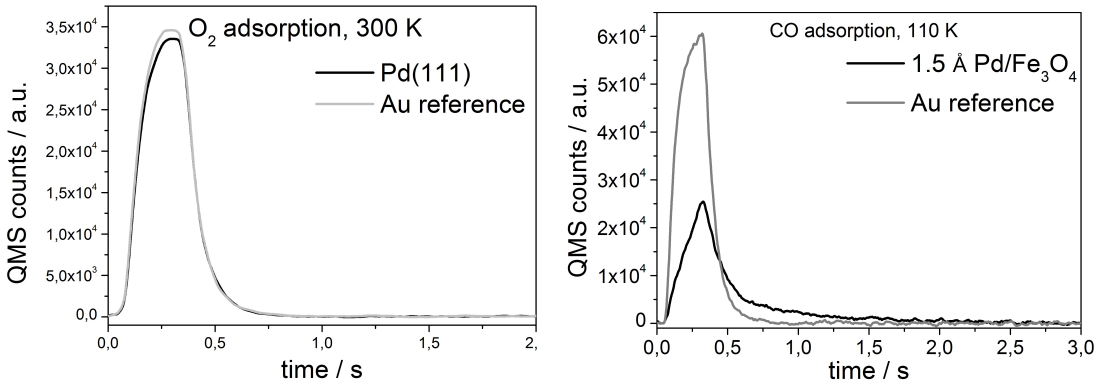

(a) (b)

significantly different. Such a situation can arise, when molecules desorb in between the pulses from the sample. In the present work, such a behavior has only be observed for CO adsorption at low temperatures (≈110 K) and close to the saturation of the adsorption sites with CO.
Campbell et al. described a procedure in which they used two different procedures for the evaluation of the QMS data in an SCAC measurement in case transient adsorption/desorption occurs in the timescale of the pulse period. For the evaluation of the surface coverage, the sticking probability for a given pulse is defined as the fraction of the molecules, which have not desorbed from

the surface before the next pulse starts to hit the surface. Accordingly, $t_{end} = t_0$. This sticking probability has been defined as the long-time sticking probability [58].
For the determination of the adsorption heat per mole adsorbed, it has to be considered that molecules initially adsorb on the surface and deposit heat. However, some of these molecules desorb later while removing heat from the sample. These desorbing molecules only influence the peak height if they desorb in between the beginning of the pulse and the time when the pulse maximum is reached, as only this time frame in the SCAC signal is used to determine the adsorption heat. Accordingly, integration of the QMS signal is performed from the beginning of the pulse until the maximum of the pulse,

$$t_{end} = t_0 + pt \tag{5.3}$$

where pt is the time until the pulse maximum. The sticking probability, calculated by this procedure has been defined by Campbell et al. to be the short-time sticking probability [58]. As the effect of molecules, which desorb in between the pulses close to saturation cannot be fully taken into account by determining the long-time sticking probability. Accordingly, an error in the determination of the number of adsorbed molecules is introduced. In that case, the determined number of adsorbed molecules is not accurate at high surface coverages where desorption of molecules between the pulses is significant.
The long-time and the short-time sticking coefficients coincide in the low coverage regime. At high coverages, however, the long-time sticking coefficient is lower compared to the short-time sticking coefficient due to desorption in between the pulses. An example is shown in Fig. 5.7, where the long-time and the short-time sticking probability for CO on 1.5 ÅPd/Fe_3O_4, measured at 110 K is plotted as a function of number of adsorbed molecules.
It should be mentioned, that Campbell et al. made an additional correction for the sticking probability in case the line shape of the heat signal changes due to transient adsorption/desorption [58]. This sticking probability has been termed the weighted short-time sticking probability. As a change in the line-shape of the SCAC signal has never been observed in our experiments, this correction has not been applied in the current work.

Abbildung 5.7: Short-time and long-time sticking probabilities for CO adsorption on 1.5 Å Pd/Fe3O4 at 110 K as a function of the number of adsorbed CO molecules

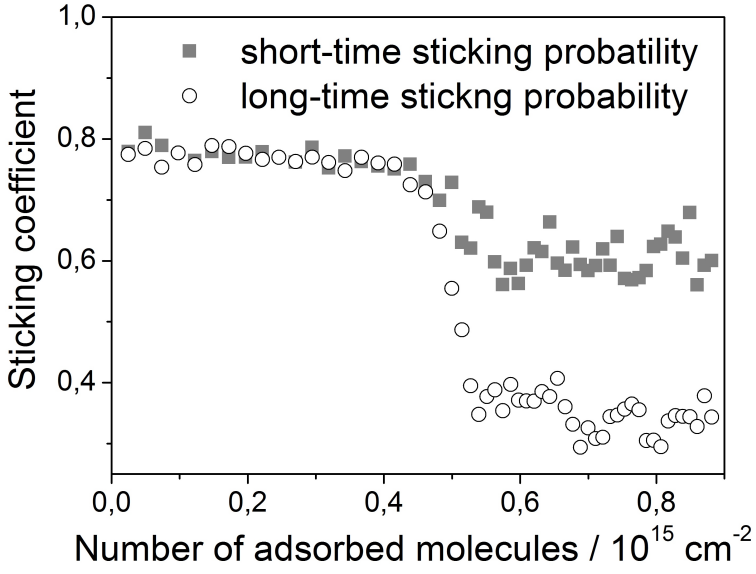

5.3 Determination of the adsorption energy and the adsorption enthalpy

According to the first law of thermodynamics, the change in the internal energy ΔU is the difference between the heat, supplied to the system and the work, which is exerted by the system. For a microcalorimetric measurement, the determined heat q_{cal} has the same modulus than the internal energy change of the system, ΔU. This change in the internal energy can be separated into two contributions due to the change in the energy of the adsorbing molecules (-ΔU_{ads}) and of the molecules, which are scattered from the surface (-ΔU_{refl}) [58].

$$q_{cal} = -\Delta U = -(\Delta U_{refl} + \Delta U_{ads}) \tag{5.4}$$

Considering, that the heat capacity of a flux of molecules is 1/2 R larger as that of a corresponding volume of an ideal gas [173], the energy change on the sample due to the molecules being reflected from the surface is given as follows:

$$\Delta U_{refl} = -N_{refl} \int_{Tsample}^{Tsource} dT\,(C_v + 1/2R) \tag{5.5}$$

N_{refl} is the number of reflected molecules (in moles), C_v is the heat capacity at constant volume. The assumption, that all molecules, being scattered from the surface, are thermally accommodated with the surface, is implicit in this formula. The energy difference between the adsorbed species and a flux of gas at 1 bar pressure and the sample temperature, ΔU^0_{ads}, is related to the

measured energy contribution ΔU_{ads} by the following equation:

$$\Delta U_{ads} = \Delta U^0_{ads} - N_{ads}\left(1/2RT_{source} + \int_{Tsample}^{Tsource} dT \cdot C_v\right) \tag{5.6}$$

The summand $-1/2N_{ads}RT_{source}$, in which N_{ads} is the number of adsorbed molecules in moles, arises because of the difference in the energy of a directed and a non directed volume of gas. The third term arises due to cooling/heating of a volume of molecules from the temperature of the beam source to the sample temperature. By inserting 5.6 and 5.5 into 5.4, it is straightforward to obtain U^0_{ads} from the measured calorimetric heat q_{cal} by dividing by the number of adsorbed molecules. The constant volume heat capacities for the molecules, which are used in this work can be found in [195].
For the case, that the gas temperature and the surface temperature are the same, the measured heat and the adsorption energy per mole of adsorbed molecules differs by $1/2$ R T, which is $\sim$1 kJ/mol. As this difference is small in comparison with the magnitude of the measured energies, this contribution is neglected in the following.

$$E_{ads} = \frac{U^0_{ads}}{N_{ads}} \tag{5.7}$$

After dividing by the number of adsorbed molecules, U^0_{ads} is normalized to Joules per mole. The standard enthalpy of adsorption includes the pressure volume work. Due to the adsorption process, $\Delta(pV) = -RT$. Thus, the standard enthalpy of adsorption can be calculated as follows.

$$\Delta H_{ads} = E_{ads} - RT \tag{5.8}$$

In general, I refer to the adsorption energy in the following, which I define here as the negative of the standard energy of adsorption, -U^0_{ads}.

5.4 Determination of the desorption prefactor

In cases, where the temperature of the measurement is similar to the desorption temperature of the molecules from the sample, molecules adsorb during the pulse (while the chopper is open) and desorb in between the pulses (while the chopper is closed). The gradual decay of the QMS signal to the background level occurs due to desorption of molecules from the active surface area. As this QMS signal is to a first approximation proportional to the desorption rate from the surface, it can be used to determine the desorption rate constant: the determination of the desorption rate constant/preexponential factor for desorption will be the subject of this chapter. Such an experiment is comparable to molecular beam relaxation spectroscopy [30, 50], in which information on the desorption energy and the preexponential factor is extracted from investigating the desorption transient with molecular beam techniques at temperatures close to the desorption temperature of the adsorbent.
In Figure 5.7b (b), the QMS pulses on the sample and the gold reference are compared for the conditions, where desorption in the timescale of the pulse period occurs (CO desorption from Pd/Fe_3O_4 at high coverages, low temperatures). The time dependent QMS intensity, which is

measured while molecular pulses impinge on the sample is differs from the QMS intensity, which is measured while pulses impinge on the gold reference: it is lower at t<300 ms due to adsorption and higher at 450ms<t<2000ms due to desorption from the sample. Kinetic information on the adsorption and the desorption process are included in these slowly varying parts of the pulse.
It will be explained in the following, how the desorption rate can be determined from the QMS data if desorption from the sample in between the pulses is significant. This analysis implies the following assumptions: The order of the desorption process is known and the coverage dependence of the desorption rate can be be neglected for the increase in the adsorbate coverage within one pulse.
A slow decay of the QMS signal after the chopper closes may not only be caused by desorption from the sample but may also arise due to the chamber behavior. As the signal decay due to the chamber behavior also occurs on the gold reference, the time dependent QMS intensity that is measured on the gold reference is substracted from the QMS intensity, measured on the sample. In this way, the chamber behavior is removed from a further analysis. In a first step, the area of the QMS peak which is measured on the gold reference is normalized to the area on the QMS peak, measured on the sample:

$$I_{gold,norm} = \frac{\int_{t_1}^{t_2} I_{sample}}{\int_{t_1}^{t_2} I_{gold}} I_{gold} \tag{5.9}$$

In Equ. 5.9, $I_{gold,norm}$ is the normalized QMS intensity on the gold reference and I_{gold} is the measured QMS intensity on the gold reference. t_1 is the beginning of the pulse and t_2 is the end of the pulse. To obtain the adsorption/desorption rate from the sample $I_{ads,des}$, $I_{gold,norm}$ is substracted from QMS intensity on the sample:

$$I_{ads,des} = I_{sample} - I_{gold,norm} \tag{5.10}$$

I_{sample} and $I_{gold,norm}$ are plotted together with $I_{ads,des}$ for the example of CO adsorption on 1.5 Å Pd/Fe_3O_4 in Fig. 5.8 .
For the case of a first order desorption process, $I_{ads,des}$ is proportional to the desorption rate between the time when the chopper closes until the time, when the next pulse hits the surface. The desorption rate $\partial[A]_{des}/\partial t$ can be expressed as,

$$\frac{\partial[A]_{des}}{\partial t} = -\frac{\partial[A]_{ads}}{\partial t} = k_{des} \cdot [A]_{ads} \tag{5.11}$$

where $\partial[A]_{des}/\partial t$ is the desorption rate, k_{des} the desorption constant and $[A]_{ads}$ the surface concentration of the adsorbate. It has to be mentioned, that k_{des} is a function of the coverage and with that also of t. However, the increase in the coverage within one pulse is typically 1-2 % and the approximation, that k_{des} is approximately constant within this coverage regime is usually good.v It is assumed in the following, that k_{des} is independent of the coverage within the coverage increase of one pulse.
By integration with respect to $\partial[A]_{ads}$ and ∂t and subsequent derivation with respect to t, one

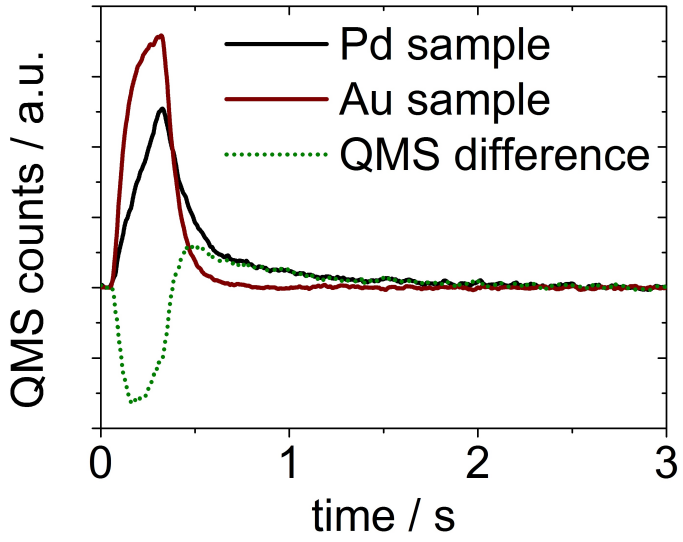

Abbildung 5.8: QMS signal during the impingement of molecular pulses on the sample (black line) and on the gold reference (dark grey signal). The dotted signal represents the difference of the two signals ($I_{ads,des}$).

obtains the following equation:

$$\frac{\partial [A]_{ads}}{\partial t} = [A]_{ads,0} \cdot k_{des} \cdot Exp[-k_{des} \cdot t] \tag{5.12}$$

After conversion, this equation yields:

$$Log\left(\frac{\partial [A]_{des}}{\partial t}\right) = Log\left([A]_{ads,0} \cdot k_{des}\right) - k_{des} \cdot t \tag{5.13}$$

Consequently, by plotting an observable, which is proportional to the desorption rate versus the time, the desorption constant can be determined. The difference between the QMS intensity on the sample and on gold, plotted as a dotted line in Figure 5.8 is such an observable. Figure 5.9 shows a corresponding plot of $Log(\partial [A]_{des}/\partial t)$ versus the time: the slope, determined from the the shown linear fit, equals k_{des}.

For first order adsorption/desorption processes, it can be anticipated, that the adsorption energy equals the desorption barrier due to the low activation energy for desorption processes, which is assumed here. As the adsorption energy is determined in the microcalorimetric measurement, the preexponential factor ν_{des} for desorption can be determined from the desorption rate constant by using the Arrhenius equation.

$$k_{des} = \nu_{des} \cdot Exp\left(\frac{-E_{des}}{kT}\right) \tag{5.14}$$

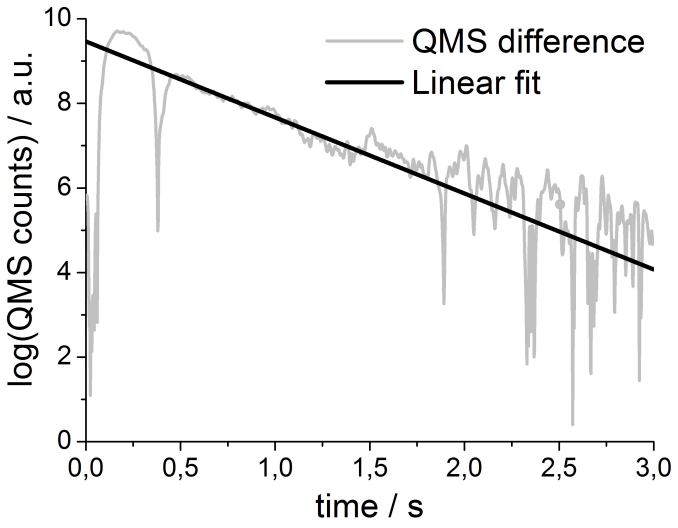

Abbildung 5.9: Plot of the Logarithm of the difference QMS signal, plotted in Figure 5.8, versus the time and a corresponding linear fit to obtain k_{des}

6 Pd particles on Iron oxide supports

Structural studies in combination with reactivity measurements on single crystal surfaces are essential for the understanding of heterogeneous catalysis. Despite the importance of such investigations, single crystals only poorly resemble industrial catalysts, which mostly consist of supported nanoparticles in the size range 3-20 nm [3]. These catalysts exhibit various additional features including different sites, support effects, size effects and many more. As the high degree of structural complexity in these systems makes atomistic-level studies difficult, model systems have been developed on which the interplay between structure, adsorption properties and reactivity can be investigated. Model systems closely resemble industrial catalysts but a higher control of the chemical composition and the structure compared to industrial catalysts is possible. Such systems can be oxide single crystals [16], ordered oxide films which are grown on metal substrates [17–21] or well defined metal nanoparticles, grown on oxide substrates [19, 22]. They usually exhibit a homogeneous, planar surface structure, and the thickness of the insulating oxide films is generally small to allow for tunneling of electrons through the oxide. Thus, standard surface science techniques can be applied to investigate these systems [21].
Model systems in general will be introduced in the first section and information on the properties of Fe_3O_4 model catalysts will be given. Subsequently, the preparation and structural properties of Pd/Fe_3O_4 systems, used in the present work will be explained. In the end of this chapter, it will be shown how structural information on Pd/Fe_3O_4 catalysts can be used to model some of its properties on the nanoscale.

6.1 Introduction

Model systems generally exhibit many features of industrial catalysts and they were designed to allow the study with surface science techniques.
To address fundamental questions on the catalysis of nanodispersed metals supported on oxides, metals can be vapor deposited from the gas phase onto well defined oxides under UHV conditions. To overcome the problem, that the use of electron and ion spectroscopic techniques is generally restricted on insulating oxides, the preparation of thin oxide films was developed through which electrons are able to tunnel. These oxide films, which are usually grown in situ can be obtained by oxidation of the host metal or metal alloys as for the growth of Al_2O_3 on NiAl alloys [196–198] or the growth of NiO on Ni substrates [199, 200]. In many cases, the preparation relies on the evaporation of a metal on a host crystal. The oxide is formed by annealing at elevated temperatures in an ambient oxygen atmosphere. In general, a low lattice mismatch between oxide and host crystal is favorable for the structural properties of the oxide.
Such supported systems exhibit a wide range of new features compared to single crystals, the most important ones are represented in Figure 6.1 together with a schematic representation of

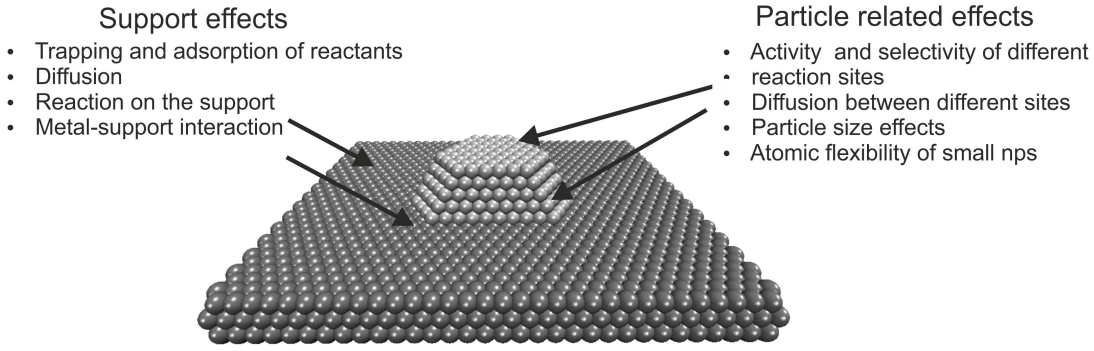

Abbildung 6.1: Schematic illustration of the most important features of supported systems with in comparison to single crystals

a supported particle. Supported catalysts display different facets, edge sites, corners and defect sites. The adsorption and reaction properties differ on the various surface sites.Adsorption sites are not independent from each other and diffusion between them can additionally influence the reactivity as observed by Libuda et al. in the transient experiments of the CO oxidation reaction on Pd/Al_2O_3 [78, 79]. The different geometric and electronic structure of supported particles compared to single crystals might strongly influence the reactivity, these differences are most prominent for small particles. For example, it has been observed, that particles with a smaller diameter than 4 nm, supported by mica [20, 201, 202], MgO [203] or γ-Al_2O_3 [29, 44, 72, 74] partially dissociate CO, whereas this has not been observed for larger particles. In addition, the support may influence the reactivity of the supported nanoparticles by the metal-particle support interaction [29, 204] or by diffusion of reactants from the oxide (so called capture zones) to the catalytically active metal [29, 73, 75]. Examples for the strong influence of the latter process on the reaction kinetics of the CO oxidation reaction on supported Pd particles can be found in [27, 46, 50, 73, 205].
The metal support interaction might strongly influence the reactivity and shape of the Pd nanoparticles [44], strong metal support interactions may even lead to the encapsulation of metal nanoparticles by the oxide [206–211].
The preparation and growth of the Fe_3O_4 film on a Pt(111) substrate has been discussed in detail in the literature [212–218]. A clean Pt(111) crystal is cleaned by repeated cycles of sputtering

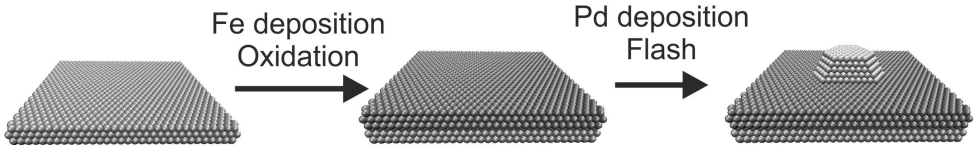

Abbildung 6.2: Schematic illustration of the preparation of supported model catalysts, more detailed information is in the text

with Ar^+ ions, oxidation at $\sim$1000 K and annealing at $\sim$1250 K.
The catalyst preparation, which follows this cleaning step is schematically shown in Figure 6.2.

Step 1 represents the preparation of the oxide. Starting from a clean Pt sample, the Fe_3O_4 film is prepared by repeated cycles of Fe deposition and oxidation. In the present setup, the deposition has been performed at ≈110 K, initially 1 ML of Fe has been deposited. After oxidation for 5 minutes at 1000 K with an oxygen pressure of $P_{O2}=10^{-6}$ mbar, the sample is cooled in O_2. Subsequently, six cycles of 4 Å iron deposition at ≈110 K and oxidation at T≈875 K in P_{O2}=5-10 10^{-7} mbar are performed to obtain a ≈ 50 Å thick Fe_3O_4 film.

The Fe_3O_4 film has been characterized in detail using several surface science techniques. After deposition of 1 ML Fe and subsequent oxidation, a Morié pattern, corresponding to the FeO(111) structure is formed. The LEED pattern which corresponds to this structure is shown in Figure 6.3 (a). This structure has been observed by various authors [47, 216, 217, 219], the oxygen layer on top is contracted by ≈0.6 Å compared to bulk FeO [215]. The LEED pattern of a typical Fe_3O_4(111) film, observed in the present studies is shown in Fig. 6.3 (b)

The deposition of a larger amount of Fe than necessary for the formation of a FeO(111) layer [214] leads to the growth of three dimensional Fe_3O_4 islands. After preparation of a 50 Å thick Fe_3O_4 layer, a closed, Fe_3O_4 film is formed. It consists of islands which are ≈50 nm wide with steps of ≈ 5 Å or a multiple of this height [47, 220].

It has been established by PES and XRD, that the deposited Fe_3O_4 forms an inverse spinell structure [215], in which the O^{2-} ions are arranged according to an ordered fcc lattice. The Fe^{3+} ions fill the tetraedric vacancies and the octaedric vacancies are filled with Fe^{2+} and Fe^{3+} ions. A schematic representation of this structure is given in Figure 6.3 (c).

The surface termination strongly depends on the preparation conditions [221]. Many authors found a structure in which 1/4 ML of iron ions over a closed oxygen lattice terminate the surface [47, 213, 216, 217, 222], both, the termination with Fe^{3+} and with Fe^{2+} has been suggested. Such structures have mainly been found, when the final oxidation step has been carried out at high temperatures (T=1000 K) or after annealing the prepared film in UHV at T=900-1000 K. Using lower oxidation temperatures of 870 K, also different structures which were often oxygen terminated were found [217, 223]. Sala et al. showed, that the surface of Fe_3O_4(111) oxide films, prepared by repeated cycles of Fe deposition and oxidation at elevated temperatures is terminated by 1/4 ML Fe ions after final annealing at 900 K in UHV [219]. A different surface termination has been observed before this final annealing step.

Abbildung 6.3: LEED image of FeO (a), LEED image of Fe_3O_4 (b) and a schematic representation of the inverse spinell structure of Fe_3O_4 (c)

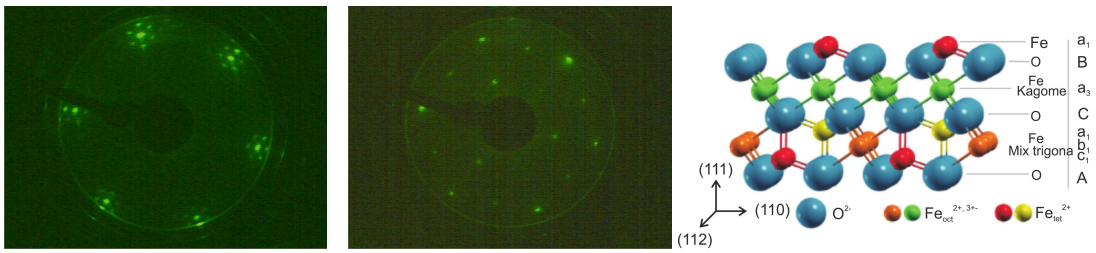

(a) (b) (c)

6.2 Pd particles supported on Fe_3O_4

Investigations on the morphology and reactivity of Pd/Fe_3O_4 catalysts, which have been prepared with the identical procedure as in our studies, have been performed by D. Starr et al. with STM [46–48]. Further studies on the adsorption properties and reactivity in the CO oxidation reaction have been done by Schalow et al. with molecular beam studies in combination with IRAS [46, 48, 83–87].
After preparation of the ≈50 Å thick Fe_3O_4 film as described above, Pd particles were formed by physical vapor deposition from an electron beam evaporator. During the deposition, the potential of the Pd rod is held at 800 V and the Pd ions are accelerated towards the sample. Hereby, the Pd coverage and thus the particle size is controlled by the deposition time. To avoid damaging of the surface by sputtering, the sample is held at a potential of 800 V. Subsequent to the Pd deposition, the crystal was heated to 580 K - 600 K.
Figure 6.4 shows the STM images for three different Pd coverages. The Pd particles are ran-

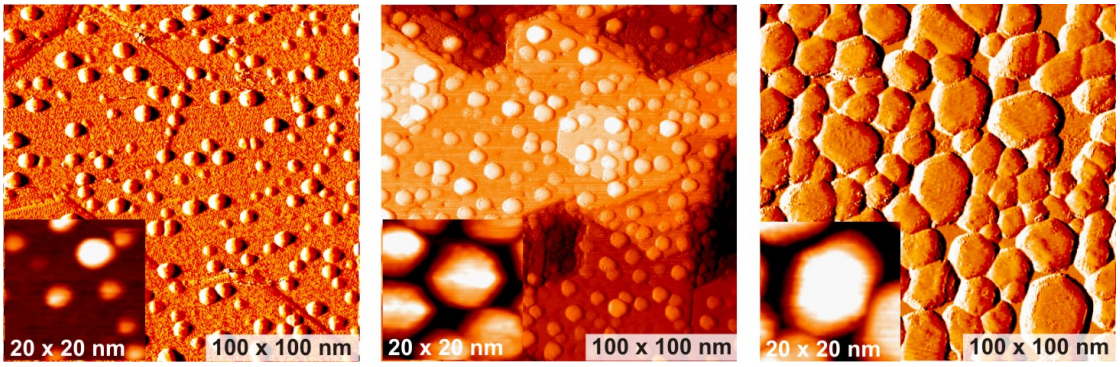

Abbildung 6.4: STM images of the Pd model catalyst supported on 50 Å Fe_3O_4/Pt(111) with different Pd coverages (a) 0.3 Å Pd (b) 4 Å Pd, (c), 7 Å Pd. The experiments were performed by D. Starr and S. Shaikhutdinov.

domly distributed on the substrate, no preferential decoration of step edges can be observed. The insets show close-ups of individual Pd islands. The nanoparticles, corresponding to a coverage of 7 Å and 4 Å Pd exhibit a hexagonal, crystalline shape with rather flat top facets. This indicates, that the particles grow in the (111) direction, accordingly, their sides are terminated by (111) or (100) facets. ≈ 80% of the particle surface is terminated by the (111) facet and 20% by the (100) facet. Measurements of the particle height for an intermediate particle size reveals, that the aspect ratio (height/diameter) is about 1/3.5 [46].
An important information from the STM images is the island density, which is given together with the number of Pd atoms per area in Table 6.1. At Pd coverages, which are smaller than 4 Å, an increasing metal coverage leads to further nucleation of Pd particles and thus to a higher particle density. For Pd coverages, which are larger than 4 Å, coalescence leads to the formation of large, elongated crystallites. No STM experiments have been performed for Fe_3O_4 oxides with the deposition coverages 0.6 Å Pd and 1.5 Å Pd. To a first approximation, the particle density can be assumed to increase linearly with the deposition coverage for low Pd coverages [21]. Accordingly, the particle density for the intermediate deposition coverages were estimated.

Nominal Pd coverage	0.3 Å	0.6 Å	1.5 Å	4 Å	7 Å
Nominal Pd coverage / atoms cm^{-2}	$2 \cdot 10^{14}$	$4 \cdot 10^{14}$	$1 \cdot 10^{15}$	$2.7 \cdot 10^{14}$	$4.8 \cdot 10^{15}$
Island density / cm^{-2}	$1.7 \cdot 10^{12}$	$1.9 \cdot 10^{12}$	$2.4 \cdot 10^{12}$	$3.8 \cdot 10^{12}$	$1 \cdot 10^{12}$
Number of Pd atoms per particle	120	218	429	716	4762
Average Pd particle diameter [1]	1.9	2.3	2.9	3.4	6.4
Surface Pd atoms atoms [2] / cm^{-2}	$1.6 \cdot 10^{14}$	$2.7 \cdot 10^{14}$	$5.3 \cdot 10^{14}$	$12 \cdot 10^{14}$	$11 \cdot 10^{14}$
Pd atoms at edges[2] / cm^{-2}	$9.9 \cdot 10^{13}$	$1.3 \cdot 10^{14}$	$2.1 \cdot 10^{14}$	$4.0 \cdot 10^{14}$	$2.0 \cdot 10^{14}$

Tabelle 6.1: Structural data of the Pd/Fe_3O_4 model catalyst. The Pd coverage and the particle density were determined experimentally. The particle diameter, the number of surface atoms per particle and the number of Pd atoms on edge sites were obtained by assuming a particle shape

The structural properties, obtained by using this assumption are shown in a gray color in Table 6.1.
Dividing the Pd coverage by the island density, obtained from the STM images, the number of Pd atoms per particle, shown in Table 6.1 is obtained. Assuming a halfspherical particle shape, the particle volume and the diameter can be calculated from the number of Pd atoms per particle (the contraction of nanoparticles has been disregarded for these estimations).
The particle diameter, shown in Table 6.1 is a convenient number to express the particle size. However, care has to be taken to not confuse it with the particle diameter in the surface plane. STM experiments show, that the aspect ratio for intermediate Pd nanoparticles is 1/3.5. Thus a better approximation for the particle shape is a half oblate spheroid. The according diameter in the surface plane is 21 % larger compared to the one calculated with a hemispherical particle shape. In principle, the particle diameter could be also obtained from the STM experiments, however, the tip convolution effect would lead to inaccurate results.
The number of surface atoms per nanoparticle, shown in Table 6.1 is calculated by using the shape of a truncated triangular pyramid. This choice is somewhat arbitrary but the difference in the surface area between different particle shapes is expected to be small (the surface area using an half oblate spheroid is 20 % smaller).
It is interesting to consider how many of the surface Pd atoms correspond to atoms on edge sites either on the particle support boundary or between the different facets. This number is shown in the last row of Table 6.1. A differentiation between facet sites and edge sites only makes sense for the largest Pd particles. For the deposition coverages 0.3 Å and 0.6 Å Pd, the number of edge sites is comparable to the total number of adsorption sites per unit area, the surface is expected to be rather homogeneous in these cases. This is indicated in the STM experiments shown in Figure 6.4, where the smaller particles rather exhibit a round shape in contrast to the hexagonal shape of larger particles, which are terminated by facets.

[1] these properties were calculated assuming a halfspherical particle shape
[2] these properties were calculated assuming the shape of a truncated triangular pyramid

7 Interaction of CO and O_2 with the support

The interaction of CO and O_2 with Fe_3O_4 influences the adsorption kinetics of both molecules on Pd/Fe_3O_4, which in turn affects the reactivity in the CO_2 evolution reaction.
In this chapter the experimental data is discussed which was obtained on the influence of the support on the CO and O_2 adsorption properties on Pd/Fe_3O_4. After a short literature summary on the interaction of CO and O_2 with oxides and the capture zone effect, the results of the SCAC measurements of CO and O_2 on Fe_3O_4 will be discussed. Subsequently, the initial sticking coefficients of CO and O_2 on Pd nanoparticles of different sizes will be explained with a model, which includes a direct and an indirect adsorption channel, the latter proceeding via trapping on the Fe_3O_4 support.

7.1 Introduction

Table 7.1 summarizes some literature data on the adsorption properties of CO on different oxides. Column three of Tab. 7.1 shows that E_{ads} on these oxides is 10-30 kJ/mol. As a comparison, the adsorption energy of CO on group ten elements is >100 kJ/mol [132]. These low adsorption energies on oxides result in a non-permanent adsorption of O_2 on the oxides, shown in Tab. 7.1 at 300 K. Nevertheless, to understand the reactivity of supported nanoparticles at elevated temperatures, it is essential to obtain information on the interaction of the reactants with the support. Ladas et al. observed in 1981, that the CO oxidation rate increases with decreasing particle size on Pd nanoparticles of the size range 1.5 nm - 8 nm, supported on polycrystalline α-Al_2O_3. This which was originally attributed to the higher sticking probability on irregular sites, which are more prominent on small particles [25]. Matolin et al., who observed the same trend, proposed that the effect arises from trapping and diffusion of reactants from the support to the particles [28]. Other observations of reactant diffusion from the support to the catalytically active metal can be found in the works of Henry and Chapron on the study of CO adsorption on supported catalysts [26, 27]. Boudart et al. carried out quantitative studies, where the model of circular collection zones around the Pd particles was applied to fit the CO oxidation rate in the temperature range 550 K - 650 K [227]. Since then, numerous studies with more advanced models have been carried out. These studies demonstrate that the adsorption and reaction properties of supported catalysts are significantly altered by reactant diffusion from the support to the active metal.
Table 7.1 displays the CO adsorption probability on Pd ($S_{Pd}(0)$) and the CO trapping probability on the oxide (α_{oxide}) from some of the literature results. The former was either assumed to be unity or the same as that on Pd(111), whereas the latter has been obtained by modeling the experimental data.
As can be seen, the trapping probability largely varies on different oxides. More detailed information on the mechanism of adsorption via trapping on the capture zone will be given below.

System	$S_{Pd}(0)$	α_{oxide}	$E_{des,oxide}$	X_D	Ref.
MgO(100)	1	0.50	13.8 kJ/mol	38 nm	[20, 50]
α-Al_2O_3	1	0.46	31-41 kJ/mol	35 nm	[27]
TiO_2(110)	0.5	0.18	38 kJ/mol	-	[207]
α-Al_2O_3(0001), oxidized	0.93	0.68	20-28 kJ/mol	9 nm	[75]
α-Al_2O_3(0001), annealed in HV	0.93	0.4	15-20 kJ/mol	3 nm	[75]
α-Al_2O_3(0001), sputtered	0.93	0.46	11-14 kJ/mol	2 nm	[75]
α-Al_2O_3(0001), reduced	0.93	0.73	28-38 kJ/mol	35 nm	[75]
Fe_3O_4(111)	-	-	28 kJ/mol	2 nm	[47, 87]
γ-Al_2O_3	0.96	1	16-21 kJ/mol	4 nm	[224]
α-Al_2O_3, oxidized	0.96	1	17-22 kJ/mol	4 nm	[224]
α-Al_2O_3(0001), annealed in HV	0.93	1	13-17 kJ/mol	2 nm	[224]
α-Al_2O_3(0001), sputtered	0.93	1	13-17 kJ/mol	2 nm	[224]

Tabelle 7.1: Literature data on the diffusion and adsorption properties of CO on different oxides at 300 K on which Pd nanoparticles were deposited. $S_{Pd}(0)$ is the initial sticking probability on Pd, α_{oxide} is the trapping probability on the oxide, E_{des} the energy of desorption from the oxide, X_d is the mean diffusion length of CO on the oxide and Ref. is the reference from which the results were extracted. The entries in gray have been estimated in the present work by assuming that the activation energy for diffusion is in between 0.12 and 0.33 of the activation energy for desorption [225, 226].

7.2 SCAC experiments on Fe_3O_4

In this section, CO adsorption on Fe_3O_4 studied with SCAC at 110 K will be discussed. The preparation and cleaning of the Pd/Fe_3O_4 model catalyst has been discussed in the previous chapter. Figure 7.1 shows the CO sticking coefficient (7.1 (a)) and the adsorption energy (7.1

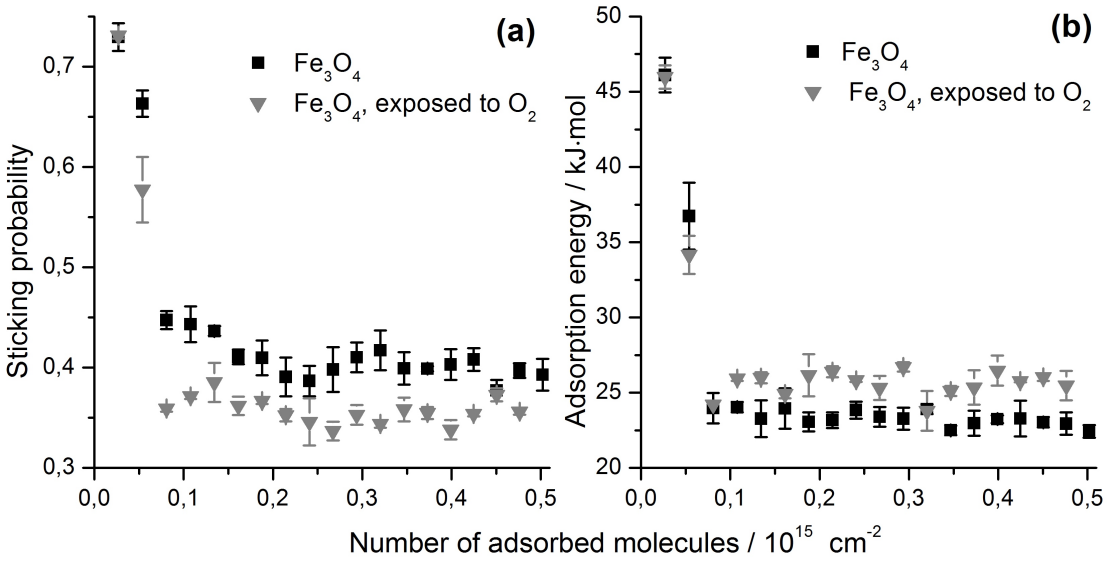

Abbildung 7.1: The initial sticking coefficient (a) and the Adsorption heat of CO (b) as a function of the number of adsorbed molecules on Fe_3O_4. The black square scatters shows the results on Fe_3O_4 as prepared, the results indicated by the gray triangular scatters were obtained after exposure to $4{\cdot}10^{16}$ mbar at 300 K. The error bars correspond to the error of the mean

(b)) on Fe_3O_4 as a function of the number of adsorbed CO molecules at ≈110 K. As discussed in Chap. 5.2, the sticking coefficient decays to a constant, nonzero value in cases where adsorption/desorption occurs in the timescale of the pulse period close to saturation of the adsorption sites. This is the case here as discussed in more detail below.

The gray triangular scatters show the results of an analogue experiment after an exposure to $3{\cdot}10^{16}$ O_2 molecules cm^{-2} at 300 K. The shown data represents the average of typically three independent measurements. For these experiments, a CO flux of $1.2 \cdot 10^{14}$ molecules cm^{-2} s^{-1}, a chopper opening time of 266 ms and a pulse period of 2-2.5 s has been used.

Figure 7.1 shows, that exposure of the oxide to oxygen does not influence the properties of Fe_3O_4 with respect to CO adsorption. The CO sticking coefficient is initially 0.73 ± 0.01, decreases during the first three CO pulses and reaches a steady-state value of ≈0.38.

By comparing the QMS pulse shape on Fe_3O_4 and on the gold reference, it is evident that transient adsorption/desorption in the timescale of the pulse occurs at high CO exposures. Therefore, the sticking coefficient does not decay to values lower than ≈0.38.The number of irreversibly adsorbed CO molecules is $6\pm1 \cdot 10^{13}$ molecules cm^{-2}. The initial adsorption energy is 46±1 kJ/mol and drops within three pulses to a value of ≈25 kJ/mol. If we assume, that CO-CO inter-

actions are negligible at such small coverages, these results suggest the existence of at least two different adsorption sites for CO.

Lemire et al. observed three TPD peaks after adsorption of CO on Fe_3O_4 with TPD maxima at 110 K (α-state), 180 K (β-state) and 230 K (γ-state) [47]. Based on the CO stretching frequencies, these peaks have been assigned to weakly bound, mobile CO (α-state), CO adsorbed on Fe^{2+} (β-state) and CO adsorbed on Fe^{3+}(γ-state), respectively. By using the Redhead assumption, the corresponding desorption energies of the 3 desorption peaks can be estimated as 28 kJ/mol (α-state), 46 kJ/mol (β-state) and 59 kJ/mol (γ-state) (the entry in Table 7.1 shows only the adsorption energy corresponding to the α-state). The desorption energy of the α-state is slightly higher than the bond energy of the weakly adsorbed species, observed in our SCAC experiments at the highest CO exposures. The adsorption energy of the β-state is in agreement with the more strongly bound CO species, observed in our experiments in the limit of zero CO coverage. The α-state desorption temperature (110 K) is similar to the temperature of our SCAC experiments, therefore, molecules adsorbing in this state are expected to desorb in between pulses in our experiments.

In many of the structural investigations of Fe_3O_4, a model in which the oxide is terminated by 1/4 ML iron ions on an oxygen layer was suggested [47, 213, 216, 217]. In the CO titration experiments of Shaikhutdinov et al., the β-state has been assigned to CO adsorption on regular Fe^{2+}-sites. Schalow et al. performed IRAS studies in combination with sticking coefficient measurements on hydroxylated and non-hydroxylated Fe_3O_4-films: based on these studies it was suggested that the β- and γ-state corresponds to CO adsorption on defect sites [221]. This would suggest a termination by oxygen ions, which has also been suggested in other studies [217, 223, 228]. It has been discussed in the previous chapter, that the surface termination is expected to be sensitively dependent on the preparation conditions.

That $6\pm1 \cdot 10^{13}$ molecules cm^{-2} adsorb permanently on the oxide could be explained with a surface that consists of two phases: one which is terminated by oxygen ions (82$\pm$3 %) and one which is terminated by iron ions (18$\pm$3 %). CO would occupy the iron sites on this phase but would not adsorb on the oxygen terminated phase at T$\geq$110 K. This would require however that the oxygen terminated surface would be absolutely defect-free, which is a very unlikely scenario.

The presence of 2 different phases agrees with the structural model of Sala et al. [219] proposed for similar preparation conditions as those which were used for the present work.

According to our data, the occupation of defect sites by the $6\pm1 \cdot 10^{13}$ more strongly adsorbed CO molecules per cm^{-2} is equally likely. In the latter case, the defect concentration would be 5$\pm$0.8 %. In both cases, no CO would adsorb on the major fraction of the surface, which suggests that this fraction (at least 82 %) is oxygen terminated.

In SCAC experiments on O_2 adsorption on Fe_3O_4 at 110 K, neither oxygen sticking on Fe_3O_4 nor a heat release could be detected. This shows that oxygen does not adsorb on Fe_3O_4 at 110 K.

As stated in section 5.4, the prefactor for desorption can be determined in cases where the measurement is carried out at temperatures which are similar to the desorption temperature of the adsorbate. This is the case for CO desorption from the adsorption state with an adsorption energy of $\approx$25 kJ/mol. To determine the desorption rate, it is assumed, that CO desorption is a first order process and that the coverage dependence of the desorption rate can be neglected. The

latter assumption is justified by the fact, that only $\approx 7 \cdot 10^{13}$ CO molecules adsorb on Fe_3O_4 during one pulse. For the determination of ν_{des}, it is assumed that the desorption energy equals the adsorption energy. From a plot of δ $CO_2/\delta t$ versus the time, a desorption rate of $k_{des}=2.1\pm0.2$ s^{-1} is calculated. Subsequently, the desorption prefactor is determined as $2 \cdot 10^{11}$ - $2 \cdot 10^{12}$ s^{-1}. Using this result to calculate the desorption energy of the α-state, introduced by Lemire et al., a desorption energy of 24-26 kJ/mol is obtained, which agrees with the adsorption energy of $\approx$25 kJ/mol, determined by SCAC for this state.

7.3 The capture zone effect for CO on Pd/Fe_3O_4

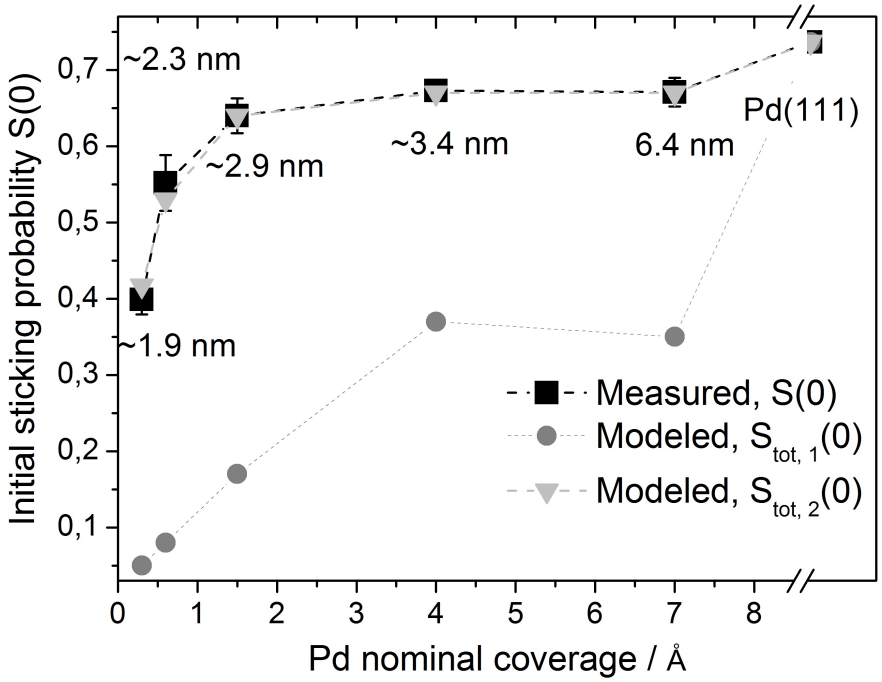

Abbildung 7.2: The initial sticking probability (black scatters) of CO on Pd/Fe_3O_4 and the corresponding modeled data (gray scatters), see text for details. The data shows the average of three to six independent measurements at 300 K, the error bars show the error of the mean.

As discussed in the introduction of this chapter, the sticking coefficient of molecules on supported particles can be significantly increased due to trapping of molecules on the oxide and diffusion to the Pd particles. Figure 7.2 shows the initial sticking coefficient of CO on Pd(111) and on Pd/Fe_3O_4 for the Pd deposition coverages 7 Å (6.4 nm), 4 Å (3.4 nm), 1.5 Å (2.9 nm), 0.6 Å (2.3 nm) and 0.3 Å (1.9 nm) [1]. This data, which has been measured with the present setup was obtained by J.-H. Fischer-Wolfarth and M. Flores [205, 229]. A molecular flux of $\approx$1.2

[1] The numbers in brackets indicate the average particle diameter

$\cdot 10^{14}$ molecules cm^{-2} s^{-1} and a shutter opening time of 266 ms has been used. Accordingly, the fraction of surface Pd atoms, which is covered by CO after the first pulse is typically a few percent. Therefore, one can assume, that the plotted initial sticking coefficient corresponds to the sticking coefficient in the zero coverage limit, S(0).
It is expected that the initial sticking coefficient of CO on Pd is structure insensitive. For modeling of CO sticking data on supported Pd nanoparticles, it is therefore usually assumed that the sticking probability on the Pd nanoparticles is the same as that on Pd(111) [29, 36, 73, 75, 207].Neglecting the capture zone effect, the CO sticking probability on Pd/Fe_3O_4 $S_{tot,1}(0)$ can be calculated in the following way,

$$S_{tot,1}(0) = S_{Pd}(0) \cdot F_{Pd} \tag{7.1}$$

where $S_{Pd}(0)$ is the initial sticking coefficient on Pd(111) and F_{Pd} is the fraction of the surface covered by Pd. $S_{Pd}(0)$ has been determined to be 0.74 ± 0.01 with the present setup on Pd(111) [205], F_{Pd} can be estimated based STM results, introduced in Section 6.2. The sticking probability of CO on the Pd nanoparticles of different sizes, estimated with Equ. 7.1 is shown in Fig. 7.2 (dark gray circles). For all particle sizes, the modeled initial sticking coefficient is much lower than the experimentally observed values (black squares). The large difference between S(0) and $S_{tot,1}(0)$ is because the capture zone effect has been neglected in this model.
In a second model for the initial CO sticking probabilities on Pd/Fe_3O_4, the capture zone effect has been included.
It has to be considered that a fraction of the CO molecules which impinge on the oxide diffuse to the Pd nanoparticles and are adsorbed on the Pd nanoparticles. In the following, this effect is taken into account by a simple model in which concentration gradients of the adsorbate on the oxide and a possible difference between the desorption prefactor and the prefactor for diffusion are neglected [2]. As discussed in the first chapter, the mean diffusion length of a molecule on a surface before desorption depends on the difference in the activation energy for desorption and diffusion and the hopping distance of the molecule on the surface. Accordingly, the mean diffusion length strongly depends on the composition of the surface and the temperature. In a simple model, it is assumed that molecules which impinge at a distance from the nanoparticles which is smaller than the mean diffusion length are adsorbed on the nanoparticles. Molecules which impinge at a distance to the nanoparticles which is larger than the mean diffusion length do not adsorb. This is equivalent to assuming a circular collection zone around the nanoparticles, molecules which impinge within this so called capture zone are adsorbed.
The initial sticking coefficient can be calculated as the sum of two contributions, adsorption via trapping on the capture zone and adsorption via direct impingement on Pd:

$$S_{tot,2}(0) = \alpha_{Fe3O4} \cdot F_{CZ} + S_{Pd}(0) \cdot F_{Pd} \tag{7.2}$$

α_{Fe3O4} is the trapping coefficient on Fe_3O_4 and F_{CZ} is the fraction of the surface that corresponds to the capture zone. $S_{tot,2}(0)$ is the initial sticking probability of CO on Fe_3O_4, calculated within this model. Here, the notation of Cassuto and King is applied, who use the letter S for sticking coefficients and α for trapping coefficients [156]. For case that the capture zone radius X_d is

[2] Modeling of sticking data with a more advanced model can be found in the literature [27, 230]

smaller than the distance between the particles, F_{CZ} can be calculated as follows:

$$F_{CZ} = N_{Pd} \cdot \pi \cdot ((r_{Pd} + X_d)^2 - r_{Pd}^2) \tag{7.3}$$

N_{Pd} is the Pd island density and r_{Pd} is the radius of the Pd nanoparticles. X_d is assumed to

Abbildung 7.3: Schematic illustration of the capture zone effect (a) large Pd particles with overlapping capture zones and (b) small particles with non overlapping capture zones (modeling of the S(0) values is performed by assuming an oblate particle shape)

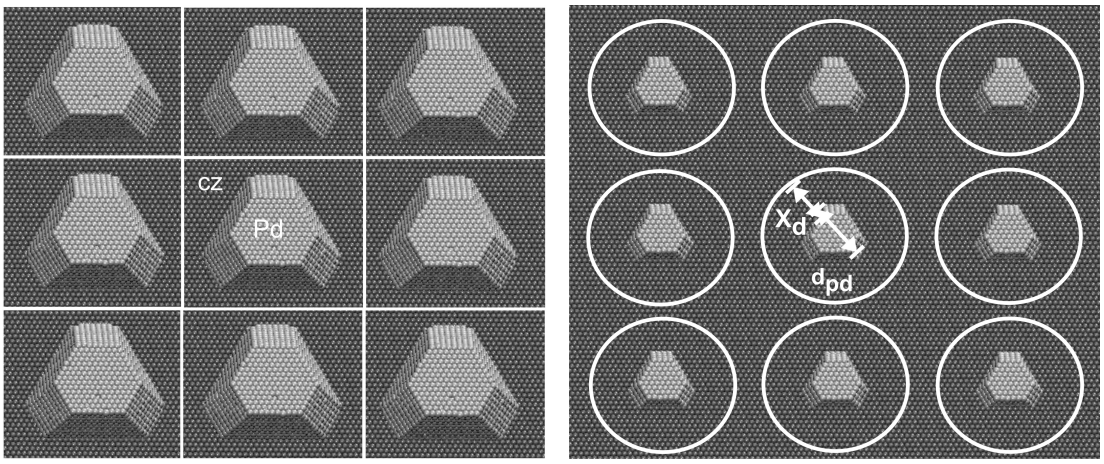

(a) (b)

be equivalent to the mean diffusion length of CO on the oxide. For the case that the distance between the Pd nanoparticles is small compared to X_d, the capture zones overlap and F_{Pd} is approximately the fraction of the surface which is not covered by Pd. The two situations are schematically shown in Figure 7.3 (a) and (b). In Fig. 7.3 (a), the distance between the Pd particles is small compared to X_d and thus diffusion from the oxide to the particles occurs from the whole fraction of the surface which is not covered by Pd. In Figure 7.3 b on the other hand, the situation is depicted where the distance between the particles is large in comparison to X_d. Diffusion from the oxide to the Pd particles occurs from a circular area around the particles.
In the following, the S(0) values for CO at 300 K on Pd nanoparticles of five different sizes is rationalized based on the capture zone model. Based on the structural properties of the various Pd/Fe_3O_4 systems, given in 6, F_{Pd} is determined. It is assumed that $S_{Pd}(0)$ equals the CO zero sticking probability on Pd(111), so only α_{Fe3O4} and r_{Pd} are to be varied to model the zero sticking coefficient of CO on Pd/Fe_3O_4.
In the following, it will be estimated if the capture zones completely cover the oxide surface for Pd nanoparticles with a deposition coverage 4 Å. Towards this goal, the distance between Pd nanoparticles is estimated. A uniform distribution of the Pd nanoparticles on the surface, as indicated in Fig. 7.4, is considered. In Fig. 7.4, the surface area per Pd nanoparticle is a^2, the radius of the Pd nanoparticles is r_{Pd} and the distance between second next nearest Pd nanoparticles is d_{Pd-Pd}. If d_{Pd-Pd} is smaller than the diffusion length of the adsorbates on the oxide, the capture

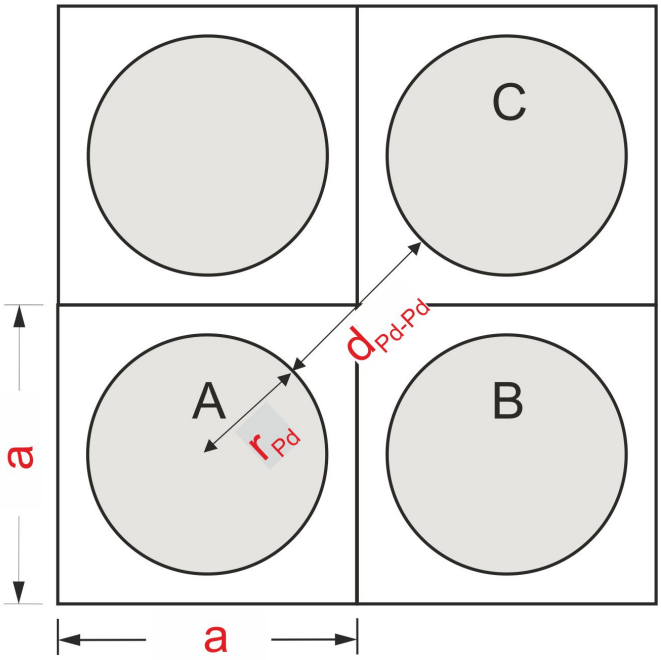

Abbildung 7.4: Catalyst with a uniform distribution of Pd nanoparticles to illustrate how the distance between neighboring Pd nanoparticles is determined. a^2 is the surface area per Pd nanoparticle, r_{Pd} the nanoparticle radius and d_{Pd-Pd} the distance between neighboring Pd nanoparticles

zones completely cover the oxide.
From the particle density $3.8{\cdot}10^{12}$ for the Pd deposition coverage 4 Å , the average surface area per nanoparticle is determined to be 5.13 nm^2. This area equals a^2 in Fig. 7.4. It has been discussed in Chapter 6 that the aspect ratio of the Pd nanoparticles was determined to be 1/3.5. Accordingly, r_{Pd} is the radius of an oblate shaped Pd nanoparticle with this aspect ratio. The distance between second next nearest Pd nanoparticles is given according to the following formula:

$$d_{Pd-Pd} = \sqrt{2} \cdot a - 2 \cdot r_{Pd} \tag{7.4}$$

For the deposition coverage 4 Å Pd, d_{Pd-Pd} is 3 nm. Accordingly, the capture zones completely cover the surface if $X_d \leq 1.5$ nm. Some values for X_d which have been determined in previous studies are displayed in Tab. 7.1 for CO. These values are all larger than 1.5 nm. Accordingly, it can be anticipated that the capture zones completely cover the oxide for that case. For the deposition coverage 7 Å Pd, a capture zone radius of $\sim$3 nm would be required in order that the capture zones cover the oxide completely. For this deposition coverage, the capture zones may only cover 75 %-95 % of the oxide.
Using equation 7.2 and assuming that the capture zones completely cover the oxide for the Pd deposition coverage 4 Å, the CO trapping coefficient on Fe_3O_4 (α_{Fe3O4}) is modeled to be 0.61. If the capture zones would overlap for all particle sizes, $S_{tot,2}(0)$ could not be smaller than 0.61, which is clearly not the case for the Pd deposition coverages 0.3 Å (1.9 nm) and 0.6 Å (2.3

nm). Having determined α_{Fe3O4}, X_d can be fitted to the S(0) values for the two smallest particle sizes. The obtained capture zone radius X_d is 2.4±0.3 nm. The modeled data compared to the experimental data is shown in Figure 7.2 with light, gray triangles. Considering, that only 2 parameters (α_{Fe3O4} and r_{Pd}) have been varied to model five data points, the agreement is surprisingly good.
Table 7.1 displays values for X_d, obtained by different groups. The capture zone radius of 2.4 nm obtained in this study is similar to the one determined by Matolin et al. on α-Al_2O_3 [75, 224] and is in good agreement with the estimation of Libuda et al. in [87]. The reported values for X_d from the studies of Henry et al. on α-Al_2O_3 and MgO are somewhat higher.

7.4 The capture zone effect for O_2 on Pd/Fe_3O_4

Figure 7.5 shows the initial sticking coefficient for O_2 on Pd(111) and on Pd/Fe_3O_4 for the Pd deposition coverages 0.6 Å (2.3 nm), 1.5 Å (2.9 nm), 4 Å (3.4 nm) and 7 Å (6.4 nm). The experiments were performed at 300 K with a molecular flux of $\approx 1.1 \cdot 10^{14}$ O_2 molecules cm^{-2} s^{-1} and a shutter opening time of 266 ms. The fraction of Pd surface atoms, covered after the first pulse is a few percent. Accordingly, one can assume, that the plotted sticking probability corresponds to an initial sticking coefficient in the zero coverage regime.
S(0)-values of 0.21-0.8 have been found for O_2 adsorption on Pd nanoparticles of different sizes, deposited on Al_2O_3 and MgO at 300 K [20, 50, 75, 207, 224]. The wide range of values can be explained by the strong correlation between S(0) and particle size/nature of the support. Therefore, only S(0)-values, measured at identical preparation conditions of the catalysts can be compared.
It is striking, that the initial sticking coefficients of 0.53 and 0.55 for the deposition coverages 7 Å Pd (6.4 nm) and 4 Å Pd (3.4 nm) are higher than the S(0) value of 0.47 on Pd(111). In the analysis of the CO sticking data, it has been assumed, that S(0) on Pd(111) and on the Pd particles are the same. When using the same assumption for the O_2 adsorption data, only an extraordinary high trapping probability of O_2 on Fe_3O_4 could explain the high S(0) values for O_2 on supported Pd nanoparticles with the Pd deposition coverages 7 Å Pd (6.4 nm) and 4 Å Pd (3.4 nm).
In contrast to CO however, O_2 adsorbs dissociatively on Pd surfaces at 300 K via a precursor state, as demonstrated for example in [91]. Winkler et al. showed, that S(0) of O_2 on Pt(111) (S(0)=0.05) is significantly lower than on Pt(112) (S(0)=0.53) at 300 K. This difference has been attributed to the activation energy for dissociative adsorption of the molecular precursor, which is strongly structure sensitive on Pt group metals [231]. For this reason, precursor mediated adsorption leads to a higher sticking coefficient on Pt(112). As expected, S(0) values for O_2 vary on the different Pd surfaces at 300 K. Values between 0.6 and 0.74 have been observed on Pd(111) [91, 232, 233], ≈0.75 on Pd(100) [234] and 0.86-0.96 on Pd(110) [97, 235, 236]. Thus, S(0) is higher on more open surfaces. Pd nanoparticles exhibit more open structures than the facets, they do not only contain different facets but additionally low coordinated sites as edge and corner sites. Accordingly, the initial sticking probability on Pd nanoparticles is expected to be higher than on Pd(111).
Also in this case, an attempt is made to model the initial sticking probability S(0) on the basis

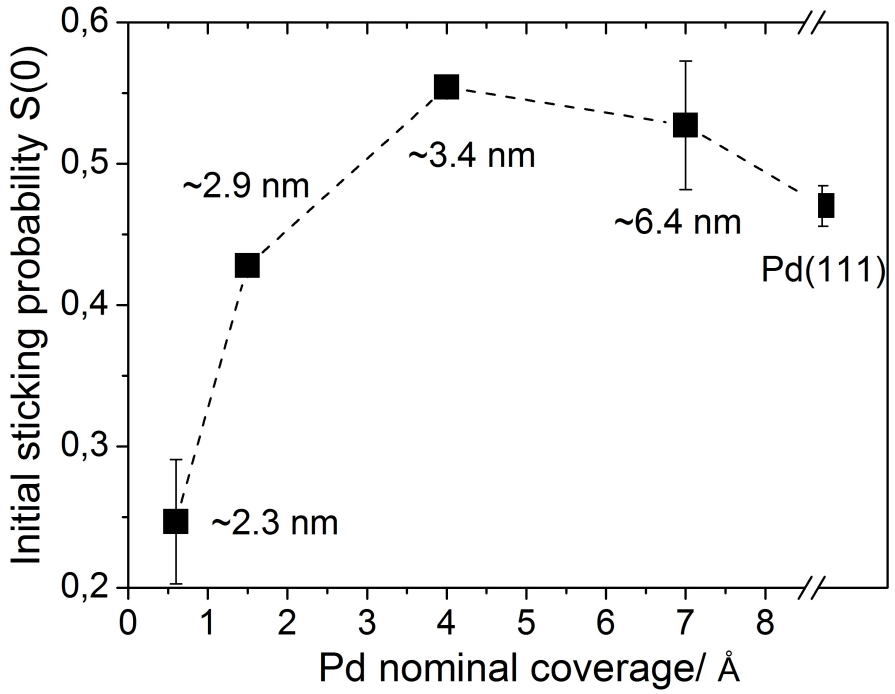

Abbildung 7.5: The initial sticking probability of O_2 on Pd/Fe_3O_4, measured at 300 K. The data was obtained as the average of three to six independent measurements, the plotted error bars indicate the error of the mean

of the model which takes into account the capture zone effect (Equ. 7.2). As described in the previous paragraph, S_{Pd} is not expected to be equal to the initial sticking probability of oxygen on Pd(111). Therefore, $S_{Pd}(0)$, α_{Fe3O4} and r_{Pd} are varied to model the sticking probability of oxygen on Pd nanoparticles of four different sizes. As the number of independent parameters is similar to the number of data points, this procedure is expected to give rather semiquantitative results.
The mean error of 0.05 is quite high for the deposition coverage 7 Å (6.4 nm). All data, plotted in Figure 7.5 have been obtained in a close timely proximity to each other but after remeasuring the data for the deposition coverage 7 Å (6.4 nm), an $S_{tot,2}(0)$ value of 0.53 and an error of 0.01 has been obtained. That the initial sticking probability for O_2 on Pd/Fe_3O_4 for the two largest nanoparticle sizes is higher than on Pd(111) indicates that the capture zones cover all of the oxide area for these two cases. This assumption is made in the following. Solving Equ. 7.2 for the deposition coverage 7 Å (6.4 nm) and 4 Å (3.4 nm) leads to an oxygen sticking coefficient of 0.9 on Pd nanoparticles and a trapping probability of 0.2 on Fe_3O_4. As α_{Fe3O4} and $S_{Pd}(0)$ have been determined, X_d can be estimated on Pd nanoparticles for the smallest nanoparticles (deposition coverage 0.6 Å (2.3 nm)). Using Equ. 7.3, a capture zone radius of 2.4 nm is calculated. This value for X_d is comparable to the capture zone radius of 0.5 nm - 2.4 nm on Pd/Al_2O_3, which has been obtained by Matolin et al. for O_2 on α-Al_2O_3 [29, 73]. It was assumed above that the capture zones completely cover the oxide for nanoparticles with a Pd deposition coverage 7 Å. For the determined X_d value of 2.4 nm however, adsorbates would only diffuse from ∼95 % of the oxide area to the Pd nanoparticles and adsorb for this deposition coverage. It is anticipated however that the corresponding error only has a minor influence on the variables X_d, α_{Fe3O4} and $S_{Pd}(0)$.
Inserting X_d into Equ. 7.3 and using Equ. 7.2 gives $S_{tot,2}(0)$=0.41 for nanoparticles prepared with the Pd deposition coverage 1.5 Å (2.9 nm). This is in good agreement with the experimentally observed sticking probability of 0.43 for this particle size.

7.5 Summary

The SCAC experiments on Fe_3O_4 have been discussed in the first section of this chapter. $6\pm1 \cdot 10^{13}$ CO molecules occupy adsorption sites with a binding energy of 46±1 kJ/mol and at least one additional type of adsorption site with a sticking probability of ≈0.4 and an adsorption energy of ≈25 kJ/mol. The adsorption energies agree very well with the TPD maxima of the α- and β-state from the data of Lemire et al., who assigned these two states to adsorption on iron ions and adsorption in a weakly bound, mobile adsorption state. That only a small amount of CO molecules adsorb in the strongly bond adsorption state would be consistent with an O-termination of the major fraction of the surface. The desorption prefactor for CO from the weakly bound state has been modeled as $2 \cdot 10^{11}$ - $2 \cdot 10^{12}$ s^{-1}.
In the second section of this chapter, the capture zone effect has been introduced. On the basis of a simple model which takes this effect into account, the structure dependence of the initial sticking coefficient of CO and O_2 on Fe_3O_4 supported Pd particles of different sizes can be explained. The parameters, used in/obtained with the model are given in Table 7.2. In agreement with earlier studies, modeling of the initial CO sticking coefficient could be performed by ass-

	$E_{ads,Fe3O4}$	$\nu_{des,Fe3O4}$	$S_{Pd}(0)$	α_{Fe3O4}	X_d
CO on Pd Fe_3O_4	25 kJ/mol	$2 \cdot 10^{11}$ - $2 \cdot 10^{12}$ s^{-1}	0.74	0.61±0.01	2.4±0.3 nm
O_2 on PdFe_3O_4	-	-	0.9	0.2	2.4 nm

Tabelle 7.2: Summary of the results on CO and O_2 interaction with Fe_3O_4 and the capture zone effect

uming that S(0) for CO is identical on Pd(111) and on Pd nanoparticles. S(0) values for O_2 on Pd nanoparticles strongly suggest that the initial sticking coefficient is higher on Pd nanoparticles than on Pd(111), which has been postulated for modeling the S(0) values for O_2. A mean diffusion length, X_d, of ≈2.4 nm on Fe_3O_4 was obtained for CO and O_2.

8 Oxygen adsorption on Pd(111) and Pd/Fe_3O_4

The interaction of oxygen with Pd surfaces is of immense importance for a variety of industrial processes such as CO oxidation and methane combustion in exhaust catalytic converters. The catalysts used for these processes consist of nanoparticles which are supported on oxides.
Due to the disadvantages of temperature programmed desorption methods to determine oxygen binding energies on supported catalysts, investigations with a direct measurement technique are necessary to address this issue.
First, an introduction to the literature on oxygen adsorption on Pd is given. Subsequently, the experimental data on the sticking coefficient and the adsorption energy as a function of the coverage on Pd(111) and supported nanoparticles will be discussed. In the following, the influence of the particle size on the initial adsorption energy of O_2 will be addressed. How particle size effects are influenced by the adsorbate coverage is discussed in the end of the chapter.

8.1 Introduction

At T«100 K, oxygen is found to adsorb molecularly on Pd surfaces, dissociation takes place at higher temperatures where oxygen adsorbate phases may form. Annealing to elevated temperatures in oxygen results in the formation of subsurface oxygen species and surface oxides. At the highest oxygen pressures, these may react to form stoichiometric bulk oxides.
It has been found in low temperature oxygen adsorption experiments, that molecular oxygen adsorbs in a peroxo-like state and a superoxo-like state at 30 K on Pd(111), a second peroxo-species was found at slightly higher temperatures [237, 238]. According to isotopic exchange experiments in combination with TPD and HREELS, adsorbed oxygen molecules dissociate upon heating to 130 K-160 K on Pd(111) [166, 237, 239, 240]. The dynamics of the adsorption process has been investigated by Sjovall et al. [232]: at T$\leq$600 K O_2 dissociation was found to occur via a molecularly chemisorbed state. This molecular adsorption state may be either directly formed upon O_2 adsorption or via trapping into a physisorbed precursor state. At oxygen translational energies of more than 0.13 eV (T_{O2}»300 K), oxygen may also be adsorbed via a direct dissociative adsorption channel which does not proceed through a molecular precursor. Upon dissociation, oxygen atoms preferentially occupy the fcc hollow sites on Pd(111) [166, 233]. At T>180 K and low oxygen exposures, agglomeration to clusters with a distance of twice the Pd-Pd distance has been observed [166]. Higher oxygen exposure leads to the formation of a closed p(2x2) monolayer, which saturates at Θ 0.25 [88–90, 166]. In most studies, this coverage is suggested to be the saturation coverage at 300 K, although ordering to more dense structures has also been reported [14, 166]. An initial sticking coefficient of 0.6-0.74 was found in molecular beam studies on Pd(111) [91, 232, 233]. At T=300 K, the O_2 sticking probability only gradually decreases with increasing coverage. Close to Θ_O=0.25, a pronounced decay of

the sticking probability has been observed [63, 232, 233]. This type of coverage dependence strongly suggests that adsorption may proceed via a precursor state, i.e. oxygen molecules are trapped in a physisorbed state before chemisorption occurs. Klötzer et al. found a decay of the sticking probability to $S(\Theta)<10^{-3}$ at $\Theta>0.25$. The saturation coverage was found to be $\Theta>0.36$ at T=323 K [91, 233]. Subsurface oxygen diffusion has been suggested to proceed in an activated process at $\Theta_O>0.25$. On the basis of UPS studies on crystals with different defect densities, oxygen subsurface diffusion at T=300 K and high oxygen exposures has been suggested to occur via diffusion from steps or defect sites [241]. The probability for subsurface oxygen formation upon O_2 exposure has been found to increase with increasing surface temperature. At T>500 K, a subsurface species has been detected with PES, HREELS and oxygen titration experiments already after an oxygen exposure of ≈40 L [89, 91, 233, 242]. TPD and STM studies have been performed in combination with DFT on Pd(111) surfaces, which have been exposed to $P_{O2}>10^{-6}$ mbar at T>500 K: it was observed, that the formation of several surface oxides can be kinetically stabilized at these temperatures. [90, 170, 243, 244]. These include Pd_9O_8, $Pd_{20}O_{18}$, $Pd_{23}O_{21}$, $Pd_{19}O_{18}$ and Pd_5O_4. At the highest oxygen chemical potentials (e.g. at an NO_2 exposure of 60 L at T=500 K), the formation of bulk PdO occurs [90, 170].

On Pd(100), initial adsorption of oxygen has been been observed to be dissociative at 80 K but a molecular state has been observed upon additional oxygen exposure [93, 94, 245–247]. At T>125 K, only an atomic oxygen species could be detected, which occupies the fourfold hollow sites. The initial sticking probability at 300 K is ≈0.75 on Pd(100) [234]. At $\Theta_O>0.25$, $S(\Theta)$ has been found to decrease by a factor of 100 [93, 94, 96, 248, 249]. This drop of the sticking probability has been connected with the transformation of the p(2x2) structure, observed at low oxygen exposures into a c(2x2) structure which saturates $\Theta = 0.5$. By comparing the Auger intensity of the oxygen and the Pd peak, Chang et al. found indications for the formation of a subsurface oxygen species at 300 K<T<400 K [96]. LEED experiments in combination with AES and HREELS showed, that a Pd surface oxide with a p(5x5) pattern starts to evolve at 400 K<T<500 K, depending on the oxygen pressure [93, 95, 96, 248, 249]. The saturation coverage of this species has been found as 0.64. At T>500 K, this structure has been observed to transform into a $(\sqrt{5}x\sqrt{5})$R27 overlayer which is saturated at Θ=0.8. The formation of the p(5x5) and the $(\sqrt{5}x\sqrt{5})$R27 phase is found to be an activated process and it has been shown conclusively, that the surface structures correspond to surface planes of PdO [243, 248, 250, 251].

On Pd(110), partial oxygen dissociation has been observed at temperatures as low as 85 K [252–254]. At T>120 K, oxygen was found to adsorb dissociatively with oxygen atoms occupying the threefold sites on Pd(110) [255]. The molecular beam experiments by Junell et al. show that oxygen adsorbs via two adsorption channels at T∼300 K [236]: Firstly direct dissociative adsorption may occur. Secondly, oxygen may adsorb in a molecular precursor state from which they may dissociate. At this temperature, S(0) has been found as 0.86-0.96 on Pd(110). At 300 K and $\Theta<0.5$, adsorption was observed to occur via a precursor state [97, 235, 236]. In several investigations, a (1x3) phase was found at low coverages which saturates in a c(2x4) structure at $\Theta_O=0.5$ [235, 252, 256]. At higher exposures, a (1x2) and a (2x3)1D phase has been observed by different groups, which is associated with a disorder of the Pd(110) surface [12, 97, 160, 252, 257]. Most interestingly, in contrast to the 100 and 111 facet, subsurface oxygen diffusion has been already observed at T<300 K in numerous studies with work function measurements, AES and XPS [97, 98, 160, 235, 256, 258, 259]. At 300 K, Θ_O has been found

to be ∼0.75. Upon annealing to T>500 K, the formation of a c(2x6) phase, which has been associated with a surface oxide takes place [160].
As steps exhibit a closer structural resemblance to the edge sites of nanoparticles than facet sites, it is interesting to consider how oxygen adsorbs on faceted crystals. LEED and STM results show, that oxygen preferentially adsorbs on step edges of stepped surfaces. A zig-zag pattern is formed, so that on the average, every edge Pd atom is bound to one oxygen atom [101, 260, 261]. After adsorption on the step sites, the facet sites become occupied. No formation of an oxide phase has been found on the stepped surfaces Pd(331) and Pd(119) at 300 K [101, 261] with work function measurements and measurements of the surface core level shift. At higher temperatures and pressures, surface oxides may be formed [260–262]. Oxygen exposure at p_{O2}=5 10^{-8} mbar and T=580 K was observed to lead to step bunching [261].
STM studies of Besenbacher and Hansen on ≈7.5 nm-sized Pd nanoparticles, supported on α-Al_2O_3 show that oxygen initially occupies the edge sites. A zig-zag pattern in which on the average one O atom is bound to one Pd atom is formed. After adsorption on the edges, adsorption occurs on the (111) and (100) facet sites [32]. After high oxygen exposures of Pd nanoparticles supported on α-Al_2O_3 and TiO_2 with a diameter of more than 7.5 nm, oxygen adsorbate structures could be resolved. On the Pd(111) facet, a p(2x2) phase forms at 300 K which is equivalent to what is observed on the Pd(111) single crystal at oxygen saturation [32, 33].
Different groups have studied the interaction of O_2 with supported Pd nanoparticles at 300 K. In the majority of the studies, no formation of a subsurface oxygen species has been found [32, 45, 84]. In oxygen sticking measurements, Matolin et al. obtained an unusually high number of adsorbed oxygen atoms for Pd nanoparticles supported on α-Al_2O_3 which has been explained with the formation of a subsurface oxygen species [29, 68]. It could be demonstrated with ion scattering techniques, that oxygen diffusion into subsurface sites may occur upon annealing to 400 K - 525 K [45]. Molecular beam measurements on Pd/Fe_3O_4 showed that an oxide species forms at T=500 K [46, 48, 83–85]: the oxygen content of this oxide species is higher when oxidizing at T=600 K and the number of adsorbed oxygen atoms per surface area was observed to be the highest for small Pd nanoparticles ($\leq$4 nm). With IRAS and PES measurements, it could be shown that the oxide is preferentially formed at the metal/oxide interface. At high oxygen pressures, PdO forms. It was observed, however, that even after oxidation at 503 K and atmospheric oxygen pressures, a metallic Pd core remains on Pd/α-Al_2O_3 [45, 167]. The decomposition of the PdO-species, present on/in Pd nanoparticles is observed at temperatures which are ∼200 K higher than for bulk PdO, which was attributed to the higher stability of this species. Gas exposure at elevated temperatures may also lead to a change in the surface structure: faceting of an oxygen covered Pd tip with a diameter of 27 nm has been observed at T=400 K-450 K and sintering of oxygen covered Pd nanoparticles was found upon annealing to the desorption temperature [45, 103, 105]. Upon performing several times a procedure that consists of oxygen exposure, CO exposure and annealing at elevated temperatures, a decrease of the particle density by 80 % has been observed by STM on ∼4 nm-sized Pd nanoparticles, supported on Fe_3O_4. This sintering process was suggested to occur via the diffusion of a PdO_X species between the Pd nanoparticles [86].
As discussed in chapter 2, the desorption energy is in general strongly coverage dependent and different for the various adsorbate structures. An overview of the literature data is given in Table 8.1, where two distinct coverages with corresponding desorption energies from different Pd fa-

Θ1	E_{des1}	Θ2	E_{des2}	Ref.
		Pd(111)		
≈0.025%	230 kJ/mol	≈0.15	230 kJ/mol	[88]
≈0.02%	201 kJ/mol	≈ 0.24	198 kJ/mol	[89]
≈0.1 %	215 kJ/mol	0.25	195 kJ/mol	[90]
≈0 %	222 kJ/mol	0.25	221 kJ/mol	[91]
≈0.1 %	210 kJ/mol	0.25	200 kJ/mol	[92]
		Pd(100)		
≈0.1	210 kJ/mol	0.25	200 kJ/mol	[93]
≈0.04	210 kJ/mol	≈0.24	205 kJ/mol	[94]
≈0	251 kJ/mol	0.25	42 kJ/mol	[95]
≈0.01	205 kJ/mol	0.25	200 kJ/mol	[96]
		Pd(110)		
≈0.01	190	0.25	230-240 kJ/mol	[97]
≈0.02	200	-	-	[98]
≈0.15	198	-	-	[256]
		Stepped Pd surfaces		
≈0.01	228 kJ/mol	Θ_{sat}	210 kJ/mol	[101]

Tabelle 8.1: Desorption energies $E_{des,1}$ and $E_{des,1}$ of oxygen from the literature at two distinct coverage Θ1 and Θ2 from Pd(111), Pd(100), Pd(110) and stepped Pd surfaces. Ref. is the reference from which the results were extracted. The energies in gray have been estimated either by the authors or in the current work based on a Redhead analysis

cets and stepped Pd surfaces are listed. The values in gray correspond to results from a Redhead analysis of TPD data. The desorption energies in black correspond to an analysis that does not require assumptions on the preexponential factor ν_{des} (Leading edge analysis, Full analysis...). On Pd(111), the initial desorption energy was found to be 200-230 kJ/mol and is approximately constant until the saturation coverage of 0.25 is reached. The desorption energies, obtained with the Redhead analysis are ∼15 kJ/mol lower than the ones obtained otherwise.
On Pd(100), an initial desorption energy of 205-251 kJ/mol has been detected. The desorption energy, obtained with the leading edge analysis [95] is significantly higher at $\Theta_O \rightarrow 0$ and significantly lower at $\Theta = 0.25$ than the results, which have been obtained with the Redhead analysis. A single desorption feature with a maximum at ≈650 K - 700 K is detected from the c(2x2)O structure on Pd(100). The desorption energy of this phase has been estimated to be 205-210 kJ/mol [263].
According to the results of Yagi et al., based on a complete analysis of the TPD data, the desorption energy of O_2 on Pd(110) is initially 190 kJ/mol. The desorption energy at low coverages, based on a Redhead analysis was found to be 8-10 kJ/mol higher. At $\Theta_O \approx 0.25$, the desorption energy was observed to increase to 230-240 kJ/mol and to decreases again at higher coverages. It was explained above, that numerous studies suggest subsurface oxygen diffusion from O/Pd(110) at T≤300 K, and desorption from subsurface sites has been associated with

a TPD peak at T=710-775 K [98, 256]. Subsurface diffusion and restructuring of the surface at 300 K and high oxygen exposures make it difficult to estimate the oxygen desorption energies at high oxygen coverages. For TPD studies on these systems, I refer to the References [97, 98, 160, 235, 256, 258].
Lambert et al. studied oxygen desorption from stepped Pd. The obtained desorption energy at $\Theta_O \approx 0.01$ from Pd(331) is measured as 228 kJ/mol. In agreement with the results from the DFT study of Reuter et al., a similar oxygen binding energy is obtained on the steps and on the facets of stepped Pd surfaces [264].
Several TPD studies of oxygen desorption from Pd nanoparticles of different sizes have been performed: Xu et al. observed a desorption maximum at 850 K for an oxygen coverage of 0.1 on ∼50 nm-sized Pd nanoparticles on SiO_2 which shifted to 800 K upon oxygen saturation (a heating rate of 10 K/s was used) [100]. Putna et al. observed TPD maxima at 800 K and 875 K on Pd nanoparticles with a diameter of 9.1 nm supported on α-Al_2O_3, whereas only one desorption feature at ∼950 K was observed on 2.1 nm-sized Pd nanoparticles (heating rate 15 K/s) [99]. Similarly, Campbell et al. found a small shift of the TPD peak to higher temperatures on smaller Pd particles and an additional low temperature shoulder on large particles in the particle size range <3 nm-5 nm [45]. These results could be explained with stronger oxygen-Pd interactions on smaller Pd nanoparticles. As mentioned above, however, oxygen has been observed to diffuse into subsurface sites and Pd nanoparticles may sinter upon annealing to the desorption temperature. These additional processes affect the reversibility of the adsorption process. But only for fully reversible process, it is possible to associate oxygen desorption energies with oxygen binding energies. In addition to that, the majority of the oxygen TPD experiments on Pd nanoparticles have been performed at oxygen saturation, where adsorbate-adsorbate interactions are prominent. Accordingly, the above results may not reflect the particle size dependence of the oxygen binding energy in the low oxygen coverage regime.

8.2 Oxygen sticking coefficient and adsorption energies on Pd(111)

In this section, the results from the measurement of the sticking coefficients and adsorption energies of oxygen on Pd(111) are discussed. The Pd(111) single crystal was cleaned by repeated cycles of sputtering with Ar^+ ions at a potential of 800 eV, oxidation at 700 K and annealing at 1000 K. The measured sticking probability of O_2 on Pd(111) as a function of the coverage is shown in Figure 8.1 (a). The adsorption energy versus the coverage is shown in Figure 8.1 (b). A molecular beam flux of $\approx 1.1 \cdot 10^{14}$ cm^{-2} s^{-1} and a chopper opening time of 266 ms has been used. The data represents the average of four independent measurements.
As the coverage reached after the first pulse is 0.01, the initial sticking coefficient and adsorption energy can be considered as the respective limiting values at Θ_O=0.
The measured initial sticking probability of 0.47 ± 0.03 is slightly lower than the values of S(0)=0.6-0.74 obtained in earlier studies [91, 232, 233]. The qualitative coverage dependence of $S(\Theta)$ is in agreement with the literature data [65, 91, 232].
As discussed above, O_2 dissociation on Pd(111) has been observed to occur via a molecularly chemisorbed state which may be either directly formed upon O_2 adsorption or via trapping into a precursor state. That adsorption proceeds via an precursor is also evident from Figure 8.1 (a). In

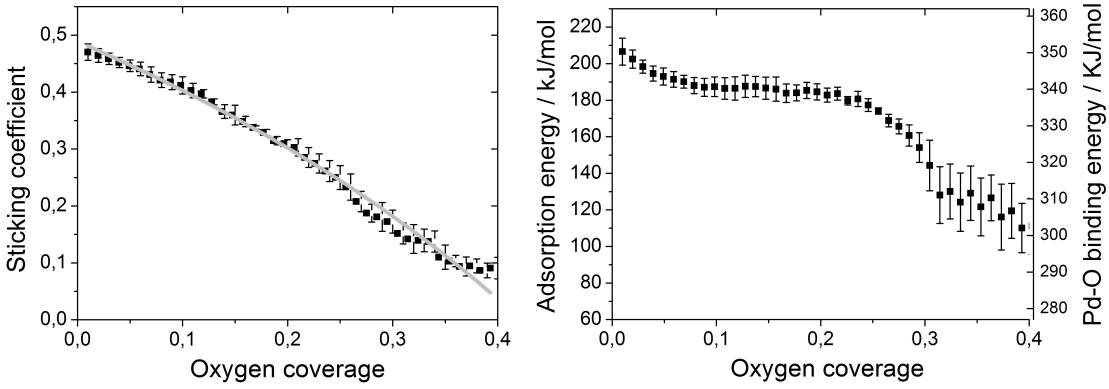

Abbildung 8.1: O_2 sticking probability (a) and adsorption energies (b) on Pd(111) as a function of the coverage, measured at T=300 K. The error bars show the mean error from four independent measurements. A molecular flux of $\approx 1.1 \cdot 10^{14}$ cm^{-2} s^{-1} and a pulse time of 266 ms has been used.

the case of immobile adsorption, S(Θ) would be proportional to $(1-\Theta)^2$. The gray line in 8.1 (a) shows the fit of the sticking probability with the Kisliuk expression for precursor mediated first order adsorption, discussed in 2.3.3 with a K-value of 2.3$\pm$0.3. As a K-value of 0 corresponds to a completely mobile precursor and a value of ∞ to a completely immobile precursor, this suggests a very mobile precursor state at Θ_O<0.25. At higher coverages, the difference between the fit and the experimental data increases. This could be caused by the lower probability of finding two empty sites for the dissociation of O_2 at high coverages. The sticking coefficient levels off at Θ=0.3-0.35, which is slightly higher than the literature value of 0.25.
Figure 8.1 (b) shows the adsorption energy, plotted versus the coverage, on the right hand axis. Also shown in Fig. 8.1 (b) is the Pd-O binding energy, which is calculated as follows:

$$E_{Pd-O} = \frac{1}{2}\left(E_{ads} + E_{O-O}\right) \tag{8.1}$$

$E_{O\text{-}O}$ is the dissociation energy of an oxygen molecule (494 kJ/mol). The determined initial adsorption energy of O_2 on Pd(111) is 206$\pm$7 kJ/mol and is slightly lower than the average of the literature values, shown in Table 8.1. It has to be considered though, that the activation energy for desorption is generally higher than the adsorption energy, the difference might not be negligible in this case [1]. The activation energy for adsorption can explain the small discrepancy between the SCAC data and the TPD literature data. The adsorption energy decreases to 186 kJ/mol at an oxygen coverage of 0.08 and is roughly constant until Θ_O=0.22, and decreases prominently at higher coverages to a value of $\approx$130 kJ/mol at the saturation coverage of 0.3-0.35. It has been observed, that oxygen initially occupies the steps on high Miller index surfaces [101, 261, 264], and the slightly higher adsorption energy at Θ_O<0.08 might be caused by initial adsorption on

[1] For further details, I refer to Chapter 2 (Equ. 2.4)

steps or defect sites with a higher adsorption energy than on the facets. The constant adsorption energy for intermediate coverages reproduces the trend observed in previous TPD studies. Table 8.1 shows similar desorption energies at $\Theta_O \rightarrow 0$ and at $\Theta_O \approx 0.25$. Such an adsorption behavior represents the case where adsorbate-adsorbate interactions are negligible. The decrease in the adsorption energy observed at $\Theta_O > 0.22$ may be caused by either direct repulsive adsorbate-adsorbate interactions or by through-surface interactions.

8.3 Sticking of oxygen on Pd/Fe_3O_4

In the following, the oxygen sticking coefficients on Pd nanoparticles deposited on Fe_3O_4 will be discussed. The Pd/Fe_3O_4 catalysts have been prepared according to the procedure, described in Chapter 6. After preparation, the Pd/Fe_3O_4 catalysts were annealed to 580 K-600 K, Directly following preparation, the adsorption measurements were carried out. Figure 8.2 shows the

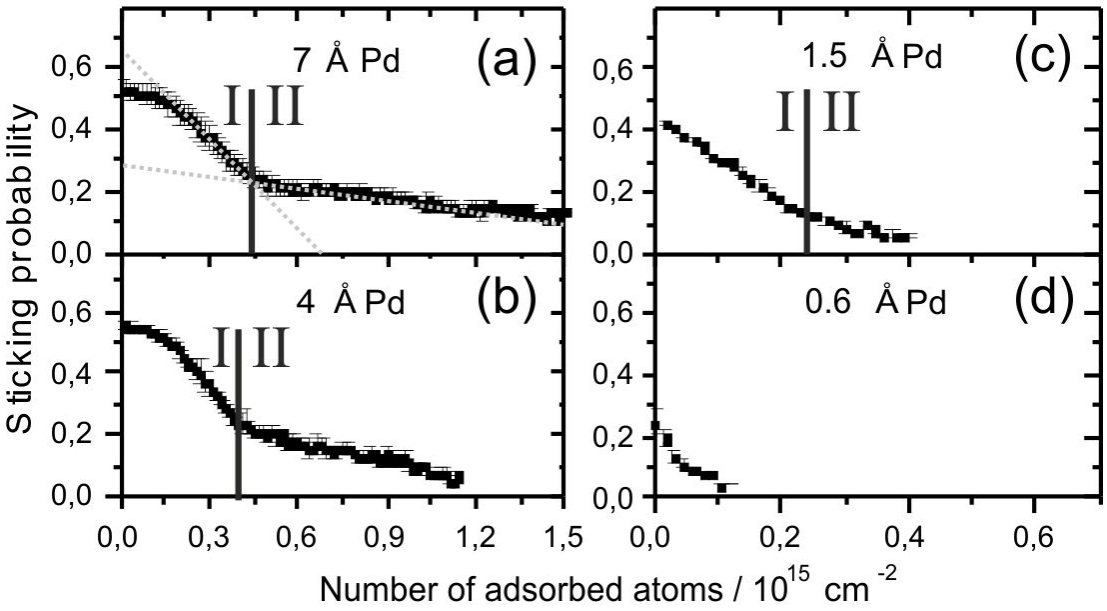

Abbildung 8.2: Sticking coefficient $S(N_O)$ of O_2 measured at 300 K plotted versus the number of adsorbed oxygen atoms on Pd nanoparticles with the Pd deposition coverage 0.6 Å (2.3 nm), 1.5 Å (2.9 nm), 4 Å (3.4 nm) and 7 Å (6.4 nm), supported on Fe_3O_4/Pt(111). A molecular flux of $\approx 1.1 \cdot 10^{14}$ cm^{-2} s^{-1} and a pulse time of 266 ms has been used. The error bars correspond to the error of the mean

sticking coefficient at 300 K as a function of the number of adsorbed atoms for four different Pd deposition coverages. The number of adsorbed atoms is the total number of oxygen atoms which is initially adsorbed on the surface, regardless of subsequent processes.
These results were obtained as the average of three to five independent measurements, carried out in an identical way to the experiments on Pd(111). The sticking coefficient of O_2 on Fe_3O_4

has been determined to be 0 at 300 K, thus sticking on Pd/Fe_3O_4 can be attributed to sticking on the nanoparticles. The initial sticking coefficient has been discussed in the previous section and has been explained with a model that includes the capture zone effect.
For the deposition coverage 7 Å Pd (6.4 nm), the initial sticking probability is 0.53±0.05 and gradually decreases until the number of adsorbed atoms is $0.10 \cdot 10^{15}$ cm^{-2} and S∼0.51. At higher oxygen exposures, S decreases more sharply until the number of adsorbed atoms is $\approx 0.44 \cdot 10^{15}$ cm^{-2}. An additional adsorption regime can be identified in Fig. 8.2 (a) in which the number of adsorbed O atoms decays more gradually is in the range $0.44 \cdot 10^{15}$- $1.35 \cdot 10^{15}$ cm^{-2}. The latter regime is termed regime II, whereas the regime in which S decays gradually and subsequently sharply is termed regime I. To determine the boundary between the two regimes, the region of the sharp decrease in S in regime I and the region of the gradual decay of S in regime II are fitted linearly. These linear fits are indicated with gray dotted lines in Fig. 8.2 (a). The intersection between the two lines is defined to be the boundary between regime I and regime II.
A gentle decay at the smallest oxygen exposures, a more prominent decay at higher oxygen exposures and a very gradual decay of the sticking coefficient at high oxygen exposures can be also identified in the sticking data for the deposition coverage 4 Å Pd (3.4 nm), shown in Fig. 8.2 (b). For the Pd deposition coverage 1.5 Å, a pronounced decay of the sticking probability is already observed at the lowest oxygen coverages. The more gradual decay of the sticking coefficient in regime II occurs after the decay of the sticking probability to ≈0.13, where the number of adsorbed oxygen atoms is $\approx 0.23 \cdot 10^{15}$ cm^{-2}. The boundary between regime I and II for the two smaller Pd nanoparticle sizes has been determined with the same procedure as the boundary for the largest particle size, described above. Due to the more gradual transition between the two regimes for the Pd deposition coverage 1.5 Å, this determination may be less accurate in this case. The two regimes are shown for all three cases in Fig. 8.2.
For the Pd deposition coverage 0.6 Å Pd (2.3 nm), the oxygen sticking probability is initially 0.25±0.08 and strongly decays with increasing oxygen exposure until saturation is reached at approximately $0.10 \cdot 10^{15}$ oxygen atoms cm^{-2}.
A similar coverage dependence of the sticking coefficient as observed in regime I for the two largest nanoparticles has been measured in oxygen sticking measurements on Pd single crystals [63, 91, 97, 232–236, 236]. The gradual decay of the sticking coefficient at low exposures is attributed to precursor mediated adsorption and trapping in the capture zone. The latter effect is not expected to be dependent on the oxygen coverage. Regime II will be discussed in detail in the next chapter. Evidence will be given that this regime corresponds to the formation of a species other than adsorbed oxygen on the Pd nanoparticles.
Although it would be an exciting challenge to model the coverage dependent adsorption probability as a function of the particle size, more information on the adsorption dynamics on the different adsorption sites and processes such as diffusion on and between the adsorption sites and diffusion from the support are necessary to perform such a task in a meaningful way.
In the following, the coverage at which oxygen saturates the surface Pd sites is discussed, which is assumed to be reached after the prominent decay of the sticking probability in regime I. This assumption is based on the following observations: in contrast to regime II, regime I has been observed in oxygen adsorption experiments on Pd single crystal facets at conditions in which only the formation of an adsorbate layer on Pd occurs. The high number of oxygen atoms which is adsorbed in regime II cannot be explained with the saturation of surface Pd atoms without the

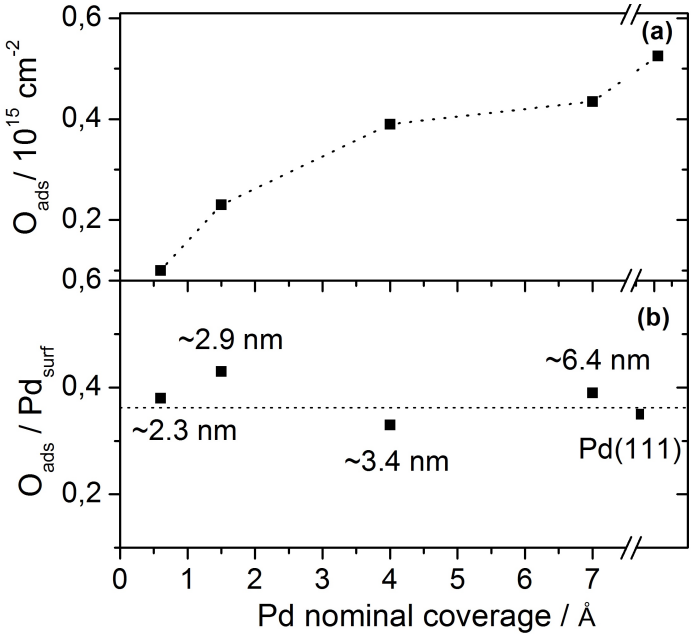

Abbildung 8.3: Number of on Pd adsorbed oxygen atoms (a) and the number of on Pd adsorbed oxygen atoms divided by the number of surface Pd atoms. The particle size is given next to the data point for each respective deposition coverage

occupation of additional sites.
The number of on Pd adsorbed oxygen atoms is plotted for the four different Pd deposition coverages and for Pd(111) in Figure 8.3 (a). As the number of surface Pd atoms decreases with decreasing Pd deposition coverage, the total number of on Pd adsorbed oxygen atoms follows the same trend. The oxygen coverage on the nanoparticles can be obtained by dividing the number of adsorbed O atoms by the number of Pd atoms at the particle surface, which is shown in Figure 8.3 (b). Details on how the number of surface Pd atoms has been estimated are given in Chapter 6.
Figure 8.3 (b) shows, that the estimated oxygen coverage at saturation is quite similar for the four different Pd particle sizes, the average oxygen coverage is 0.38 ± 0.04.
STM experiments have been performed at 300 K on Pd nanoparticles supported on α-Al_2O_3 and TiO_2 with a diameter of more than 8 nm: it could be shown, that the oxygen overlayer structures are the same on the facets of the Pd nanoparticles and on the corresponding single crystal facets [32, 33]. Therefore, the saturation coverage of the Pd/Fe_3O_4 systems can be estimated based on the ratio of (111) facets (80%) to (100) facets (20%) and the saturation coverage on these facets. In most studies, a p(2x2) structure with a saturation coverage of 0.25 has been found on Pd(111) [88, 166, 233], although large O_2 exposures have been found to result in higher O coverages (Θ>0.36) [91, 233]. Hansen et al. observed the formation of a p(2x2)O structure on $\sim$7.5 nm Pd particles, supported by Al_2O_3 after an oxygen exposure that was higher than in our studies. Therefore, the formation of a p(2x2)O phase is expected to form on the Pd(111) facets with the conditions, used here. Based on the literature, the saturation coverage on the Pd(100) facet

is assumed to be 0.50 [93, 94, 249]. This gives an average saturation coverage of 0.30 on the Pd nanoparticles. In the present sticking probability measurements, described above, an oxygen coverage of 0.30-0.35 has been determined on Pd(111). When using this for the estimation, an oxygen coverage of 0.34-0.38 is obtained.
This range of oxygen coverages is in agreement with the experimentally obtained oxygen coverage of 0.38±0.04 on Pd nanoparticles. Henry et al. obtained a saturation coverage of 0.40±0.08 [77] on Pd nanoparticles, supported on MgO(100), which also agrees quite well with the oxygen coverage, determined here.

8.4 Adsorption energy of oxygen on Pd/Fe_3O_4

In this section, the adsorption energies of O_2 on Pd nanoparticles of four different sizes, which have been determined from the same data as the sticking coefficients, will be discussed. The adsorption energies as a function of Θ_O are shown in Figure 8.4 for all investigated particle sizes. For the deposition coverage 7 Å Pd (6.4nm), the initial adsorption energy is 247±9 kJ/mol and decays roughly linearly to ≈105 kJ/mol as the number of adsorbed oxygen atoms reaches $0.43 \cdot 10^{15} cm^{-2} s^{-1}$, which corresponds to the saturation of the Pd surface sites. A similar trend can be observed for the other particle sizes.
On single crystals, direct adsorbate-adsorbate interactions, which are mostly electrostatic in-

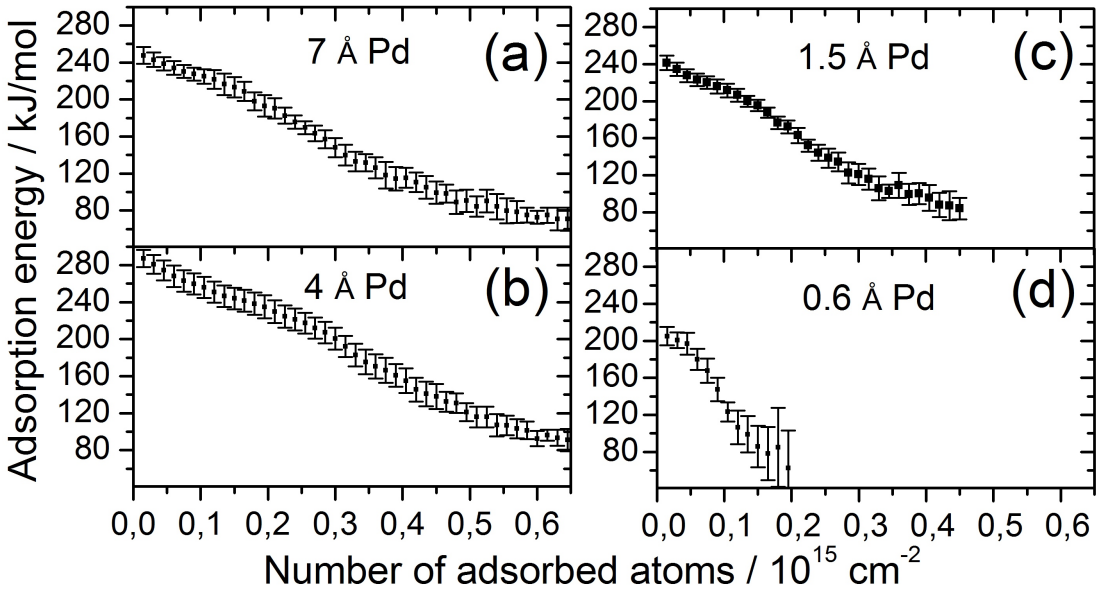

Abbildung 8.4: Oxygen adsorption energy for O_2, plotted versus the number of adsorbed atoms on Pd particles with the Pd deposition thickness 0.6 Å (2.3 nm), 1.5 Å (2.9 nm), 4 Å (3.4 nm) and 7 Å (6.4 nm) supported on Fe_3O_4/Pt(111). The error bars correspond to the error of the mean

teractions can be responsible for the decay of the adsorption energy with increasing coverage. Through-surface interactions, which have been discussed in detail in Chapter 2 can result in a decrease of the adsorption energy at high adsorbate exposures.
On nanoparticles, a different effect can result in the same trend: the successive occupation of sites with different oxygen binding energies, such es edge and corner sites, and the different facet sites could lead to a decrease in the adsorption energy with increasing adsorbate coverage. A separation between changes in the binding energy due to adsorbate-adsorbate interactions and due to the occupation of different binding sites is not possible here without theoretical investigations.
In Fig. 8.4 (a), higher initial adsorption energy for large Pd nanoparticles (275±14 kJ/mol at $0.01 \cdot 10^{15}$ O atoms cm^{-2}) in comparison to Pd(111) (205±7 kJ/mol at $0.01 \cdot 10^{15}$ O atoms cm^{-2}) is be observed. Such a high binding energy for oxygen on Pd nanoparticles has not been found in TPD studies so far, neither on low Miller index surfaces nor on stepped single crystals [45, 88, 89, 89–98, 100, 101, 238, 252, 264, 265]. Thus, this high initial adsorption energy must be related to some structural features inherent to Pd nanoparticles, which cannot be reproduced even by the steps of the high Miller index Pd surfaces. Such adsorption sites on Pd nanoparticles might be the low coordinated surface sites (edges or corners), which are occupied before the facet sites according to [32].
CO titration experiments in combination with IRAS have been carried out in order to verify this explanation. CO was previously stated to be a suitable probe molecule for the identification of different adsorption sites on Pd nanoparticles, such as low-coordinated adsorption sites and regular adsorption sites on the terraces [266]. Figure 8.5 shows an IRAS spectrum on 6 nm-sized Pd nanoparticles, obtained at 120 K after dosing $\approx 8 \cdot 10^{15}$ CO molecules cm^{-2} at 300 K on the clean Pd nanoparticles (black curve). Fig. 8.5 also shows the IRAS spectrum on the identical sample on which $\approx 10^{14}$ O atoms cm^{-2} were adsorbed at 300 K to produce a sub-monolayer coverage of oxygen (gray curve) followed by adsorption of the same amount of CO as in the previous experiment. The spectrum of CO on pristine Pd nanoparticles is dominated by a sharp adsorption feature at 1980 cm^{-1} (1). Additionally, a peak of lower intensity at 1956 cm^{-1} (2) is observed together with a broad low-frequency shoulder at 1950-1820 cm^{-1} (3). For Pd nanoparticles of a similar size, the low frequency features (between 1820 cm^{-1} and 1970 cm^{-1}) have been previously assigned to CO adsorption on bridge and hollow sites on on the (111) facet. The strong absorption band at 1980 cm^{-1} (1) has been found to originate from a superposition of bridge-bonded CO, adsorbed at low coordinated surface sites (edges/corners) and on (100) facets [266]. However, since the (100) facets are tilted with respect to the surface plane, the relative contribution of the CO molecules, adsorbed on these sites are expected to be small [146]. It has to be noted, however, that the relative intensities of the vibrational features do not directly reflect the relative abundance of the corresponding sites due to dipole-coupling effects [267, 268]. After adsorption of oxygen, drastic changes are observed in the CO spectrum. The edge-related peak at 1980 cm^{-1} (1) is strongly attenuated, whereas the feature at 1956 cm^{-1} gains in intensity. This indicates that CO adsorption at particle edge/corner sites is blocked by adsorbed oxygen. The gain in intensity at 1956 cm^{-1} is most likely from the reduced intensity transfer to high frequency features.
From these observations, it can be concluded that oxygen preferentially adsorbs at the low-coordinated sites (particle edges and corners). Furthermore, the high initial adsorption energy

(275±14 kJ/mol) measured in a calorimetric experiment on supported Pd nanoparticles, can be attributed to oxygen adsorption at edge and corner sites. However, further experimental or theoretical studies are needed in order to rationalize why the edge sites of Pd nanoparticles interact so strongly with adsorbed oxygen [32, 104, 105].

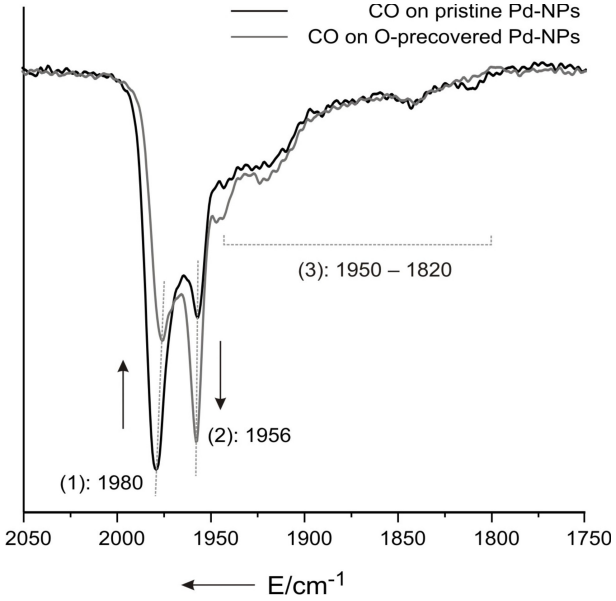

Abbildung 8.5: IRAS spectra for CO, adsorbed on Pd nanoparticles (Pd deposition thickness 4 Å(6 nm)) supported on Fe_3O_4/Pt(111). The black curve corresponds to adsorption on the pristine sample, the gray curve to the sample which has been exposed to $\approx 10^{14}$ O atoms/cm^{-2}.

8.5 The effect of the particle size on the oxygen binding energy

The particle size dependence of the oxygen adsorption energies can be best understood by comparing the oxygen adsorption energies in the zero coverage limit, where adsorbate-adsorbate interactions are negligible. To estimate the coverage after the first pulse of oxygen molecules, the average number of adsorbed oxygen atoms after the first pulse has been determined and is given in Table 8.2. The average oxygen coverage is obtained by dividing this number by the number of Pd atoms on the particle surface, which is given in the 4th row of Table 8.2. That the average surface coverage is 0.02-0.05 after the first pulse suggests that adsorbate-adsorbate interactions are negligible. Thus, the initial adsorption energies represent the values in the limiting case of a single molecule interacting with a nanoparticle.

A plot of the initial oxygen adsorption energies for the Pd deposition coverages 0.6 Å (2.3 nm), 1.5 Å (2.9 nm), 4 Å (3.4 nm), 7 Å (6.4 nm) and for Pd(111) is given in Figure 8.6 (a), the data has been extracted from the data set of the coverage dependent adsorption energies, shown in Fig. 8.4. The right ordinate axis shows the Pd-O bond energy which is calculated according to Equ. 8.1. The dependence of the initial oxygen adsorption energy on the particle size shows a

Nominal Pd coverage	0.6 Å	1.5 Å	4 Å	7 Å
Particle diameter / nm	2.3	2.9	3.4	6.4
N_O per particle	7	10	8	28
N_O per surface Pd, / cm^{-2}	0.05	0.04	0.02	0.03
N_O on edge sites / cm^{-2}	0.1	0.11	0.07	0.14

Tabelle 8.2: Number of adsorbed oxygen atoms during the first pulse, abbreviated with N_O per particle, per Pd atoms at the surface UHV interface and per Pd atoms on edge sites

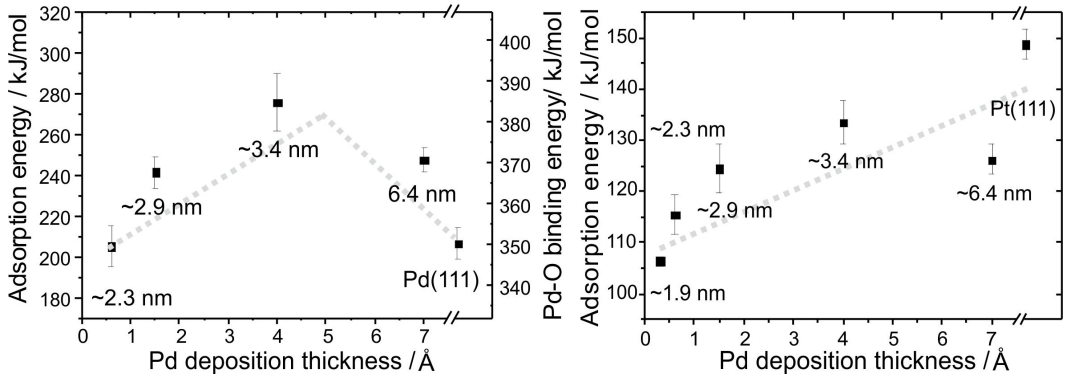

(a) (b)

Abbildung 8.6: Initial adsorption energy for O_2 (a) and CO (b) molecules plotted plotted versus the nominal Pd coverage on the Fe_3O_4/Pt(111) samples. The error bars show the error of the mean. In (a), the Pd-O bond energy is given on the right abscissa

clear trend. It strongly increases from ≈205 kJ/mol on Pd(111), where oxygen adsorbs in the threefold hollow site to 250-275 kJ/mol on large Pd nanoparticles, where oxygen adsorbs at the edge site sites, as evidenced by the IRAS data. A reduction of the particle size, however, results in a decrease of the initial adsorption energy to a value of 205 kJ/mol on the smallest Pd nanoparticles. The shift in binding energy caused by the reduction of the particle size is comparable to the binding energy shift caused by a change of the local adsorption environment. The decreasing adsorption energy with decreasing particle size coincides with the findings obtained with the same experimental setup for CO adsorption on Pd particles, which have previously been reported [123, 205]. The Pd/Fe_3O_4 systems in these studies have been prepared in the same way as the ones used for the present study. As a comparison, the initial CO adsorption energies are given in Figure 8.6 (b), these results show a pronounced decrease in the adsorption energy for small clusters. In contrast to O_2, the change of the adsorption site from a three-fold hollow site on Pd(111) to the strongest binding site on Pd nanoparticles does not result in an increase of the CO adsorption energy. This observation agrees well with the literature data, suggesting that the degree of coordination of the surface Pd atoms, both on low Miller index surfaces and on stepped Pd surfaces, does not significantly affect the CO binding energy [101, 269, 270].
Comparing the CO and O_2 adsorption data on Pd(111) and Pd nanoparticles of different sizes

leads to the conclusion that two effects can be clearly separated, which affect the binding energy: a change of the local adsorption environment and a change in the particle size. For O_2, the change in the local adsorption site from three-fold hollow on Pd(111) to edge sites on Pd nanoparticles leads to an increase of the O_2 adsorption energy by ≈70 kJ/mol. No comparable effect can be observed for CO. The higher adsorption energy of oxygen on edge sites is in agreement with the findings that O-atoms first adsorb on steps of stepped crystals and on edge sites of Pd nanoparticles [32] before the facet sites are occupied [101, 260, 261].
The second effect, the decrease of the initial adsorption energy with decreasing Pd nanoparticle size, has been observed both for oxygen and CO. This effect can be explained with two microscopic effects: weakening of the chemisorptive interaction and reduction of the VdW-interaction. The decrease of the adsorption energy of CO has been predicted in a recent theoretical study for Pd clusters [271]. According to these results, the interatomic Pd-Pd bond length in small metal particles decreases with decreasing particle size, which results in lower adsorption energies than on the bulk metal. A contraction of small nanoparticles has also been observed in electron microscopy studies [40–42]. According to the BOC model, introduced in chapter 2, an increased bond order of the surface Pd-Pd bond caused by the contraction of Pd nanoparticles results in a decrease of the bond order to the adsorbate. This would result in a smaller adsorption energy.
A second reason for the decrease of the adsorption energy of a gas-phase molecule on the small metal clusters is a feasible weakening of the VdW interaction strength. As discussed above, this type of interaction is induced by charge density fluctuations, which result in an induced dipole. Since smaller clusters contain fewer electrons, available for this dynamic response, the dispersive interaction strength can weaken. The relative magnitude of both effects has to be still tested with theoretical calculations.
It is an interesting question why the adsorption energy for the Pd deposition coverage 7 Å (6.4 nm) is somewhat lower than for the Pd coverage 4 Å (3.4 nm). Because in both cases, oxygen adsorb on edge sites. One possible explanation is that the adsorption energy for the Pd deposition thickness 7 Å (6.4 nm) is decreased due to coverage effects. Table 8.2 shows the fraction of edge sites, which are occupied during the first pulse. The coverage is twice as large on the edge sites for the Pd deposition coverage 7 Å (6.4 nm) than for the deposition coverage 4 Å (3.4 nm). At Θ_O=0.14, direct intermolecular repulsions are expected to be weak but a through-metal interaction could lead to a decrease of the adsorption energy. Although this is a plausible explanation for the lower adsorption energy for the largest particles, further experimental or theoretical effort is necessary to understand this observation.

8.6 Particle size effects at higher coverages

Particle size effects in the zero coverage regime have been discussed in the previous section. It is now an interesting question how the difference between the adsorption energies on the different systems changes with increasing oxygen coverage. To examine this effect, the oxygen coverage for the different particle sizes and Pd(111) was normalized to the total number of adsorbed oxygen atoms, shown in Figure 8.3 (a). The normalized coverage $\Theta^N(N_{O,ads})$ for the different

Pd nanoparticle sizes has been determined in the following way:

$$\Theta^N(N_{O,ads}) = \frac{N_{O,ads}}{N_{Pd,surf}} \tag{8.2}$$

$N_{O,ads}$ is the number of adsorbed oxygen atoms, which is dependent on the pulse number and $N_{Pd,surf}$ is the number of Pd surface atoms, which is shown in Fig. 8.3 for the different Pd coverages.
The oxygen adsorption energy versus this normalized coverage, $\Theta^N(N_{O,ads})$, for the investigated Pd/Fe_3O_4 systems and Pd(111) is shown in Figure 8.7. The difference in the adsorption energy

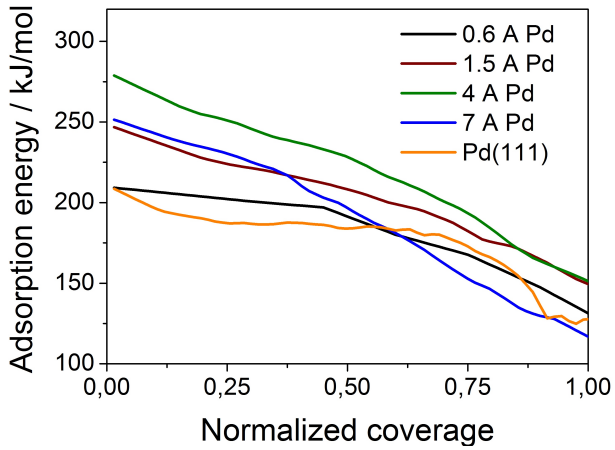

Abbildung 8.7: Oxygen adsorption energy versus the normalized coverage, $\Theta^N(N_{O,ads})$, for Pd nanoparticles of different sizes and Pd(111)

between the different systems is large in the zero coverage regime (70±17 kJ/mol). At high oxygen coverages, the difference in the binding energies for the different Pd surfaces become less pronounced. At saturation of the surface Pd sites, this difference in the binding energies decays to ≈35 kJ/mol.
It has been shown with IRAS experiments, that oxygen initially adsorbs on low coordinated sites such as edge and corner sites. Accordingly, the strong particle size dependence of the oxygen adsorption energy at low coverages results from the different binding energies of oxygen on these low coordinated adsorption sites. After saturation of the edge sites, oxygen occupies the (100) and (111) facets on large nanoparticles. Adsorption on sites with weaker oxygen binding energies and prominent adsorbate-adsorbate interactions at higher oxygen coverages could be responsible for the smaller difference in the adsorption energy between the different Pd/Fe_3O_4 systems.
A significant higher binding energy on edge sites of Pd particles has not been found in earlier TPD studies [45, 99, 272]. This disagreement can be, besides to the limitations of TPD to probe oxygen adsorption energies, attributed to the fact that these studies were performed mostly at the oxygen saturation coverage. The major contribution to the desorption peak at oxygen saturation arises due to desorption from ordered adsorbate structures from facet sites on large nanoparticles or sites with a similar adsorption energy in comparison to these sites on smaller particles.

The oxygen desorption energy on these sites is similar to that on the Pd(111) facet, which could explain why such effects have not been observed in TPD studies so far.

8.7 Summary

The coverage dependent adsorption energy and sticking coefficient of O_2 has been measured on Pd(111) and on Pd nanoparticles with the Pd deposition coverage 0.6 Å (2.3 nm), 1.5 Å (2.9 nm), 4 Å (3.4 nm) and 7 Å (6.4 nm). The sticking probability and the adsorption energy, measured as a function of the coverage, on Pd(111) are in good agreement with the literature results. The coverage dependence of the sticking coefficient on the Pd nanoparticles shows a complex behavior. Saturation of the surface Pd sites has been determined at an oxygen coverage of 0.38 ± 0.04, which is in good agreement with the findings of Henry et al. [77]. The adsorption energy of O_2 on Pd nanoparticles decreases strictly monotonically until the saturation coverage. The initial adsorption energy of 275 ± 14 kJ/mol on large Pd nanoparticles is significantly higher compared to the initial adsorption energy of 206 ± 7 kJ/mol on Pd(111). With complementary IRAS measurements, it was found that this high initial adsorption energy results from a change of the adsorption site from threefold hollow on Pd(111) to edge sites on Pd nanoparticles. By comparing the oxygen adsorption energy on Pd nanoparticles of different sizes, a second effect has been found to influence the oxygen binding energy. The decrease of the Pd nanoparticle size results in a decrease in the oxygen binding strength which has also been measured for CO adsorption on Pd/Fe_3O_4. This general phenomenon can be explained with two microscopic effects: weakening of the chemisorption interaction and reduction of the VdW-interaction due to a contraction of small Pd nanoparticles.
It has been observed that the difference in the oxygen adsorption energy between Pd nanoparticles of different sizes strongly decreases with increasing coverage. Accordingly, differences in the oxygen binding energy between the different systems are less pronounced at high oxygen coverages.

9 Interaction of oxygen with Pd particles at high oxygen exposures

At the lowest temperatures, oxygen adsorbs molecularly on Pd surfaces. Between 85 K and 200 K, dissociation takes place [94, 166, 237, 239, 246, 252, 254] and atomic overlayer structures are formed, which have been discussed in the previous chapter. At even higher temperatures and pressures, oxygen atoms diffuse into the substrate. Subsurface diffusion and surface oxide formation may occur and oxygen may form bulk oxides at high oxygen chemical potentials. The catalytic properties generally change with the oxygen concentration in the catalyst [160, 167].
In this chapter, oxygen adsorption on Pd nanoparticles at 300 K will be discussed. It will be shown with combined microcalorimetry and sticking coefficient measurements, that a large number of oxygen atoms occupy sites which do not correspond to adsorption sites on surface Pd atoms. Oxygen could be quantitatively converted to CO_2 upon titration with CO at 300 K.
After showing the oxygen sticking probabilities on Pd/Fe_3O_4 systems, the CO titration measurements on oxygen covered Pd will be discussed. Subsequently, the number of adsorbed oxygen atoms and evolved CO_2 molecules on Pd/Fe_3O_4 catalysts are compared and discussed.

9.1 Oxygen sticking measurements on Pd particles

In this chapter, oxygen adsorption on Pd(111) and two kinds of Pd/Fe_3O_4 systems will be discussed. Both Pd/Fe_3O_4 systems have been prepared according to the procedure described in chapter 6. The first Pd/Fe_3O_4 systems was directly transfered as prepared into the reaction chamber to perform the microcalorimetry experiments. This system will be referred to as [Pd/Fe_3O_4]1 in the following. The second substrate was exposed to $\approx 1.1 \cdot 10^{14}$ O_2 molecules $cm^{-2}s^{-1}$ for $\approx$50 s and subsequently to a CO flux of $\sim 1.5 \cdot 10^{14}$ CO molecules $cm^{-2}s^{-1}$ for t=20 min at 490 K and annealed to T=580 K without CO exposure for t=5 min. The surfaces, which have been subject to this procedure once or twice are referred to as [Pd/Fe_3O_4]2 and [Pd/Fe_3O_4]3.
The sticking probability measurements for O_2 on Pd(111) and on Pd nanoparticles of different sizes, deposited on Fe_3O_4, have already been discussed in the previous chapter. Figure 9.1 shows the oxygen sticking probability as a function of the number of adsorbed oxygen atoms (N_O). In these experiments, a chopper opening time of 266 ms, a pulse period of 2 s and a beam intensity of 1.1 10^{14} molecules cm^{-2} s^{-1} was used. The black squares, the red circles and the olive triangles show the sticking probability on the freshly prepared systems and after one or two cycles of O_2 and CO exposure at 300 K and cleaning in CO at 490 K before annealing to $\approx$580 K.
Each plotted data set is the average of three to seven independent measurements. The error bars indicate the error of the mean.
As discussed above, S(0) on Pd(111) (black squares) is 0.47 ± 0.03 and decays strictly monotonously with increasing coverage until the saturation coverage is reached. As the number of

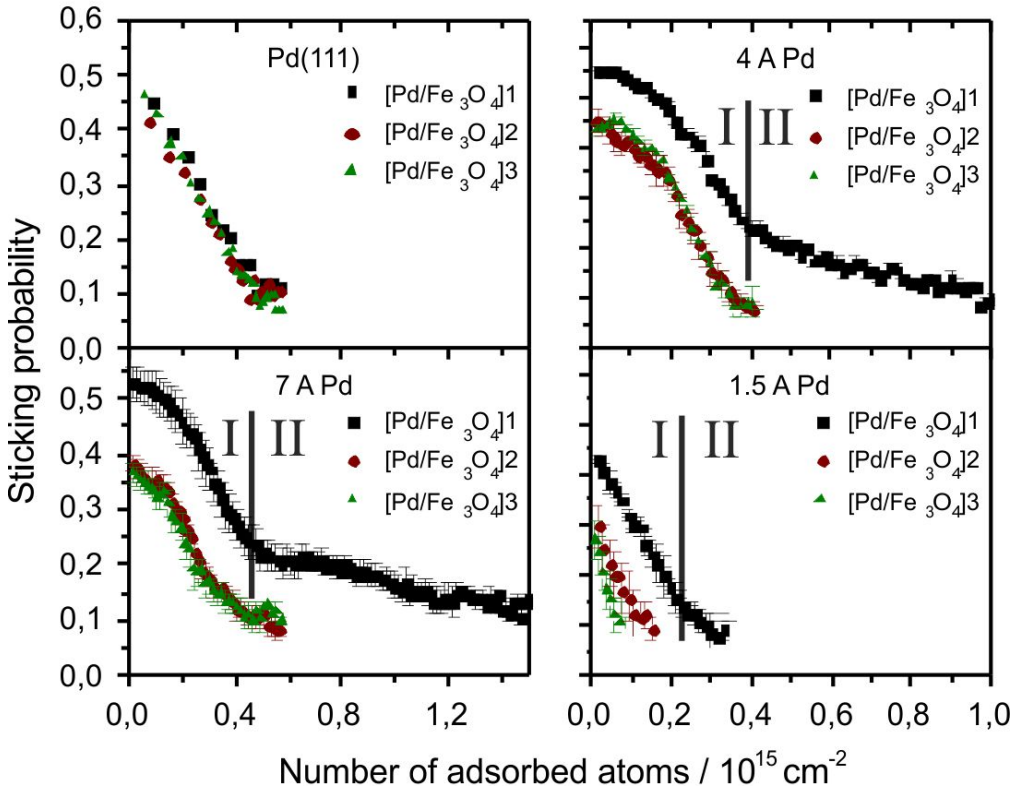

Abbildung 9.1: Oxygen sticking probability plotted versus the number of adsorbed oxygen atoms on Pd(111) and on Pd/Fe_3O_4 for three different Pd coverages. The black scatters show the sticking probabilities on the freshly prepared catalysts after annealing to 600 K. The red and green scatters show the oxygen sticking probabilities for the same catalysts, once or twice exposed to O_2 at 300 K and cleaning in CO at T=490 K before annealing to ≈580 K.

adsorbed oxygen atoms reaches 0.45-0.5 10^{15} cm^{-2}, saturation of the Pd surface sites is reached on Pd(111).

Figure 9.1 also shows the coverage dependent sticking coefficient for O_2 after one (red circles) and two (green triangles) cycles of O_2 and CO exposure at 300 K, extended CO exposure at T=490 K and annealing at T=580 K. It can be observed, that the coverage dependent sticking probability is similar to that on [Pd/Fe_3O_4]1. This demonstrates the reproducibility of the sticking probability measurements.

On large Pd nanoparticles, the sticking probability decays gradually at low oxygen exposures. A more pronounced decay is observed as the number of adsorbed oxygen atoms increases. For the deposition thickness 1.5 Å, a pronounced decay of the sticking probability is already observed at the lowest oxygen exposures. The sticking data at a lower number of adsorbed atoms as the end of this prominent decay of the sticking probability is denoted as regime I. It has been argued in Chap. 8 that the number of adsorbed molecules in regime I corresponds to an average coverage

of 0.38±0.04 on the Pd nanoparticles. Similar values for the oxygen saturation coverage on Pd nanoparticles have been found in previous studies [77]. Accordingly, regime I can be assigned to the saturation of the surface Pd sites. In regime II, a slow decrease of the sticking coefficient with further exposure can be observed on [Pd/Fe_3O_4]1. For the deposition coverage 7 Å Pd, there is a clear separation between regime I and II on [Pd/Fe_3O_4]1. A more gradual transition between the two regimes is observed for the deposition coverage 4 Å Pd, and even more for 1.5 Å Pd. The total number of adsorbed oxygen atoms is determined to be 14.7 10^{14} cm^{-2}, 9.6 10^{14} cm^{-2} and 4 10^{14} cm^{-2} for the deposition coverages 7 Å (6.4 nm), 4 Å (3.4 nm) and 1.5 Å (2.9 nm), respectively.
The oxygen sticking probability is much different on [Pd/Fe_3O_4]2 and [Pd/Fe_3O_4]3 than on [Pd/Fe_3O_4]1 for all three particle sizes. The measured initial sticking probability is lower by 0.15, 0.1 and 0.12 for the Pd deposition coverages 7 Å, 4 Å and 1.5 Å. The determined total number of adsorbed oxygen atoms on [Pd/Fe_3O_4]2 and [Pd/Fe_3O_4]3 is significantly lower compared to the systems directly after preparation and amounts to 0.5 10^{14} cm^{-2}, 0.39 10^{14} cm^{-2} and 0.16 10^{14} cm^{-2} for the Pd deposition coverages 7 Å (6.4 nm), 4 Å (3.4 nm) and 1.5 Å (2.9 nm).
The gradual decay of $S(N_O)$ in regime II cannot be observed on [Pd/Fe_3O_4]2 and [Pd/Fe_3O_4]3. Therefore, the sites which are saturated in regime II on [Pd/Fe_3O_4]1 cannot be occupied on [Pd/Fe_3O_4]2 and on [Pd/Fe_3O_4]3.

9.2 CO titration experiments

To check, if the sites, which are covered in regime II on [Pd/Fe_3O_4]1 are irreversibly occupied, CO titration experiments have been performed.
Initially, the Pd surfaces have been exposed to $3{\cdot}10^{16}$ O_2 molecules cm^{-2}. Subsequently, CO titration experiments are performed with a CO beam intensity of $1.8{\cdot}10^{14}$ molecules cm^{-2} s^{-1}, a chopper opening time of 500 ms and a pulse period of 8 s.
The number of CO molecules, which occupy the Pd surface sites and react with adsorbed oxygen to CO_2 can be determined from the CO adsorption experiments. The number of evolved CO_2 molecules can be evaluated from the QMS intensity data of CO_2.
In the following, the CO adsorption experiments are discussed. Upon CO adsorption at 300 K, two processes may occur: CO molecules either react with adsorbed oxygen atoms on the Pd nanoparticles to form CO_2 or adsorb without reaction. The total CO sticking probability is the fraction of the initially adsorbed CO molecules that undergo either process. Similarly, the number of adsorbed CO molecules corresponds to the number of CO molecules which react with oxygen and the number of CO molecules which are adsorbed without reaction.
As the CO titration experiments have been performed on catalysts which have been saturated with oxygen, these systems are referred to as O/[Pd/Fe_3O_4]1, O/[Pd/Fe_3O_4]2 and O/Pd(111) in the following.
Figure 9.2 shows the total CO sticking coefficient versus the number of adsorbed CO molecules on oxygen covered Pd(111) and on O/[Pd/Fe_3O_4]1 and O/[Pd/Fe_3O_4]2 for the Pd deposition coverages 7 Å and 4 Å. On Pd(111), S(0) is 0.72 and decays with increasing number of adsorbed CO molecules. Saturation is reached as the number of adsorbed CO molecules reaches $\sim 10^{15}$

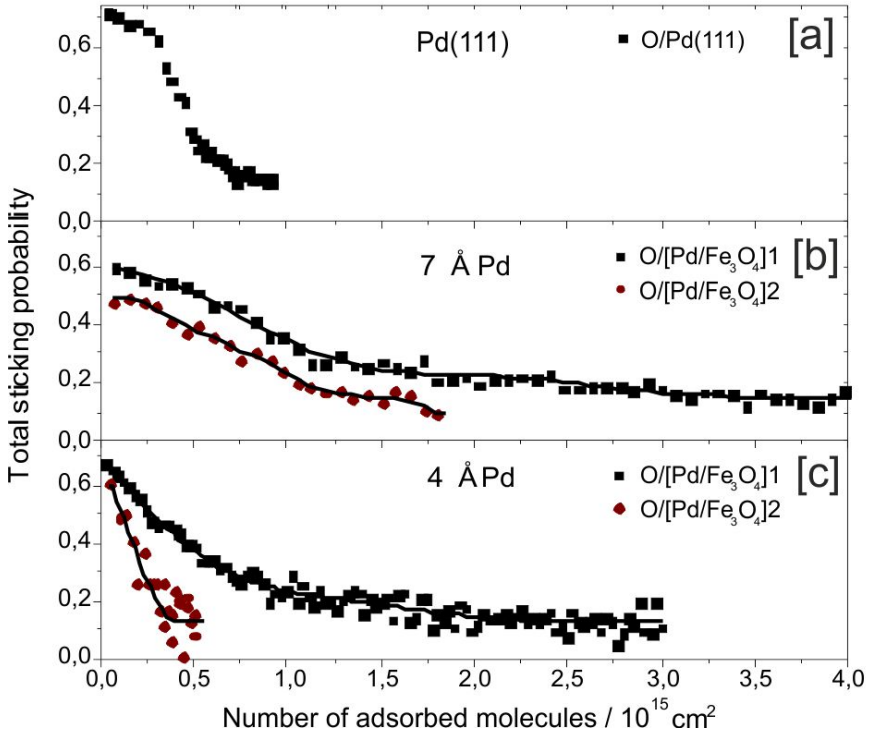

Abbildung 9.2: CO sticking coefficient vs the number of adsorbed CO molecules following oxygen adsorption on Pd/Fe_3O_4]1 and on [Pd/Fe_3O_4]2 on Pd(111) and Pd nanoparticles of two different sizes. A chopper opening time of 500 ms and a pulse period of 8 s has been used

cm^{-2}.

Significant transient adsorption/desorption from Pd nanoparticles at high CO exposures, which cannot be quantified from the present measurements at the conditions used here [205, 273], hampers the determination of the exact number of adsorbed molecules at high CO coverages. Nevertheless, the qualitative change in the total CO sticking coefficient as a function of the number of adsorbed CO molecules gives valuable information on the change in the adsorption behavior due to the cleaning procedure.

The initial total sticking probability of CO on O/[Pd/Fe_3O_4]1 with the Pd deposition coverages 7 Å Pd and 4 Å Pd is 0.6 and 0.67 and decays strictly monotonically with increasing CO exposure. On O/[Pd/Fe_3O_4]2, the initial total sticking coefficient of CO is reduced to 0.49 and 0.6 for the Pd deposition coverages 7 Å Pd and 4 Å Pd. It is also evident that the number of adsorbed CO molecules is significantly lower on the Pd nanoparticles after O_2 and CO exposure at 300 K and cleaning at elevated temperatures (O/[Pd/Fe_3O_4]2).

These results can be compared with the oxygen sticking measurements: the higher number of adsorbed oxygen atoms on [Pd/Fe_3O_4]1 compared to [Pd/Fe_3O_4]2 agrees with a higher number of adsorbed CO molecules on O/[Pd/Fe_3O_4]1 in comparison to O/[Pd/Fe_3O_4]2. The large number of adsorbed CO molecules on O/[Pd/Fe_3O_4]1 may occur due to CO adsorption and reaction

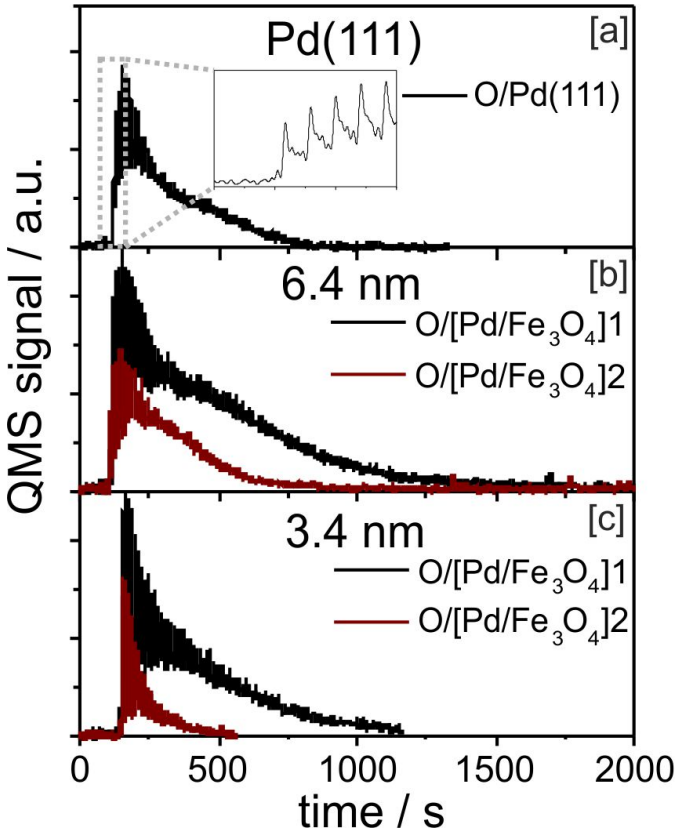

Abbildung 9.3: Intensity of the CO_2 signal as a function of the time, measured on Pd(111) (a) and Pd nanoparticles corresponding to the Pd deposition coverages 7 Å and 4 Å Pd after oxygen exposure. The black and red line correspond to the CO_2 intensities on O[$PdFe_3O_4$]1 and O/[$PdFe_3O_4$]2. A chopper opening time of 500 ms and a pulse period of 8 s has been used

with oxygen that adsorbs in regime II of the oxygen sticking data.
To find further evidence for this hypothesis, the CO_2 QMS signal, measured during the CO titration measurements, can be considered. Figure 9.3 shows the CO_2 signal, which is measured during CO exposure of oxygen covered Pd(111) and Pd nanoparticles of two different sizes. The corresponding total sticking probabilities for CO are given in Figure 9.2.
The background of the CO_2 signal from O/Pd(111), shown in Fig. 9.2 (a), increases prominently, then is approximately constant for a few seconds, and then gradually decreases. This behavior has been measured and modeled by several authors on supported nanoparticles in molecular beam measurements with continuous beams. A discussion on this subject can be found in the references [20, 77–79]. The strong variations of the signal, which are most prominent during the rise of the CO_2 intensity occur due to an increasing CO_2 evolution during the on time of the pulse (500 ms) and a decay during the off time of the pulse. These variations can be clearly distinguished from the rise in the CO_2 background in the inset of Fig. 9.2 (a).
Fig. 9.2 (b) and (c) show the CO_2 signals on oxygen covered Pd nanoparticles for the Pd depo-

sition coverages 7 Å and 4 Å for the freshly prepared system (black line) and for the catalysts after one cycle of oxygen and CO exposure and cleaning at elevated temperatures (red line). It can be clearly seen that the CO_2 release is significantly higher on O/[Pd/Fe_3O_4]1 compared to O/[Pd/Fe_3O_4]2. To obtain a quantitative measure for the amount of oxygen that reacts during CO exposure, the background substracted CO_2 peak area was integrated. By calibrating the CO_2 peak area from O/[PdFe_3O_4]1 and O/[PdFe_3O_4]2 to the CO_2 area from O/Pd(111), the number of evolved CO_2 molecules has been determined. Note, that adsorbed oxygen atoms on Pd nanoparticles can be completely removed upon CO exposure at 300 K on O/Pd(111) [65, 69, 70, 233]. The CO_2 release, obtained in this manner can be compared to the number of adsorbed oxygen

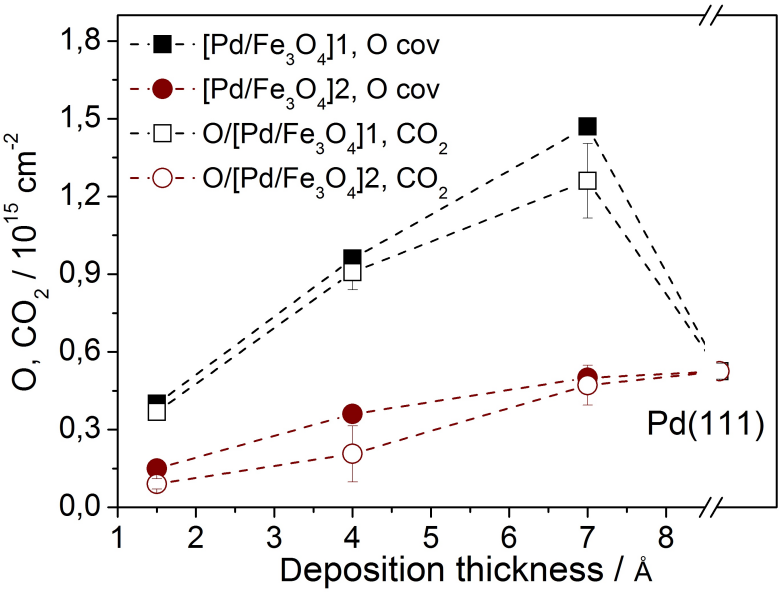

Abbildung 9.4: Comparison of the number of adsorbed molecules on [PdFe$_3$O$_4$]1 (squares) and [PdFe$_3$O$_4$]2 (circles): the filled symbols indicate the number of adsorbed oxygen atoms which are obtained by sticking coefficient measurements, the hollow symbols show the measured CO_2 release, the error bars indicate the standard deviation

atoms on Pd/Fe_3O_4 systems, determined from the oxygen sticking measurements (Fig. 9.1). Both quantities are shown for the investigated Pd deposition coverages on [Pd/Fe_3O_4]1 (black scatters) and on [PdFe$_3$O$_4$]2 (red scatters) in Figure 9.4. The filled black squares indicate the number of adsorbed oxygen atoms, the hollow black squares show the measured CO_2 release on [Pd/Fe_3O_4]1. The number of adsorbed oxygen atoms and the CO_2 release on [Pd/Fe_3O_4]1 is very similar for the three particle sizes, thus the major oxygen fraction can be removed upon CO exposure at 300 K. The number of adsorbed oxygen atoms is 1.26-1.47 $\cdot 10^{15}$ cm^{-2}, 0.9-0.96 $\cdot 10^{15}$ cm^{-2} and 0.37-0.4 $\cdot 10^{15}$ cm^{-2} for the deposition coverage 7 Å Pd , 4 Å Pd , 1.5 Å Pd on the freshly prepared system. The filled and the hollow red circles show the number of adsorbed oxygen atoms and the number of evolved CO_2 molecules on [Pd/Fe_3O_4]2. Also in that case, the number of adsorbed oxygen atoms and the CO_2 release is in good agreement but the number of

adsorbed O atoms is significantly lower than on [Pd/Fe_3O_4]1.

9.3 Discussion of the oxygen adsorption and CO titration results

To obtain a better measure for the amount of adsorbed oxygen, the number of adsorbed oxygen atoms, $N_{O,tot}$, is divided by the number of surface Pd atoms $N_{Pd,surf}$. $N_{Pd,surf}$ for [Pd/Fe_3O_4]1 has been estimated in Chap. 6.
$N_{O,tot}/N_{Pd,surf}$, which is equivalent to the determined oxygen coverage on the Pd nanoparticles is plotted in Fig. 9.5. This ratio is 1.3, 0.8 and 0.8 for the nanoparticles after preparation with the Pd deposition coverages 7 Å, 4 Å and 1.5 Å. Such a high $N_{O,tot}/N_{Pd,surf}$ ratio by far exceeds the oxygen coverage on the Pd nanoparticles which has been determined as ∼0.38 in the previous chapter. Figure 9.5 also shows $N_{O,tot}/N_{Pd,surf}$ for the Pd/Fe_3O_4 systems after oxygen and CO ex-

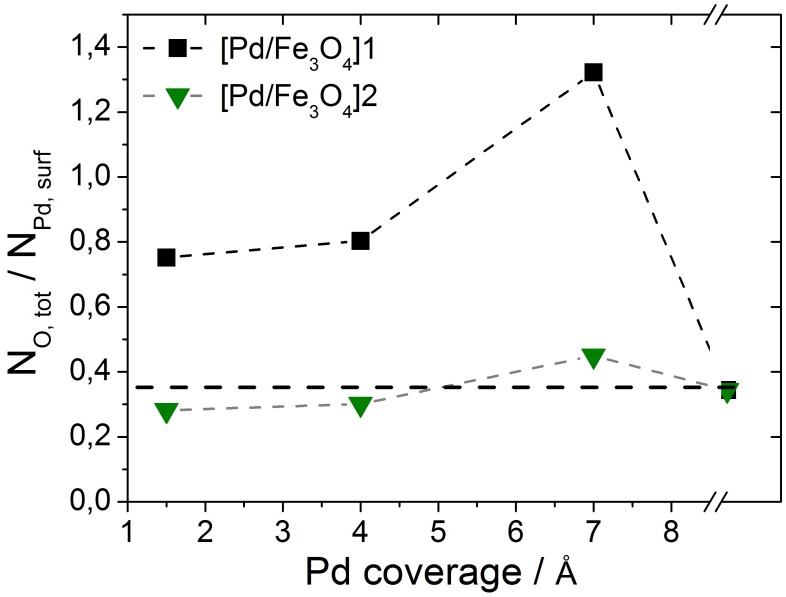

Abbildung 9.5: Number of adsorbed oxygen atoms in total ($N_{O,tot}$) divided by $N_{Pd,surf}$ for [Pd/Fe_3O_4]1 (black squares) and [Pd/Fe_3O_4]2 (green triangles)

posure at 300 K and by cleaning at elevated temperatures ([Pd/Fe_3O_4]2). It has to be mentioned that $N_{Pd,surf}$ has been assumed to be the same as on the freshly prepared systems. As discussed below, the possibility has to be considered that the particle morphology changes during the cleaning procedure. When neglecting possible structural changes during the cleaning procedure, the oxygen saturation coverage on [Pd/Fe_3O_4]2 is in reasonable agreement with what would be expected if oxygen exclusively saturates the Pd surface sites on the Pd nanoparticles.
As the number of adsorbed O atoms on [Pd/Fe_3O_4]1 is significantly higher than the number of oxygen atoms that are expected to adsorb on the Pd nanoparticles, the question arises what the nature of the additional sites, occupied by oxygen, are.
Different possibilities for O incorporation are are schematically shown in Fig. 9.6. Option one is

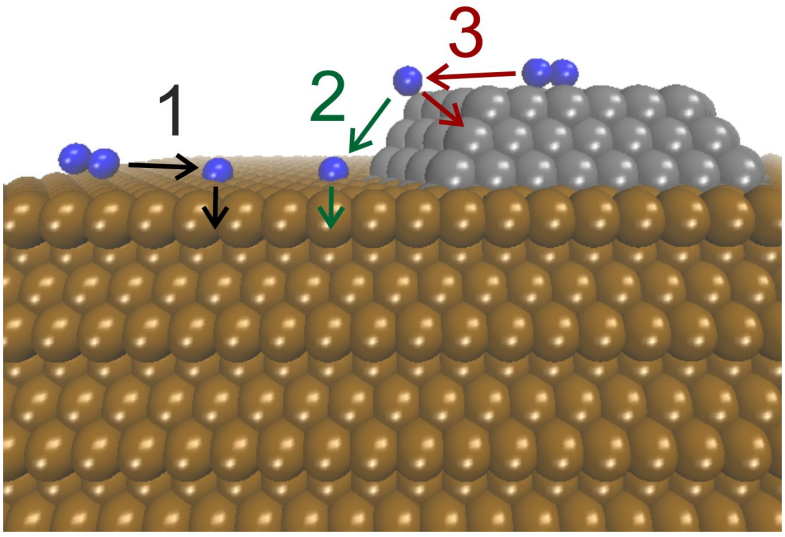

Abbildung 9.6: Schematical illustration of various possibilities for oxygen incorporation into the Pd/Fe_3O_4 catalysts.

dissociative oxygen adsorption on Fe_3O_4 and O diffusion into Fe_3O_4. This possibility can be excluded from oxygen adsorption measurements on Fe_3O_4 in which neither a measurable amount of adsorbed oxygen nor a heat release upon oxygen adsorption could be detected.
A second possibility, shown in Fig. 9.6, is dissociative O_2 adsorption on Pd, oxygen spillover onto Fe_3O_4 and O diffusion into Fe_3O_4. Upon CO exposure, O atoms within Fe_3O_4 would react with CO to CO_2. Schalow et al. performed isotopic exchange experiments in which they prepared the Fe_3O_4 film with $^{18}O_2$ and exposed the Pd/$Fe_3^{18}O_4$ catalyst subsequently to 130 L $^{16}O_2$ at 500 K [84, 221]. In case of oxygen diffusion into the oxide, a fraction of the ^{16}O atoms would exchange the ^{18}O atoms in Fe_3O_4, which could react with $C^{16}O$ to $C^{16}O^{18}O$. At T=500 K, ∼5 % of the total CO_2 release was observed to be $C^{16}O^{18}O$. It was concluded in this work, that oxygen exchange between the Pd nanoparticles and the Fe_3O_4 support is slow at 500 K. The oxygen exchange is expected to be even lower at T=300 K, the temperature at which the CO titration experiments, described here, are performed. Oxygen could however occupy interstitial sites or oxygen vacancies in the surface region of Fe_3O_4 which could react to CO_2 upon CO exposure. This has been discussed by Meyer et al., who suggested reaction of CO with the iron oxide during TPR experiments on Pd/Fe_3O_4 (T_{max}∼480 K) [220]. It is however an open question if O atoms can occupy these interstitial sites or oxygen vacancies on Fe_3O_4 at T=300 K and if CO can react with these oxygen species at 300 K.
The third possibility, indicated in Fig. 9.6 is dissociative oxygen adsorption on Pd nanoparticles and subsequent subsurface oxygen diffusion into the nanoparticles. As discussed in the previous chapter, subsurface oxygen diffusion and the formation of surface oxides starts with a significant rate at T>500 K on Pd(111), at T>400 K on Pd(100) but already at T<300 K on Pd(110). Quantitative measurements of the O storage on the present system have only been published for Pd/Fe_3O_4 after performing a stabilization procedure: The Pd/Fe_3O_4 systems were exposed 5-6

Pd coverage	1.5 Å Pd/Fe_3O_4	4 Å Pd/Fe_3O_4	7 Å Pd/Fe_3O_4
		$[Pd/Fe_3O_4]1$	
Adsorbed O atoms in total / $10^{15} cm^2$	0.4	0.96	1.47
Fraction of O in bulk	0.31	0.34	0.29
Estimated energy of additional species / kJ/mol	160-200	160-200	120-130
		$[Pd/Fe_3O_4]2$	
Adsorbed O atoms in total / $10^{15} cm^2$	0.16	0.36	0.5
Fraction of O in bulk	0.04	0.04	0.04

Tabelle 9.1: Number of adsorbed oxygen atoms in total and per Pd atom in the bulk of the Pd nanoparticles for the case that oxygen diffuses into Pd. For $[Pd/Fe_3O_4]1$, an estimation for the formation energy of the oxygen species, which is formed in addition to adsorbed oxygen on the Pd nanoparticles is given

times to $\sim 10^{17}$ O_2 molecules cm^{-2} and to $5 \sim 10^{17}$ CO molecules cm^{-2} at 500 K. During this procedure, the catalyst structure has been observed to change dramatically. Oxygen incorporation into the Pd nanoparticles on these stabilized catalysts was not detected below 400 K-500 K [46, 48, 84]. As the Pd/Fe_3O_4 systems which have been used here have not been subject to this stabilization procedure, the adsorption properties may be different in that case. It has been shown above, that also the adsorption/reaction properties of the Pd/Fe_3O_4 systems directly after preparation and after cleaning at elevated temperatures significantly differ from the adsorption/reaction properties of the freshly prepared systems.
Libuda et al. performed PES studies on Pd/Fe_3O_4 systems and Campbell et al. on Pd/α-Al_2O_3 directly after preparation and annealing: in both studies, absorption on the 3d edge of Pd was measured but no indication of the formation of a palladium oxide has been found [45, 84]. Matolin et al. on the other hand found an unusual high number of adsorbed oxygen atoms on Pd/Al_2O_3 catalysts at 410 K and 300 K directly after preparation, which has been explained by Pd subsurface oxygen diffusion [29, 68]. Subsurface oxygen diffusion would also provide a possible explanation for the high number of adsorbed oxygen atoms observed in the present work on $[Pd/Fe_3O_4]1$.
Both possibilities, oxygen diffusion into Fe_3O_4 (2 in Fig. 9.6) and oxygen diffusion into the Pd nanoparticles (3 in Fig. 9.6) are consistent with the available experimental data. Based on our experimental data and the available literature data [29, 45, 46, 48, 68, 84, 87, 93, 160, 220, 221, 233], we cannot say conclusively whether the "additional" oxygen goes (1) exclusively into the oxide or (2) exclusively into the subsurface region of the Pd nanoparticles. It is likely that a fraction of the oxygen atoms diffuses into the oxide and a fraction into the Pd nanoparticles.
For the case that oxygen diffusion into Pd would take place, it is interesting to consider the oxygen content in the Pd nanoparticles $F_{O,bulk}$, which can be estimated as follows:

$$F_{O,bulk} = \frac{N_{O,tot} - N_{O,surf}}{N_{Pd,tot} - N_{Pd,surf}} \tag{9.1}$$

where $N_{O,tot}$ is the total number of adsorbed oxygen atoms and $N_{O,surf}$ is the number of adsorbed oxygen atoms on Pd nanoparticles. $N_{Pd,tot}$ is the total number of Pd atoms on the surface and $N_{Pd,surf}$ the number of surface Pd atoms.
It has been determined above, that $N_{O,surf} \sim 0.38 \cdot N_{Pd,surf}$. Within this approximation, the oxygen content in the Pd nanoparticles has been estimated and is given in Table 9.1. The resulting oxygen content in the Pd bulk would be roughly 30 %, independent of the Pd nanoparticle size. It is remarkable that the number of adsorbed oxygen atoms is not proportional to the surface area but to the particle volume and is an indication that oxygen may diffuse into the bulk of the Pd nanoparticles. A similar estimation for [Pd/Fe_3O_4]2 gives an oxygen content in the Pd bulk of $\sim$4 %. An oxygen content of 4 % is within the error of this estimation.
Although oxygen diffusion into Pd could explain the high number of adsorbed oxygen atoms on [PdFe_3O_4]1, oxygen spillover and diffusion into Fe_3O_4 provides an alternative explanation for our experimental observations. From the microcalorimetry experiments, the initial formation energy of the oxygen species which is formed in addition to adsorbed oxygen on the Pd nanoparticles can be estimated. The initial formation energies are given in Table 9.1 and are estimated as 120-130 kJ/mol, 160-200 kJ/mol and 160-200 kJ/mol for the Pd deposition coverages 7 Å (6.4nm), 4 Å (3.4 nm) and 1.5 Å (2.9 nm).
It has been discussed above, that the adsorption and reaction properties of the Pd nanoparticles are significantly different after one experimental cycle of O_2 and CO exposure at 300 K and cleaning at elevated temperatures compared to the system directly after preparation. One explanation for the changed reaction properties of the [Pd/Fe_3O_4]2 catalysts would be changes in the catalyst structure during the cleaning procedure. These structural changes could be responsible for modifications in the reactivities towards O_2 and CO.
Numerous studies have been performed which demonstrate changes in the particle morphology and structure of supported Pd catalysts upon annealing in combination with gas exposure. Granoui et al. observed the formation of well defined facets on sputtered Pd tips with field ion microscopy during annealing at 450 K and exposure to 3 L O_2 [105]. Penner et al. measured an onset of the sintering process upon annealing to T>670 K [45]. Shaikhutdinov et al. performed STM experiments on Pd/Fe_3O_4 which have been studied directly after preparation. The preparation procedure for these systems is identical to the one used here. Secondly, they performed STM experiments on supported model systems which have been subject to a stabilization procedure: The Pd/Fe_3O_4 systems were exposed 5-6 times to $\sim 10^{17}$ O_2 molecules cm^{-2} and to 5 $\sim 10^{17}$ CO molecules cm^{-2} at 500 K. Significant changes in the catalyst structure mainly due to Pd nanoparticle sintering have been observed in STM experiments subsequent to this procedure. As the cleaning procedure applied in the present work significantly differs from this stabilization procedure, no information on the catalyst structure after the present cleaning procedure exists.
Evidence for structural changes can be found by comparing S(0) of O_2 on [Pd/Fe_3O_4]1 with S(0) on [Pd/Fe_3O_4]2. The oxygen sticking probability is reduced by 0.15, 0.1 and 0.12 for the Pd deposition coverages 7 Å , 4 Å and 1.5 Å on [Pd/Fe_3O_4]2. A reduction of the initial sticking probability would be also expected after nanoparticle sintering, as the fraction of the area covered by Pd and the area of the capture zone would significantly decrease in that case. The changes in the adsorption/reaction probabilities of [Pd/Fe_3O_4]2 may however also be connected to modifications in the surface structure of Fe_3O_4 [220], changes in the Pd-oxide interface structure or other modifications in the Pd nanoparticle morphology that do not include Pd nanoparticle

sintering.
To summarize this section, two possibilities were found that could explain the high number of adsorbed oxygen atoms on [Pd/Fe_3O_4]1 which cannot be rationalized by only considering saturation of the oxygen adsorption sites on Pd: firstly dissociative oxygen adsorption on Pd, spillover onto Fe_3O_4 and diffusion into Fe_3O_4 and secondly oxygen subsurface diffusion into the Pd nanoparticles. The different adsorption/reaction properties of [Pd/Fe_3O_4]2 compared to [Pd/Fe_3O_4]1 may be caused by a change in the catalyst structure as e.g. during sintering of the Pd nanoparticles.

9.4 Summary

In this chapter, it has been shown with oxygen sticking coefficient measurements, that in addition to the regime in which oxygen saturates the Pd surface sites, a second regime exists, which has only been measured on Pd/Fe_3O_4 catalysts directly after preparation and not on the Pd/Fe_3O_4 systems after performing a cleaning procedure, which is described above. Complementary CO titration experiments showed that the number of adsorbed CO molecules is higher on O/[Pd/Fe_3O_4]1 than on O/[Pd/Fe_3O_4]2. The number of adsorbed O atoms is determined to be 3-4 times higher on [Pd/Fe_3O_4]1 in comparison to [Pd/Fe_3O_4]2. The number of evolved CO_2 molecules and the number of adsorbed O atoms are in good agreement.
Two possibilities were found which could explain the higher number of adsorbed oxygen atoms on [Pd/Fe_3O_4]1: Firstly, dissociative oxygen adsorption on Pd, spillover onto Fe_3O_4 and diffusion into Fe_3O_4 or secondly oxygen diffusion into the Pd nanoparticles. Based on the present results and the available literature data, both processes are feasible. For the case that oxygen diffuses into the Pd nanoparticles, the oxygen content in the Pd nanoparticles would be $\sim$30%, independent of the nanoparticle size.
The formation energy of the species, which is formed in addition to the adsorbate layer on the Pd nanoparticles has been estimated as 160-200 kJ/mole for the deposition coverages 1.5 Å Pd, 4 Å Pd and and 120-130 kJ/mole for the Pd deposition coverage 7 Å .
The different adsorption/reaction properties of [Pd/Fe_3O_4]2 compared to [Pd/Fe_3O_4]1 may be caused by a change in the catalyst structure as e.g. during sintering of the Pd nanoparticles.

10 Interaction between CO and oxygen on Pd(111) and supported Pd particles

The formation of the various adsorbate phases on surfaces are governed to a large extent by the energetics of adsorbate-adsorbate and adsorbate-surface interactions. Although adsorbate structures can be studied with various surface science tools, quantitative information on adsorbate-adsorbate interaction energies can often only be obtained indirectly as e.g. with desorption based techniques. Our SCAC-setup provides the possibility to examine adsorbate-adsorbate interactions directly with a full control of the adsorbate coverage.
In this chapter, the interaction between CO and O in mixed adsorbate structures on Pd(111) and on Pd/Fe_3O_4 is discussed. After a short literature summary, I will show results, obtained in the present work, on the sticking coefficients and the adsorption energies of CO on bare Pd(111) and on oxygen covered Pd(111). Afterwards, I will focus on the CO adsorption experiments on bare and oxygen covered Pd/Fe_3O_4 systems with the Pd deposition coverages 4 Å (3.4 nm) and 1.5 Å (2.9 nm). Before giving a short summary, adsorbate-adsorbate interactions on all three systems are discussed.

10.1 Introduction

The term adsorbate-adsorbate interaction has been introduced in chapter 2 for one adsorbate species on a substrate. If different kinds of adsorbates are present, mixed adsorbate structures may form which are often structurally significantly different from the adsorbate phases of one of the species. In such cases, changes in the adsorption energy may not exclusively result from direct and indirect adsorbate-adsorbate interactions. Modifications in the adsorbate structure (geometric effects) may additionally lead to energetic changes. In the most general definition, which will be used in the following, adsorbate-adsorbate interactions include all changes in the binding energy of one surface species due to the presence of the same and/or other surface species in some concentration [122].
CO has been found to adsorb non dissociatively on Pd facets with the molecular axis perpendicular to the surface [269, 274]. On Pd(111), CO randomly occupies fcc hollow sites at low coverages, higher exposures have been found to lead to island formation in a p($\sqrt{3}x\sqrt{3}$)$R30°$ structure with a saturation coverage of 1/3 [146, 161, 162]. Upon further CO exposure, a c(2x4) overlayer is formed which saturates at a coverage of 0.5, where both, fcc and hcp hollow sites are occupied [163–165]. At T»200 K, this structure is observed upon saturation of Pd(111) with CO [146], but at T$\leq$200 K the transformation into a more dense structure occurs. A high density CO phase with a diffuse LEED pattern was found at a coverage of 0.6-0.66 in early studies [14, 82, 146, 275]. CO was suggested to occupy threefold hollow sites and presumably on top sites in this adsorbate phase [146]. Saturation of the surface leads to the formation of a (2x2)3-CO

structure with a coverage of 0.75 below room temperature [82, 146, 162, 165, 275]. The IRAS features for this phase were assigned to CO adsorption on fcc and hcp hollow sites and on top sites.
As the Pd nanoparticles are terminated by (111) and (100) facets, CO adsorption on Pd(100) is relevant as well. On Pd(100), CO adsorbs in islands and forms a $(2\sqrt{2}x\sqrt{2})R45^\circ$ structure which saturates at a coverage of 0.5. This adsorbate phase is compressed into a $(3\sqrt{2}x\sqrt{2})R45^\circ$ overlayer with Θ_{CO}=0.67 upon further exposure. Saturation is reached at a coverage of Θ_O=0.75, where a $(4\sqrt{2}x\sqrt{2})R45^\circ$ phase is formed [146, 276–281].
The structure dependence of the CO adsorption energy was found to be relatively moderate on Pd surfaces. An initial adsorption energy of 142 kJ/mol has been found on Pd(111), which increases by 4-7 kJ/mol on stepped surfaces and by up to 11 kJ/mol on Pd(100), according to the results of Ertl et al. [269]. Other authors found that the adsorption energy is 1-15 kJ/mol higher on Pd(100) in comparison to Pd(111) [101, 270], which is in agreement with results from theoretical investigations [282].
CO adsorption on an oxygen saturated Pd(111) surface was found to result in separate oxygen and CO domains: a $(\sqrt{3}x\sqrt{3})R30^\circ$CO and a $(\sqrt{3}x\sqrt{3})R30^\circ$O phase were suggested to coexist on the surface [14, 106]. CO_2 evolution in this phase was observed at T>180 K. Upon O_2 and CO adsorption below room temperature, the formation of a (2x1) phase was found, which has been always accompanied by a p$(\sqrt{3}x\sqrt{3})R30^\circ$ phase [14, 69, 70]. The p$(\sqrt{3}x\sqrt{3})R30^\circ$ structure has been assigned to a pure CO phase with Θ_{CO}=1/3. It has been suggested that the (2x1) phase is a mixed oxygen-CO phase which consists of alternating O and CO rows with Θ_O=Θ_{CO}=0.5 [14, 69, 106, 107]. Other results suggested, that the (2x1) phase is a pure oxygen phase [108, 109].
Adsorption of CO on Pd(100) with Θ_O<0.25 was found to result in separate O and CO domains, in which CO forms a $(2\sqrt{2}x\sqrt{2})R45^\circ$ structure with $\Theta_{CO} = 0.5$ whereas oxygen was suggested to adsorb in p(2x2) and c(2x2) islands, in which no CO is adsorbed at low CO coverages. Indications for the formation of O-Pd-O complexes in the interior of the O islands were found upon higher CO exposures [94]. Unfortunately, no experimental information on mixed CO-O adsorbate structures at higher oxygen coverages are available in the literature on Pd(100), although theoretical investigations on different hypothetical coadsorbate phases have been performed by Scheffler et al. [281].

10.2 Experimental strategy

In Chapters 8 and 9, results from O_2 adsorption experiments probed by SCAC on Pd(111) and Pd nanoparticles of different sizes, supported by Fe_3O_4, have been shown. These results are relevant for determining how the catalyst structure influences the oxygen adsorption behavior, but may additionally contribute to understanding the energetics of the CO oxidation path.
In the limiting case of a reaction on an oxygen covered Pd catalyst, the CO oxidation reaction may be separated into the three steps, schematically shown in Fig. 10.1. The first step would be O_2 adsorption on oxygen covered Pd. ΔE_1 can be extracted from the SCAC measurements of oxygen adsorption on Pd(111) and on Pd nanoparticles of different sizes. In order to probe the second step of the reaction path, CO adsorption on oxygen covered Pd, measurements have to

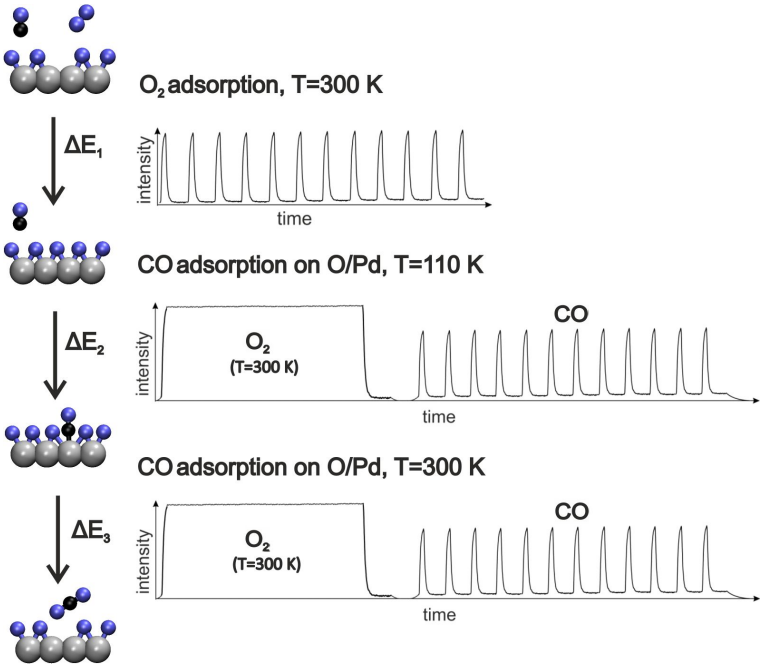

Abbildung 10.1: Schematic illustration of the reaction steps of the CO oxidation in the limiting case of a reaction on an oxygen covered surface. A sketch of an experimental procedure for determining the energetics of these three steps is shown.

be performed at temperatures at which no CO oxidation occurs. The results of these experiments are discussed in the present Chapter, in which CO adsorption on O/Pd is compared with CO adsorption on bare Pd. As indicated on the right hand side of Fig. 10.1, where the gas intensities on the catalysts are schematically shown, the surface is first exposed to oxygen at T=300 K. SCAC measurements of CO adsorption are then performed at a temperature of 110 K. The initial adsorption energy of CO on the oxygen covered Pd catalysts corresponds to ΔE_2.
In principle, the CO oxidation energy on the Pd surfaces, ΔE_3, can be probed by CO adsorption experiments on oxygen covered Pd surfaces at a temperature of 300 K, at which CO_2 evolution takes place. ΔE_3 will be discussed in the next Chapter.

10.3 CO-O coadsorption on Pd(111)

To obtain information on the CO-O interaction on Pd(111), CO adsorption experiments on oxygen covered Pd(111) have been performed at T$\sim$110 K. At such conditions, no CO_2 evolution has been observed previously [14, 70, 108]. CO adsorption on bare Pd(111) is compared with CO adsorption on oxygen covered Pd(111), to obtain information on the CO-O interaction. Oxygen saturation has been achieved by exposure at P_{O2}=5 $\cdot 10^{-7}$ mbar at 300 K for $\approx$5 minutes. Directly afterwards, the sample was cooled down to perform the CO adsorption experiments at 110 K. A pulse time of 266 ms and a CO molecular beam flux of 1.2 $\cdot 10^{14}$ has been chosen for these experiments.

The sticking coefficient and the adsorption energy as a function of the CO coverage is given in Figure 10.2. All shown results are the average of at least three independent measurements. Due to transient CO adsorption during the pulse and CO desorption in between the pulses at high CO exposures, which will be discussed in more detail below, the sticking coefficient remains relatively high close to saturation. On pristine Pd(111) at 110 K, the initial CO sticking coefficient

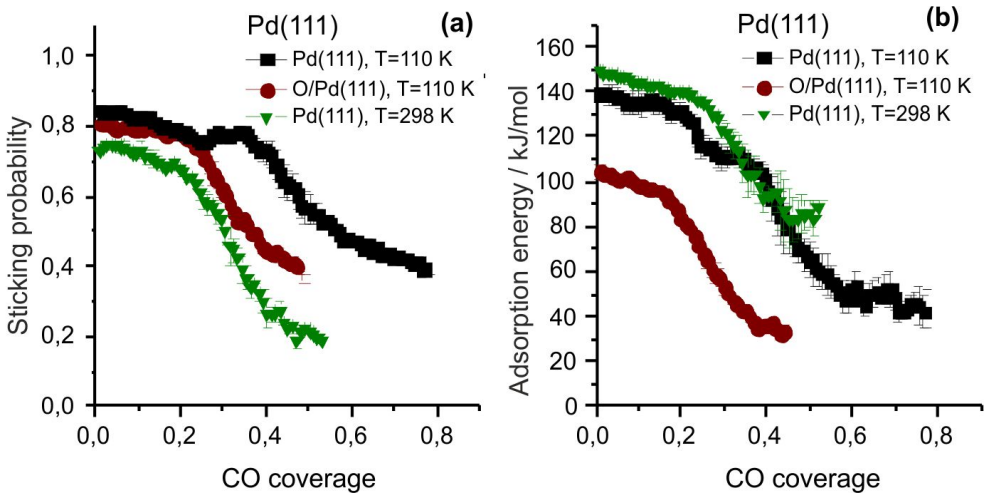

Abbildung 10.2: Sticking probability and adsorption energy for CO, measured at 110 K, plotted versus the CO coverage on bare Pd(111) (black square scatters) and after 5 min oxygen exposure at $P_{O2}=5\cdot10^{-7}$ mbar at 300 K (red circular scatters). The green triangular scatters show the sticking coefficient and adsorption energy for CO, measured at 300 K on bare Pd(111).

of 0.84 is slightly lower than the literature value of 0.92-0.95, measured under similar conditions [242, 269, 283]. The initial adsorption energy of 149±2 kJ/mol is in reasonable agreement with the binding energy, measured by Ertl et al. (142 kJ/mol) with TPD [269] and in excellent agreement with earlier SCAC-results (149±3 kJ/mol) [205].

The CO sticking coefficient on Pd(111) is approximately constant until a CO coverage of 0.35, which indicates precursor mediated adsorption. Examples for such a behavior can be widely found in the literature [156, 284]. Whereas the sticking coefficient is approximately constant until a coverage of 0.35, the adsorption energy drops to a lower value at a coverage of 0.23. A sudden decrease in the desorption energy at $\Theta_{CO}=0.33$ has been observed in TPD studies by Ertl et al. and associated with a transformation of the adsorbate structure. The prominent decay of E_{ads} and S at the coverage 0.35 can be rationalized with the transformation of the $p(\sqrt{3}x\sqrt{3})R30^{\circ}$ phase into the c(2x4) phase at $\Theta_{CO}\geq0.33$, observed in previous studies [163–165]. A lower adsorbate binding energy in the more dense c(2x4) phase is expected due to stronger adsorbate-adsorbate interactions.

The adsorption energy reaches a constant value at a coverage of 0.64±0.05 and the sticking probability remains constant at a CO coverage of 0.7-0.8. It can be additionally considered at which coverage the heat, which is evolved per pulse on the sample, reaches a constant value. At $\Theta_O>0.75$, the heat release changes by less than 4 % with respect to the initial heat release. In

good agreement between the sticking measurements and the consideration of the heat release per pulse, saturation of the surface is reached at $\Theta_{CO} \approx 0.75$. This value agrees with the literature [82, 146, 146, 162, 165, 275, 275]. As mentioned before, the relatively high sticking coefficient of ≈0.4 at saturation can be explained with transient CO adsorption of $\sim 10^{13}$ molecules cm^{-2} during the pulse and the same amount of molecules desorbing in between the pulses.
S(0) of CO on O/Pd(111) is slightly lower (0.81±0.01) and the adsorption energy is significantly lowered by 35±4kJ/mol compared to CO adsorption on bare Pd(111). The sticking coefficient is constant until the CO coverage reaches a value of about 0.2 and decays at higher coverages, whereas the adsorption energy already starts to decay at higher CO coverages than 0.08. At a coverage of ∼0.4, E_{ads} and the sticking coefficient remain constant. T0.17 Thus saturation of the Pd surface sites is reached at this coverage. The measured heat release per pulse remains constant at a coverage of ∼0.46.
In the following, changes in the sticking coefficient and the adsorption energy as a function of the CO coverage on oxygen covered Pd(111) are compared with changes in the adsorbate phases observed in previous structural and spectroscopic studies.
The saturation coverage of CO is in agreement with the structural model of a mixed c(2x1) phase together with a pure p($\sqrt{3}x\sqrt{3}$)$R30°$CO phase, as one expects a total CO coverage of 0.42 from the adsorbate phases, determined with microscopic studies [14, 69, 70]. If the (2x1) phase was a pure oxygen phase as has been suggested by other authors [108, 109], the total CO coverage was ∼0.17, which is definitely not the case.
During the transformation of the oxygen p(2x2) overlayer into the p($\sqrt{3}x\sqrt{3}$)$R30°$ phase, which is completed at $\Theta_{CO} = 0.08$, the sticking coefficient and the adsorption energy are approximately constant. Upon further CO exposure, the c(2x1) structure is formed, which coincides with a decrease of the sticking coefficient at a CO coverage which is higher than 0.08. From the literature data, it is not clear if the mixed c(2x1) is formed in a stepwise process, i.e. initial formation of the c(2x1)O phase and subsequent CO adsorption in this phase or if these two processes happen simultaneously.
In the first case, saturation of the c(2x1)O phase would occur at Θ_{CO}=0.17. Figure 10.2 shows a pronounced decay of the CO sticking probability and the adsorption energy as the CO coverage reaches ∼0.2. This indicates, that the mixed c(2x1) phase is formed in a stepwise process. Further investigations with IRAS or PES are necessary to verify this hypothesis, however.
As a comparison to the above results, the adsorption energy and sticking coefficient as a function of the coverage, obtained at 300 K on bare Pd, is shown in Figure 10.2. The initial sticking coefficient of 0.73 is lower than the sticking probability of 0.85±0.01 measured at 110 K. In comparison to the measurements at 110 K, the sticking coefficient and adsorption energy decay prominently at Θ_{CO}∼0.2. The heat release per pulse reaches a constant value at a coverage of 0.47-0.53, the sticking probability remains constant at $\Theta_{CO} > 0.53$. Accordingly, the saturation coverage, determined in the present studies, is ∼0.5. This is in good agreement with the CO saturation coverage of 0.5 found in the literature for CO adsorption at 300 K. The adsorption energy at this coverage is 86±5 kJ/mol.
Compared to the measurements at 110 K, the sticking coefficient, measured at 300 K, starts to decay at lower coverages. This could be explained by a shorter lifetime of the precursor state at higher temperatures. Accordingly, less ordered adsorption structures would be formed, resulting in a decay of E_{ads} at lower CO coverages [165]. Due to the less compact adsorbate structures

close to saturation, the adsorption energy in this regime is higher at 300 K. Significantly less transient CO adsorption/desorption at 300 K results in a decay of the CO sticking coefficient to lower values close to saturation at this temperature.

10.4 CO adsorption on bare and oxygen covered Pd/Fe_3O_4

10.4.1 Sticking coefficient and coverage

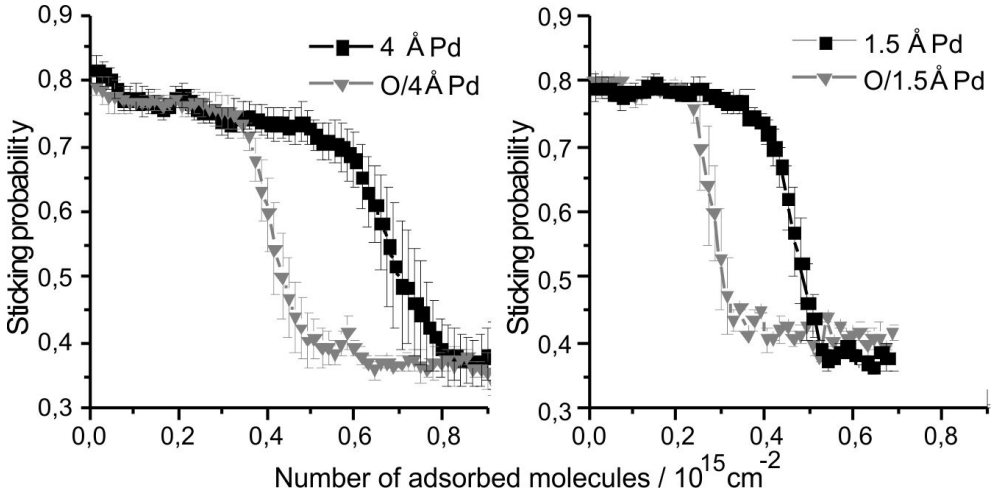

Abbildung 10.3: CO sticking probability on Pd/Fe_3O_4 at 110 K for the Pd deposition coverage 1.5 Å (2.9 nm) and 4 Å (3.4 nm), plotted versus the number of adsorbed CO molecules. The black and green scatters show the sticking probability on the Pd/Fe_3O_4 systems as prepared and after an oxygen exposure of $4 \cdot 10^{16}$ molecules cm^{-2} at 300 K.

Figure 10.3 shows the CO sticking coefficient on supported Pd nanoparticles with the Pd deposition coverages 4 Å (3.4 nm) and 1.5 Å (2.9 nm) after preparation (black squares) and after oxygen exposure at $P_{O2}=5 \cdot 10^{-7}$ mbar for t=5min. The modulation of the molecular beam is similar to the equivalent measurements on Pd(111).
Based on the results of chapter 7, the diffusion length of CO on iron oxide was estimated to be in the micrometer range at 110 K. Accordingly, the capture zones would completely cover the Fe_3O_4 surface.
The initial sticking coefficient of 0.82 ± 0.02 and 0.79 ± 0.02 for the Pd deposition coverages 4 Å (3.4 nm) and 1.5 Å (2.9 nm) are similar to the sticking coefficient of 0.84 ± 0.01 on Pd(111). The sticking coefficient is constant over a wide coverage range, both on oxygen covered and on bare Pd/Fe_3O_4.
The sticking probability strongly decays as the number of adsorbed CO molecules reaches $0.56 \cdot 10^{15}$ and $0.39 \cdot 10^{15}$on bare Pd nanoparticles for the Pd deposition coverages 4 Å (3.4 nm) and 1.5 Å (2.9 nm). On the oxygen covered Pd nanoparticles, the sticking coefficient decays as the number of adsorbed CO molecules reaches $0.33 \cdot 10^{15}$ and $0.22 \cdot 10^{15}$ for the Pd deposition

System	k_{des} / s^{-1}	System	k_{des} / s^{-1}
Pd(111)	1.1±0.1	O/Pd(111)	1.1±0.2
4 Å Pd/Fe_3O_4	2.1±0.1	O/4 Å Pd/Fe_3O_4	2.1±0.2
1.5 Å Pd/Fe_3O_4	2.3±0.2	O/1.5 A Pd/Fe_3O_4	2.2±0.3
Fe_3O_4	2.1±0.2	O/Fe_3O_4	2.0±0.3

Tabelle 10.1: Desorption rate of CO from Pd(111), Pd/Fe_3O_4 and from bare Fe_3O_4 per time and number of adsorbed molecules at T=110 K on the bare surfaces and with oxygen exposure at T=300 K prior to the measurements (O/"catalyst")

coverages 4 Å and 1.5 Å . The sticking probability decays to a constant, non-zero value which is the same for the two particle sizes and is not changed by the oxygen treatment. Due to transient CO adsorption close to saturation, a quasi-steady state regime is reached where the number of adsorbed molecules during the pulse equals the number of molecules which desorb in between the pulses.
In this regime, the QMS intensity, which is measured after closing the beam shutter until the next pulse impinges on the surface can be used to model the CO desorption rate. Details on this evaluation are given in Chapter 5. Shortly, the QMS intensities on the sample and on the gold reference are compared to separate the decay of the QMS intensity due to desorption and due to the chamber behavior. To determine the desorption rate, it is assumed that CO desorbs in a first order process. Furthermore, it is assumed that the coverage dependence of the desorption rate can be neglected for the increase in the CO coverage within one pulse.
The desorption rate for CO on Pd(111) and Pd/Fe_3O_4 with and without O_2 exposure is given in Table 10.1. O/"catalyst" indicates, that the model systems have been exposed to $4 \cdot 10^{16}$ O_2 molecules cm^{-2} at 300 K prior to the measurement. Each value is the average of typically three to six independent measurements. To model the desorption rate, it is assumed that CO desorption is a first order process and that the coverage dependence of the desorption rate can be neglected. The latter assumption is justified by the fact that only $\sim 7 \cdot 10^{13}$ CO molecules adsorb during one pulse on the model catalysts in the CO saturation regime. It has been often observed, that the desorption rate in the first ∼1000 ms after the chopper closes is slightly higher than the subsequent desorption rate. Table 10.1 shows the initial desorption rate after the chopper closes.
The oxygen desorption rates from Pd/Fe_3O_4 are identical within the error to the desorption rates from Fe_3O_4. Accordingly, transient CO adsorption on Pd/Fe_3O_4 during the on time of the pulse can be attributed to CO adsorption on Fe_3O_4. The observation that the desorption rate is the same from oxygen covered Pd/Fe_3O_4 and from pristine Pd/Fe_3O_4 would be in line with this result. It is also possible that CO additionally desorbs from the Pd nanoparticles with a similar desorption rate. The determined desorption rate of 1.1±0.1 s^{-1} from Pd(111) and from O/Pd(111) is significantly lower than the desorption rate from the Pd/Fe_3O_4 catalysts of ∼2.1 s^{-1}. As discussed in chapter 7, the desorption prefactor for CO from Fe_3O_4 is estimated to be ν_{des}=$2 \cdot 10^{-11}$-$2 \cdot 10^{-12}$ s^{-1} by assuming that the measured adsorption energy of 25 kJ/mol equals the desorption barrier.
Saturation of the Pd/Fe_3O_4 model catalysts can be assumed to be reached after the pronounced decay of the CO sticking probability in Fig. 10.3. The total number of adsorbed CO molecules may be rationalized by considering the abundance of the different Pd facets on the Pd nanopar-

	Adsorbed CO molecules / 10^{15} cm^2	
	as prepared estimated	as prepared measured
Pd(111)	1.14	1.19
4 Å $PdFe_3O_4$	0.90	0.84
1.5 Å $PdFe_3O_4$	0.40	0.54

Tabelle 10.2: Estimated number of adsorbed CO molecules based on the CO coverage on the single crystal facets and the particle morphology (see text) compared with the measured number of adsorbed CO molecules on Pd catalysts.

ticles and their respective CO saturation coverages.
Recent STM studies on 20-30 nm large Pd nanoparticles, supported on TiO_2, showed that the CO adsorbate structures on the (111) facet of supported particles are identical to the ones on the Pd(111) single crystal [33]. No structural studies on the Pd(100) facet of Pd nanoparticles have been performed however. It is unclear if ordered adsorbate structures are also formed on the significantly smaller Pd nanoparticles which are used in the present studies. It is interesting though to consider the case that the CO phases which have been observed on the Pd(111) and Pd(100) facets are also formed on the respective facets of the Pd nanoparticles and compare the corresponding number of adsorbed molecules with the experimentally observed ones.
Based on this consideration, the CO saturation coverage on the Pd nanoparticles can be estimated by taking into account the ratio of (111) facets (80 %) to (100) facets (20 %) and the saturation coverage of CO at 110 K on these facets. On Pd(100), a saturation coverage of 0.75 has been determined by various groups [146, 276–281] and a saturation coverage of 0.75 has been determined on Pd(111) in recent studies [82, 146, 162, 165, 275]. Based on the abundance of the (111) and (100) facets, the CO saturation coverage on these facets and the number of surface Pd atoms, the number of CO molecules that are expected to adsorb on the freshly prepared Pd/Fe_3O_4 catalysts was calculated and is given in Table 10.2. Note, that the number of adsorbed CO molecules is given in 10^{15} cm^{-2} in contrast to Figure 10.2.
Table 10.2 shows, that the estimated CO coverage on Pd(111) of $1.14 \cdot 10^{15}$ cm^{-2} is in a good agreement with the measured value of $\sim 1.19 \cdot 10^{15}$ cm^{-2}. For the Pd deposition coverage 4 Å (3.4 nm), the estimated number of adsorbed CO molecules of $0.90 \cdot 10^{15}$ cm^{-2} is in reasonable agreement with the experimentally determined value of $\sim 0.84 \cdot 10^{15}$ CO molecules cm^{-2}. $\sim 0.54 \cdot 10^{15}$ CO molecules cm^{-2} are adsorbed for the Pd deposition coverage 1.5 Å (2.9 nm). This value is significantly higher than the estimated number of adsorbed CO molecules of $0.40 \cdot 10^{15}$ cm^{-2}. The larger discrepancy between the measured and the estimated number of adsorbed CO molecules for the smallest particle size can be explained with a larger error in the estimation of the CO coverage or of $N_{Pd,surf}$. But as mentioned above, it is also possible that no ordered adsorbate structures are formed on the smaller Pd nanoparticles.
Due to the saturation of the Pd catalysts with O_2, the number of adsorbed CO molecules decreases. The difference in the number of adsorbed molecules between the bare catalysts and the oxygen covered catalysts is determined to be $\sim 0.6 \cdot 10^{15}$ CO molecules cm^{-2} , $0.29 \cdot 10^{15}$ CO molecules cm^{-2} and $0.18 \cdot 10^{15}$ cm^{-2} on Pd(111), 4 Å Pd/Fe_3O_4 (3.4 nm) and 1.5 Å Pd/Fe_3O_4

(2.9 nm).

10.4.2 Adsorption energy

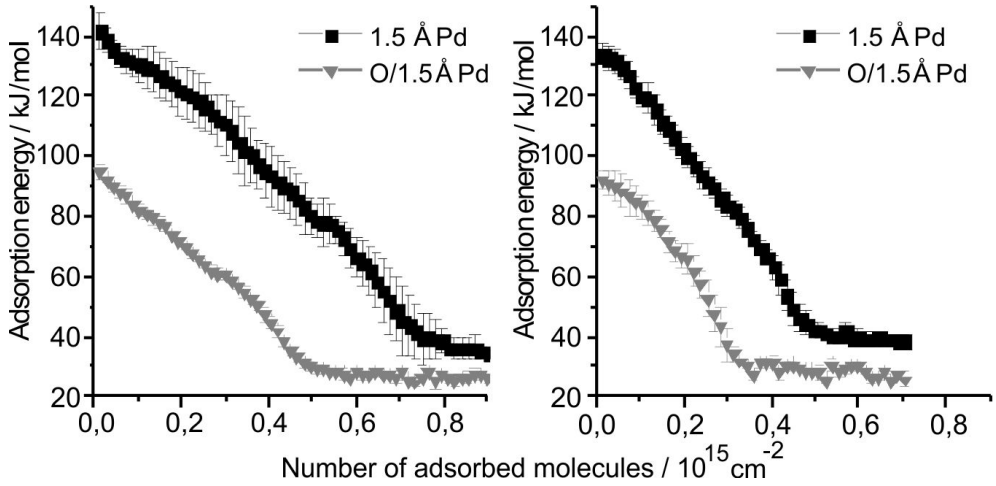

Abbildung 10.4: CO adsorption energy as a function of the number of adsorbed CO molecules at 110 K for the Pd deposition coverage 4 Å (3.4 nm) and 1.5 Å (2.9 nm), supported on Fe_3O_4. The black square scatters show the adsorption energies on the freshly prepared systems, the gray triangular scatters show the adsorption energy after O_2 exposure at P_{O2}=5 $\cdot 10^{-7}$ mbar for t=5min directly after preparation.

The adsorption energy of CO on bare Pd/Fe_3O_4 and on oxygen covered Pd/Fe_3O_4 is shown in Figure 10.4 for the Pd deposition coverages 4 Å (3.4 nm) and 1.5 Å (2.9 nm). Analogous results for adsorption experiments on Pd(111) are shown in Fig. 10.2. The data corresponds to the same experimental data used to calculate the sticking coefficients, discussed above. The initial CO adsorption energies of 142±6 kJ/mol and 134±4 kJ/mol are in reasonable agreement with the adsorption energies of 134±4 kJ/mol and 125±5 kJ/mol, measured previously with SCAC at 300 K on Pd/Fe_3O_4 systems. The Pd/Fe_3O_4 catalysts, used for the studies at 300 K have been prepared with the identical preparation procedure as the systems which are used for the present studies at 110 K [205, 229]. Figure 10.4 shows that the CO adsorption energy on Pd/Fe_3O_4 decreases strictly monotonically with an increasing number of adsorbed molecules, whereas it is constant until the number of adsorbed CO molecules reaches a value of $0.55 \cdot 10^{15}$ cm^{-2} on Pd(111). The CO adsorption energy on O/Pd/Fe_3O_4 is reduced by 47±6 kJ/mol and 42±5 kJ/mol for the Pd deposition coverages 4 Å (3.4 nm) and 1.5 Å (2.9 nm) with respect to the bare catalysts. This decrease is the result of adsorbate-adsorbate interactions between CO and oxygen.

It is remarkable that the slope of the CO adsorption energy as a function of the number of adsorbed CO molecules on oxygen covered Pd/Fe_3O_4 is roughly the same as the one on bare Pd/Fe_3O_4. On bare Pd(111), the adsorbate structures transform from a p($\sqrt{3}x\sqrt{3}$)$R30°$ phase into a c(2x4) phase, a c(2x2)3-CO phase is formed at the highest CO exposures [14, 82, 146,

146, 161–165, 275]. On oxygen covered Pd(111), where a p(2x2)O structure is present, separate $\sqrt{3}x\sqrt{3})R30°$O and $\sqrt{3}x\sqrt{3})R30°$CO domains are formed upon CO exposure. At the highest CO exposures, a high density c(2x1) phase was observed which was found to be accompanied by a p($\sqrt{3}x\sqrt{3})R30°$CO phase [14, 69, 70, 106–109]. Thus, CO adsorption on an oxygen covered Pd(111) surface leads to significantly different CO adsorbate phases than on bare Pd(111). If it is assumed that similar adsorbate transformations also occur on the Pd nanoparticles, a different coverage dependence of the CO adsorption energy would be expected on bare and on the oxygen covered Pd nanoparticles.
But Fig. 10.4 shows a very similar dependence of the CO adsorption energy on the number of adsorbed molecules on bare and on oxygen covered Pd nanoparticles.
Figure 10.5 shows the difference in the CO adsorption energy between pristine Pd and oxygen

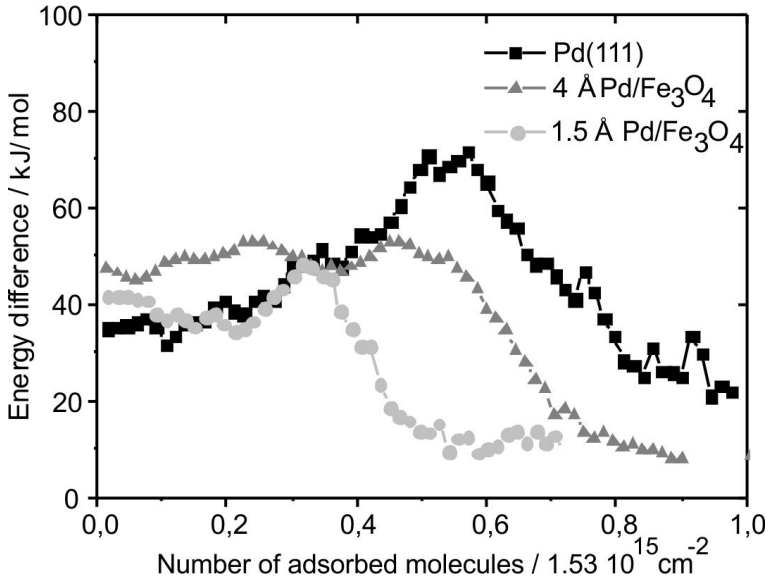

Abbildung 10.5: Difference between E_{ads} for CO on bare Pd and after O_2 exposure at P_{O2}=5 · 10^{-7} mbar for t=5 min (Ediff) as a function of the number of adsorbed CO molecules. The black square scatters, the dark gray triangular scatters and the bright gray circles show Ediff for adsorption on Pd(111), 4 Å Pd/Fe_3O_4 and 1.5 Å Pd/Fe_3O_4

covered Pd (Ediff) as a function of the coverage. Ediff is a measure for the change of the CO binding strength due to the presence of oxygen on the catalyst. Ediff is initially 40-50 kJ/mol and only slightly differs for the three systems. As discussed above, CO adsorption on oxygen covered Pd(111) leads to the formation of a dense coadsorbate structure at Θ_{CO}=0.17 on O/Pd(111), which causes a decay in the CO adsorption energy, whereas an analogous decrease in the adsorption energy is observed at higher coverages on bare Pd(111). As a consequence, Ediff is roughly constant until the number of adsorbed CO molecules is 0.17, reaches a maximum shortly before E_{ads} decays on Pd(111), and decreases at higher CO exposures.
On the supported systems, Ediff is roughly constant until CO saturation is reached for both Pd

deposition coverages. Accordingly, the difference in the CO adsorption energy due to saturation with oxygen is largely independent of Θ_{CO} on Pd/Fe_3O_4.

10.5 Summary

CO-O coadsorption experiments on Pd(111) and Pd/Fe_3O_4 have been discussed in this chapter. The experiments were performed at a temperature of 110 K at which no CO_2 evolution occurs. The sticking data shows that CO adsorbs via precursor states on all three substrates. On oxygen covered and bare Pd/Fe_3O_4, transient CO adsorption occurs in a weakly bound, physisorbed state on Fe_3O_4 close to CO saturation, although it cannot be excluded that transient CO adsorption occurs on the Pd nanoparticles as well. The CO desorption rate was modeled based on the assumption that CO desorption is a first order process and that the CO desorption energy is constant during the adsorption of $\sim 7 \cdot 10^{13}$ molecules cm^{-2}. The desorption rate is determined to be $\sim 2.1\ s^{-1}$.
The measured CO coverage on bare Pd(111) and on oxygen covered Pd(111) is in good agreement with the literature data. Based on the number of adsorbed CO molecules on Pd/Fe_3O_4 catalysts, it can be estimated that the CO coverage on the nanoparticle facets is comparable to the one on the respective single crystals in both cases.
The initial CO adsorption energy on pristine Pd(111) and on Pd/Fe_3O_4 is in agreement with earlier SCAC measurements. Due to CO-O interactions, the CO adsorption energy decreases by 35 ± 4 kJ/mol on Pd(111). This energy difference increases at an intermediate CO coverage and decreases again close to CO saturation. In contrast, CO-O interactions cause a decrease in the CO adsorption energy by 40-50 kJ/mol on oxygen covered Pd/Fe_3O_4 catalysts. This value is largely independent of the CO coverage until saturation.

11 CO oxidation

Catalytic oxidation of CO on platinum group metals is one of the most widely studied surface reactions, partially due to its relatively simple mechanism but also due to its practical importance. Nevertheless, information from experimental studies on the energetics of the various reaction steps on single crystal facets and especially on supported nanoparticles is still incomplete.
The energetics of oxygen adsorption and CO adsorption on the oxygen covered catalysts, investigated with the current SCAC setup, has been discussed in the previous chapters. In this chapter, our results on transient CO_2-evolution and the energetics of the reaction steps of the CO oxidation reaction on oxygen covered catalyst will be discussed.
In the first section of this chapter, the CO oxidation experiments on Pd(111) and Pd/Fe_3O_4 catalysts with the Pd deposition coverage 4 Å Pd (3.4 nm) and 1.5 Å Pd (2.9 nm) are discussed. In the second section, an estimate for the surface reaction energies of the three systems is given and the relative reaction energies on Pd(111) and Pd/Fe_3O_4 are compared.

11.1 Introduction

An introduction on the CO oxidation reaction on Pd facets and Pd nanoparticles has already been given in chapter 2. The overall reaction, which occurs via a Langmuir-Hinshelwood-mechanism, can be separated into several reaction steps: (i) the dissociative adsorption of O_2, (ii) the molecular adsorption of CO, (iii) the recombination of adsorbed CO and O and (iv) the desorption of CO_2. The literature on CO oxidation shows that the reaction constant is strongly dependent on the chemical composition of the surface and the surface concentration of CO and oxygen. The activation energy for CO oxidation on Pd(111) was found to be ∼105 kJ/mol for small CO and oxygen coverages [65, 66], ∼67 kJ/mol for $\Theta_{CO} < 0.25$ on an oxygen covered surface [65, 66, 68] and ∼41 kJ/mol at the highest CO and oxygen exposures [70].
The various mixed CO-O adsorbate structures, introduced in Chapter 10, were observed to exhibit different activities in the CO oxidation reaction. At 300 K on Pd(111), no reaction could be detected before or during compression of the oxygen p(2x2) phase into the $(\sqrt{3}x\sqrt{3})R30^\circ$ structure and reaction in the $(\sqrt{3}x\sqrt{3})R30^\circ$ phase has not been observed below 200 K, while reaction of the mixed c(2x1) adsorbate structure was found at temperatures as low as 136 K [69, 70, 108]. Also on Pd(100), an increased reactivity towards CO oxidation has been observed at higher adsorbate coverages: increasing the oxygen coverage from 0.04 to 0.24 at a fixed CO coverage of Θ_{CO}=0.05 leads to a decrease of the TPR peak from 422 K to 360 K [94].
Structure, size and support effects for CO oxidation on Pd have been observed. Matolin et al. found an activation barrier of 32 kJ/mol and 19 kJ/mol for CO oxidation on oxygen covered Pd nanoparticles with the particle sizes 27 nm and 2.5 nm, supported on α-Al_2O_3. An activation energy of 45 kJ/mol was found on oxygen covered Pd(111) [34, 68]. Due to the capture zone

effect, the turnover rate on Pd nanoparticles of different sizes supported on alumina have been observed to vary by one order of magnitude [26, 27]. Matolin et al. studied the reactivities of Pd nanoparticles of similar sizes supported on alumina supports which have been either oxidized, reduced or annealed prior to the experiment. Qualitative changes in the reactivity have been observed on these different supports [73]. For Pd nanoparticles with a smaller diameter than 4 nm, supported by mica [20, 201, 202], MgO [203] or γ-Al_2O_3 [29, 44, 72, 74], dissociative CO adsorption could be detected in several studies, whereas this has not been observed for larger particles. Dissociative CO adsorption may lead to carbon poisoning during the reaction.
Libuda et al. studied the particle size dependence of the the CO oxidation reaction with molecular beam experiments as a function of the relative fluxes of CO and O_2 on Pd/Al_2O_3 [78–80, 82]. At a low relative CO flux, where the nanoparticles are mainly covered by oxygen, CO adsorption is the rate limiting step: In this regime, the turnover rate was found higher on 6 nm-sized Pd nanoparticles compared to 1.8 nm-sized Pd nanoparticles by a factor of more than 2. At a high relative CO flux, the surface is almost completely CO covered and dissociative O_2 adsorption is the rate limiting step: In this regime, the turnover rate was observed to be higher on the smaller Pd nanoparticles. On 6 nm-sized Pd nanoparticles, strong changes in the IRAS features were observed as a function of the relative CO flux whereas these changes were found to be significantly weaker on Pd nanoparticles with the average size 1.8 nm. Communication effects could be observed in transient measurements on Pd/Al_2O_3 [76, 80, 81].

11.2 Reactivity measurements

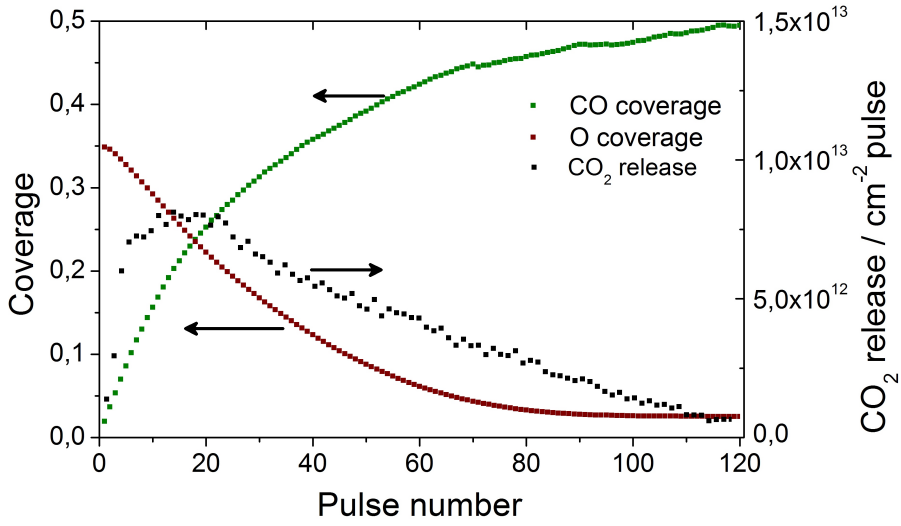

Abbildung 11.1: Plot of the oxygen and CO coverage together with the CO_2 release versus the pulse number on Pd(111). The corresponding adsorption measurement has been performed on an oxygen covered Pd(111) single crystal at 300 K with a chopper opening time of 500 ms and a CO flux of $1.8 \cdot 10^{14}$ cm^{-2}.

In the following section, the CO_2 evolution during CO exposure of different oxygen covered Pd

surfaces at 300 K is compared. Similar to the coadsorption experiments at ∼110 K, described in the previous chapter, the Pd surfaces have been exposed to $5{\cdot}10^{-7}$ mbar O_2 at 300 K for ∼5 minutes. Subsequently, CO dosing was performed via the molecular beam with a chopper opening time of 500 ms and a flux of $1.8{\cdot}10^{14}$ cm^{-2} at 300 K.
The CO and oxygen concentration together with the CO_2 release from such an experiment on Pd(111) is plotted versus the pulse number in Fig. 11.1. The CO coverage versus the pulse number has been measured directly in the CO sticking measurements. The initial oxygen coverage has been experimentally determined in Chap. 8. The variation of the oxygen concentration with the pulse number was determined based on the dependence of the CO_2 intensity with the pulse number.
Fig. 11.1 illustrates that CO adsorbs on Pd and additionally reacts with adsorbed oxygen to CO_2 at 300 K. With increasing pulse number, the adsorbed oxygen is consumed while CO covers the catalyst. The initial oxygen coverage of 0.35 decays to zero with increasing pulse number while the CO coverage increases to 0.5.
The CO_2 release is low at the beginning of the reaction and mainly CO adsorption takes place. With increasing CO coverage, the reaction rate increases and reaches a maximum between pulse number 8 and 18. The induction period for CO oxidation on Pd(111) is well documented in the literature [14, 67, 69, 70, 77, 168, 285] and has been attributed to the compression of the p(2x2) phase into the $(\sqrt{3}x\sqrt{3})R30°$ overlayer structure, as CO only reacts with the latter phase at 300 K [14, 65, 69, 70].
In Figure 11.2, the CO_2-release on O/ Pd(111) and on O/[Pd/Fe_3O_4]1, for the Pd deposition

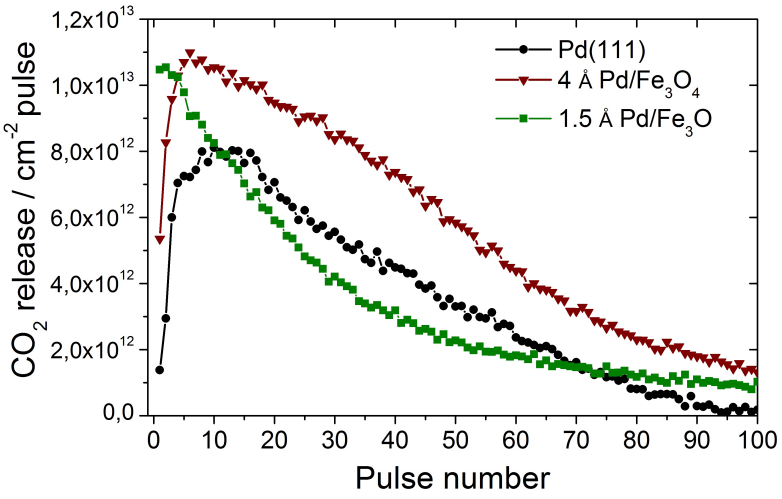

Abbildung 11.2: Comparison of the CO_2 release on O/Pd(111) (black scatters) and on O/[Pd/Fe_3O_4] with the Pd deposition coverage 4 Å (3.4 nm) (wine scatters) and 1.5 Å (2.9 nm) (olive scatters) Pd at 300 K versus the pulse number.

coverages 4 Å (3.4 nm) and 1.5 Å (2.9 nm), versus the pulse number is shown.
On O/Pd(111), $2{\cdot}10^{12}$ CO_2 molecules cm^{-2} are evolved during the first pulse, whereas $8{\cdot}10^{12}$ CO_2 molecules cm^{-2} and $15{\cdot}10^{12}$ CO_2 molecules cm^{-2} are evolved on Pd nanoparticles with the Pd deposition coverages 4 Å (3.4 nm) and 1.5 Å(2.9 nm). The CO_2 release is significantly

Surface	S(0)	$N_{Pd,surf}$ /cm^{-2}	$N_{CO}/N_{Pd,surf}$
Pd(111)	0.66	$1.53 \cdot 10^{15}$	0.03
4 Å Pd/Fe_3O_4	0.63	$1.20 \cdot 10^{15}$	0.04
1.5 Å Pd/Fe_3O_4	0.40	$5.32 \cdot 10^{15}$	0.05

Tabelle 11.1: Initial CO sticking coefficient, number of surface Pd atoms and ratio of adsorbed CO molecules to surface Pd atoms after the first pulse on Pd(111) and Pd/Fe_3O_4 for the Pd deposition coverages 4 Å (3.4 nm) and 1.5 Å (2.9 nm).

higher on the Pd/Fe_3O_4 catalysts. As only the reactivity on catalysts with a similar surface concentration of the reactive adsorbates can be directly compared, the different CO concentrations on the three catalysts after the first pulse have to be considered. Taking into account the initial CO sticking coefficient and the number of surface Pd atoms, given in Table 11.1, the fraction of the number of initially adsorbed CO molecules per surface Pd atom is calculated. Although the CO coverage on Pd(111) after the first two pulses is 17-50 % larger as that on O/[Pd/Fe_3O_4]1 after the first pulse, the number of evolved CO_2 molecules is 50-73 % lower on O/Pd(111) compared to the oxygen covered Pd nanoparticles. The reaction rate on O/Pd(111) does not reach the initial reaction rate on Pd nanoparticles with the deposition coverage 1.5 Å (2.9 nm).
Consequently, the CO oxidation rate is higher on Pd/Fe_3O_4 compared to Pd(111). The higher initial reaction rate on Pd nanoparticles, and the absence of an induction period, might be caused by a more rapid reaction on the Pd facets or by a fast reaction on different reaction sites such as the ones at the particle periphery, which has been suggested in the literature [220, 286].

11.3 Energetics of the CO oxidation reaction

The experimental strategy for determining the energetics of the CO oxidation steps on Pd(111) and Pd/Fe_3O_4 is illustrated in Fig. 11.3 and has already been discussed in Chap. 10. ΔE_1 can be determined from the SCAC data of O_2 adsorption on Pd, ΔE_2 corresponds to the CO adsorption energy on O/Pd, discussed in the previous Chapter. To obtain ΔE_3 experimentally, CO adsorption measurements on oxygen covered Pd(111) and Pd/Fe_3O_4 can be performed at temperatures at which CO_2 evolution occurs. This is indicated in Fig. 11.3. During CO adsorption on O/Pd at T=300 K, CO may react with adsorbed oxygen to CO_2 or adsorb permanently on Pd. As the CO adsorption energy on oxygen covered Pd is known from the CO adsorption measurements on oxygen covered Pd surfaces at 110 K, this contribution can be taken into account to determine ΔE_3.
Attempts to probe ΔE_3 with this procedure failed however due to the low reaction probability of CO with O on Pd at T=300 K of $\sim$1 %. As the absolute number of evolved CO_2 molecules is very low compared to the number of adsorbed CO molecules on Pd(111) and Pd/Fe_3O_4 at 300 K, the error in the determined reaction heat is very high after substraction of the large contribution due to CO adsorption.
An alternative route to determine ΔE_3 is illustrated in Fig. 11.4. The gas phase reaction energy ΔE_4 can be obtained from thermodynamic tables, ΔE_4 = 282 kJ/mol [287]. As the energy of a

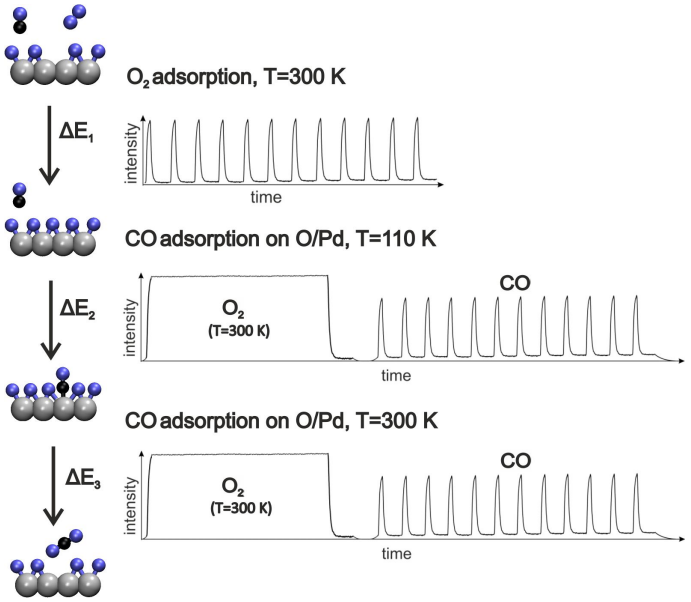

Abbildung 11.3: Schematic illustration of the reaction steps of the CO oxidation in the limiting case of a reaction on an oxygen covered surface. A sketch of an experimental procedure for determining the energetics of these three steps also shown.

system is a state function, the total energy change during a reaction is independent of the reaction path. Accordingly, ΔE_3 can be obtained as follows:

$$\Delta E_3 = \Delta E_4 - \Delta E_2 - \Delta E_1 \tag{11.1}$$

The estimated energies of the different CO oxidation reaction steps are given in Tab. 11.2. As discussed below, two different cases which lead to the energy contributions $\Delta E_{1,DPd}$ and $\Delta E_{1,DO}$, are considered for CO_2 evolution on Pd/Fe_3O_4.

ΔE_1 is the adsorption energy of 1/2 mole oxygen molecules on the oxygen covered surface. On Pd(111), oxygen was observed to adsorb on Pd(111) in a p(2x2) phase. Accordingly, ΔE_1 for Pd(111) is 1/2 of the O_2 adsorption energy at the saturation coverage of this phase and amounts to 60-93 kJ/mol.

The sticking measurements on Pd/Fe_3O_4 directly after preparation showed that after formation of an adsorbate layer on Pd, a second species with a lower formation energy is formed. For the determination of ΔE_1, it is necessary to know whether this weakly bound species participates in the reaction or not.

It was discussed in Chapter 9, that oxygen may diffuse into the oxide or occupy subsurface Pd sites at high oxygen exposures. Considering the boundary case that oxygen exclusively diffuses into Pd, this weakly bound species could participate in the CO oxidation reaction. Accordingly, ΔE_1 would be the adsorption energy measured at the highest oxygen exposures in the oxygen sticking measurements. The corresponding energy values for 1/2 mole of oxygen are denoted as $\Delta E_{1,DPd}$ in Tab. 11.2.

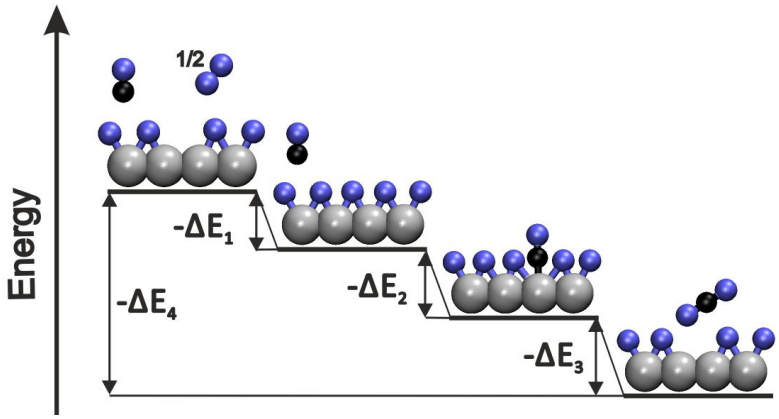

Abbildung 11.4: Schematical representation of the reaction steps of CO oxidation starting from an initially oxygen covered surface. The corresponding energy changes are indicated together with a sketch of the reaction system at each step.

Catalyst	ΔE_1		ΔE_2	ΔE_3	
Pd(111)	60-93		104	84-117	
Catalyst	$\Delta E_{1,DPd}$	$\Delta E_{1,DO}$	ΔE_2	$\Delta E_{3,DPd}$	$\Delta E_{3,DO}$
4 Å Pd/Fe_3O_4	32 - 47	80-100	95	140 - 155	91-111
1.5 Å Pd/Fe_3O_4	40 - 73	80-100	92	116 - 149	94-114

Tabelle 11.2: Energy changes during the reaction steps of the CO oxidation reaction starting from an oxygen covered surface, the nomenclature is analogue to Figure 11.4. All energies are given in kJ/mol. $\Delta E_{1,DPd}$ and $\Delta E_{3,DPd}$ correspond to ΔE_1 and ΔE_3 for the case that CO reacts with the weakly bound oxygen species on Pd. $\Delta E_{1,DO}$ and $\Delta E_{3,DO}$ correspond to ΔE_1 and ΔE_3 when assuming that CO exclusively reacts with adsorbed oxygen on the Pd nanoparticles

The second boundary case that oxygen exclusively diffuses into the oxide at high oxygen exposures has been discussed in Chap. 9 as well. By assuming, that CO does not react with this weakly bound species at 300 K, ΔE_1 would correspond to the oxygen adsorption energy close to saturation of the surface Pd sites on the Pd nanoparticles. This energy contribution is denoted as $\Delta E_{1,DO}$ in Tab. 11.2. As the coverage at which the saturation coverage is formed had to be estimated, this value may be subject to an additional systematic error.
The second step in the reaction path is CO adsorption on O/Pd in the limiting case of a zero CO coverage, the corresponding energy contribution ΔE_2 is also shown in Tab. 11.2 for the three different catalysts.
The surface reaction energy ΔE_3 is a very interesting quantity, as it reflects the gain in the total energy if the reaction takes place. As discussed above, this energy contribution can be estimated by using Equ. 11.1. It is assumed in this evaluation, that adsorbed CO reacts with the most weakly bound oxygen species on Pd. In case of for example a reaction of trapped CO on Fe_3O_4 at the particle periphery, ΔE_3 may be different.

Table 11.2 lists two values for the surface reaction energy on the supported catalysts. $\Delta E_{3,DPd}$ corresponds to the energy contribution for the case that CO reacts with the weakly bound O species that forms in addition to adsorbed oxygen on the Pd nanoparticles. For this case, the reaction energy would be $\sim$40 kJ/mol higher on Pd/Fe_3O_4 compared to Pd(111) for the two deposition coverages used here. $\Delta E_{3,DO}$ shows the surface reaction energy for the boundary case that oxygen exclusively reacts with adsorbed oxygen on the Pd nanoparticles. The range of $\Delta E_{3,DO}$ is similar to the one of ΔE_3, thus the reaction energy for that case would be similar on Pd(111) and on Pd/Fe_3O_4 for the two deposition coverages, used here.

11.4 Summary

In this chapter, the CO oxidation reaction on Pd(111) and on supported Pd nanoparticles with the particle sizes 3.4 nm and 2.9 nm have been discussed. It was shown that the turnover rate is more than two times higher on Pd/Fe_3O_4 than on Pd(111) at the lowest CO coverages used here. The energetics of the CO oxidation path on O/Pd(111) and O/[Pd/Fe_3O_4]1 has been discussed. To determine the surface reaction energy ΔE_3, two boundary cases have been considered in which oxygen either reacts with the weakly bound species that forms in addition to the oxygen adsorbate layer on Pd or not. In the former case, the reaction energies in the oxygen saturation regime are determined to be $\sim$40 kJ/mol higher on Pd nanoparticles with the Pd deposition coverages 4 Å and 1.5 Å. For the case that oxygen exclusively reacts with adsorbed oxygen on the Pd nanoparticles, the estimated surface reaction energies on Pd/Fe_3O_4 in the oxygen saturation regime is similar to the estimated surface reaction energy on Pd(111).

12 Adsorption of Propylene oxide on chirally modified Pt(111)

Chiral molecules are found in two enantiomeric forms which are non-superimposable mirror images of each other. These two enantiomers often react differently with other chiral molecules. One enantiomer of a drug may be effective in the treatment of a disease while the other enantiomer may be very harmful.
Therefore, there is an increasing need of chiral synthesis in pharmaceutical and agro industries [110, 111]. Today, homogeneous catalysts are used predominantly for the enantioselective synthesis in the industry but due to the numerous advantages of heterogeneous catalysts such as the easier handling and lower operational costs, the development of enantioselective heterogeneous catalysts is of an immense practical importance.
One approach towards asymmetric heterogeneous catalysis is via the chiral modification of surfaces. One enantiomer of a so called modifier is adsorbed on the surface to impose chirality to the surface. Subsequently, the reactant, which is a different molecule than the modifier, adsorbs enantioselectively on this modified surface. In some cases enantiomeric excesses of up to 93 % could be achieved with this strategy [114, 288, 289].
As the mechanism of this process is still unclear, we employ SCAC in order to obtain quantitative information on the energetics of the interaction between modifier and reactant as a function of the reactant coverage. The information, gained by such a study, could contribute to a more detailed understanding of the reaction process.
In this chapter, SCAC results on the enantioselective adsorption of propylene oxide (PropO) onto chirally modified Pt(111) by 1-(1-naphthyl)ethylamine (NEA) will be shown. In the first section of this chapter, I will introduce relevant literature results. Subsequently, the evolution of the NEA coverage as a function of the deposition time, probed by CO titration experiments, will be discussed before the microcalorimetric data on PropO adsorption on NEA modified Pt(111) is presented. In the end, I will compare the initial PropO adsorption energy for the two different enantiomers on R-NEA.

12.1 Introduction

Two mechanisms have been identified to promote enantioselective adsorption on chirally modified surfaces: the modifier may form a one-to-one complex with the reactant on the catalyst [119, 290–294]. Secondly, chiral modifiers may form a template on which specifically one reactant enantiomer may adsorb [295, 296].
Successful examples for the application of the second approach are the hydrogenation of β-ketoesters with tartaric acid modified nickel catalysts [112, 113] and the hydrogenation of α-ketoesters using platinum catalysts, modified by cinchona alkaloids [114–121]. Cinchona alka-

loids contain a quinoline ring which is believed to help anchor the modifier to the surface. A tertiary amine group may bind to acidic centers and a chiral center may promote enantioselectivity [297–299]. The most simple version of a combination of these functionalities are present in NEA.
Adsorption of either NEA enantiomer leads to an enhanced number of adsorbed molecules of the respective PropO enantiomer in some coverage range as has been observed with 2-butanol [297, 300–302] and 2-Methylbutanoic Acid [297, 303] on Pt(111) and Pd(111). The narrow coverage range in which the enantiomeric effect is observed indicates a cooperative effect.
IRAS data of Zaera et al. indicates that at low coverages, NEA adsorbs with the amino group towards the surface and the naphtalene ring standing up along its short axis on the surface at low exposures, while after reaching 0.5-2/3 of the saturation coverage, NEA adsorbs with the naphtalene ring standing up along its long axis on the surface [304, 305], the latter result is in agreement with the STM and NEXAFS results of Lambert et al., who observed a tilting angle of $46\pm5^\circ$ at saturation [306, 307]. On Pd(111) on the other hand, NEA seems to adsorbs in a flat configuration with a random occupation of Pd sites at 265 K, the coverage has been estimated to be $\sim$0.1 [308–310] while it is approximately 0.055 on Pt(111) [306]. On both surfaces, no long range order of NEA can be observed. Upon heating the NEA-covered Pt(111) surface, dimerisation with hydrogen elimination occurs at $\sim$320 K, further cleavage of C-H hydrogen bonds happens in several steps between 410 K and 650 K.
PropO adsorbs molecularly on Pt(111) at T<180 K. Above this temperature, molecular desorption competes with decomposition of PropO [311]. Coadsorbed with NEA, another desorption feature at $\approx$200 K is observed, indicating strong intermolecular interactions [304]. Zaera et al. found, that adsorption of PropO and NEA with the same chirality leads to a higher desorption temperature by 5 K with respect to PropO and NEA with opposite chirality. Furthermore, they could show that significantly more PropO adsorbs on a surface covered by NEA with the same chirality as opposed to adsorption on an NEA covered surface with the opposite chirality. This effect is only observed at NEA coverages of 0.5-2/3. From the IRAS intensities of PropO adsorbed on a NEA covered surface, the same conclusion could be drawn.
With Monte Carlo modeling, the high TPD yields for PropO in the homonuclear combination at intermediate NEA coverages could be reproduced quantitatively with models that take into account cooperative effects [312]. On the other hand, the stronger NEA-PropO interaction over a wide coverage range when both molecules have the same chirality suggests a one-to-one mechanism.

12.2 NEA coverage as a function of the exposure

In this section, the dependence of the R-NEA coverage on the R-NEA exposure, investigated by CO titration experiments, will be discussed. The Lewis structures of the two enantiomeric forms of NEA are displayed in Fig. 12.1. The enantiomeric center is located at the carbon atom, directly bound to the NH_2 group. NEA was held at a temperature of 273.5-273.8 K during the deposition. Prior to each experiment, NEA has been cleaned by several freeze-pump-thaw cycles. Subsequently, the gas doser was flushed for 20 minutes before the deposition of R-NEA at

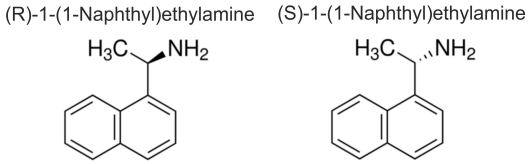

Abbildung 12.1: Lewis structures of the two NEA-enantiomers

≈110 K. After NEA exposure, the sample was transfered into the main chamber and the SCAC experiments were performed. For the molecular beam experiments, pulse time of 2 s and a CO flux of ≈1.2 ·10 ^{14} cm^{-2} s^{-1} was chosen. Figure 12.2 (a) shows the coverage dependent sticking

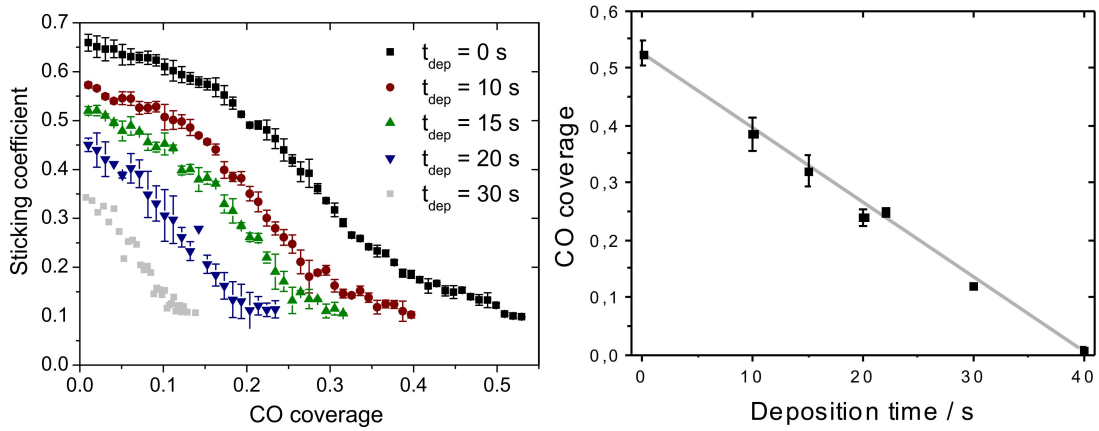

(a) (b)

Abbildung 12.2: (a) CO sticking coefficient measurements as a function of the coverage for different NEA exposures, and (b) the dependence of the CO coverage on the NEA deposition time (t_{dep}). The error bars correspond to the error of the mean, the gray line in b is an eyeguide.

coefficient on pristine Pt(111) and on Pt(111) after the deposition of NEA. On bare Pt(111), the sticking coefficient is initially high and decays strongly at an intermediate coverage. The coverage dependent sticking coefficient suggests precursor mediated adsorption as has been reported in the literature for CO adsorption on Pt(111) at 300 K [273, 313, 314]. The coverage dependence of the initial sticking coefficient is very similar to what has been observed by other authors, but the initial sticking coefficient of 0.66±0.02 is somewhat lower than the initial sticking probability of 0.75-0.8 reported in the literature [273, 313, 314]. If NEA is deposited on the surface, the initial sticking coefficient is smaller as well as the initial range, in which the slow decrease of the sticking coefficient is observed.
In Figure 12.2 (b), the obtained final CO coverage for the different NEA deposition times is plotted, which shows a linear dependence. The linear dependence shows that the NEA sticking coefficient is independent of the coverage at 110 K and is most likely close to unity.
For the case of cooperative effects, which lead to a more densely packed adsorbate overlayer

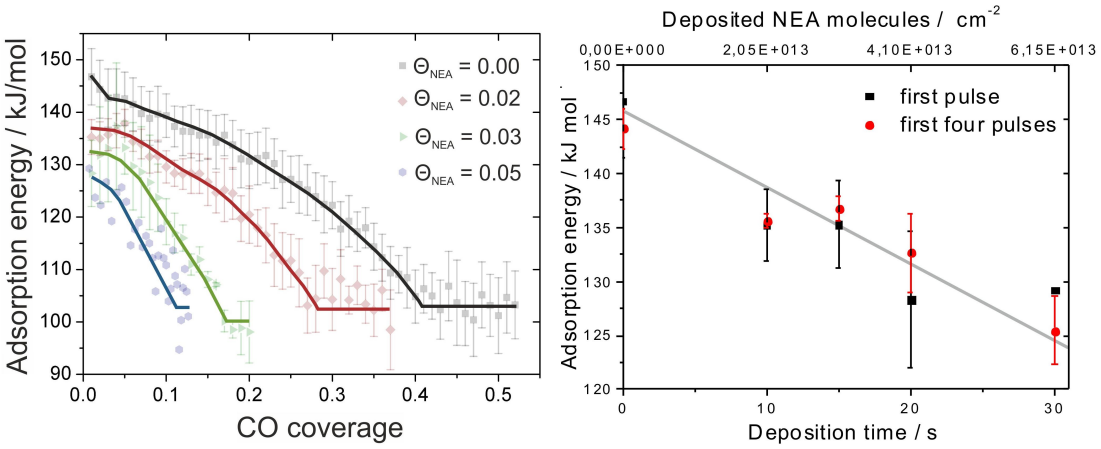

(a) (b)

Abbildung 12.3: (a) CO adsorption energy plotted as a function of the CO surface coverage for various NEA deposition coverages and (b) the dependence of the initial adsorption energy on the deposition time of R-NEA (b). The number of adsorbed NEA molecules has been calculated with the saturation coverage of a monolayer from [306]. The solid lines in a are eyeguides

as has been evidenced by Zaera et al. upon coadsorption with PropO [304], a deviation from the linear dependence would be observed in some coverage regime. Two reasons could be responsible for the fact that no significant deviation from the linear dependence is detected. Either cooperative effects occur in a coverage regime in which no CO titration experiments have been performed or they are only observable in coadsorption experiments with PropO.

The coverage dependent CO adsorption energy for various NEA coverages has been determined with microcalorimetric measurements. The results are shown in Figure 12.3 (a). The initial adsorption energy of 146±5 kJ/mol is in good agreement with earlier TPD measurements [313–315] (138-143 kJ/mol), but is significantly lower than the initial adsorption energy measured by King et al. with SCAC (187±11 kJ/mol) [132]. It should be mentioned that King et al. used a reflectivity value of 67 % for this evaluation. A reflectivity of 74 % has been measured at T∼110 K with the present setup, which is in good agreement with the literature [55, 316]. As the determined adsorption energy directly depends on the reflectivity, this could explain the discrepancy in the initial CO adsorption energies.

The adsorption energy decreases strictly monotonically with increasing coverage and reaches a constant value of 102±2 kJ/mol at CO saturation. With increasing NEA coverage, the adsorption energy decays to the final value at lower CO coverages. Figure 12.3 (b) shows the dependence of the initial adsorption energy on the NEA deposition time/NEA coverage. The black scatters show the initial adsorption energies and the red scatters show the adsorption energy averaged over the first four pulses. Lambert et al. have estimated the number of NEA molecules in a monolayer to be $\sim 8.2 \cdot 10^{13}$ [306]. Using this information, the deposition time was converted to number of deposited NEA molecules, which is shown in the upper x axis. It can be seen that the

CO adsorption energy decreases roughly linearly with the number of deposited NEA molecules.

12.3 Adsorption of R- and S-Propylene oxide on R-NEA

In the following section, PropO adsorption experiments on Pt(111), covered with different amounts of NEA, are discussed. For these experiments, the NEA flux has been increased by a factor of 2 compared to the experiments which were explained in the previous section. Accordingly, the formation of an NEA monolayer is completed after 20 s of deposition, which has been confirmed by CO titration studies. In these experiments, the pulse time has been chosen to be 266 ms and the PropO flux was 8.3 $\cdot 10^{13}$ molecules cm^{-2} s^{-1}. The sticking probability of PropO on Pt(111) at 110 K has been found to be 1 on NEA covered Pt(111) and on a PropO monolayer/multilayer. Figure 12.4 shows the adsorption energies of PropO on Pt(111), covered by 0, 0.5, 0.75 and 1

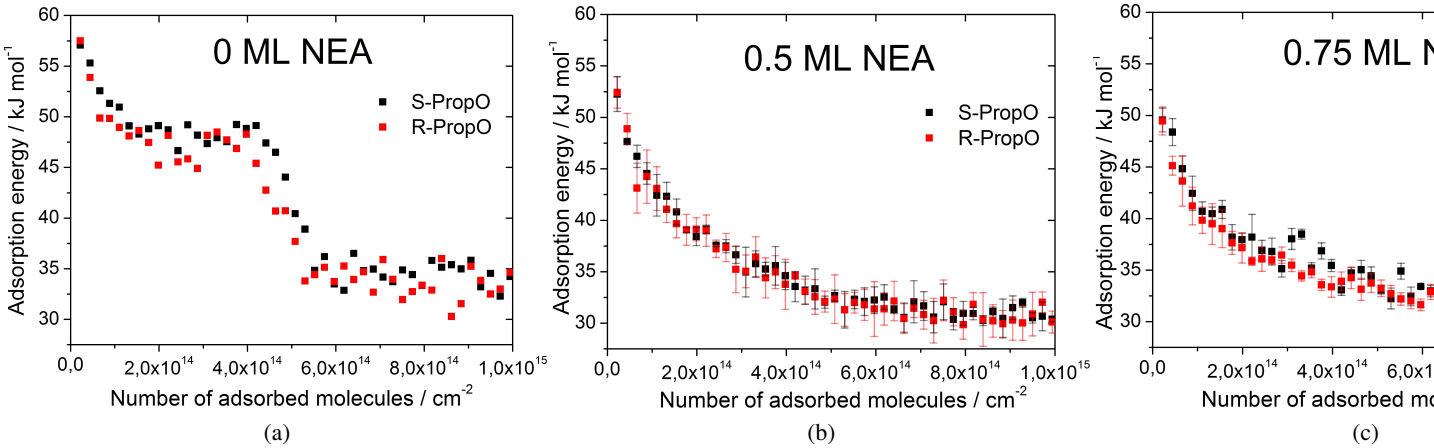

Abbildung 12.4: S-PropO molecules (black) and R-PropO molecules (red) versus the number of adsorbed molecules. The Figure headings show the R-NEA coverage.

ML of R-NEA as a function of the number of adsorbed PropO molecules. In 12.4 (a), the adsorption energies of R-PropO and S-PropO on bare Pt(111) are compared. The coverage dependence of the adsorption energy for the two enantiomers is roughly identical within the statistical error. The initial adsorption energy of 57±0.5 kJ/mol decays to 48±1 kJ/mol and is constant until the number of PropO molecules reaches 4-5$\cdot 10^{14}$ cm^{-2}. The constant adsorption energy at intermediate exposures suggests that the initial decay of the adsorption energy does not correspond to repulsive adsorbate-adsorbate interactions. This would be expected to result in a strictly monotonous decay of the adsorption energy until saturation. It seems more likely that the initial high adsorption energy is associated with adsorption on irregular Pt sites. That E_{ads} does not decay further until ∼30% of the Pt sites are filled suggests that the repulsive adsorbate-adsorbate interactions are relatively weak for PropO. The surface coverage of PropO on bare Pt(111) can be estimated to be ∼0.33.
The constant adsorption energy over a wide coverage range of 44.7±0.9 kJ/mol on bare Pt(111) is assigned to adsorption on regular Pt sites. After formation of the PropO monolayer as the

number of adsorbed molecules reaches 4.2-5.8 $\cdot 10^{14}$ cm^{-2}, adsorption on the multilayer with an adsorption energy of 33.8±1.5 kJ/mol takes place. The TPD measurements of Ding et al. agree well with our results: Using a Redhead analysis, the position of their TPD peaks correspond to values of 58 kJ/mol, 45 kJ/mol and 34 kJ/mol for the initial desorption energy, the desorption energy at submonolayer coverage and the desorption energy on the PropO multilayer [311], respectively.

The PropO adsorption energy on 1 ML NEA on Pt(111) is shown in Figure 12.4 (d). The initial adsorption energy is 44.3±0.9 kJ/mol for R-PropO and 43.2±0.8 kJ/mol for S-PropO, which is 12.7 kJ/mol and 24.8 kJ/mol lower in comparison to adsorption on bare Pt(111). E_{ads} for the two enantiomers decays to 32.6±0.7 kJ/mol at the highest exposures. As PropO increasingly occupies the adsorption sites on NEA, the PropO adsorption energy decays to the resublimation energy from the PropO multilayer, which is measured to be 32.6±0.7 kJ/mol. In principle, it would also be possible that NEA dissolves in the PropO multilayer during PropO adsorption. From the adsorption energy of structurally similar molecules compared to NEA of more than 130 kJ/mol [317], breaking of the NEA-Pt bond in favor of the PropO-Pt bond is highly unlikely, therefore this possibility can be neglected. Fig. 12.4 (d) also shows that there is no difference in the adsorption energy between R-PropO and S-PropO on R-NEA.

The PropO adsorption energy as a function of the number of adsorbed molecules on 0.5 ML NEA on Pt(111) is depicted in Figure 12.4 (b). The initial adsorption energy of 52.3±1.7 kJ/mol and 52.4±1.5 kJ/mol for S- and R-PropO is in between what has been observed on bare Pt(111) and on NEA covered Pt(111). The adsorption energy decays roughly exponentially to the adsorption energy on the PropO multilayer, which is measured to be 31.0±0.8 kJ/mol. A similar trend is observed on 0.75 ML NEA/Pt(111), here the initial PropO adsorption energy is 49.6±1.1 kJ/mol and 49.5±1.4 kJ/mol for R- and S- PropO, both dropping to a value of 32.4±0.7 kJ/mol. Figure 12.4 shows no noticeable difference of the PropO adsorption energy within the experimental error for the two enantiomers at the R-NEA coverage of 0.5 ML and 0.75 ML. In this coverage range, enantiospecific PropO adsorption was observed based on TPD experiments [304]. The initial and the final adsorption energy for the measured deposition coverages are directly compared in Figure 12.5. As already discussed, the initial adsorption energy decreases with increasing NEA coverage. Figure 12.5 also shows that the adsorption energy on the PropO multilayer does not depend on the NEA coverage.

From Figure 12.5 it is obvious that the difference in the initial adsorption energy between R- and S-PropO is smaller than a few kJ/mol, but also at higher coverages no significant difference in the adsorption energy of the two enantiomers is observed for adsorption on 0.5 and 0.75 ML NEA/Pt(111). This is in agreement with the results of Lee et al. [304]. The difference in the TPD maxima between R- and S-PropO of 5 K suggests that the difference in the adsorption energy between the two enantiomers is 1-2 kJ/mol. It has to be mentioned however that kinetic effects, which could also lead to differences in the TPD maxima between R- and S-PropO have been neglected in this analysis. The difference in the TPD maxima between the two PropO enantiomers could arise due to differences in the desorption kinetics. This would be in agreement with our results.

Lee et al. additionally found that the number of adsorbed PropO molecules on NEA is significantly higher if both molecules have the same chirality compared to the situation in which PropO has the opposite chirality than NEA in the NEA coverage range 0.5-2/3. For the case

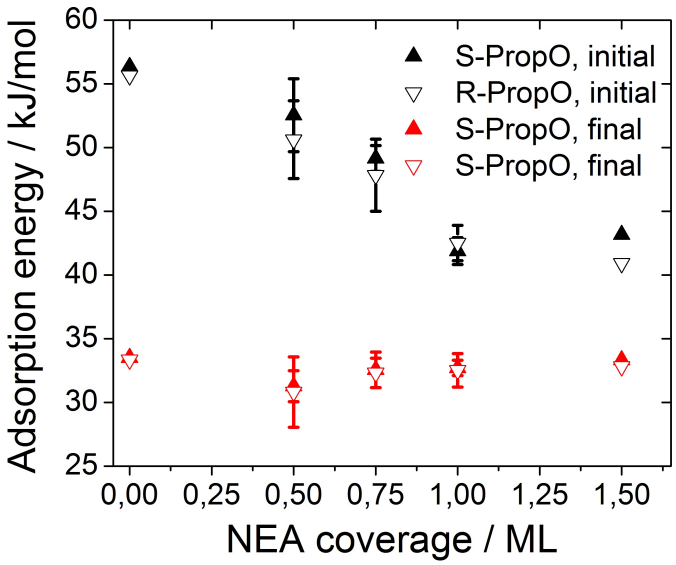

Abbildung 12.5: Comparison of the initial (black) and final (red) adsorption energy of S-PropO (filled triangles) and R-PropO (hollow triangles) dependent on the R-NEA coverage

that more R-PropO compared to S-PropO can be adsorbed in a monolayer on R-NEA covered Pt(111), one would expect to observe differences in the coverage dependent adsorption energy of R- and S-PropO on R-NEA/Pt(111). This has not been observed in our SCAC results, which could indicate that the corresponding differences in the adsorption energy are very subtle. Another explanation is that the dense adsorbate layer of NEA and PropO with the same chirality on Pt(111) can only be formed at 110 K<T<145 K (the upper boundary indicates the desorption maximum of the PropO multilayer). In this scenario, the same amount of R-PropO and S-PropO adsorb in a monolayer on R-NEA/Pt(111) at 110 K. Upon annealing to the desorption temperature, a larger number of R-PropO molecules compared to S-PropO adsorb in the monolayer on R-NEA/Pt(111).

12.4 Summary

To determine the evolution of the R-NEA coverage with the deposition time, CO titration experiments have been performed. It has been shown that the NEA coverage increases linearly with the deposition time until the formation of one NEA monolayer, which shows that the NEA sticking coefficient is constant for NEA deposition at 110 K.
PropO adsorbs on Pt(111) and on NEA/Pt(111) with an adsorption energy of 57±0.5 kJ/mol and a sticking probability of 1 at 110 K. The saturation coverage on bare Pt(111) is ∼1/3. After an initial decay of the adsorption energy on NEA/Pt(111), the adsorption energy is constant until ∼25% of the Pt sites are occupied and decays subsequently to the PropO adsorption energy on the multilayer. The adsorption energy on 1 ML NEA/Pt(111) is 43-44 kJ/mol and decreases strongly with an increasing number of adsorbed PropO molecules. On 0.5 ML NEA/Pt(111),

the initial adsorption energies for S- and R-PropO are 52.3±1.7 kJ/mol and 52.4±1.5 kJ/mol. For 0.75 ML NEA/Pt(111), the initial adsorption energies for the two enantiomers are 49.5±1.4 kJ/mol and 49.6±1.1 kJ/mol. No difference between the R-PropO and S-PropO adsorption energy has been detected independent of the PropO coverage for 0.5 ML R-NEA/Pt(111) and 0.75 ML R-NEA/Pt(111).
This result is in agreement with the TPD data of Lee et al., which suggest a difference in the adsorption energy at saturation of the two PropO enantiomers of 1-2 kJ/mol over a wide NEA coverage range.

13 Summary and conclusions

One of the most important tasks in heterogeneous catalysis is to optimize the activity and selectivity of a desired reaction pathway by systematically tuning the properties of the catalyst. For supported catalysts, which are extensively applied in the industry, such properties include the composition and surface area of the active component, the particle size/structure and the nature of the support. These properties are challenging to investigate as they are difficult to control independently. The correlation between the catalyst structure and the thermodynamics of surface processes is traditionally investigated by desorption-based methods, which cannot be applied to non-fully-reversible processes.
In order to overcome these issues, the preparation of well-defined model catalysts has been combined with the SCAC setup, developed by Campbell et al. [62, 123].
Quantitative information on the energetics of gas-surface interactions on these well defined model systems have been obtained. The influence of the nanoparticle size on the adsorption/reaction properties of CO and oxygen was investigated. The model catalysts on which these studies have been performed consisted of a $\sim$50 Å thick $Fe_3O_4(111)$ film, grown on a Pt(111) substrate. Pd nanoparticles have been deposited on top of the iron oxide film. The structure of this system has been studied previously in detail for various Pd deposition coverages: The Pd nanoparticles are terminated by (111) and (100) facets as well as edge and corner sites, the abundance of these different sites could be modeled on the basis of the STM data.
Before considering adsorption processes on Pd(111) and Pd nanoparticles of different sizes, an overview of the SCAC results on oxygen and CO interaction with the oxide support is given. CO and O_2 adsorption experiments have been performed at $\sim$110 K on $Fe_3O_4(111)$. It was found, that $\sim 6 \pm 1 \cdot 10^{13}$ CO molecules adsorb on adsorption sites with a binding energy of 46 ± 1 kJ/mol on the Fe_3O_4 support. Further CO molecules are trapped in a more weakly bound adsorption state with a binding energy of $\approx$25 kJ/mol and a desorption prefactor of $2 \cdot 10^{11}$-$2 \cdot 10^{12} s^{-1}$. The finding, that only a small amount of adsorbed CO molecules are bound strongly is consistent with the adsorption at defect sites or an O-termination of the major fraction of the surface. In contrast to CO, no transient or permanent O_2 sticking could be measured at 110 K.
CO adsorption experiments have been performed on Pd nanoparticles of five different sizes in the particle size range 1.9 nm-6.4 nm, whereas O_2 adsorption was measured on Pd nanoparticles of five different sizes in the particle size range 2.3 nm-6.4 nm. In both cases, it was found that the initial sticking probability on Pd/Fe_3O_4 was significantly higher at T=300 K than expected if the capture zone effect was neglected.
In order to obtain information on the capture zone effect, the initial sticking coefficient of CO and O_2 on Pd nanoparticles in the size range 1.9 nm-6.4 nm has been modeled: According to these results, CO and O_2 molecules which are trapped at a distance of $\leq$2.4 nm from the Pd nanoparticles at T=300 K diffuse to the Pd nanoparticles and adsorb. In agreement with earlier studies, modeling of the initial CO sticking coefficient could be performed by assuming that

S(0) for CO is identical on Pd(111) and on Pd nanoparticles. The initial sticking probability of O_2 on Pd nanoparticles with the sizes 6.4 nm and 3.4 nm strongly suggests that the dissociative sticking probability S(0) is higher on Pd nanoparticles than on Pd(111): the S(0)-value on Pd nanoparticles is modeled to be $\sim$0.9 as compared to an S(0)-value of 0.47$\pm$0.01 on Pd(111).
Oxygen adsorption was studied with SCAC on Pd(111) and Pd nanoparticles with the estimated average sizes 2.3 nm, 2.9 nm, 3.4 nm and 6.4 nm, supported on Fe_3O_4 .
On Pd(111) an initial oxygen adsorption energy of 206$\pm$7 kJ/mol was found. After a slight decay, the adsorption energy remains approximately constant until close to the saturation coverage of Θ=0.3-0.35, at which E_{ads} is $\approx$130 kJ/mol. In contrast, the adsorption energy decreases strictly monotonically with increasing oxygen coverage on Pd nanoparticles of different sizes. The adsorption energy in the zero coverage limit of 275$\pm$14 kJ/mol on large Pd nanoparticles is significantly higher compared to the adsorption energy of 206$\pm$7 kJ/mol on Pd(111). To correlate this large difference in the initial adsorption energy with changes in the local adsorption environment of oxygen, IRAS measurements with CO as a probe molecule have been performed. It could be established that while oxygen atoms adsorb in the threefold hollow position on Pd(111), edge sites are initially covered by oxygen on large Pd nanoparticles. Accordingly, the change of the local adsorption environment leads to the significantly higher oxygen adsorption energy on Pd nanoparticles. A decrease in the Pd nanoparticle size results in a decrease in the initial oxygen adsorption energy in the particle size range 2.3 nm-3.4 nm. On nanoparticles which are 2.3 nm in size, the initial adsorption energy was found to be 205$\pm$10 kJ/mol. A similar decrease in the initial CO adsorption energy with decreasing particle size has been observed previously. This decrease in the adsorption energy with decreasing particle size can be rationalized with two different effects. Firstly, a contraction of the nanoparticles may causes a decrease in the O-Pd bond strength, as can be rationalized e.g. with the BOC model. Secondly, the reduced number of free electrons in small Pd nanoparticles may result in a decrease of the VdW-interaction between adsorbate and substrate but this effect is expected to be minor for oxygen interaction with Pd. The change of the local oxygen adsorption environment from Pd(111) to large Pd nanoparticles and the decrease of the Pd nanoparticle size results in a non-monotonic structure dependence of the oxygen adsorption energy. This dependence is schematically illustrated in Fig. 13.1.
As the relative adsorbate coverage increases, the difference in the oxygen adsorption energy

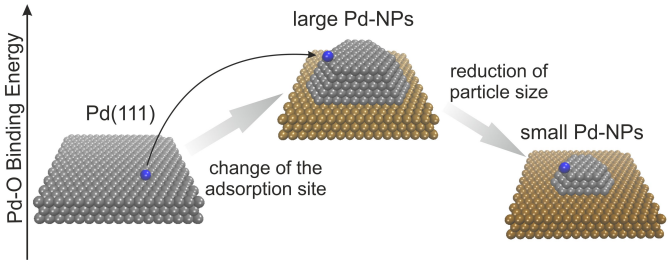

Abbildung 13.1: Trend of the particle size dependent oxygen adsorption energy together with a microscopic illustration of the adsorption systems

between the different adsorption systems decreases from $\approx$70 kJ/mol in the zero coverage limit to $\approx$35 kJ/mol close to the saturation coverage. The strong structure dependence of the oxygen

adsorption energy is less prominent at high oxygen coverages.
The coverage dependence of the oxygen sticking coefficient shows a precursor mediated adsorption behavior on large Pd nanoparticles. After a prominent decay of the sticking coefficient on Pd/Fe_3O_4 at intermediate oxygen coverages, the Pd surface sites become saturated with oxygen. The average number of oxygen atoms per surface Pd atoms was found to be 0.38 ± 0.04.
It has been observed, that oxygen adsorption continues after saturation of the Pd surface sites. The total number of adsorbed oxygen atoms by far exceeds the amount which is able to adsorb on the Pd nanoparticles with the sizes 6.4 nm, 3.4 nm and 2.9 nm. Interestingly, the regime in the coverage dependent sticking coefficient corresponding to this process is not observed when performing a cleaning procedure, which consists of O_2 exposure at 300 K, CO exposure at 490 K and annealing to 580 K in UHV before the adsorption measurements.
Complementary CO titration experiments at 300 K showed that significantly more CO reacts with oxygen on the freshly prepared Pd nanoparticles which have been exposed to O_2 as compared to the same system after cleaning. Accordingly, the large amount of oxygen in the system is able to react with CO to CO_2 at 300 K, which has been confirmed quantitatively by evaluating the number of evolved CO_2 molecules. It has been suggested that dissociative oxygen adsorption, spillover to Fe_3O_4 and O diffusion into Fe_3O_4 may take place when exposing the freshly prepared catalysts to oxygen at 300 K. Secondly, the possibility of O atom diffusion into the freshly prepared Pd nanoparticles at high oxygen exposures has been suggested. On the basis of the current results, both possibilities have to be considered.
For the case that oxygen diffuses into the Pd bulk, the oxygen content in Pd has been estimated to be $\sim$30 % for the particle sizes 6.4 nm, 3.4 nm and 2.9 nm.
The initial formation energy of the oxygen species which is formed in addition to adsorbed oxygen on the Pd nanoparticles can be estimated to be 160-200 kJ/mol for the Pd particle sizes 2.9 nm and 3.4 nm, whereas it was found to be 120-130 kJ/mol for the Pd particle size 6.4 nm.
The initial oxygen sticking coefficient and the oxygen saturation coverage is found to drop after the O_2 and CO treatment at 300 K, CO exposure at 490 K and annealing at 580 K in UHV. This would be in agreement with sintering of the nanoparticles during gas exposure/annealing but may also result from other structural changes of the catalysts. These structural changes are suggested to be responsible for the strong changes in the adsorption properties of the Pd/Fe_3O_4 catalysts after exposure to O_2 at 300 K, CO at 490 K and annealing at 580 K in UHV.
In a further study, the CO-O interaction has been investigated on Pd(111) and Pd nanoparticles of two different sizes. For this investigation, CO adsorption experiments have been performed at $\approx$110 K on the bare catalysts and on the same systems after exposure to $\sim 3\cdot10^{16}$ O_2 molecules cm^{-2}. The CO coverage on bare Pd(111) and on O/Pd(111) agrees well with the coverages which are extracted from the structural data from previous studies on these systems. CO adsorption is observed to be strongly precursor mediated on Pd(111) and Pd/Fe_3O_4. The number of adsorbed CO molecules is determined to be $0.29\cdot10^{15}$ cm^{-2}, and $0.18\cdot10^{15}$ cm^{-2} higher on the bare catalysts as compared to the oxygen covered catalyst for the Pd deposition coverages 4 Å Pd/Fe_3O_4 and 1.5 Å Pd.
After saturation of the surface Pd sites, CO transiently adsorbs during the pulse and desorbs in between the pulses. By modeling the desorption process on Pd/Fe_3O_4 with the particle size 3.4 nm and 2.9 nm and on Fe_3O_4, a desorption rate of $\sim$2.1 s^{-1} was obtained, which has been attributed to desorption from a weakly bound, physisorbed state on Fe_3O_4 at 110 K, although it

cannot be excluded that transient adsorption/desorption occurs on the Pd nanoparticles as well.
The CO adsorption energy on Pd(111) and on Pd/Fe_3O_4 in the zero coverage limit, measured at 110 K, agrees well with the data which was previously measured at 300 K. Saturation with oxygen causes the adsorption energy to drop by 35$\pm$4 kJ/mol on Pd(111) and by 40-50 kJ/mol on Pd/Fe_3O_4 for the particle sizes 2.9 nm and 3.4 nm. This difference in the adsorption energy can be attributed to adsorbate-adsorbate interactions between CO and O in the limit of zero CO coverage. The difference between the CO adsorption energy on bare and on oxygen covered Pd(111) increases with increasing CO coverage to $\sim$70 kJ/mol at a CO coverage of $\approx$1/3 and decreases at even higher coverages to $\approx$22 kJ/mol at the saturation coverage of 0.75. The difference in the CO adsorption energy between pristine and oxygen covered Pd nanoparticles barely changes with increasing CO coverage until shortly before saturation of the surface with CO is reached.
The energetic changes during the reaction steps of the CO oxidation reaction has been estimated based on the following information: the determined oxygen adsorption energy on Pd(111) and Pd/Fe_3O_4, the measured CO binding energy on O/Pd(111) and oxygen covered Pd nanoparticles and the gas phase reaction energy. The surface reaction energy for CO oxidation in the zero CO coverage limit and at oxygen saturation was estimated to be 84-117 kJ/mol on Pd(111). For CO oxidation on Pd/Fe_3O_4 with the nanoparticle sizes 3.4 nm and 2.9 nm, two boundary cases were considered: reaction of oxygen with the weakly bound species that is formed in addition to adsorbed oxygen on the Pd nanoparticles, or no reaction with this species. For the former case, the surface reaction energy was estimated to be $\sim$40 kJ/mol higher on the Pd nanoparticles than on Pd(111). For the boundary case that CO exclusively reacts with the adsorbed oxygen layer on the Pd nanoparticles, the surface reaction energy was estimated to be 91-114 kJ/mol on the Pd nanoparticles which is similar than on Pd(111).
Transient CO oxidation experiments at 300 K on oxygen saturated catalysts showed a more than two times higher turnover rate on Pd/Fe_3O_4 as compared to Pd(111) at the lowest CO coverages for the two Pd deposition coverages which are used here.
In order to understand the mechanism of asymmetric hydrogenation of unsaturated hydrocarbons on chirally modified surfaces, extensive effort is currently made in order to understand the interaction between reactant and modifier. In a further study, adsorption of R-Propylene oxide on Pt(111), modified by 1-(1-naphthyl)ethylamine, has been investigated by SCAC. Determining the dependence between the NEA-coverage and the NEA-deposition time in CO titration experiments lead to the conclusion that the fraction of the surface covered by R-NEA increases linearly with the R-NEA deposition time. Lee et al. observed more dense NEA adsorbate structures for the case that NEA was coadsorbed with Propylene oxide in some NEA coverage regime [304]. Such effects could not be found in the present study when adsorbing NEA without Propylene oxide.
The sticking probability of PropO on Pt(111), NEA/Pt(111) and on the PropO multilayer was found to be close to unity at 110 K. The saturation coverage on bare Pt(111) is found to be $\sim$0.33. The initial PropO adsorption energy on bare Pt(111) in the zero coverage regime is 57-58 kJ/mol and decreases roughly linearly with increasing coverage of the R-NEA modifier to 43-44 kJ/mol on 1 ML R-NEA. No difference within the experimental error between the R-PropO and S-PropO adsorption energy on the Pt(111) surface, covered with 0 ML, 0.5 ML, 0.75 ML and 1 ML R-NEA could be detected, independent of the PropO coverage.

Zusammenfassung

Um die komplexen Eigenschaften industrieller Katalysatoren zu verstehen werden vermehrt Studien an Modellkatalysatoren durchgeführt, die eine geziehlte Kontrolle struktureller und chemischer Eigenschaften erlauben [16–19, 318]. In der vorliegenden Arbeit wird dieser Ansatz mit Einkristalladsorptionskalorimetrie kombiniert, um die Energetik von Gas-Oberflächenwechselwirkungen quantitativ zu messen [123, 205, 229]. Auf den präparierten Fe_3O_4-Katalysatoren adsorbiert CO auf 5±0.8 % der Oberflächenplätzen mit einer Adsorptionsenergie von 46±1 kJ/mol, weitere CO Moleküle werden in einen Adsorptionszustand mit einer Bindungsenergie von ≈25 kJ/mol und einem Desorptionsvorfaktor von $2 \cdot 10^{11} - 2 \cdot 10^{12}$ s^{-1} CO^{-1} adsorbiert. Durch Modellieren der Anfangshaftkoeffizienten von CO und O_2 konnte gezeigt werden, dass jene Moleküle, die in einer Entfernung von weniger als ∼2.4 nm zu den Pd Nanopartikeln auf der Oxidoberfläche physisorbiert werden zu den Nanopartikeln diffundieren und dort adsorbieren.
Die Adsorptionsenergie bei einer infinitesimal kleinen Sauerstoffbedeckung steigt von 206±7 kJ/mol auf Pd(111) auf einen Wert von 275±14 kJ/mol auf 3.4 nm-6.4 nm großen Pd Nanopartikeln an. Mit IRAS-Messungen konnte gezeigt werden, dass dieser starke Anstieg der Bindungsenergie durch die Änderung des Adsorptionsplatzes von einer vielfach gebundenen Position auf Pd(111) zu Kantenplätzen auf Nanopartikeln zustande kommt. Im Gegensatz dazu bewirkt die Verringerung der Partikelgröße eine kleiner werdende Adsorptionsenergie. Eine schwächere Bindung mit kleiner werdender Partikelgröße konnte kürzlich bereits für CO Adsorption auf Pd Nanopartikeln beobachtet werden [205]. Die starke Differenz in der Adsorptionsenergie zwischen den großten und kleinen Pd Nanopartikeln sinkt mit steigender Adsorbatbedeckung auf ≈35 kJ/mol bei der Sättigungsbedeckung von Sauerstoff.
Die bestimmte Aufnahme an Sauerstoffatomen ist 3-4 mal höher als erwartet, wenn lediglich Bildung einer Adsorbatstruktur auf Pd Nanopartikeln in Betracht gezogen wird. CO Haftkoeffizientenmessungen belegen, dass ungewöhnlich viel CO auf sauerstoffvorbelegten Pd Nanopartikeln reagiert. Die Menge an gebildetem CO_2 bei 300 K entspricht der Menge an Sauerstoff, die ursprünglich adsorbiert wurde. Die hohe Sauerstoffaufnahme könnte zum einen durch Sauerstoffdiffusion in Fe_3O_4 und zum anderen durch Diffusion von Sauerstoff in die Pd Nanopartikel erklärt werden. Die Adsorptionsexperimente von O_2 und CO nach dem Reinigen der Partikel bei erhöhten Temperaturen zeigen eine wesentlich geringere Sauerstoffaufnahme nach dieser Reinigungsprozedur.
In dieser Arbeit wurde erstmalig die Energetik der CO-O Wechselwirkung auf Pd Nanopartikeln durch direkte experimentelle Studien untersucht. Die in dieser Arbeit bestimmte Wechselwirkungsenergie zwischen CO und Sauerstoffatomen bei einer infinitesimal kleinen CO Bedeckung beträgt 35±4 kJ/mol auf Pd(111) und 40-50 kJ/mol auf Pd Nanopartikeln zweier verschiedener Größen. Auf Pd(111) konnte ein Anstieg dieses Wertes bei mittleren CO-Bedeckungen und ein Abfall bei hohen Bedeckungen beobachtet werden, wohingegen sich die CO-O Wechselwirkung

auf Pd Nanopartikeln sich nicht signifikant mit der CO-Bedeckung ändert.
Weiterhin wurde eine CO Oxidationsenergie von 84-117 kJ/mol auf Pd(111) bestimmt. Für den Fall, dass Sauerstoff bei hohen Bedeckungen in die Pd Nanopartikel diffundiert wurde die CO Oxidationsenergie als um $\sim$40 kJ/mol höher auf Pd Nanopartikeln als auf Pd(111) ermittelt. Eine ähnliche CO Oxidationsenergie auf Pd Nanopartikeln und Pd(111) wurde für den Fall bestimmt, dass bei hohen Sauerstoffbedeckungen Diffusion in Fe_3O_4 stattfindet.
Zur Untersuchung der enantioselektiven Adsorption auf chiral modifizierten Oberflächen wurden R- und S-Propylenoxid auf durch R-1-(1-Naphthyl)ethylamin (NEA) modifizierte Pt(111) Oberflächen als Funktion der Bedeckung von Propylenoxid adsorbiert. Bei den R-NEA Konzentrationen 0, 0.5, 0.75 und 1 auf Pt(111) konnte kein Unterschied in der Adsorptionsenergie der beiden PropO Enantiomere als Funktion der Propylenoxidbedeckung gemessen werden.

Literaturverzeichnis

[1] G. Ertl, H. Knözinger, and J. Weitkamp. *Handbook of Heterogeneous Catalysis*, volume 4. Wiley VCH, Weinheim, 1997.

[2] J. N. Armor. *Appl. Catal., B*, 1:221–256, 1992.

[3] J. M. Thomas and W. J. Thomas. *Principle and Practice of heterogeneous catalysis*. Wiley VCH, Weinheim, 1997.

[4] G. C. Bond. *Heterogeneous Catalysis*. Oxford University Press, Oxford, 1974.

[5] H. W. Harring. *Industrial Gases Processing*. Wiley VCH, Weinheim, 2008.

[6] A. Kohl and R. Nielsen. *Gas Purification*. Gulf Publishing Company, Houston, 1997.

[7] L. Albright. *Hydrogenation (partial) of triglycerides*. Encyclopedia of Food Science. Avi Publishing, Westport, 1978.

[8] R. J. Farrauto. *R. J. Farrauto*. Handbook of Industrial Chemistry and Biotechnology. Springer, New York, 2007.

[9] G. Ertl. *Angew. Chem. Int. Ed.*, 29:1219–1227, 1990.

[10] R. I. Masel. *Principles of Adsorption and Reaction on Solid Surfaces*. Wiley VCH, Weinheim, 1996.

[11] D. P. Woodruff. *The Chemical Physics of Solid surfaces*, volume 11. Elsevier, Amsterdam, 2003.

[12] G. Ertl and P. Rau. *Surf. Sci.*, 15:443–465, 1969.

[13] D. G. Castner, B. A. Sexton, and G. A. Somorjai. *Surf. Sci.*, 71:519–540, 1978.

[14] H. Conrad, G. Ertl, and J. Küppers. *Surf. Sci.*, 76:323–342, 1978.

[15] A. Winkler, X. Guo, H.R. Siddiqui, P.L. Hagans, and J.T. Yates. *Surf. Sci.*, 201:419–443, 1988.

[16] P. L. J. Gunter, J. W. Niemantsverdriet, F. H. Ribeiro, and G. A. Somorjai. *Catal. Rev. Sci. Eng.*, 39:77–168, 1997.

[17] D.W. Goodman. *Chem. Rev.*, 95:523–536, 1995.

[18] U. Diebold, J.-M. Pan, and T. E. Madey. *Surf. Sci.*, 331-333:845–854, 1995.

[19] H.-J. Freund. *Angew. Chem. Int. Ed. Engl.*, 36:452–156, 1997.

[20] C.R. Henry. *Surf. Sci. Rep.*, 31:231–325, 1998.

[21] M. Bäumer and H-J Freund. Metal deposits on well-ordered oxide films. *Prog. Surf. Sci.*, 61:127–198, 1999.

[22] C. T. Campbell. *Surf. Sci. Rep.*, 27:1–111, 1997.

[23] U. Heiz, F. Vanolli, L. Trento, and W.-D. Schneider. *Rev. Sci. Instrum.*, 68:1986–1995, 1997.

[24] M. D. Kane, F. S. Roberts, and S. L. Anderson. *Faraday Discuss.*, 162:1–17, 2013.

[25] S. Ladas, H. Poppa, and M. Boudart. *Surf. Sci.*, 102:151–171, 1981.

[26] F. Rumpf, H. Poppa, and M. Boudard. *Langmuir*, 4:722–728, 1988.

[27] C.R. Henry. *Surf. Sci.*, 223:519–526, 1989.

[28] V. Matolin and E. Gillet. *Surf. Sci.*, 166:L115–L118, 1986.

[29] I. Stara, V. Nehasil, and V. Matolin. *Surf. Sci.*, 365:69–77, 1996.

[30] C. R. Henry, C. Chapon, and C. Duriez. *Physics and chemistry of small clusters*, volume 158 of *Nato ASI Series*. New York, 1987.

[31] A. K. Santra and D. W. Goodman. *Electrochim. Acta*, 47:3595–3609, 2002.

[32] K. Hojrup Hansen, Z. Sljivancanin, E. Lagsgaard, F. Besenbacher, and I. Stensgaard. *Surf. Sci.*, 505:25–38, 2002.

[33] C. M. Yim, C. L. Pang, D. S. Humphrey, C. A. Muryn, K. Schulte, R. Perez, and G. Thornton. *Faraday Discuss.*, 162:191–200, 2013.

[34] I. Stara and V. Matolin. *Surf. Rev. Lett.*, 4:1353–1358, 1997.

[35] M. Frank, S. Andersson, J. Libuda, S. Stempel, M. Bäumer, M. Martensson, and H.-J. Freund. *Chem. Phys. Lett.*, 279:92–99, 1997.

[36] C. Becker and C. R. Henry. *Surf. Sci.*, 352-354:457–462, 1996.

[37] S. Kunz, F. F. Schweinberger, V. Habibpour, M. Röttgen, C. Harding, M. Arenz, and U. Heiz. *J. Phys. Chem. C.*, 114:1651–1654, 2010.

[38] B. Y. Yoon, U. Landman, Y. Habipour, C. Harding, S. Kunz, U. Heiz, M. Moseler, and M. Walter. *J. Phys. Chem. C.*, 116:9594–9607, 2012.

[39] W. F. Kaden, W. A. Kunkel, M. D. Kane, and S. L. Anderson. *JACS*, 132:13097, 2010.

[40] C. W. Mays, J. S. Vermaak, and D. Kuhlmann-Wilsdorf. *Surf. Sci.*, 12:134–140, 1968.

[41] Ryszard Lamber, Stefan Wetjen, and Nils I. Jäger. *Phys. Rev. B: Condens. Matter*, 51: 10968–10973, 1995.

[42] S. A. Nepijko, M. Klimenkov, M. Adelt, H. Kuhlenbeck, R. Schlögl, and H.-J. Freund. *Langmuir*, 15:5309–5313, 1999.

[43] A. Sandell, J. Libuda, P. Brühwiler, S. Andersson, A. Maxwell, M. Bäumer, N. Martensson, and H.-J. Freund. *J. Electron. Spectrosc. Relat. Phenom.*, 76:301–306, 1995.

[44] N. Tsud, V. Johanek, I. Stara, K. Veltruska, and V. Matolin. *Surf. Sci.*, 467:169–176, 2000.

[45] S. Penner, P. Bera, S. Pedersen, L. T. Ngo, J. J. W. Harris, and Charles T. Campbell. *J. Phys. Chem. B*, 110:24577–24584, 2006.

[46] T. Schalow, B. Brandt, D. E. Starr, M. Laurin, S. K. Shaikhutdinov, S. Schauermann, J. Libuda, and H.-J. Freund. *Phys. Chem. Chem. Phys.*, 9:1347–1361, 2007.

[47] C. Lemire, R. Meyer, V.E. Henrich, Sh. Shaikhutdinov, and H.-J. Freund. *Surf. Sci.*, 572: 103–114, 2004.

[48] T. Schalow, B. Brandt, D. E. Starr, M. Laurin, S. K. Shaikhutdinov, S. Schauermann, J. Libuda, and H-J Freund. *Angew. Chem. Int. Ed.*, 45:1–6, 2006.

[49] C. R. Henry, C. Chapon, C. Goyhenex, and R. Monot. *Surf. Sci.*, 272:283–288, 1992.

[50] C.R. Henry, C. Chapon, and C. Duriez. *J. Chem. Phys.*, 95:700–705, 1991.

[51] I. Stara and V. Matolin. *Surf. Sci.*, 313:99–106, 1994.

[52] J. Kleis, J. Greeley, N. A. Romeo, J. K. Norskov, and K. W. Jacobsen. *Catal. Lett.*, 141 (1067-1071), 2011.

[53] D. R. Rainer, M. Koranne, S. M. Vesecky, and D. W. Goodman. *J. Phys. Chem. B*, 101: 10769–10774, 1997.

[54] N. Al-Sarraf, J. T. Stuckless, C. E. Wartnaby, and D. A. King. *Surf. Sci.*, 283:427–437, 1993.

[55] H. M. Ajo, H. Ihm, D. E. Moilanen, and C. T. Campbell. *Rev. Sci. Instrum.*, 75:4471–4480, 2004.

[56] O. Lytken, W. Lew, and C. T. Campbell. *Chem. Soc. Rev.*, 37:2172–2179, 2008.

[57] M. Peter, J. M. Flores-Camacho, S. Adamovski, L. K. Ono, K-H. Fostert, C. P. O'Brien, B. Roldan Cuenya, S. Schauermann, and H-J. Freund. *Angew. Chem. Int. Ed.*, 52:5175–5179, 2013.

[58] O. Lytken, W. Lew, J. J. W. Harris, E. K. Vestergaard, J. M. Gottfied, and C. T. Campbell. *J. Am. Chem. Soc*, 130:10247–10257, 2008.

[59] D. A. Kyser and R. I. Masel. *J. Vac. Sci. Technol. A*, 4:1431–1432, 1986.

[60] R. I. Masel and D. A. Kyser. *Rev. Sci. Instrum.*, 58:2141–2144, 1987.

[61] C. E. Borroni-Bird and D. A. King. *Rev. Sci. Instrum.*, 62:2177–2185, 1991.

[62] J. T. Stuckless, N. A. Frei, and C. T. Campbell. *Rev. Sci. Instrum.*, 69:2427–2438, 1998.

[63] T. Engel and G. Ertl. *Adv. Catal.*, 28:41, 1979.

[64] M. P. D'Evelyn and R. J. Madix. *Surf. Sci. Rep.*, 3:413–495, 1984.

[65] T. Engel. *J. Chem. Phys.*, 69:373–385, 1978.

[66] T. Engel and G. Ertl. *J. Chem. Phys.*, 69:1267–1281, 1978.

[67] F. Gao, S.M. McClure, Y. Cai, K.K. Gath, Y. Wang, M.S. Chen, Q.L. Guo, and D.W. Goodman. *Surf. Sci.*, 603:65–70, 2009.

[68] I. Stara, V. Nehasil, and V. Matolin. *Surf. Sci.*, 331-333:173–177, 1995.

[69] I. Nakai, H. Kondoh, T. Shimada, A. Resta, J. Andersen, and T. Ohta. *J. Chem. Phys.*, 124:224712, 2006.

[70] S. H. Kim, J. Mendez, J. Wintterlin, and G. Ertl. *Phys. Rev. B: Condens. Matter*, 72: 155414(1–5), 2005.

[71] Jan Kaspar, Paolo Fornasiero, and Neal Hickey. *Catal. Today*, 77:419–449, 2003.

[72] I. Stara and V. Matolin. *Surf. Sci.*, 313:99–106, 1994.

[73] I. Jungwirthova, I. Stara, and V. Matolin. *Surf. Sci.*, 377-379:644–649, 1997.

[74] D. E. Starr, J. T. Stuckless, D. J. Bald, and C. T. Campbell. *J. Chem. Phys.*, 107:5547–5553, 1997.

[75] V. Matolin and I. Stara. *Surf. Sci.*, 398:117–124, 1998.

[76] L. Piccolo, C. Becker, and C.R. Henry. *Eur. Phys. J. D*, 9:415–419, 1999.

[77] Laurent Piccolo, Conrad Becker, and Claude R. Henry. *Appl. Surf. Sci.*, 164:156–162, 2000.

[78] J. Libuda, I. Meusel, J. Hoffmann, J. Hartmann, L. Piccolo, C.R. Henry, and H.-J. Freund. *J. Chem. Phys.*, 114:4669–4683, 2001.

[79] J. Hoffmann, I. Meusel, J. Hartmann, J. Libuda, and H.-J. Freund. *J. Catal.*, 204:378–392, 2001.

[80] J. Hoffmann, S. Schauermann, V. Johanek, J. Hartmann, and J. Libuda. *J. Catal.*, 213: 176–190, 2003.

[81] J. Hoffmann, S. Schauermann, J. Hartmann, V.P. Zhadanov, B. Kasemo, J. Libuda, and H.-J. Freund. *Chem. Phys. Lett.*, 354:403–408, 2002.

[82] J. Libuda and H.-J. Freund. *Surf. Sci. Rep.*, 57:157–298, 2005.

[83] T. Schalow, M. Laurin, B. Brandt, S. Schauermann, S. Guimond, H. Kuhlenbeck, D. E. Starr, S. K. Shaikhutdinov, J. Libuda, and H-J Freund. *Angew. Chem. Int. Ed.*, 44:7601–7605, 2005.

[84] T. Schalow, B. Brandt, M. Laurin, S. Schauermann, S. Guimond, H. Kuhlenbeck, J. Libuda, and H.-J. Freund. *Surf. Sci.*, 600:2528–2542, 2006.

[85] T. Schalow, B. Brandt, M. Laurin, S. Schauermann, J. Libuda, and H-J. Freund. *J. Catal.*, 242:58–70, 2006.

[86] T. Schalow, B. Brandt, M. Laurin, S. Schauermann, SK Shaikhutdinov, J. Libuda, and H-J Freund. *Catal. Lett.*, 107:189–196, 2006.

[87] B. Brandt, T. Schalow, M. Laurin, S. Schauermann, J. Libuda, and H.-J. Freund. *J. Phys. Chem. C.*, 111:938–949, 2007.

[88] H. Conrad, G. Ertl, G. Kuppers, and E. E. Latte. *Surf. Sci.*, 65:245–260, 1977.

[89] B. A. Banse and B. E. Koel. *Surf. Sci.*, 232:275–285, 1990.

[90] G. Zheng and E.I. Altman. *Surf. Sci.*, 462:151–168, 2000.

[91] Bernhard Klötzer, Konrad Hayek, Christoph Konvicka, Edvin Lundgren, and Peter Varga. *Surf. Sci.*, 482-485:237–242, 2001.

[92] X. Guo, A. Hoffman, and J. T. Yates. *J. Chem. Phys.*, 90:5787–5792, 1989.

[93] G. Zheng and E.I. Altman. *Surf. Sci.*, 504:253–270, 2002.

[94] E.M. Stuve, R.J. Madix, and C.R. Brundle. *Surf. Sci.*, 146:155–178, 1984.

[95] K. Klier, Y. Wang, and G.W. Simmons. *J. Phys. Chem.*, 97:633–640, 1993.

[96] S.-L. Chang and P.A. Thiel. *J. Chem. Phys.*, 88:2071–2082, 1987.

[97] K. Yagi, D. Sekiba, and H. Fukutani. *Surf. Sci.*, 442:307–317, 1999.

[98] V. A. Bondzie, P. Kleban, and D. J. Dwyer. *Surf. Sci.*, 347:319–328, 1996.

[99] E. S. Putna, J. M. Vohs, and R. J. Gorte. *Surf. Sci.*, 391:L1178–L1182, 1997.

[100] X. Xu and D. W. Goodman. *J. Phys. Chem.*, 97:7711–7718, 1993.

[101] P. W. Davies and R.M. Lambert. *Surf. Sci.*, 110:227–249, 1981.

[102] X. Xu, J. Szanyi, Q. Xu, and D. W. Goodman. *Catal. Today*, 21:57–69, 1994.

[103] H. Graoui, S. Giorgio, and C.R. Henry. *Surf. Sci.*, 417:350–360, 1998.

[104] P. Nolte, A. Stierle, N. Kasper, H. Y. Jin-Phillipp, N. Jeuter, and H. Dosch. *Nano Lett.*, 11:4697–4700, 2011.

[105] Robert Bryl, Thomasz Olewicz, Thierry Visart de Bocarme, and Norbert Kruse. *J. Phys. Chem. C.*, 114:2220–2226, 2010.

[106] G. Odörfer, E.W. Plummer, H.-J. Freund, H. Kuhlenbeck, and M. Neumann. *Surf. Sci.*, 198:331–359, 1988.

[107] T. Matsushima and H. Asada. *J. Chem. Phys.*, 85, 1986.

[108] J. Mendez, S. H. Kim, J. Wintterlin, and G. Ertl. *Phys. Rev. B: Condens. Matter*, 71: 085409(1–13), 2005.

[109] A.P. Seitsonen, Y.D. Kim, S. Schwegmann, and H. Over. *Surf. Sci.*, 468:176–186, 2000.

[110] H. U. Blaser, F. Spindler, and M. Studer. *Appl. Catal., A*, 221:119–143, 2001.

[111] A. M. Thayer. *Chem. Eng. News*, 85:11–19, 2007.

[112] Y. Izumi. *Adv. Catal.*, 32:215–271, 1983.

[113] T. Isoda, A. Ichikavwa, and T. Shimamoto. *Rikagaku Kenkyusho Hokoku*, 34:134, 1958.

[114] Y. Orito, S. Imai, and S. Niwa. *Nippon Kagaku Kaishi*, 8:1118–1128, 1979.

[115] B. Minder, M. Schürch, T. Mallat, A. Baiker, T. Heinz, and A. Pfalz. *J. Catal.*, 160: 261–268, 1996.

[116] J. Hong, I. Lee, and F. Zaera. *Top. Catal.*, 54:1340–1347, 2011.

[117] L. D. Pachon, I. Yosef, T. Z. Markus, R. Naaman, D. Avnir, and G. Rothenberg. *Nature Chemistry*, pages 160–164, 2009.

[118] H-U. Blaser and M. Studer. *Acc. Chem. Res*, 40:1348–1356, 2007.

[119] H-U. Blaser, H-P. Jalett, M. Müller, and M. Studer. *Catal. Today*, 37:441–463, 1997.

[120] Z. Cakl, S. Reinmann, E. Schmidt, A. Moreno, T. Mallat, and A. Baiker. *J. Catal.*, 280: 104–115, 2011.

[121] E. Schmidt, C. Bucher, G. Santarossa, T. Mallat, R. Gilmour, and A. Baiker. *J. Catal.*, 289:238–248, 2012.

[122] S. T. Marshall and J. W. Medlin. *Surf. Sci. Rep.*, 66:173–184, 2011.

[123] J-H. Fischer Wolfarth, J. Hartmann, J. A. Farmer, J. M. Flores-Camacho, C. T. Campbell, S. Schauermann, and H-J. Freund. *Rev. Sci. Instrum.*, 82:024102 (1–15), 2011.

[124] K. Christmann. *Surface Physical Chemistry*. Topics in Physical Chemistry. Steinkopff Verlag, Darmstadt, 1991.

[125] K. Christmann and J. E. Demuth. *Surf. Sci.*, 120:291–318, 1982.

[126] A.V. Kiselev. In *2nd Int. Congr. Surfacity Activity*, volume 2, page 168, Butterworths, 1957.

[127] A. Szabo and N. S. Ostlund. *Modern Quantum Chemistry*. Courier Dover Publications, Mineola, 1989.

[128] R. M. Martin. *Electronic Structure*. Cambridge University Press, New York, 2004.

[129] S. Grimme. *J. Comput. Chem.*, 27:1787–1799, 2006.

[130] J. Antony and S. Grimme. *Phys. Chem. Chem. Phys.*, 8:5287–5293, 2006.

[131] A. Tkatchenko and M. Scheffler. *Phys. Rev. Lett.*, 073005-1-073005-4, 2009.

[132] W. A. Brown, R. Rose, and D. A. King. *Chem. Rev.*, 98:797–831, 1998.

[133] T. N. Rhodin and G. Ertl. *The Nature of the Surface Chemical Bond*. North-Holland Publ., Amsterdam, 1978.

[134] J.M. Ziman. *The Physics of metals*. Cambridge University press, Cambridge, 1969.

[135] W.A. Harrison. *Electronic Structure and the Properties of Solids*. Dover, San Francisco, 1980.

[136] E. Shustorovich. *Surf. Sci. Rep.*, 6:1–63, 1986.

[137] P. W. Anderson. *Phys. Rev.*, 235:41–53, 1961.

[138] D. M. Newns. *Phys. Rev.*, 178:1123–1135, 1968.

[139] P. J. Feibelman and D. R. Hamann. *Surf. Sci.*, 149:48, 1985.

[140] W. Yang and R. G. Parr. *Proc. Natl. Acad. Sci*, 82:6723–6726, 1985.

[141] J. Koutecky. *Trans. Faraday Soc.*, 54:1038–1052, 1957.

[142] T. L. Einstein and J. R. Schrieffer. *Phys. Rev. B: Condens. Matter*, 7:3629–3648, 1973.

[143] D. L. Adams. *Surf. Sci.*, 42:12–36, 1974.

[144] P. J. Feibelman. *Annu. Rev. Phys. Chem.*, 40:261–290, 1989.

[145] W. N. Unertl. *Physical Structure of Solid Surfaces*. North-Holland Publ., Amsterdam, 1996.

[146] F.M. Hoffmann. *Surf. Sci. Rep.*, 3:107–192, 1983.

[147] J. E. Hurst, L. Wharton, K.C. Janda, and D.J. Auerbach. *J. Chem. Phys*, 83:1376–1381, 1985.

[148] C. T. Rettner, E. K. Schweizer, and C. B. Mullins. *J. Chem. Phys*, 90:3800–3813, 1988.

[149] G.P. Brivio and T.B. Grimley. *Surf. Sci. Rep.*, 17:1–84, 1992.

[150] W. H. Weinberg and R. P. Merrill. *J. Vac. Sci. Technol.*, 8:718–728, 1971.

[151] J. K. Norskov and B. I. Lundquist. *Surf. Sci.*, 89:251–261, 1979.

[152] G. P. Brivio. *Surf. Sci.*, 89:226–237, 1979.

[153] A. Fick. *Ann. Phys.*, 17:59–86, 1855.

[154] Anand Udaykumar Nilekar, Jeff Greeley, and Manos Mavrikakis. *Angew. Chem. Int. Ed.*, 45:7046–7049, 2006.

[155] M. Bowker. *J. Phys.: Condens. Matter*, 22:2–13, 2010.

[156] A. Cassuto and D. A. King. *Surf. Sci.*, 102:388–404, 1981.

[157] H.-J. Freund, G. Meijer, M. Scheffler, R. Schlögl, and M. Wolf. *Angew. Chem. Int. Ed.*, 50:10064–10094, 2011.

[158] G. Ertl. *Surf. Sci.*, 299:742–754, 1994.

[159] C.T. Campbell, G. Ertl, H. Kuipers, and J. Segner. *J. Chem. Phys.*, 69:5862–5873, 1980.

[160] S. Ladas, R. Imbihl, and G. Ertl. *Surf. Sci.*, 280:14–22, 1993.

[161] H. Ohtani, M. A. Van Hove, and G. A. Somorjai. *Surf. Sci.*, 187(2-3):372–386, 1987.

[162] M. K. Rose, T. Mitsui, J. Dunphy, A. Borg, D. F. Ogletree, M. Salmeron, and P. Sautet. *Surf. Sci.*, 512:48–60, 2002.

[163] D. Loffreda, D. Simon, and P. Sautet. *Surf. Sci.*, 425:68–80, 1999.

[164] T. Giessel, O. Schaff, C. J. Hirschmugl, V. Fernandez, K.-M. Schindler, A. Theobald, S. Bao, R. Lindsay, W. Berndt, A. M. Bradshaw, C. Baddeley, A. F. Lee, R. M. Lambert, and D. P. Woodruff. *Surf. Sci.*, 406:90–102, 1998.

[165] S. Surnev, M. Sock, M. G. Ramsey, F. P. Netzer, M. Wiklund, M. Borg, and J. N. Andersen. *Surf. Sci.*, 470:171–185, 2000.

[166] M.K. Rose, A. Borg, J. C. Dunphy, T. Mitsui, D.F. Ogletree, and M. Salmeron. *Surf. Sci.*, 561:69–78, 2004.

[167] Katrin Zorn, Suzanne Giorgio, Erich Halwax, Claude R. Henry, Henrik Grönbeck, and Guenther Rupprechter. *J. Phys. Chem. C.*, 115:1103–1111, 2010.

[168] Mats Eriksson and Lars-Gunnar Ekedahl. *Surf. Sci.*, 412/413:430–440, 1998.

[169] H. Gabasch, A.K-Gericke, R. Schlögl, M. Borasio, C. Weilach, G. Rupprechter, S. Penner, B. Jenewein, K. Hayek, and B. Klötzer. *Phys. Chem. Chem. Phys.*, 9:533–540, 2007.

[170] H. Gabasch, W. Unterberger, K. Hayek, B. Klötzer, G. Kresse, C. Klein, M. Schmid, and P. Varga. *Surf. Sci.*, 600:205–218, 2005.

[171] N. F. Ramsey. *Molecular Beams*. Oxford University Press, Oxford, 1956.

[172] M. Zhen and G. Scoles. *Atomic and Molecular Beam Methods*, volume 1. Oxford University Press, Oxford, 1988.

[173] G. Comsa and R. David. *Surf. Sci. Rep.*, 5:145–198, 1985.

[174] L. Hladek. *J. Sci. Instrum.*, 42:198–202, 1964.

[175] G.W.H. Höhne, W.F. Hemminger, and H.-J. Flammersheim. Springer, 2003.

[176] G. Wedler. *Z. Phys. Chem.*, 24:76–86, 1960.

[177] R.J. Cvetanovic and Y. Amenomiya. *Cat. Rev. Sc. Eng.*, 6(1):21–48, 1972.

[178] M. Kovar and S. Cerny. *Proc. Conf. Assoc. France Calorim. Anal. Therm*, pages 97–102, 1990.

[179] D. E. Starr and C. T. Campbell. *J. Phys. Chem. B*, 105:3776–3782, 2001.

[180] J. H. Larsen, D. E. Starr, and C. T. Campbell. *J. Chem. Thermodyn.*, 33:333–345, 2001.

[181] D. E. Starr, S. F. Diaz, J. E. Musgrove, J. T. Ranney, D. J. Bald, L. Nelen, H. Ihm, and C. T. Campbell. *Surf. Sci.*, 515:13–20, 2002.

[182] S. F. Diaz, J. F. Zhu, J. J. W. Harris, P. Götsch, L. R. Merte, and C. T. Campbell. *Surf. Sci.*, 598:22–34, 2005.

[183] H. Ihm, H. M. Ajo, J. M. Gottried, P. Bera, and C. T. Campbell. *J. Phys. Chem. B*, 108: 14627–14633, 2004.

[184] J. M. Gottfried, E. K. Vestergaard, P. Bera, and C. T. Campbell. *J. Phys. Chem. B*, 110: 17539–17545, 2006.

[185] G. Ehrlich. *Adv. Catalysis*, 14:255–427, 1963.

[186] D. A. King, T. E. Madey, and J. T. Yates. *J. Chem. Phys.*, 55:3236–3246, 1971.

[187] A. A. Bell and R. Gomer. *J. Chem. Phys.*, 44:1065–1076, 1966.

[188] D. A. King and M. G. Wells. *Surf. Sci.*, 29:454–482, 1972.

[189] E. Uggerud, S. Petrie, D. K. Bohme, F. Turecek, D. Schröder, D. Plattner H. Schwarz, T. Wyttenbach, M. T. Bowkers, P. B. Armentrout, S. A. Truger, T. Junker, G. Suizdak, and M. Brönstrup. *Topics in Current Chemistry: Modern Mass Spectrometry*. Springer-Verlag, Berlin, 2003.

[190] G. Ertl and J. Küppers. Wiley VCH, Weinheim, 2nd edition, 1985.

[191] D. P. Woodruff and T. A. Delchar. *Modern techniques of Surf. Sci.* Cambridge University Press, Cambridge, 1986.

[192] W. Lew, O. Lytken, J. Farmer, M. C. Crowe, and C. T. Campbell. *Rev. Sci. Instrum.*, 81: 024102 (1–9), 2010.

[193] J. T. Stuckless, N. A. Frei, and C. T. Campbell. *Sens. Actuators B*, 62:13–22, 2000.

[194] J.-H. Fischer-Wolfarth. *Adsorption Energetics on Model Catalysts by Microcalorimetry*. Mathematisch-Naturwissenschaftliche Fakultät 1. Humboldt-Universität, Berlin, 2010.

[195] J. D. Cox, D. D. Wagman, and V. A. Medvedev. *CODATA - Key Values for Thermodynamics*. CODATA, Series on Thermodynamic Properties. Hemisphere Publishing Corp., New York, 1989.

[196] R.M. Jäger, H. Kuhlenbeck, H.-J. Freund, M. Wuttig, W. Hoffmann, R. Franchy, and H. Ibach. *Surf. Sci.*, 259:235–252, 1991.

[197] J. Libuda, F. Winkelmann, M. Bäumer, H.-J. Freund, Th. Bertrams, H. Neddermeyer, and K. Müller. *Surf. Sci.*, 318:31–73, 1994.

[198] P. Gassmann. *Surf. Sci.*, 319:95–109, 1994.

[199] M. Bäumer, D. Cappus, H. Kuhlenbeck, H.-J. Freund, G. Wilhelmi, A. Brodde, and H. Neddermeyer. *Surf. Sci.*, 253:116–126, 1991.

[200] C. M. Truong, M.-C. Wu, and D. W. Goodman. *J. Chem. Phys.*, 97:9447–1453, 1992.

[201] D. L. Döring, H. Poppa, and J. T. Dickinson. *J. Catal.*, 73:104–119, 1982.

[202] D. L. Döring, H. Poppa, and J. T. Dickinson. *J. Vac. Sci. Technol., A*, 17(1):198–200, 1979.

[203] V. Matolin and E. Gillet. *Surf. Sci.*, 238:75–82, 1990.

[204] R. Koch and H. Poppa. *J. Vac. Sci. Technol., A*, 5:1845–1848, 1987.

[205] J. M. Flores-Camacho, J.-H. Fischer-Wolfarth, M. Peter, C. T. Campbell, S. Schauermann, and H.-J. Freund. *Chem. Phys. Phys. Chem.*, 13:16800–16810, 2011.

[206] O. Dulub, W. Hebenstreit, and U. Diebold. *Phys. Rev. Lett.*, 84:3646–3649, 2000.

[207] M. Bowker, P. Stone, R. Bennett, and N. Perkins. *Surf. Sci.*, 497:155–165, 2002.

[208] Y. N. Sun, Z. H. Qin, M. Lewandowski, S. Kaya, S. Shaikhutdinov, and H.-J. Freund. *Catal. Lett.*, 126:31–35, 2008.

[209] Z-H. Qin, M. Lewandowski, Y-N. Sun, S. Shaikhutdinov, and H-J. Freund. *J. Phys.: Condens. Matter*, 21:134019 (1–6), 2009.

[210] Y.-N. Sun, Z.-H. Qin, M. Lewandowski, S. Shaikhutdinov, and H.-J. Freund. *Surf. Sci.*, 603:3099–3103, 2009.

[211] M. Lewandowski, Y. N. Sun, Z.-H. Qin, S. Shaikhutdinov, and H.-J. Freund. *Appl. Catal. A*, 391:407–410, 2011.

[212] W. Weiss, A. Barbieri, M. A. Van Hove, and G. A. Somorjai. *Phys. Rev. Lett.*, 71:1848–1851, 1993.

[213] A. Barbieri, W. Weiss, M.A. Van Hove, and G.A. Somorjai. *Surf. Sci.*, 302:259–279, 1994.

[214] W. Weiss. *Surf. Sci.*, 377-379:943–347, 1997.

[215] Y. J. Kim, C. Westphal, R. X. Ynzunza, Z. Wang, H. C. Galloway, M. Salmeron, M. A. Van Hove, and C. S. Fadley. *Surf. Sci.*, 416:68–111, 1998.

[216] M. Ritter and W. Weiss. *Surf. Sci.*, 432:81–94, 1999.

[217] S. Shaikhutdinov, M. Ritter, X.-G. Wang, H. Over, and W. Weiss. *Phys. Rev. B: Condens. Matter*, 60:11062–11069, 1999.

[218] W. Weiss and W. Ranke. *Prog. Surf. Sci.*, 70:1–151, 2002.

[219] A. Sala, H. Marchetto, Z.-H. Qin, S. Shaikhutdinov, Th. Schmidt, and H.-J. Freund. *Phys. Rev. B: Condens. Matter*, 86:155430(1–10), 2012.

[220] R. Meyer, S. K. Shaikhutdinov, and H.-J. Freund. *Z. Phys. Chem.*, 218:905–914, 2004.

[221] T. Schalow. *Bildung und katalytische Aktivität partiell oxidierter Pd Nanopartikel*. PhD thesis, Technische Universität, 2006.

[222] L. Liu, B. R. Quezada, and P. C. Stair. *J. Phys. Chem. C.*, 114:17105–17111, 2010.

[223] A. Savara. personal correspondence. 2012.

[224] V. Matolin and I. Stara. *Surf. Sci.*, 398:117–124, 1997.

[225] A. Kapoor, R.T. Yang, and C. Wong. *Cat. Rev. - Sci. Eng.*, 31:129–214, 1989.

[226] R. Gomer, R. Wortman, and R. Lundy. *J. Chem. Phys.*, 26:1147–1164, 1956.

[227] M. Boudart and G. Djega-Mariadassou. Kinetics of heterogeneous catalytic reactions. *Princeton Univ. Press*, 1984.

[228] L. Zhu, K.L. Yao, and Z. L. Liu. *Phys. Rev. B: Condens. Matter*, 74:035409(5–10), 2006.

[229] J. H. Fischer-Wolfarth, J. A. Farmer, J. M. Flores-Camacho, A. Genest, I. V. Yudanov, N. Rösch, C. T. Campbell, S. Schauermann, and H-J. Freund. *Phys. Rev. B: Condens. Matter*, 81:241416(1–4), 2010.

[230] R. L. Whetten, D. M. Cox, D. J. Trevor, and A. Kaldor. *Phys. Rev. Lett.*, 54:1494–1497, 1985.

[231] A. Eichler, F. Mittendorfer, and J. Hafner. *Phys. Rev. B: Condens. Matter*, 62:4744–4755, 2000.

[232] P. Sjovall and P. Uvdal. *J. Vac. Sci. Technol., A*, 16:943–947, 1998.

[233] F. P. Leisenberger, G. Koller, M. Sock, S. Surnev, M. G. Remsey, F. P. Netzer, K. B. Klötzer, and K. Heyek. *Surf. Sci.*, 445:380–393, 2000.

[234] Andrea Gerbi, Letizia Savio, Luca Vattuone, Fernando Pirani, David Cappellletti, and Mario Rocca. *Angew. Chem. Int. Ed.*, 45:6655–6658, 2006.

[235] J. Goschnick, M. Wolf, M. Grunze W.N. Unertl, J.H. Block, and J. Loboda-Cackovic. *Surf. Sci.*, 178:831–841, 1986.

[236] P. Junell, K. Honkala, M. Hirsimaki, M. Valden, and K. Laasonen. *Surf. Sci.*, 546:L797–L802, 2003.

[237] R. Imbihl and J.E. Demuth. *Surf. Sci.*, 173:395–410, 1986.

[238] F. Mittendorfer, N. Seriani, O. Dubay, and G. Kresse. *Phys. Rev. B: Condens. Matter*, 76: 233413(1–4), 2007.

[239] T. Matsushima. *Surf. Sci.*, 157(297-318), 1985.

[240] M. Wolf, E. Hasselbrink, J. M. White, and G. Ertl. *J. Chem. Phys.*, 93:204–213, 1990.

[241] D. L. Weissman-Wenocur, M. L. Shek, P. M. Stefan, I. Lindau, and W. E. Spicer. *Surf. Sci.*, 127:513–525, 1983.

[242] S. Nagarajan, K. Thirunavukkarasu, and C.S. Gopinath. *J. Phys. Chem. C.*, 113:7385–7397, 2009.

[243] E. Lundgren, G. Kresse, C. Klein, M. Borg, J.N. Andersen, M. De Santis, Y. Gauthier, C. Konvicka, M. Schmid, and P. Varga. *Phys. Rev. Lett.*, 88:246103–1246103–4, 2002.

[244] J. Klikovits, E. Napetschnig, M. Schmid, N. Seriani, O. Dubaz, G. Kresse, and P. Varga. *Phys. Rev. B: Condens. Matter*, 76:045405(1–9), 2007.

[245] C. Nyberg and C. G. Tengstal. *Surf. Sci.*, 126:163–169, 1983.

[246] N. Ohta, Y. Ohno, and T. Matsushima. *Surf. Sci. Lett.*, 276:L1–L6, 1992.

[247] T. Matsushima, Y. Ohno, and J. Murakami. *Surf. Sci.*, 287:192–195, 1993.

[248] T. W. Orent and S. D. Bader. *Surf. Sci.*, 115:323–334, 1981.

[249] G. W. Simmons, Y. N. Wang, J. Marcos, and K. Klier. *J. Phys. Chem.*, 95:4522–4528, 1991.

[250] M. Saidy, O.L. Warren, P.A. Thiel, and K.A.R. Mitchell. *Surf. Sci. Rep.*, 494:L799–L804, 2001.

[251] M. Todorova, E. Lundgren, V. Blum, A. Mikkelsen, S. Gray, J. Gustafson, M. Borg, J. Rogal, K. Reuter, J.N. Andersen, and M. Scheffler. *Surf. Sci.*, 541:101–112, 2003.

[252] J.-W. He and P.R. Norton. *Surf. Sci.*, 204:26–34, 1988.

[253] M. Nishijima, M. Jo, Y. Kuwahara, and M. Onchi. *Solid State Commun.*, 60:257–260, 1986.

[254] T. Matsushima. *Surf. Sci.*, 217:155–166, 1989.

[255] K. Yagi and H. Fukutani. *Surf. Sci.*, 412/413:489–494, 1998.

[256] J. W. He, U. Memmert, and P. R. Norton. *J. Chem. Phys.*, 90:5088–5093, 1989.

[257] K. Yagi, K. Higashiyama, and H. Fukutani. *Surf. Sci.*, 295:320–240, 1993.

[258] M. Jo, Z. Kuwahara, M. Onchi, and M. Nishijima. *Chem. Phys. Lett.*, 131:106–111, 1986.

[259] M. Milun, P. Pervan, M. Vajic, and K. Wandelt. *Surf. Sci.*, 211-212:887–895, 1989.

[260] R. Westerström, J. Gustafson, A. Resta, Am. Mikkelsen, J. N. Andersen, E. Lundgren, F Mittendorfer, P. Varger, M. Frenken, and A. Stierle. *Phys. Rev. B: Condens. Matter*, 76: 155410(1–9), 2007.

[261] F. Li, F. Allegretti, S. Surnev, F. P. Netzer, Y. Zhang, W.-B. Zhang, and K. Reuter. *Surf. Sci.*, 604:1813–1819, 2010.

[262] A. Vlad, A. Stierle, R. Westerström, S. Blomberg, A. Mikkelsen, and E. Lundgren. *Phys. Rev. B: Condens. Matter*, 86:035407 (1–9), 2012.

[263] S.-L. Chang, P. A. Thiel, and J. W. Evans. *Surf. Sci.*, 205:117–142, 1988.

[264] Y. Zhang, J. Rogal, and K. Reuter. *Phys. Rev. B: Condens. Matter*, 74:125414(1–9), 2006.

[265] A. N. Salanov, A. I. Titkov, and V. N. Bibin. *Kinet. Catal.*, 47:430–436, 2004.

[266] K. Wolter, O. Seiferth, H. Kuhlenbeck, and M. Bäumer. *Surf. Sci.*, 399:190–198, 1998.

[267] P. Hollins. *Surf. Sci. Rep.*, 16:51–94, 1992.

[268] J. T. Yates and T. E. Madey. *Vibrational Spectroscopy of Molecules on Surfaces*. Springer, Weinheim, 1987.

[269] H. Conrad, G. Ertl, J. Kocha, and E.E. Latta. *Surf. Sci.*, 43:462–480, 1974.

[270] R.D. Ramsier, K.-W. Lee, and J.T. Yates. *Surf. Sci.*, 322:243–255, 1995.

[271] Ilya V. Yudanov, Manuela Metzner, Alexander Genest, and Notker Rösch. *J. Phys. Chem. C.*, 112:20269–20275, 2008.

[272] Pen Chou and M. Albert Vannice. *J. Catal.*, 105:342–351, 1987.

[273] Y. Y. Yeo, L. Vattuone, and D. A. King. *J. Chem. Phys.*, 106:1990–1996, 1997.

[274] A. M. Bradshaw and F. Hoffmann. *Surf. Sci.*, 52:449–454, 1975.

[275] M. Tüshaus, W. Berndt, H. Conrad, A.M. Bradshaw, and B. Persson. *Appl. Phys. A.*, 51: 91–98, 1990.

[276] A. M. Bradshaw and F. M. Hoffmann. *Surf. Sci.*, 72:513–535, 1978.

[277] R. J. Behm, K. Christmann, G. Ertl, and M. A. Van Hove. *J. Chem. Phys.*, 73:2984–2995, 1980.

[278] P. Uvdal, P.-A. Karlsson, C. Nyberg, S. Andersson, and N. V. Richardson. *Surf. Sci.*, 202: 167–182, 1988.

[279] J. N. Anderson, M. Qvarford, R. Nyholm, S. L. Sorensen, and C. Wigren. *Phys. Rev. Lett.*, 67:2822–2825, 1991.

[280] W. Berndt and A.M. Bradshaw. *Surf. Sci. Lett.*, 279:L165–L169, 1992.

[281] Jutta Rogal, Karsten Reuter, and Matthias Scheffler. *Phys. Rev. B: Condens. Matter*, 75: 205433(1–11), 2007.

[282] U. V. Yudanov, R. Sahnoun, K. M. Neyman, N. Rösch, J. Hoffmann, S. Schauermann, V. Johanek, H. Unterhalt, G. Rupprechter, J. Libuda, and H. J. Freund. *J. Phys. Chem. B*, 107:255–264, 2002.

[283] I. Stara, E. Tomkova, and V. Matolin. *Czech. J. Phys.*, 43:1023, 1993.

[284] S. A. King. *Critical Rev. Solid State Mater. Sci.*, 7:167, 1978.

[285] U. Burghaus, I. Z. Jones, and M. Bowker. *Surf. Sci.*, 454-456:326–330, 2000.

[286] A. V. Kalinkin, V. I. Savchenko, and A. V. Pashis. *Catal. Lett.*, 59:115–119, 1999.

[287] J. D. Cox, D. D. Wagman, and V. A. Medvedev. *CODATA Key Values for Thermodynamics*. Hemisphere Publishing Corp., New York, 1989.

[288] S. Diezi, M. Hess, E. Orglmeister, T. Mallat, and A. Baiker. *J. Mol. Cat. A.*, 239:49–56, 2005.

[289] E. Orglmeister, T. Mallat, and A. Baiker. *Adv. Synth. Catal.*, 347:78–86, 2005.

[290] T. Bürgi and A. Baiker. *Acc. Chem. Res*, 37:909–917, 2004.

[291] S. Lavoie, M-A. Laliberte, and P. McBreen. *Catal. Lett.*, 97:111–114, 2004.

[292] S. Lavoie, M-A. Laliberte, I. Temprano, and P. H. McBreen. *JACS*, 128:7588–7593, 2006.

[293] G. Vayner, K. N. Houk, and Y.-K. Sun. *JACS*, 126:199–203, 2004.

[294] N. Maeda, K. Hungerbühler, and A. Baiker. *JACS*, 133:19567–19569, 2011.

[295] R. Raval. *CATTECH*, 5:12–28, 2001.

[296] T. Osawa, T. Harada, and O. Takayasu. *Curr. Org. Chem.*, 10:1513, 2006.

[297] F. Zaera. *J. Phys. Chem.*, 112:16196–16203, 2008.

[298] T. Mallat, E. Orglmeister, and A. Baiker. *Chem. Rev.*, 107:4863–4890, 2007.

[299] S. Lavoie, M.-A. Laliberte, and P. H. McBreen. *JACS*, 125:15756–15757, 2003.

[300] I. Lee and F. Zaera. *J. Phys. Chem. B*, 109:12920–12926, 2005.

[301] F. Gao, Y. Wang, L. Burkholder, and W. T. Tysoe. *JACS*, 129:15240–15249, 2007.

[302] D. Stacchiola, L. Burkholder, and W. T. Tysoe. *JACS*, 124:8984–8989, 2002.

[303] I. Lee and F. Zaera. *JACS*, 128:8890–8898, 2006.

[304] I. Lee, Z. Ma, S. Kaneko, and F. Zaera. *JACS*, 130:14597–14604, 2008.

[305] A. D. Gordon and F. Zaera. *Angew. Chem. Int. Ed.*, 52:1–5, 2013.

[306] J. M. Bonello, F. J. Williams, and R. M. Lambert. *JACS*, 125:2723–2729, 2003.

[307] J. M. Bonello, E. C. H. Sykes, R. Lindsay, F. J. Williams, A. K. Santra, and R. M. Lambert. *Surf. Sci.*, 482-485:207–214, 2001.

[308] L. Burkholder, D. Stacchiola, J. A. Boscoboinik, and W. T. Tysoe. *J. Phys. Chem. C.*, 113:13877–13885, 2009.

[309] J. A. Boscoboinik, Y. Bai, L. Burkholder, and W. T. Tysoe. *J. Phys. Chem. C.*, 115: 16488–16494, 2011.

[310] L. Burkholder, M. Garvey, M. Weinert, and W. T. Tysoe. *J. Phys. Chem. C.*, 2011.

[311] A. Dinger, C. Lutterloh, J. Biener, and J. Küppers. *Surf. Sci.*, 449:1–18, 2000.

[312] J. L. Sales, V. Gargiulo, I. Lee, F. Zaera, and G. Zgrablich. *Catal. Today*, 158:186–196, 2010.

[313] C. T. Campbell, G. Ertl, H. Kuipers, and J. Segner. *Surf. Sci.*, 107:207–219, 1981.

[314] H. Steininger, S. Lehwald, and H. Ibach. *Surf. Sci.*, 123:264–282, 1982.

[315] G. Ertl, M. Neumann, and K. M. Streit. *Surf. Sci.*, 64:393–410, 1977.

[316] A. Y-C. Yu, W. E. Spicer, and G. Hass. *Phys. Rev. B: Condens. Matter*, 171:834–835, 1968.

[317] G. Santarossa, M. Iannuzzi, A. Vargas, and A. Baiker. *ChemPhysChem*, 9:401–413, 2008.

[318] D. W. Goodman. *Surf. Sci.*, 299-300:837–848, 1994.

Danksagungen

Ich danke Prof. Dr. Freund für die Möglichkeit, meine Promotion im CP Department des Fritz-Haber-Insituts durchzuführen: Die Fragestellungen waren sehr interessant und die experimentellen Möglichkeiten in der Gruppe sind ausgezeichnet.

Ich danke Prof. Dr. Joachim Sauer für die Bereitschaft meine Arbeit zu begutachten.

Ich danke PD Dr. Swetlana Schauermann für wichtige Diskussionen, die maßgeblich zum Erfolg dieser Doktorarbeit beigetragen haben.

Ich danke Dr. Sergey Adamovsky für viele anregende Diskussionen und die Hilfe beim Lösen experimenteller Probleme. Ich arbeitete auch mit Dr. Jose Manuel Flores-Camacho zuammen, der mir eine gründliche Einführung in die Molekularstrahlanlage gab. Ich danke Petr Dementyev, der derzeit experimentelle Studien an der Mikrokalorimetrieanlage durchführt und mit dem ich mehrere Monate gut zusammenarbeitete. Ich danke auch Dr. Jan-Hendrik Fischer-Wolfarth und Jens Harmann: Ich hatte die Möglichkeit an einem gut funktionierenden experimentellen Aufbau zu arbeiten.

Ich danke Dr. Aditya Savara, Karl-Heinz Dostert und Dr. Casey O'Brian für anregende Diskussionen.

Ich danke auch den Mitarbeitern der Werkstädten und Klaus-Peter Vogelgesang für ihre Unterstützung bei Reparaturen.

Ich danke allen Mitarbeitern und Mitstudenten des Departments für Chemische Physik für die nette Arbeitsatmosphäre und die gute Zusammenarbeit.

Schlussendlich danke ich meiner Familie, besonders meinen Eltern, die mich mein ganzes Leben liebten. Dank ihnen hatte ich eine sorglose und behütete Kindheit.

Selbständigkeitserklärung

Ich erkläre, dass ich die vorliegende Arbeit selbständig und nur unter Verwendung der angegebenen Literatur und Hilfsmittel angefertigt habe.

Berlin, den 29.10.2013 Matthias Peter